

An Intercomparison of Intraseasonal Variability in General Circulation Models and Observations

**Chung-Kyu Park, David M. Straus,
Ka-Ming Lau, and Siegfried D. Schubert**

August 1990

(NASA-TM-100764) AN INTERCOMPARISON OF
INTRASEASONAL VARIABILITY IN GENERAL
CIRCULATION MODELS AND OBSERVATIONS (NASA)
122 B CSCL 043

N90-27273

Unclas
G3/47 0297562



An Intercomparison of Intraseasonal Variability in General Circulation Models and Observations

Chung-Kyu Park
Centel Federal Services Corporation
Reston, Virginia

David M. Straus
Center for Ocean-Land-Atmosphere Interactions
Department of Meteorology
University of Maryland
College Park, Maryland

Ka-Ming Lau and Siegfried Schubert
Laboratory for Atmospheres
NASA-Goddard Space Flight Center
Greenbelt, Maryland



National Aeronautics and
Space Administration

Goddard Space Flight Center
Greenbelt, MD

1990

TABLE OF CONTENTS

ACKNOWLEDGMENTS

LIST OF FIGURES

ABSTRACT

I. INTRODUCTION

II. DESCRIPTION OF THE GCMS AND OBSERVATIONAL DATA

III. GENERAL FEATURES OF INTRASEASONAL VARIABILITY

a 200 mb velocity potential

b Vertical heating profile

IV. COMPOSITE ANALYSIS

a Horizontal structure of wind and height

b Vertical structure of the zonal component of wind

c Vertical structure of moisture

V. TROPICAL/EXTRATROPICAL INTERACTIONS

VI. DISCUSSION AND CONCLUSIONS

VII. REFERENCES

APPENDIX: SEASONAL MEAN PATTERNS

A. Longitude-latitude maps

B. Latitude-pressure sections

C. Longitude-pressure sections

Acknowledgments

This work was supported by the climate program at the NASA/ Goddard Space Flight Center through NASA grant NAG 5-1094. We would like to thank Laura Rumburg for drafting the figures.

LIST OF FIGURES

- Figure 1 Total variance distribution of five-day means of the 200 mb velocity potential. (a) GLAS GCM, (b) UCLA GCM, (c) GLA GCM, (d) ECMWF analyses. Contour interval is $2.0 \times 10^{12} \text{ m}^4 \text{ s}^{-2}$.
- Figure 2 As in Figure 1, except for the filtered time series for 30-60 day periods. Contour interval is $1.0 \times 10^{12} \text{ m}^4 \text{ s}^{-2}$.
- Figure 3 Power spectra of 200 mb velocity potential at selected grid points for ECMWF analyses. Units are $10^{11} \text{ m}^4 \text{ s}^{-2}$. Abscissa represents period in days.
- Figure 4 As in Figure 3, except for the GLAS GCM.
- Figure 5 As in Figure 3, except for the UCLA GCM.
- Figure 6 As in Figure 3, except for the GLA GCM.
- Figure 7 Hovmoller diagram of filtered 200 mb velocity potential in the tropics (20°S - 20°N) for ECMWF analyses for 1984-86. Contour interval is $1.0 \times 10^6 \text{ m}^2 \text{ s}^{-1}$. Values greater than $1.0 \times 10^6 \text{ m}^2 \text{ s}^{-1}$ are shaded. Negative values are represented by dotted lines. Zero contours are not drawn.
- Figure 8 As in Figure 7, except for GLAS GCM.
- Figure 9 As in Figure 7, except for UCLA GCM.
- Figure 10 As in Figure 7, except for GLA GCM.
- Figure 11 One-point correlation of 200 mb velocity potential using a base point of 120°E at the equator for five-day mean ECMWF analyses, with lags of (a) -10 days, (b) -5 days, (c) 0 days, (d) +5 days, and (e) +10 days. Correlations are computed from filtered data, with isolines drawn for every 0.1 for values exceeding ± 0.1 .
- Figure 12 As in Figure 11, except for the GLAS GCM.
- Figure 13 As in Figure 11, except for the UCLA GCM.
- Figure 14 As in Figure 11, except for the GLA GCM.

- Figure 15 Wavenumber-frequency spectra of 200 mb velocity potential at the equator for (a) GLAS, (b) UCLA, (c) GLA GCMs and (d) ECMWF analyses. Left (right) hand panels correspond to westward (eastward) propagating waves. Contour interval is $2.0 \times 10^{11} \text{ m}^4 \text{ s}^{-2}$. For values greater than $2.0 \times 10^{12} \text{ m}^4 \text{ s}^{-2}$, contour interval is $8.0 \times 10^{11} \text{ m}^4 \text{ s}^{-2}$.
- Figure 16 As in Figure 15, except at 30°N .
- Figure 17 As in Figure 15, except at 30°S .
- Figure 18 Latitude-frequency spectra of 200 mb velocity potential for zonal wavenumber one for (a) GLAS, (b) UCLA, (c) GLA GCMs and (d) ECMWF analyses. Left (right) hand panels correspond to westward (eastward) propagating waves. Contour interval is $4.0 \times 10^{11} \text{ m}^4 \text{ s}^{-2}$. For values greater than $2.0 \times 10^{12} \text{ m}^4 \text{ s}^{-2}$, contour interval is $12.0 \times 10^{11} \text{ m}^4 \text{ s}^{-2}$.
- Figure 19 As in Figure 18, except for zonal wavenumber two.
- Figure 20 As in Figure 18, except for zonal wavenumbers 3-10.
- Figure 21 Longitude/pressure section of diabatic heating along the equator for the 30-60 day oscillation, based on the velocity potential in the region 10°S - 10°N , 120°E - 180° for GLAS, UCLA and GLA GCMs. See text for details. Contour interval is 1.0°K/day . Positive regions are shaded. Diabatic heating greater than 3.0°K/day is represented by darker shading.
- Figure 22 As in Figure 21, except for vertical profile of diabatic heating averaged in the western tropical Pacific (10°S - 10°N , 120°E - 180°). Units are $^\circ\text{K/day}$.
- Figure 23 Tropical 200 mb flow for the Indian Ocean - western Pacific composite for GLAS, UCLA and GLA GCMs. Reference vector for 2 m/sec is shown at the bottom.
- Figure 24 As in Figure 23, except for 850 mb flow. Reference vector for 1 m/sec is shown at the bottom.
- Figure 25 As in Figure 23, except for 200 mb geopotential height. Contour interval is 10.0 m. Negative regions are shaded.

- Figure 26 Longitude-height sections of the u-wind for the Indian Ocean-western Pacific composite along the equator (see text for details) from ECMWF analyses, for lags of -10 days, -5 days, 0 days, +5 days, and +10 days. Units are m s^{-1} .
- Figure 27 As in Figure 26, except for the GLAS GCM.
- Figure 28 As in Figure 26, except for the GLA GCM.
- Figure 29 Longitude - height sections of the specific humidity for the Indian Ocean - western Pacific composite along the equator (see text for details) from ECMWF analyses, for lags of -10 days, -5 days, 0 days, +5 days, and +10 days. Units are g kg^{-1} .
- Figure 30 As in Figure 29, except for the GLAS GCM.
- Figure 31 As in Figure 29, except for the GLA GCM.
- Figure 32 Seasonal mean patterns of 200 mb u-wind for the GLAS, UCLA, GLA GCMs and ECMWF analyses for the Northern Hemisphere winter (October-March). Contour interval is 5.0 ms^{-1} . Easterlies are shaded.
- Figure 33 As in Figure 32, except for the Northern Hemisphere summer (April-September).
- Figure 34 Cross-correlation pattern of 200 mb zonal wind and the 200 mb velocity potential located at the equator and 120°E , for the northern winter (October-March) from ECMWF analyses, for lags of -5 days, 0 days, and +5 days. Contour interval is 0.2. Values greater than 0.3 or less than -0.3 are shaded. Dotted lines are used for negative values.
- Figure 35 As in Figure 34, except for the northern summer (April-September).
- Figure 36 As in Figure 34, except for the GLAS GCM.
- Figure 37 As in Figure 35, except for the GLAS GCM.
- Figure 38 As in Figure 34, except for the UCLA GCM.
- Figure 39 As in Figure 35, except for the UCLA GCM.
- Figure 40 As in Figure 34, except for the GLA GCM.
- Figure 41 As in Figure 35, except for the GLA GCM.

ABSTRACT

Low-frequency variability is examined with a focus on the 30-60 day oscillations in General Circulation Model (GCM) integrations made with the GLAS GCM, the UCLA GCM, and the GLA GCM. A comparison with global ECMWF analyses of 1984-1986 was carried out. One purpose of this study is to illuminate some key issues critical to present theories about intraseasonal oscillation through intercomparison of the three GCMs and observations, and thus to provide insight for improving the critical parameterizations needed for better simulation of low-frequency variability. All three GCMs are grid point models with a 4 x 5 degree latitude/longitude resolution and with 9 layers in the vertical. The models were integrated for at least two years in the seasonal cycle mode. Each of the three GCMs employs a different scheme for computing finite differences.

The GLAS GCM simulates a realistic eastward propagation of the 30-60 day oscillation in the tropical upper-level divergent flow. The oscillation becomes quasi-stationary over the Indonesian region and accelerates over the central Pacific, as observed. In the GLA GCM, the oscillation propagates into the higher latitudes of both hemispheres as the waves leave the convective region. The eastward propagating oscillation is not obvious in the UCLA GCM. The wavenumber-frequency spectra of 200mb velocity potential reveal that all the GCMs have a significantly weaker signal of eastward propagation in the 30-60 day range than do the analyses. The spectrum for the GLAS GCM is dominated by 20-60 day periods, while the GLA GCM has a spectral peak around the 20-30 day periods. There is a weak peak near 15 days for eastward propagation in the UCLA GCM. The relationship between dominant phase speeds of the oscillation and the vertical profile of heating in the GCMs is in general agreement with current theory.

The composite patterns of the observations indicate that a Kelvin wave-type structure is dominant in the tropics near the center of the oscillation. The simulated winds are fairly realistic, although the meridional component is too strong, especially in the GLA GCM. The vertical structures of the zonal component of wind and moisture suggest that mobile wave-CISK (Lau and Peng, 1987) is an important mechanism in maintaining the intraseasonal oscillation in these GCMs. The vertical distribution of the moisture field further suggests that evaporation-wind feedback (Neelin, et al., 1987) may play a role in maintaining the eastward propagating waves in the tropics. The differences in the structures of the oscillation in the GLAS GCM and GLA GCM appear to be a consequence of the different numerical schemes used. The GCMs have preferred zones for diabatic

heating, with *turn-on* heating when the rising branch of the intraseasonal oscillation passes over these convective regions.

All three GCMs fail to capture the detailed evolution of the different stages of the development and decay of the oscillation. Results suggest that an improvement of the boundary layer moisture processes may be crucial to a better simulation of the oscillation. In addition, both the deficiencies in basic state circulations of the models and deficiencies in the 30-60 day oscillation appear to produce the unrealistic tropical-extratropical interactions in the GCMs.

I. INTRODUCTION

In recent years, there have been a large number of GCM simulation experiments of tropical intraseasonal oscillations. In general, these experiments fall into two categories. First, are experiments based on realistic boundary conditions such as observed sea surface temperatures, snow-ice distributions and topographic forcing (e.g. Lau and Lau, 1986; Hayashi and Golder, 1986; Geisler and Pitcher, 1988; Von Storch et al., 1987, Tokioka et al., 1988 and others). Many of the experiments in this category were not initially designed for studies of intraseasonal oscillations *per se*, but were motivated by more general climate concerns. Second, are simplified GCM experiments which were designed to study the basic mechanisms of intraseasonal oscillations using idealized boundary conditions i.e., aqua-planet experiments (Hayashi and Sumi, 1986, Swinbank et al., 1988) and swamp ocean experiments (Lau et al., 1988). Both categories of experiments have provided rich sources of information and testing grounds for validating theories of intraseasonal oscillations (e.g. Lau and Peng, 1987, Wang, 1988, Chang and Lim, 1988, Emanuel, 1987, Neelin et al., 1987, Hendon, 1988 and many others).

The results of the above diverse GCM experiments are generally consistent with the simple idea that the structure and eastward propagation of intraseasonal oscillations are due to the interaction between low-level moisture convergence and mid-tropospheric latent heat release from deep convection, i.e., the so-called mobile wave-CISK mechanism (Lindzen, 1974; Lau and Peng, 1987). However, a number of discrepancies still exist between model results and observations. One of the most serious difficulties is that almost all the GCM results produce oscillations with associated periods which are about 20-50% faster than the observed results (20-30 days instead of 30-60 days). Lau and Peng (1987), Sui and Lau (1989) and Takahashi (1987) suggest that the phase speed of propagation is sensitive to the level of maximum heating and that a lower level of heating will give rise to a slower phase speed of the oscillations. More recently Lau and Shen (1988) suggest that

some degree of coupling with the ocean may be required to produce the observed phase speed of these oscillations. On the other hand, Hayashi and Golder (1986) indicate that a distinct low-frequency signal at 40 days can be obtained by simply increasing the spatial resolution of the GCM. Overall, it appears that all GCM simulations indicate that some form of mobile wave-CISK mechanism is at work. Yet this mechanism is unable to explain the observed continual eastward propagation around the globe of the upper level wind field which occurs in spite of the lack of latent heat forcing over the eastern Pacific sector. Another problem is that the most "realistic" simulation of the intraseasonal oscillations appears to be associated with a turn-on latent heating over the maritime continent and tropical western Pacific rather than a propagating heat source as observed over these regions. The aqua-planet experiments simulate very well the combined eastward propagation of convection and circulation but fail to reproduce the stationary component of the oscillations. In reality, both propagating and stationary components are present in these oscillations (Lau and Chan, 1985).

Obviously, much work is still needed in GCM modeling, theory and observations in order to fully understand the dynamics of intraseasonal oscillations. In view of the diverse model structure and physical parameterizations in different GCMs, there is a need to compare the results of the climatology of intraseasonal oscillations in various GCMs as they relate to the model characteristics. This will provide us with clues for the model differences and hopefully, new insights for improving the critical parameterizations needed for better simulation of these oscillations. Archives of multiyear GCM climate integrations that now reside in various research laboratories can provide a rich repository of information from which these intercomparison studies can now be conducted without further straining resources needed for extended integrations. In this paper, a modest step is taken in this direction. Obviously, the results of this work are not going to resolve in any definitive way the aforementioned problems, but they will illuminate some key issues critical to present theories of intraseasonal oscillation and in doing so, demonstrate a methodology by which

model intercomparison can be carried out in the future. For this paper, we have had to work under the constraints that only a limited set of common parameters had been saved and that due to institutional changes and other factors, the integrations cannot be repeated exactly or extended to pin down the causes of specific differences. However, based on the present results, we shall provide some guidelines for further study of GCM intraseasonal oscillations. As our personal preference, we shall use the general terminology "intraseasonal oscillation" to refer to the 30-60 day or 40-50 day oscillation, or the Madden and Julian Oscillation, names which are also commonly used in the literature. They will be used interchangeably in the paper. The seasonal mean patterns, latitude-pressure sections and longitude-pressure sections for selected parameters are shown in the Appendix.

II. DESCRIPTION OF THE GCMS AND OBSERVATIONAL DATA

This study examines low frequency variability in General Circulation Model (GCM) integrations with the GLAS GCM, the UCLA GCM, and the GLA GCM. This is compared with global ECMWF analyses of 1984-1986. All three GCMs are grid point models with a 4×5 degree latitude/longitude resolution and with 9 layers in the vertical, and were integrated for at least two years (three in the case of the UCLA GCM) in the seasonal cycle mode. That is a smooth seasonal cycle in insolation including diurnal variation and all the other boundary conditions were introduced into the model integrations. The GLAS and GLA models use identical formulations of all physical processes, including radiation, boundary layer processes and cumulus convection. The parameterization of physical processes in the UCLA GCM are completely different and are substantially more sophisticated. Each of the three GCMs employs a different scheme for computing finite differences. They all use the vertical differencing of Arakawa and Suarez (1983).

The GLAS GCM is described in some detail by Randall (1982). This model employs a staggered grid (the so-called B grid), and the second order finite-difference scheme for horizontal momentum advection conserves momentum and kinetic energy. The cumulus parameterization scheme of Arakawa (1969, 1972), developed originally for the three-level UCLA GCM, was modified for use in a nine-level model by Somerville et al. (1974). This was accomplished by combining the lowest six layers pairwise into three layers for the purpose of cumulus convection, and restricting this process from extending into the uppermost three layers. This constraint (also present in the GLA GCM, to be described below) strongly influences the simulation of intraseasonal oscillations in the tropics. The boundary layer parameterization follows Deardorff (1972) with the assumption that the depth of the boundary layer is 500 meters everywhere. Vertical diffusion of momentum, sensible heat, and moisture above the boundary layer are negligible. Long-wave radiation (Krishnamurthy, 1982) was called once every five hours,

but the heating rates were applied every 30 minutes, while short-wave radiation (Davies, 1982) was called every 30 minutes. The two-year integration studied in this paper was described in detail by Straus and Shukla (1988a, 1988b).

The GLA GCM is *identical* to the GLAS GCM in terms of all physical parameterizations, and so differs from it only in terms of the numerical methods used. The GLA GCM utilizes an unstaggered grid (the so-called A grid) with a quadratic (energy) conserving scheme of fourth-order accuracy (Kalnay *et al.*, 1983). Sixteenth-order Shapiro filters are used in the horizontal in both the GLA and GLAS GCMs, although they are used in different ways. With the staggered grid (GLAS GCM) the filter is not necessary to integrate the model, but the filter is necessary to prevent a divergence of the solution when the unstaggered grid (GLA GCM) is used (Randall, personal communication).

The UCLA GCM (described in detail in Randall, *et al.*, 1985) uses a more recent parameterization of cumulus convection due to Arakawa and Schubert (1974) and Lord *et al.* (1982). One distinctive feature of this GCM is that the planetary boundary layer top is a prognostic variable and acts as a coordinate surface. Mass sources and sinks for the planetary boundary layer are large-scale divergence, turbulent entrainment and cumulus mass flux (Randall, 1979, 1984). The surface flux determination is that due to Deardorff (1972), and the radiation that of Schlesinger (1976). The horizontal differencing scheme uses a staggered grid, the so-called C grid. In this scheme, nondivergent flow conserves kinetic energy, while potential enstrophy is conserved by the full flow. In addition, advection of vorticity and temperature are of fourth-order accuracy.

While the global analyses prepared by the European Centre for Medium-Range Weather Forecasts (ECMWF) since 1980 were available, we chose to use only the more recent analysis of 1984-1986 because prior to 1984 the interannual variability of the divergent wind component was not reliable (Trenberth and Olson, 1988). In this study we worked primarily with five-day average fields for both the GCMs and the observations (analyses). In each case the time mean (over the entire length of the dataset) and the annual

and semiannual harmonics were removed. (These harmonics were calculated by least-squares fitting for each year separately, followed by averaging over the individual years.) For many of the diagnostics presented, the time series of five-day means was further filtered by calculating the raw Fourier components, retaining only the periods between 30 and 60 days, and performing the inverse transform.

III. GENERAL FEATURES OF INTRASEASONAL VARIABILITY

a. 200 mb velocity potential

Following previous work, we use the 200 mb velocity potential as the primary field with which to detect the presence of the tropical intraseasonal oscillations. Figures 1 and 2 show the geographical distribution of the total variance of this field (after the seasonal cycle is removed) and the low-frequency variance (filtered to retain only periods of 30-60 days), respectively for the three GCMs and the ECMWF analyses. The analyses [Figures 1(d) and 2(d)] show that the total variance maxima occur in the Indian Ocean and western Pacific region and that the strongest degree of 30-to-60 day variability occurs over the Indian Ocean, with large variability also seen over the western Pacific, and extending across the equatorial Atlantic from South America to western Africa. This pattern is similar to the structure found in the observational studies of Lau and Chan (1985, 1986) using outgoing long-wave radiation (OLR). The GLAS GCM results [Figures 1(a) and 2(a)] indicate enhanced variability over the western Pacific (although the maximum is shifted about 30 degrees too far east) and over South America. Noticeable is the absence of a distinct maximum in variability over the Indian Ocean, the region where the observed signal is the largest. The magnitude of the simulated variability is quite weak compared to observations. This is even more so in the case of the UCLA results [Figures 1(b) and 2(b)]. The GLA GCM [Figures 1(c) and 2(c)] is most realistic in terms of the overall variance pattern, but the simulated variance is still not as strong as is observed, especially over the Indian Ocean. The simulated maxima in the western Pacific region in the GLAS and GLA models are closely tied to the locations of the maxima in mean diabatic heating in these GCMs.

The variance distribution in the frequency domain is examined by spectral analysis. In Figures 3-6, each panel shows the spectral density of 200 mb velocity potential at the location represented by longitude and latitude (dotted) lines. The analyses [Figure 3] show

that the spectral power is pronounced in the period range of 20-70 days, with double peaks around 30 day and 60 day periods, in the extensive region over the Indian Ocean and western Pacific. These spectral peaks are substantially weaker in the central Pacific and high latitudes except over East Asia. The GLAS GCM [Figure 4] shows a realistic spectral distribution but much weaker 30-60 day oscillation (note different scales of y-axis). The spectral peaks are shifted toward higher frequencies. In the UCLA GCM [Figure 5], the spectra have no concentrated power in the 30-60 day period range. In the GLA GCM [Figure 6], the 30-60 day oscillation is pronounced only in the limited region over the western Pacific.

The presence of eastward propagation is described by a Hovmöller diagram of the five day mean 200 mb velocity potential in the tropics (20°S-20°N) in Figures 7 - 10 for the GCMs and the ECMWF analyses. The analyses [Figure 7] shows more coherent eastward propagation during the northern winter. The oscillation is enhanced in the Indian Ocean and western Pacific region and in the Atlantic. The GCMs [Figures 8-10] show eastward propagation, but the amplitude is substantially weaker. The GLAS GCM [Figure 8] properly simulates the enhanced amplitude and more coherent propagation during the northern winter. As indicated earlier, the UCLA GCM [Figure 9] shows very weak amplitude of eastward propagation. In the GLA GCM [Figure 10], the oscillation has too strong a standing component in the Indian Ocean and western Pacific and it is not weakened during the northern summer.

The eastward propagation feature is also revealed by one-point correlation maps of the five day mean 200 mb velocity potential. The correlations are computed from the filtered data with respect to a base point at the Equator and 120°E, as shown for the GCMs and the ECMWF analyses in Figures 11 - 14. Lags of - 10 to + 10 days are considered. The propagation is quite evident in Figure 11 for the observations, as the planetary scale (zonal wavenumber one) structure gradually moves eastward, appears to become more stationary over the Indonesian region, and then speeds up over the central Pacific. This is

consistent with the observed propagation of OLR and wind patterns for the 30 - 60 day oscillation (e.g. Lau and Chan, 1985; Knutson et al., 1986). Both theoretical analysis (Lau and Shen, 1988) and observational study (Gutzler and Madden, 1989) have suggested that the reduced phase speed of the disturbance may be related to moist Kelvin wave modes associated with enhanced convection over the warm SSTs in the western Pacific, and the increased phase speed further east to dry circulation modes due to the lack of convection over the cooler waters.

Figure 12 indicates that the GLAS GCM successfully simulates the eastward moving 30 - 60 day oscillation in the upper level divergent flow, including the acceleration of the wave after it passes the convectively active region. The one-point correlation maps of the UCLA GCM (Figure 13) are much less realistic. Only local stationary signals are apparent. These signals disappear at ± 10 days. For the GLA GCM (Figure 14), the waves are nearly stationary at the base point in the tropics, but propagate eastward dispersively into the higher latitudes of both hemispheres as the wave leaves the Indonesian region. The zonal wavenumber one character, so evident in the correlation maps of the ECMWF analyses, is present in the results from the GLAS and GLA GCMs, but is much less obvious in the UCLA correlations.

The dominant space and time scales of the eastward traveling waves can be further elucidated by the use of wavenumber - frequency spectra for the 200 mb velocity potential. Figures 15-17 show the wavenumber-frequency spectra at the Equator, 30°N and 30°S, respectively. The spectra were calculated using a Hamming window with a truncation point equal to half the total number of data points. In these figures, the ECMWF spectrum is dominated by zonal wavenumber one contribution and eastward propagation with periods of 30 to 60 days, with peaks at 30 and 60 days. The spectrum for the GLAS GCM is dominated by similar time-scales (20 to 60 days) for eastward propagation, but the overall strength of the signal is significantly weaker than observed, consistent with Figure 2. There is no indication of a distinct oscillation in the 30 to 60 day range in the UCLA

GCM spectrum, although an eastward propagating peak near 15 days is suggested at the Equator and 30°N. The GLA GCM, which has more power in the 30 to 60 day range than does the GLAS GCM but less than the ECMWF analyses, is dominated by eastward moving waves with a peak around 20 - 30 days. Thus while the GLA spectrum shows more power in the 30 - 60 day range than the GLAS spectrum, the overall *shape* of the latter is more realistic.

The latitude-frequency distribution of spectral power for zonal wavenumber one in the ECMWF analyses [Figure 18] shows that the 30-60 day oscillation is global in extent and nearly symmetric about the Equator. Planetary-scale waves in the 200 mb divergence field with 30-50 day periods were also described by Lorenc (1984) using ECMWF analyses of FGGE year. However, any equatorially trapped divergence field may possess a much larger scale velocity potential because of the relationship between the two fields (Hendon, 1986). It is noted that the eastward propagating 30-60 day waves in the velocity potential of the GLAS GCM and the UCLA GCM are more closely confined to the Equator than is the case in the analyses. The latitude-frequency spectra for zonal wavenumber two in the ECMWF analyses [Figure 19] show the dominant eastward propagating waves around 45-60 day period range in the Northern Hemisphere. It is noted that the GLA GCM has unrealistically strong eastward propagating waves in the Southern Hemisphere, with periods around 45 days and 23 days at 40°S and period around 11 days at 30°S. The latitude-frequency spectra for the zonal wavenumbers 3-10 [Figure 20] show much weaker signal in the 30-60 day oscillation in the tropics with a comparable power in the eastward and westward components. The GCMs and analyses show somewhat stronger eastward travelling component off the Equator in the Southern Hemisphere.

b. Vertical heating profile

In a series of simple numerical experiments, Lau and Peng (1987) and Sui and Lau (1989) showed that the phase speed of the intraseasonal oscillation depends in a sensitive

way upon the vertical structure of the convective heating. In order to define a diabatic heating associated with the oscillation in the GCMs, we composited the total diabatic heating on the basis of the time series of the filtered (five-day mean) velocity potential averaged over the western tropical Pacific ($10^{\circ}\text{S} - 10^{\circ}\text{N}$, $120^{\circ}\text{E} - 180^{\circ}$), and included in the composite only periods in which the velocity potential exceeded one standard deviation below the sample mean. (A minimum in the velocity potential is associated with divergence.) Longitude/height sections of the composite total diabatic heating are shown for all three GCMs in Figure 21. While the GLAS and GLA GCMs show much stronger heating rates in the composite than does the UCLA GCM, there is an important difference in vertical structure as well. The heating profile of the UCLA GCM is nearly uniform with height throughout much of the troposphere. In contrast, the other two models have their heating concentrated in the mid-troposphere, with a well-defined maximum near 500 mb and small heating rates at upper levels.¹ However, the vertical profile of composite heating averaged over the above-mentioned region [Figure 22] reveals that the region of largest heating in the GLAS GCM heating extends further downward than in the GLA GCM, so that while the latter model produces the stronger heating at its peak (near 450 mb), the GLAS GCM heating is stronger at 700 mb. Furthermore, the GLAS GCM heating exhibits only one center while the GLA GCM shows double maxima separated by 30° longitude.

According to a simple theory by Sui and Lau (1989), the downward displacement of the GLAS GCM's heating profile in comparison to that of the GLA GCM should be reflected in the phase speed of the wave, with the latter (GLA) model having the faster phase speed. This is clearly seen in the spectra, as discussed above. The absence of an intraseasonal oscillation signal in the 30 - 60 day range in the UCLA GCM is consistent with the nearly uniform profile of vertical heating, as shown by Tokioka et al. (1988) in the

¹The form of the vertical profile of diabatic heating in the GLAS and GLA GCMs is a direct consequence of the manner in which the Arakawa cumulus convection scheme was implemented in these models. In particular, no convection was allowed to penetrate into the top three model layers.

context of experiments with a five-level aqua-planet model utilizing the same Arakawa-Schubert cumulus convection scheme as in the UCLA GCM. These authors find only a fast eastward propagating wave (with a period of 10 days), which is to be compared with the period of 15 days we find in the UCLA model. However, by setting a lower limit to the entrainment of environmental air in the cumulus parameterization, thereby inhibiting very deep convection, Tokioka et al. show that a 30-60 day oscillation then does appear in conjunction with diabatic heating profiles which have a distinct peak in mid-troposphere.

The longitudinal positioning of the largest heating in the composites for each of the three GCMs coincides with the maximum of velocity potential variance in the western Pacific for that GCM seen in Figure 2. This positioning also coincides with the longitude of maximum *mean* equatorial heating in each model, as seen from maps of seasonal mean precipitation [Appendix A25-A27]. This strongly suggests that the diabatic heating associated with the intraseasonal oscillation is triggered as the sector of the wave with low-level convergence passes the region in which the model tends to produce heating in any case. Similar *turn-on* heating is found in a number of simulations of the 30 -60 day oscillation by GCMs which incorporate realistic lower boundaries (e.g. Lau and Lau, 1986; Geisler and Pitcher, 1988; Von Storch, et al. 1987). This should be contrasted to results of aqua-planet models (i.e., those with axisymmetric ocean or swamp lower boundaries), in which the precipitation follows the wave (Hayashi and Sumi, 1986; Swinbank et al. 1988; Lau, et al., 1988). The observational study of Lau and Chan (1985) showed evidence of both propagation and stationary components of convection associated with the 30-60 day oscillations.

IV. COMPOSITE ANALYSIS

In order to examine the detailed structure of the eastward propagating oscillation as it appears in the Indian Ocean and western Pacific sectors of the models and in the analyses, we use a compositing scheme which portrays the oscillation in a frame of reference moving with the wave. This scheme is a modified form of the one introduced by Lau et al. (1988), who studied this oscillation in a model with axisymmetric boundary conditions and so did not confine their attention to one particular sector. The first step of this scheme is to average each five-day mean velocity potential (from the filtered series) from 10°S to 10°N and retain only the first three zonal wavenumbers, yielding a smooth field which varies only in longitude. A translation T^- is defined which maps the minimum of the smoothed velocity potential to the origin of longitude. A second translation T^+ , which maps the maximum to the origin, is also defined. The translations T^- and T^+ are applied to whatever field (F) is to be composited, leading to the translated fields F^- and F^+ , respectively. The difference ($F^- - F^+$) is taken and is averaged over all available pentads, regardless of season. In this average, each pentad is weighted by the longitudinal rms deviation of the field F , thus serving to emphasize periods when the oscillation is strong. This average weighted difference defines the oscillation in a frame of reference attached to the moving wave. The only modification we have introduced to the scheme of Lau et al. is to exclude from the average those periods when the minimum of the velocity potential did not fall in the sector 60°E - 180°, so that we are looking at the structure of the oscillation only in the Indian Ocean - western Pacific sector.

This series of steps has been repeated using temporal lags or leads, so that the data fields being composited and the longitude shifts used refer to different times. More specifically, only one longitudinal coordinate system is used for the various time lags of a given composite, and that system gives the position with respect to the arrival of the

composite wave at zero lag. The non-zero lag composites show the fields some days before or after the arrival of the wave in this wave coordinate system. Further details are given in Lau et al. (1988).

a. Horizontal structure of wind and height

The upper level (200 mb) composite tropical circulation is shown for the GCMs and the analyses at zero lag in Figure 23. The reader should keep in mind that the composite essentially follows the wave within the broad Indian Ocean - western Pacific region, so that longitude in Figure 23 and subsequent figures is a coordinate with respect to the center of the wave. The ECMWF analyses show a very broad region of outflow dominated by the zonal component of the wind, with easterlies to the west and westerlies to the east of the wave center. The structure near the Equator clearly resembles that of a Kelvin wave, with a possibly weak Rossby wave component. The 850 mb flow (Figure 24) is nearly opposite to this. The upper-level GLAS GCM results also show outflow dominated by the zonal wind component, although the simulated meridional winds along the Equator are too strong. At 850 mb the GLAS GCM does simulate inflow, but contrary to the observations there are only very weak westerlies to the west of the reference longitude. Remarkably, the 200 mb flow simulated by the GLA model is significantly different from both the GLAS model and the observations, with very weak flow along the Equator and strong meridional outflow regions in the *subtropics* of both hemispheres. The GLA model also shows a more realistic inflow region at 850 mb, although the meridional extent of the inflow region is too narrow. The UCLA GCM shows only a weak circulation more or less in the same sense as the observation. The model does a slightly better job for the equatorial zonal wind at 850 mb, but elsewhere the circulation features are not very realistic.

The 200 mb height composite [Figure 25] for the ECMWF analyses shows a weak positive anomaly to the east (ahead) and a weak negative anomaly to the west (behind) of the oscillation center in the tropics, which are followed by enhanced subtropical response to

the north and south of the negative anomaly in the tropics. The wave-like response which appears to be emanating from the tropics is clearly identified in the extratropics. The GLAS GCM simulates a similar wave-like pattern although the subtropical response in the Southern Hemisphere is not clear. The UCLA GCM also simulates a similar pattern, but the amplitude of the response is too weak. The extratropical response pattern in the GLA GCM is significantly different from that in the observations. The unrealistic subtropical response in this model seems to be related to the upper level divergent wind with too strong a meridional component in the tropics, as indicated in Figure 23.

b. Vertical structure of the zonal component of wind

Because of the weak signals in the UCLA model, from here on we shall focus on the comparison between the GLAS model and GLA model. The evolution of the observed vertical structure of the oscillation can be seen in longitude/height sections of the composite zonal wind component at the Equator for lags ranging from -10 days to +10 days (Figure 26). The zero-lag composite shows strongest low-level inflow at about 600 mb, and strongest outflow at 200 mb, with the transition occurring at about 400 mb. The maximum low-level inflow in the u-winds is clearly above the planetary boundary layer. This characteristic signal is generally confined to a longitudinal strip extending from -60° (60° west of the wave center) to $+90^{\circ}$ (90° east of the wave center), although the upper level westerlies extend to $+120^{\circ}$. The low-level westerlies penetrate the center of oscillation at the lowest layer. A weak westward tilt with height is apparent in the low-level inflow. The composites for 5 days previous to and 5 days after the arrival of the wave have a structure which is generally similar to but weaker than the zero-lag composite. The composites for +10 days and -10 days (which are nearly the opposite of each other) retain the upper-level structure (but shifted in longitude) of the zero-lag composite with a relatively weak low-level pattern. The evolution of the waves appears to have different stages characterized by different phase speeds. Using the upper-level easterlies as

reference the phase speeds are estimated to be about $10 - 12 \text{ m s}^{-1}$ between ± 10 day and ± 5 day and $1 - 2 \text{ m s}^{-1}$ between zero day and ± 5 day. The westward tilt of zonal wind perturbations with height represents an eastward propagating unstable mode. It can be seen that the westward tilt of the wave axis becomes large as the lead or lag increases and the tilt is very small as the wave becomes concentrated and most intense at zero lag. This is consistent with the theoretical expectation of these waves as they intensify and slow down (Lau and Peng, 1987). Murakami and Nakazawa (1984) also observed the eastward propagating zonal wind perturbations with the westward tilt of wave axis.

The GLAS GCM zero-lag composite (Figure 27) shows a realistic upper level configuration and a low-level easterly wind sector to the east of the wave center. The longitudinal extent of the pattern is somewhat less than is observed. The low-level westerly winds are too weak, as discussed above, although the westward tilt with height is well simulated in the upper troposphere above the 700 mb level. The same is true of the ± 5 day composites; the fields are realistic except that the observed westerly inflow from the west is nearly absent in the model. The low-level convergence is well above the planetary boundary layer, as is observed. The wind pattern is quasi-stationary between -5 day and +5 day. There appears to be faster eastward propagation for the far-field features between ± 10 day and ± 5 day. These are qualitatively in agreement with the observations.

While the u-wind zero-lag composite from the GLA GCM (Figure 28) also indicates convergence below and divergence aloft, the convergent inflow is too strong and extends too high in the model atmosphere, with the maximum inflow occurring near 400 mb and the transition from inflow to outflow above 300 mb. The 200 mb winds are also too weak, as we have emphasized previously. The whole pattern is slightly broader in east-west extent than in the GLAS model, but is not as broad as in the analyses. There is also a strong center of westerlies at about 350 mb, located at $+120^\circ$, *to the east* of the easterly inflow branch. While westerlies at this location are in fact observed, the strong divergence apparent in the GLA results near $+80^\circ$ at 350 mb is not. The composites for lags of +5

days and -5 days are very similar to that at zero lag. The westward tilt of phase with height is very pronounced at zero lag and 5-day lag. The phase speed of the wave is quite uniform at about $3\text{--}4\text{ m s}^{-1}$.

c. Vertical structure of moisture

The Indian Ocean - western Pacific composites of specific humidity from the ECMWF analyses are shown in Figure 29. At low levels the moisture is greatest to the east of (ahead of) the wave center at zero lag, while the driest air is behind the wave. The moist air extends all the way to the surface. Because the pattern tilts westward with height, the moistest air lies almost at the wave center at mid-levels. The composites for various time lags show basically similar patterns, although translated in the zonal direction. The relatively slow motion of the wave in the build-up phase (between - 5 days and zero lag) compared to the subsequent large 5-day shift is an evidence of the wave acceleration eastward of the region of maximum convection mentioned in Section III. While the compositing technique averages the structure of the wave across the very wide Indian Ocean / western Pacific sector, a remnant of this dramatic acceleration in the eastern portion of the sector survives the averaging process. The overall signature of the oscillation is even broader in the moisture field (around 200° of longitude at zero lag) than was the case for the u-wind. The above features suggest that there is a dramatic difference in the basic physics between the build-up and decay phases of these intraseasonal oscillations.

The large-scale structure of the moisture field in the GLAS GCM composite at zero lag (Figure 30) is generally realistic, although it is far noisier than in the observations, and more narrowly confined in longitude. The low-level moisture maximum ahead of the wave center, the drying behind it, and the westward tilt with height are all present, although the region of highest moisture content (over 0.4 g /kg) does not extend to the surface, as it does in the ECMWF analyses. While the - 5-day lag composite correctly shows little shift in the position of the maximum from the zero lag composite, the shift seen in the

observations at + 5 days is absent in the model. Instead we see a new area of high moisture well ahead of the wave center. Smoothing this simulated field would give a result more comparable to the analyses at + 5 days.

The equatorial specific humidity composite at zero lag for the GLA GCM (Figure 31) is similar to that from the GLAS GCM down to about 850 mb, but near the surface the GLA GCM shows substantial drying. Apparently, moisture convergence in the boundary layer itself is not required to sustain the oscillation; convergence above the boundary layer is sufficient. The configuration of the moisture field in the longitudinal range of -60° to $+60^\circ$ is like that of the GLAS GCM, only shifted up in the vertical. This upward displacement of the whole wave pattern was also seen in the u-winds discussed above. The rapid movement of the low-level moist tongue seen in the ECMWF composites in going from 0 to 5 days is also reproduced in this model.

In general, the vertical structure of moisture appears to be closely coupled with the zonal circulation in the equatorial plane, in both the observations and the GCMs. The zonal circulation supplies moisture to the east of the oscillation center in the convergence zone and leaves the dry zone behind the low-level westerlies, consistent with the presence of the evaporation-wind feedback mechanism for maintaining the oscillation. However, it is not clear that this mechanism is essential for the existence of the oscillation. For example, the composites of the oscillation in the study of Lau et al. (1988) with and without evaporation-wind feedback look nearly identical. It must be stressed that determining the cause of the oscillation from composited fields may be quite difficult, since the relevant maintenance terms in the thermodynamic and moisture budgets are likely to be very small residuals.

V. TROPICAL/EXTRATROPICAL INTERACTIONS

The connection between the tropical convection fluctuations and midlatitude circulation anomalies on a 30-60 day time scale has been examined in a number of studies (e.g. Weickmann, et al., 1985; Lau and Phillips, 1986; Knutson and Weickmann, 1987; Nitta, 1987, Schubert and Park, 1990). In this section we examine the global features of anomalous circulation in association with the tropical oscillations by one-point correlation using the 200 mb zonal component of wind from the ECMWF global analyses and GCMs. The correlations were computed between the filtered zonal component of wind and a grid point of the filtered 200 mb velocity potential located at the Equator and 120°E for the Northern Hemisphere winter (October-March) and the Northern Hemisphere summer (April-September), separately. The 6-month data period was used to increase the significance of the correlation. The 200 mb zonal wind for the GCMs and analyses are shown in Figures 32 and 33 for the Northern Hemisphere winter and the Northern Hemisphere summer, respectively. The observations show the easterly maximum in the Indonesian region and wide westerly zone in the eastern tropical Pacific during the Northern Hemisphere winter. The tropical easterlies are intensified in the Indian Ocean during the Northern Hemisphere summer. The easterlies in the models are somewhat too weak in both seasons. None of the models properly simulate the northeast tilt of the North Atlantic subtropical jet axis in the Northern Hemisphere winter. It is noted that the Southern Hemispheric subtropical jet is too strong in the GLA GCM, particularly in the Northern Hemisphere winter.

Figure 34 shows the cross correlation patterns of the 200 mb zonal wind with respect to the 200 mb velocity potential located at the Equator and 120°E during the Northern Hemisphere winter from the observations. The patterns are shown separately for the Eastern Hemisphere in the left-hand side and for the Western Hemisphere in the right-

hand side for the lags of -5, 0 and +5 days. The dominant pattern is an eastward propagating wavenumber one structure in the tropics. The most coherent extratropical signal is found in the subtropical western Pacific near the East Asian jet region which shows a dipole pattern straddling the jet. This pattern shows an eastward shift of about 20° longitude in 10 days. The dipole patterns seem to be reminiscent of standing oscillations of global circulation modulated by eastward propagating tropical oscillations in the Indian Ocean and western Pacific regions. Although the extratropical signal is generally weaker in the Southern Hemisphere, the positive correlations in the Southeast Australia and South America regions appear to be related to the tropical oscillations.

The Northern Hemisphere winter pattern of upper level wind from the observations [Figure 32] indicates that the western tropical Pacific is characterized by strong easterlies and the tropical Atlantic and eastern Pacific regions are covered by westerlies. The localized dipole structure of the correlation in the western Pacific may be due to the restricted meridional wave propagation in the easterly zone. On the other hand, the wave-like pattern in the Atlantic may be related to increased meridional wave propagation possibly in the westerly region. This is in agreement with the results of Lau et al. (1990).

The Northern Hemisphere summer correlation patterns from the observations are shown in Figure 35. The tropics again show an eastward propagating wavenumber one pattern. The most pronounced extratropical response is found in the western Pacific and East Asian regions at day -5. The correlation patterns suggest that the divergent mode of tropical oscillations is related to anomalous anticyclonic/cyclonic circulation in the midlatitudes of continental East Asia. It is noted that there are some indications of northward propagating disturbances in the eastern Pacific. The structure of the correlation in the North Atlantic suggests that wave propagation from the high latitudes into the tropics is particularly strong 5-days prior to the extreme divergence/convergence over Indonesia. The connection between the Pacific dipole pattern and the pattern over the eastern Atlantic is not immediately clear. The wave-like patterns are not as clear as those in the Northern

Hemisphere winter. The extratropical signal becomes weaker in the summer hemisphere as the oscillation center moves into the western Pacific. The signal is pronounced near the Australian jet region (although not clearly seen in this projection) at day +5 which seems to be related to the anomalous tropical circulation south of Indonesia. We found little evidence for wave propagations in the Southern Hemisphere extratropics.

The correlation patterns for the GLAS GCM are shown in Figures 36 and 37 for the Northern Hemisphere winter and the Northern Hemisphere summer, respectively. These figures show that the large-scale eastward travelling wavenumber one pattern found in the ECMWF analyses is not well established in the model tropics for both seasons. Since the realistic eastward propagating features were detected in the GLAS model from the irrotational part of wind in Figure 12, the stationary features of wind associated with eastward travelling tropical oscillations in these correlation patterns are probably associated with the nondivergent part of wind dominant in the model tropics. The most pronounced tropical/extratropical teleconnection is found in the Australian and East Asian sector during the Northern Hemisphere winter. The extratropical response in East Asia propagates northward and appears to propagate into the Western Hemisphere. The basic state circulations [Figure 32] with westerly bias in the model tropics may provide unrealistically favorable conditions for wave propagation in the western Pacific. It is also indicated that the patterns are somewhat shifted northward compared to the observations shown in Figure 34. The Northern Hemisphere winter patterns of upper level wind [Figure 32] indicate that the East Asian jet is shifted farther north in the GLAS GCM compared to the observations. The model simulates realistic extratropical signals in the Southeast Australia and South America regions. In Figure 37, the tropics and extratropics relationship is not clear in the model during the Northern Hemisphere summer. The model results of Simmons et al. (1983) and Branstator (1983) suggested that the basic state circulation is an important factor in determining the extratropical circulation anomaly responding to the tropical heating fluctuations. The substantially different basic state circulations [Figure 33] in the model

and the observations suggest one reason for the unrealistic response of extratropical circulations to the tropical oscillations.

The correlation patterns for the UCLA GCM [Figures 38 and 39] are unrealistic, showing little coherence in the large scale. As described earlier, the model has much weaker-than-observed power in the period range of the 30-60 days. This deficiency may be responsible for the overall failure of the proper tropical response and the extratropical teleconnection in the UCLA GCM. The correlation patterns for the GLA GCM show more coherence but show little connection with the patterns from the ECMWF analyses. The tropics/extratropics interactions in the GLA GCM [Figures 40 and 41] are also not realistic. The unrealistic correlation patterns may be due to the inappropriate upper level divergent flow associated with the tropical oscillations. As indicated by the composite wind patterns [Figure 23], the upper level divergent flow is dominated by meridional component of wind in the tropics.

VI. DISCUSSION AND CONCLUSIONS

A summary of the attributes of the simulation of tropical intraseasonal oscillations in the 30 to 60 day range by the various GCMs is given in Table 1. Several features of interest emerge. Neither strong variability in the 30 to 60 day band nor an accurate geographical placement of such variability is enough to guarantee realistic propagation characteristics, as witnessed by the comparison of the GLAS and GLA GCMs. The former model does a reasonable job of simulating the propagation characteristics of the eastward propagating waves as they pass the convectively active regions in the Pacific, in spite of having a rather weak signal. The latter model, although exhibiting a stronger signal, tends to propagate it more towards higher latitudes after the wave passes the convective area. This appears to be related to the excessive meridional flow at upper levels for the GLA model. The placement of the convective areas (synonymous with the region of largest variability) is tied to the region where the GCM tends to produce maximum vertically integrated diabatic heating (precipitation) in general.

The overall vertical structure of the oscillation, as seen in the moving composites, is basically realistic in both the GLAS and GLA GCMs. The GLAS model does a slightly better job in capturing the different stages of development of the oscillation. The dry conditions near the center of oscillation in the bottom layer of the GLAS GCM and GLA GCM are possibly related to insufficient moisture supply near the surface due to excessive drying of the lower troposphere by deep convection and/or a deficient wind-evaporation coupling at the surface. Particularly, the GLA GCM compensates for a lack of convergence in the planetary boundary layer by displacing the moisture convergence upward which may be related to the relatively weak zonal flow and an excessive meridional flow at 200 mb. This suggests the need to improve the boundary layer of these models, with possibly the inclusion of shallow convection.

There is a close relationship between the dominant periods that emerge from the spectrum and the overall vertical structure of diabatic heating associated with the intraseasonal oscillations. This relationship, which associates deeper heating with more rapidly moving waves, can be understood from earlier theory and simulations. It explains why the UCLA GCM, with its very deep, nearly uniform heating profile shows oscillations in the 15 day range instead of the observed 30-60 day range, and also helps to understand how the subtle difference between the GLAS and GLA GCM heating profiles (the former extends further downwards from its 450 mb maximum) leads to a more realistic (slower) phase speed for the disturbances in the GLAS GCM. This difference in heating profile is fairly robust, also appearing in composites of the diabatic heating in the moving frame of reference (not shown). The filtering which retains only 30-60 day periods is partially responsible for the different structures of low-frequency oscillation in the GLAS GCM and GLA GCM. It should be pointed out that the unrealistic heating profile in the UCLA GCM is not necessarily a result of deficiencies in model physics per se, and that the mid-tropospheric heating maxima in the GLAS GCM and GLA GCM were produced by a constraint inhibiting very deep convection.

As we have emphasized, the GLAS and GLA GCMs differ from each other *only* in the numerical methods employed in solving the equations; the formulation of the physical parameterizations is *identical* in the two models. It would require further experimentation to determine unambiguously the mechanisms by which the differences in numerical techniques result in the observed differences of the tropical intraseasonal oscillations. Although we are not able to perform these experiments, our results strongly suggest the diabatic heating as one important mechanism. In particular, the geographical location of the dominant tropical cumulus convection and its vertical profile are important in defining the regions of enhanced intraseasonal variability and its vertical structure. While the tropical mean flows of these two models do exhibit differences, the consequences of these differences to the intraseasonal oscillations we present here are likely to be secondary to the

effects of diabatic heating. However, the extent of the easterlies in the time-mean flow may significantly affect the nature and strength of the tropical-extratropical teleconnections (e.g. Schubert and Park, 1990). The different basic state circulations in the model and observations appear to be responsible for the the unrealistic extratropical circulation anomalies in the GCMs. Particularly, in the GLA GCM the overall failure of simulating the realistic tropical-extratropical interactions appears to be related to the inappropriate upper level divergent flow with too strong a meridional component in the tropics associated with the oscillation.

The models examined here have strongly preferred zones for diabatic heating, and the oscillation is forced as the region of large-scale ascent enters these preferred convective regions. Such a *turn-on* heating is observed in the intraseasonal oscillations produced by other GCMs with realistic lower boundaries. Finally, the present analysis is focused on the convective regime of the 30-60 day oscillations. Observations indicate that there is also a dry regime where the circulations seem to be maintained (with faster phase speed) in the absence of convection. The reasons for the fixed nature of the heating in realistic models, as opposed to the highly mobile convection in models with idealized lower boundaries, and the maintenance of the circulation in the absence of convection during part of its journey around the globe are major concerns for future investigation.

Table 1. Summary of GCM Performance

	GLAS GCM	UCLA GCM	GLA GCM
Spectral Signal			
Strength	weak	very weak	moderately weak
Dominant periods	realistic (30-60 days)	far too short (15 days)	slightly too short (20-60 days)
Spatial Signal			
Pacific Ocean	shifted eastward moderately weak	? very weak	realistic location strong
Indian Ocean	shifted westward very weak	? very weak	realistic location moderately weak
Local Propagation (Indonesian region)			
	realistic	too stationary	disperses to high latitudes 10 days after passing Indonesia
850 mb flow (along the Equator)			
	westerly flow west west of reference longitude weak	reasonable but noisy	realistic
200 mb flow (along the Equator)			
	reasonable	no signal	zonal flow much too weak meridional flow too strong
Vertical profile of heating			
	center above 500 mb extends to low levels	very deep	center above 500 mb

VII. REFERENCES

- Arakawa, A., 1969: Parameterization of cumulus convection. Proc. WMO/IUGG Symposium on Numerical Weather Prediction, Tokyo, 26, November-4 December, 1968, Japan Meteor. Agency, IV, 8, 1-6.
- , 1972: Design of the UCLA general circulation model. Numerical simulation of weather and climate. Technical report No. 7, Department of Meteorology, UCLA, Los Angeles.
- , and W. H. Schubert, 1974: Interaction of a cumulus cloud ensemble with the large-scale environment, Part I. J. Atmos. Sci., **31**, 674-701.
- , and M. J. Suarez, 1983: Vertical differencing of the primitive equations in sigma coordinates. Mon. Wea. Rev., **111**, 34-45.
- Branstator, G., 1983: Horizontal energy propagation in a barotropic atmosphere with meridional and zonal structure. J. Atmos. Sci., **40**, 1689-1708.
- Chang, C.-P., and H. Lim, 1988: Kelvin wave-CISK: A possible mechanism for the 30-50 day oscillations. J. Atmos. Sci., **45**, 1709-1720.
- Davies, R., 1982: Documentation of the solar radiation parameterization in the GLAS climate model. NASA Technical Memorandum 83961, 57 pp.
- Deardorff, J. W., 1972: Parameterization of the planetary boundary layer for use in general circulation models. Mon. Wea. Rev., **100**, 93-106.
- Emanuel, K. A., 1987: An air-sea interaction model of intraseasonal oscillations in the tropics. J. Atmos. Sci., **44**, 2324-2340.
- Geisler, J. E., and E. J. Pitcher, 1988: On the representation of the 40-50 day oscillation in terms of velocity potential and streamfunction. J. Atmos. Sci., **45**, 1850-1854.
- Gutzler, D. S., and R. A. Madden, 1989: Seasonal variations in the spatial structure of intraseasonal tropical wind fluctuations. J. Atmos. Sci., **46**, 641-660.
- Hayashi, Y., and D. G. Golder, 1986: Tropical intraseasonal oscillations appearing in a GFDL general circulation model and FGGE data. Part I: Phase propagation. J. Atmos. Sci., **43**, 3058-3067.
- , and -----, 1988: Tropical intraseasonal oscillations appearing in a GFDL general circulation model and FGGE data. Part II: Structure. J. Atmos. Sci., **45**, 3017-3033.
- , and S. Miyahara, 1987: A three-dimensional linear response model of the tropical intraseasonal oscillation. J. Meteor. Soc. Japan, **65**, 843-852.
- Hayashi, Y.-Y., and A. Sumi, 1986: The 30-40 day oscillations simulated in an "aquaplanet" model. J. Meteor. Soc. Japan, **64**, 451-467.

- Hendon, H. H., 1986: Streamfunction and velocity potential representation of equatorially trapped waves. J. Atmos. Sci., 43, 3038-3042.
- , 1988: A simple model of the 40-50 day oscillation. J. Atmos. Sci., 45, 569-584.
- Kalnay, E., R. Balgovind, W. Chao, D. Edlmann, J. Pfaendtner, L. Takacs, and K. Takano, 1983: Documentation of the GLAS fourth order general circulation model. Volume 1: Model documentation. NASA Technical Memorandum 86064.
- Knutson, T. R., and K. M. Weickmann, 1987: 30-60 day oscillations: composite life cycles of convection and circulation anomalies. Mon. Wea. Rev., 115, 1407-1436.
- , K. M. Weickmann and J. E. Kutzback, 1986: Global scale intraseasonal oscillations of outgoing longwave radiation and 250 mb zonal wind during Northern Hemisphere summer. Mon. Wea. Rev., 114, 605-623.
- Krishnamurthy, V., 1982: The documentation of the Wu-Kaplan radiation parameterization. NASA Technical Memorandum 83926, 93 pp.
- Lau, K.-M., and P. H. Chan, 1985: Aspects of the 40-50 day oscillation during the northern winter as inferred from outgoing longwave radiation. Mon. Wea. Rev., 113, 1889-1909.
- , and P. H. Chan, 1986: Aspects of the 40-50 day oscillation during the northern summer as inferred from outgoing longwave radiation. Mon. Wea. Rev., 114, 1354-1367.
- , and L. Peng, 1987: Origin of low-frequency (intraseasonal) oscillations in the tropical atmosphere. Part I: Basic theory. J. Atmos. Sci., 44, 950-972.
- , and T. J. Phillips, 1986: Coherent fluctuations of extratropical geopotential height and tropical convection in intraseasonal time scales. J. Atmos. Sci., 43, 1164-1181.
- , and S. Shen, 1988: On the dynamics of intraseasonal oscillations and ENSO. J. Atmos. Sci., 45, 1781-1797.
- , I.-S. Kang, and P.J.. Sheu, 1990: Principal modes of intraseasonal variations in atmospheric angular momentum and tropical convection. J. Geophys. Res. Atmos., In press.
- Lau, N.-C., and K.-M. Lau, 1986: The Structure and propagation of intraseasonal oscillations appearing in a GFDL general circulation model. J. Atmos. Sci., 43, 2023-2047.
- , I.M. Held, and J.D. Neelin, 1988: The Madden-Julian oscillation in an idealized general circulation model. J. Atmos. Sci., 45, 3810-3832.
- Lindzen, R. S., 1974: Wave-CISK in the tropics. J. Atmos. Sci., 31, 156-179.
- Lord, S. J., W. C. Chao, and A. Arakawa, 1982: Interaction of a cumulus cloud ensemble with the large-scale environment, Part IV. The discrete model. J. Atmos. Sci., 39, 104-113.

- Lorenc, A.C., 1984: The evolution of planetary-scale 200mb divergent flow during the FGGE year. Quart. J. Royal Meteor. Soc., 110, 427-441.
- Madden, R. A., and P. R. Julian, 1971: Detection of a 40-50 day oscillation in the zonal wind in the tropical Pacific. J. Atmos. Sci., 28, 702-708.
- , and -----, 1972: Description of global scale circulation cells in the tropics with a 40-50 day period. J. Atmos. Sci., 29, 1109-1123.
- Murakami, T., and T. Nakazawa, 1984: On the 40-50 day oscillation during the 1979 Northern Hemisphere summer. Part I: Phase propagation. J. Meteor. Soc. Japan, 62, 440-468.
- Neelin, J. D., I. M. Held, and K. H. Cook, 1987: Evaporation-wind feedback and low-frequency variability in the tropical atmosphere. J. Atmos. Sci., 44, 2341-2348.
- Nitta, T., 1987: Convective activities in the tropical western Pacific and their impact on the Northern Hemisphere summer circulation. J. Meteor. Soc. Japan, 65, 373-390.
- Randall, D. A., 1979: The entraining moist boundary layer. Preprint volume, Fourth Symposium on Turbulence, Diffusion, and Air Pollution, Reno, Nevada, Amer. Meteor. Soc., 467-470.
- , 1982: Monthly and seasonal simulations with the GLAS climate model. Proc. Workshop on intercomparison of large-scale models used for extended range forecasts, Reading, ECMWF, pp 107-166.
- , 1984: Buoyant production and consumption of turbulence kinetic energy in cloud-topped mixed layers. J. Atmos. Sci., 41, 402-413.
- , J. A. Abeles, and T. G. Corsetti, 1985: Seasonal simulations of the planetary boundary layer and boundary-layer stratocumulus clouds with a general circulation model. J. Atmos. Sci., 42, 641-676.
- Schlesinger, M. E., 1976: A numerical simulation of the general circulation of atmospheric ozone. Ph. D. dissertation, UCLA, 375 pp.
- Schubert, S.D. and C. K. Park, 1990: Low frequency intraseasonal tropical/extratropical interactions. Accepted to J. Atmos. Sci.
- Simmons, A.J., J.M. Wallace and G.W. Branstator, 1983: Barotropic wave propagation and instability, and atmospheric teleconnection patterns. J. Atmos. Sci., 40, 1363-1392.
- Somerville, R. C. J., P. H. Stone, M. Halem, J. E. Hansen, J. S. Hogan, L. M. Druryan, G. Russell, A. A. Lacis, W. J. Quirk, and J. Tenenbaum, 1974: The GISS model of the global atmosphere. J. Atmos. Sci., 31, 84-117.
- Straus, D. M., and J. Shukla, 1988a: A comparison of a GCM simulation of the seasonal cycle of the atmosphere with observations. Part I: Mean fields and the annual harmonic. Atmosphere-Ocean, 26, 541-574.

- , and -----, 1988b: A comparison of a GCM simulation of the seasonal cycle of the atmosphere with observations. Part II: Stationary waves and transient fluctuations. Atmosphere-Ocean, 26, 575-607.
- Sui, C.-H., and K.-M. Lau, 1989: Origin of low frequency (intraseasonal) oscillations in the tropical atmosphere. Part II: Structure and propagation by mobile wave-CISK modes and their modification by lower boundary forcings. J. Atmos. Sci., 46, 37-56.
- Swinbank, R., T. N. Palmer, and M. K. Davey, 1988: Numerical simulations of the Madden and Julian oscillation. J. Atmos. Sci., 45, 774-788.
- Takahashi, M., 1987: A theory of the slow phase speed of the intraseasonal oscillation using the wave-CISK. J. Meteor. Soc. Japan., 65, 43-49.
- Tokioka, T., K. Yamazaki, A. Kitoh, and T. Ose, 1988: The equatorial 30-60 day oscillation and the Arakawa-Schubert penetrative cumulus parameterization. J. Meteor. Soc. Japan., 66, 883-901.
- Trenberth, K. E., and J. G. Olson, 1988: ECMWF global analyses 1979-1986: Circulation statistics and data evaluation. NCAR Tech. Note NCAR/TN-300+STR.
- Von Storch, J.H., T. Bruns, I. Fischer-Bruns and K. Hasselmann, 1987: Principal oscillation pattern analysis of the 30-60 day oscillation in a GCM equatorial troposphere. Max-Planck Institut fur Meteorologie, Report NO. 7.
- Wang, B., 1988: Dynamics of tropical low-frequency waves: an analysis of moist Kelvin waves. J. Atmos. Sci., 45, 2051-2065.
- Weickmann, K. M., G. R. Lussky, and J. E. Kutzbach, 1985: Intraseasonal (30-60 day) fluctuations of outgoing longwave radiation and 250 mb streamfunction during northern winter. Mon. Wea. Rev., 113, 941-961.

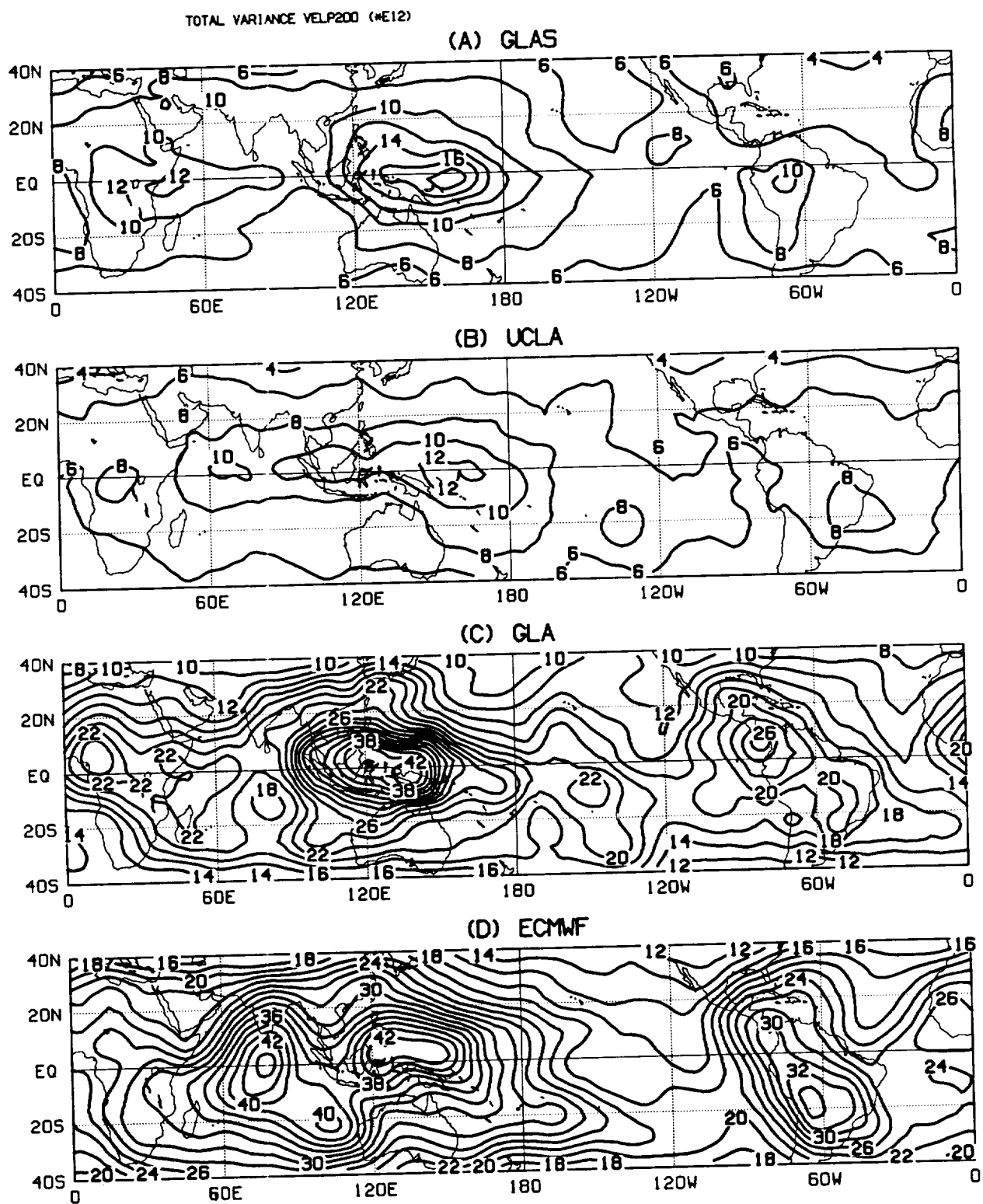
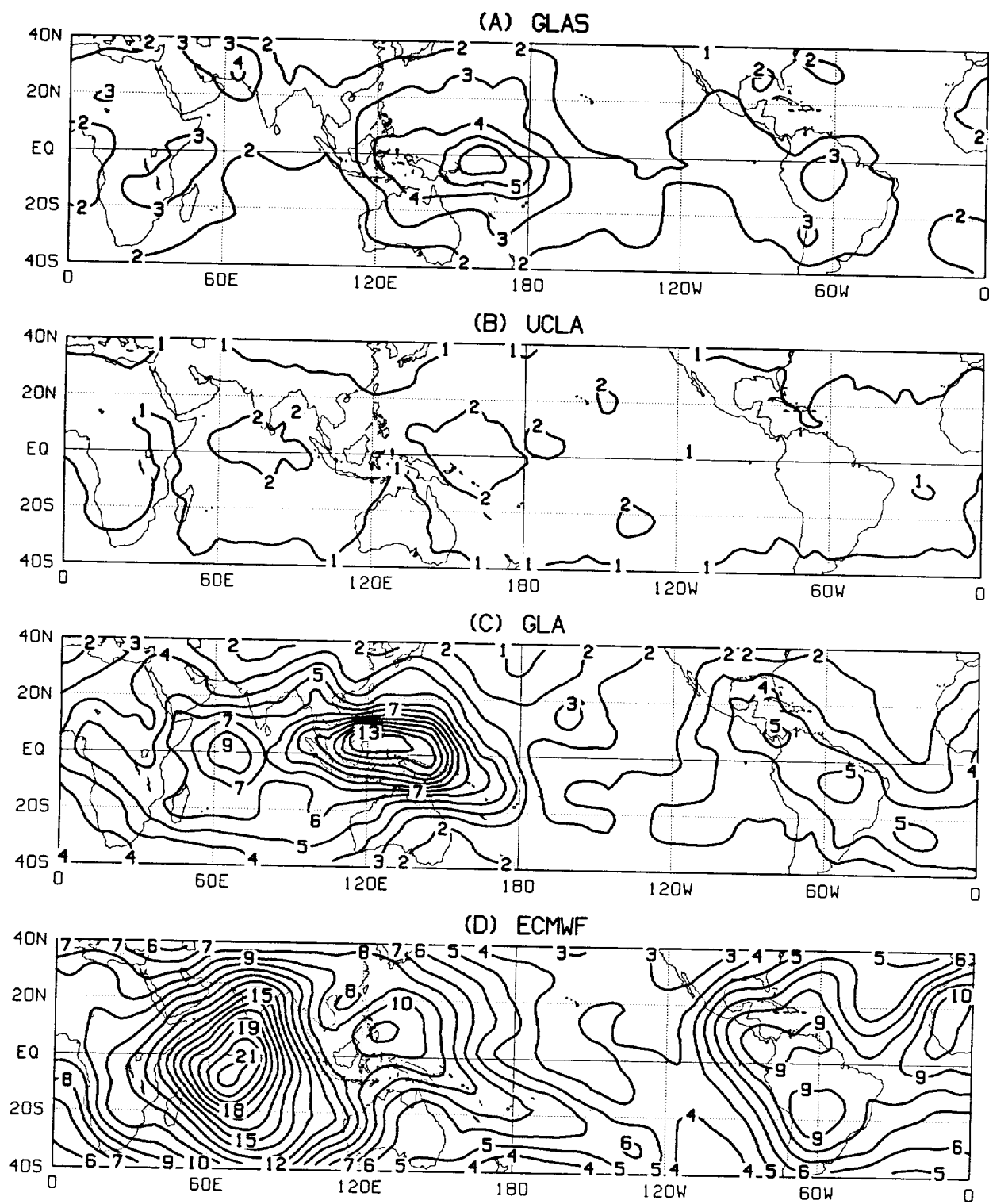


Figure 1



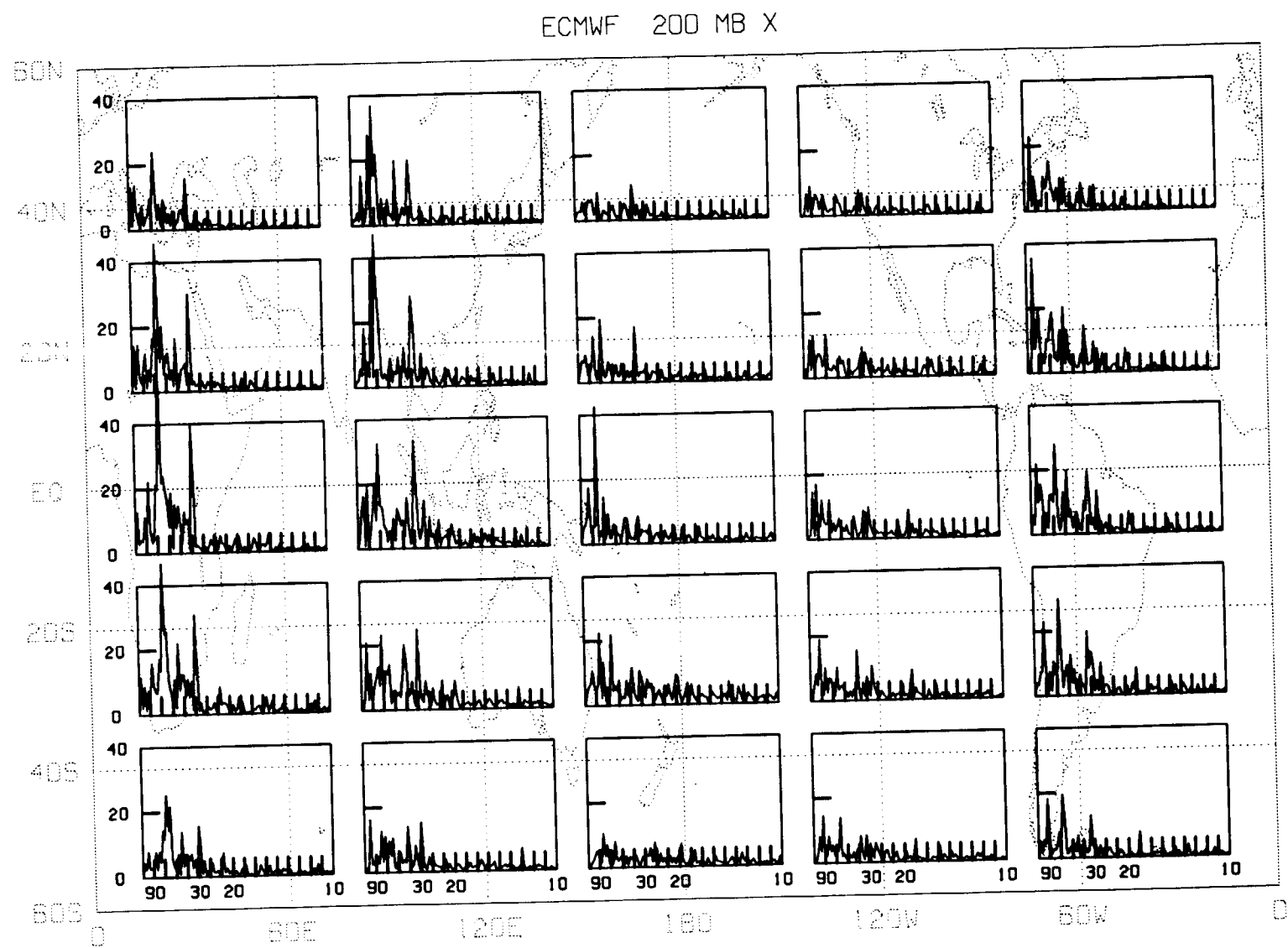


Figure 3

GLAS 200 MB X

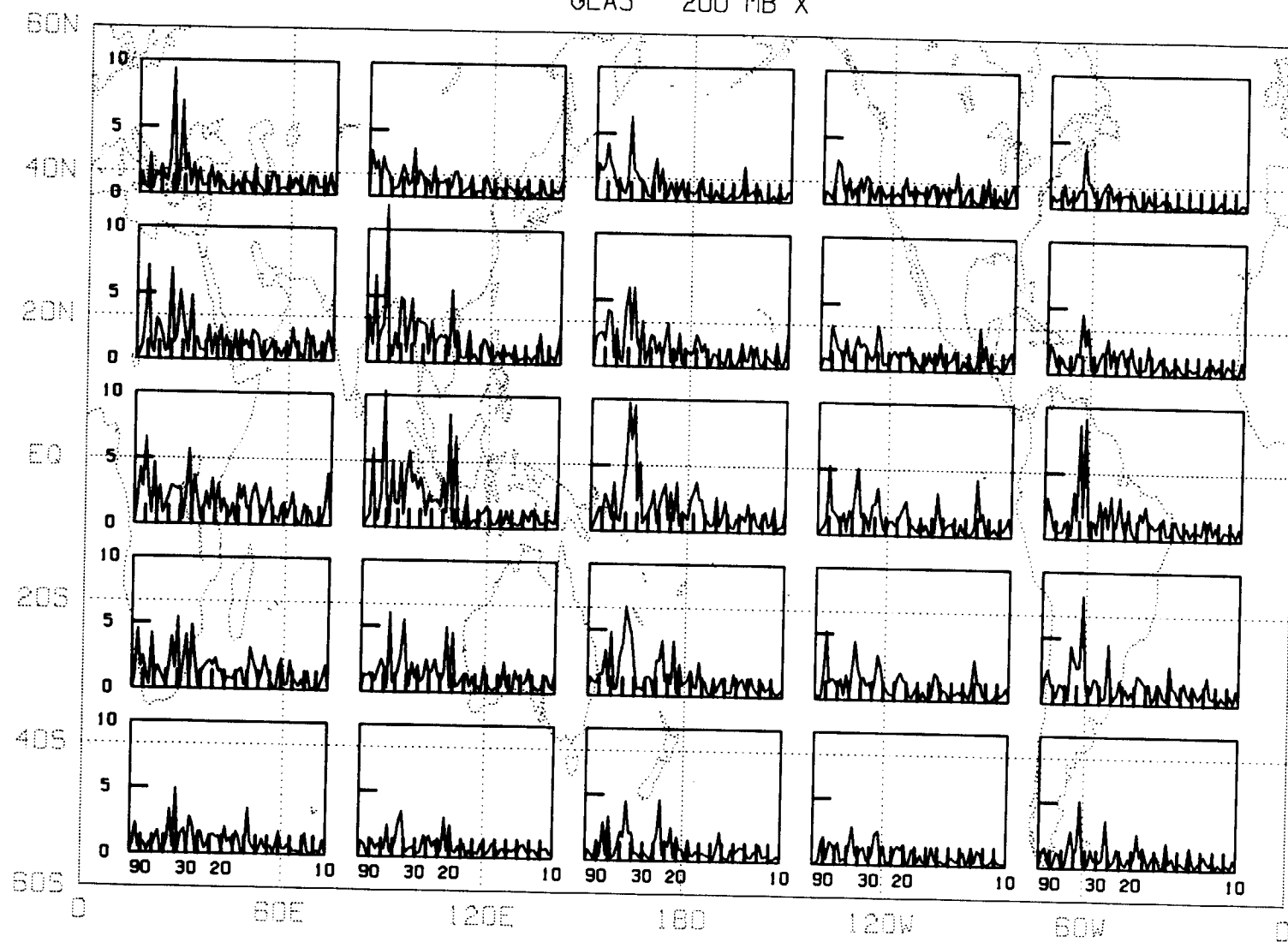


Figure 4

UCLA 200 MB X

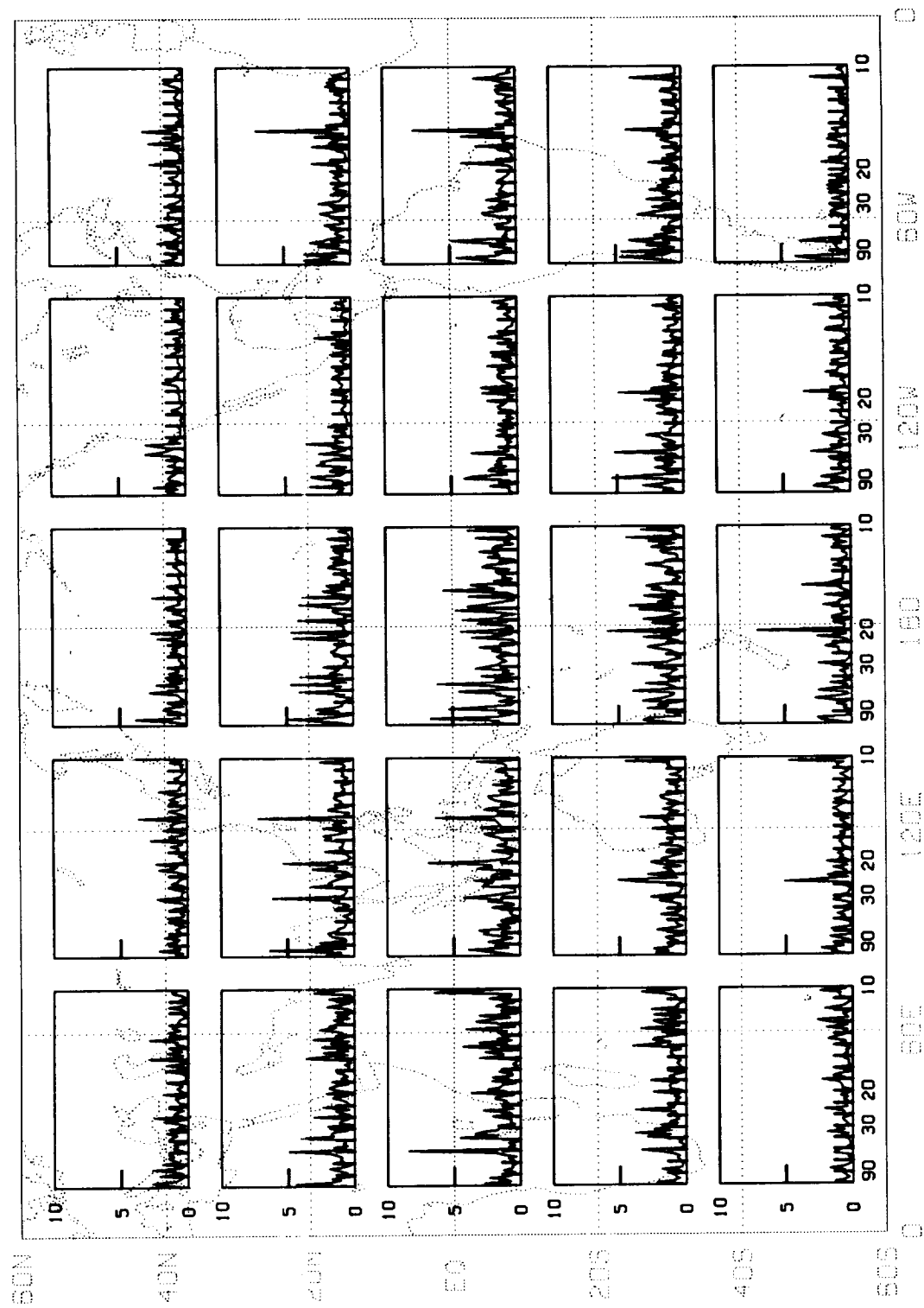


Figure 5

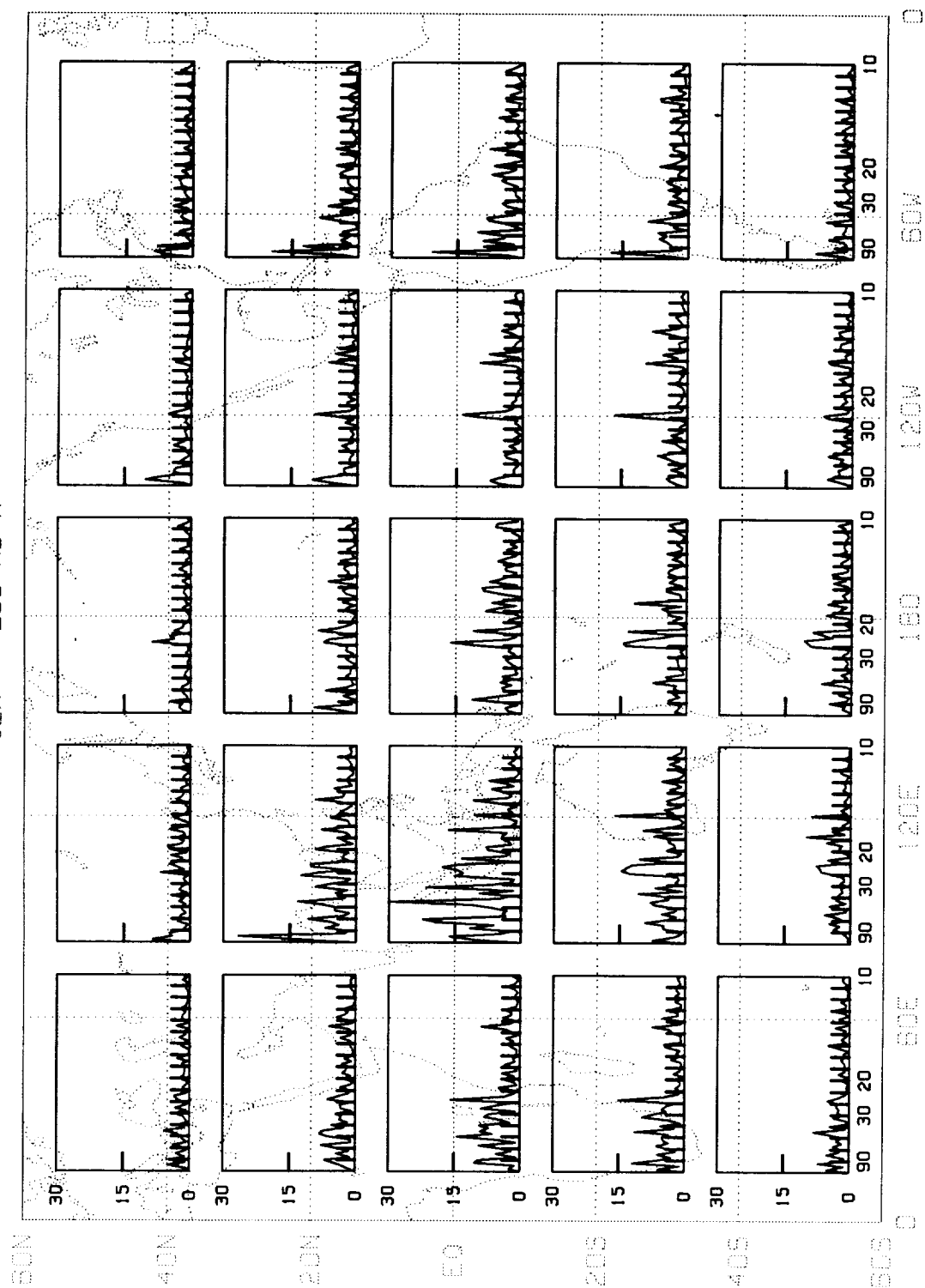


Figure 6

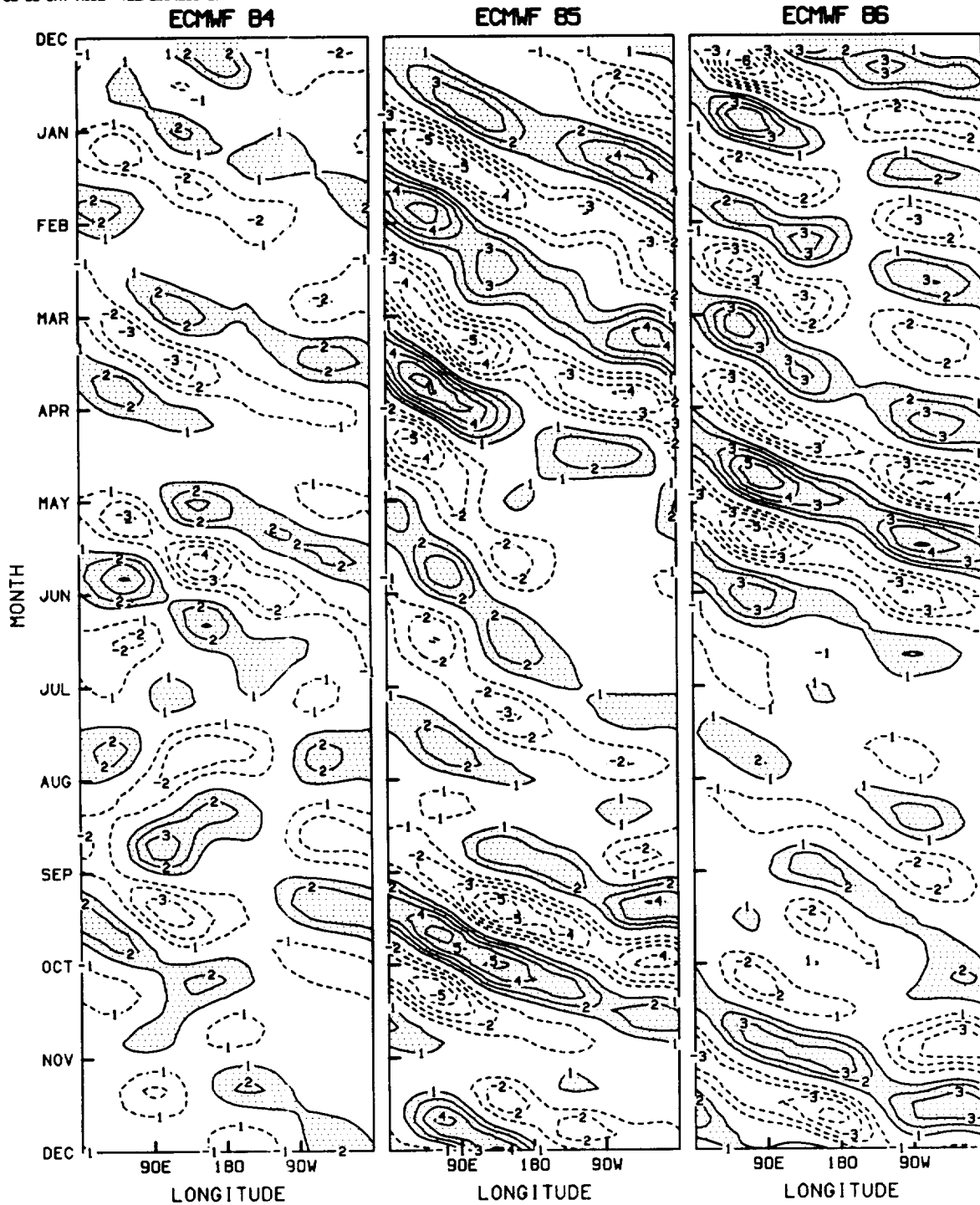
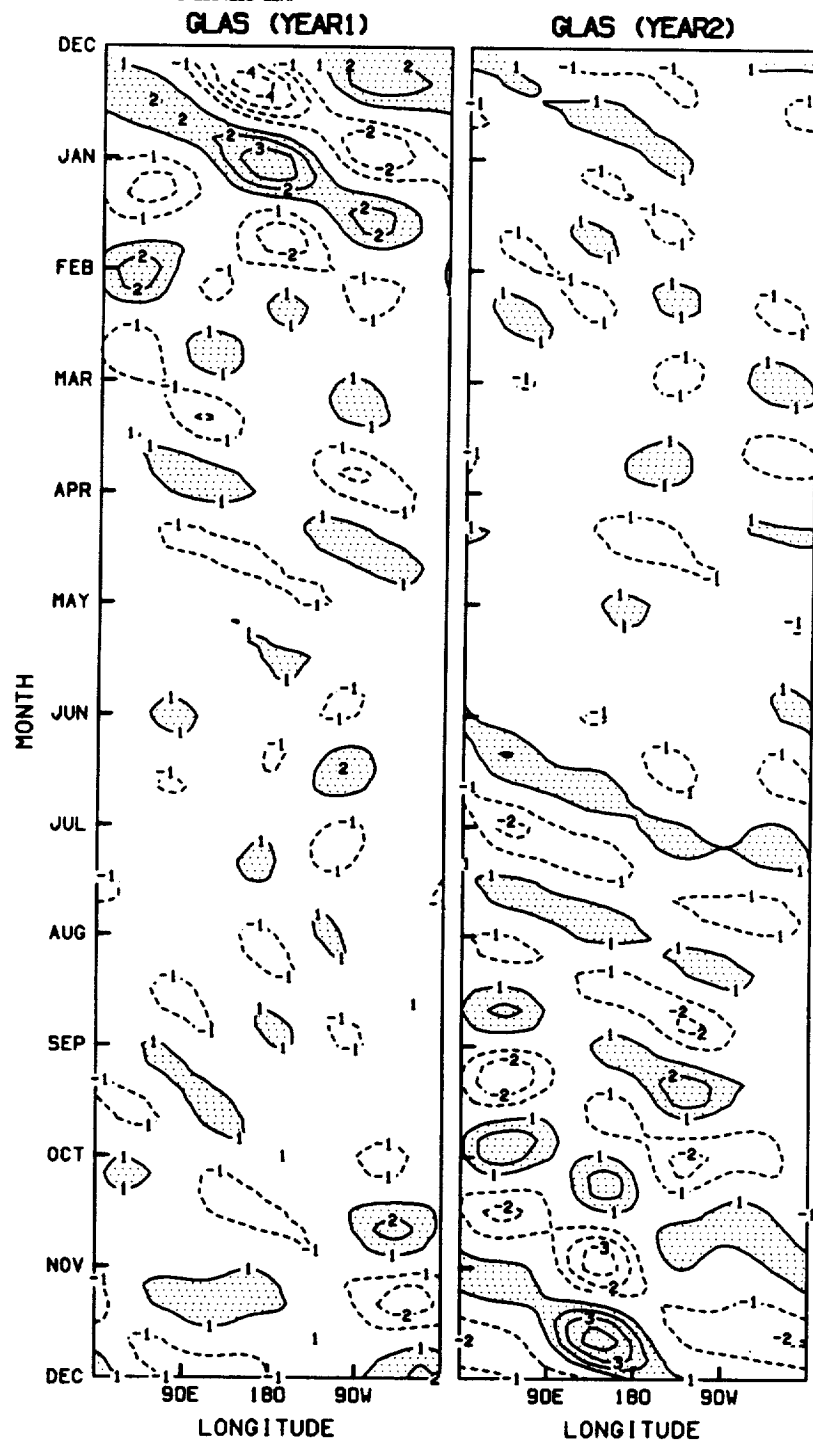


Figure 7



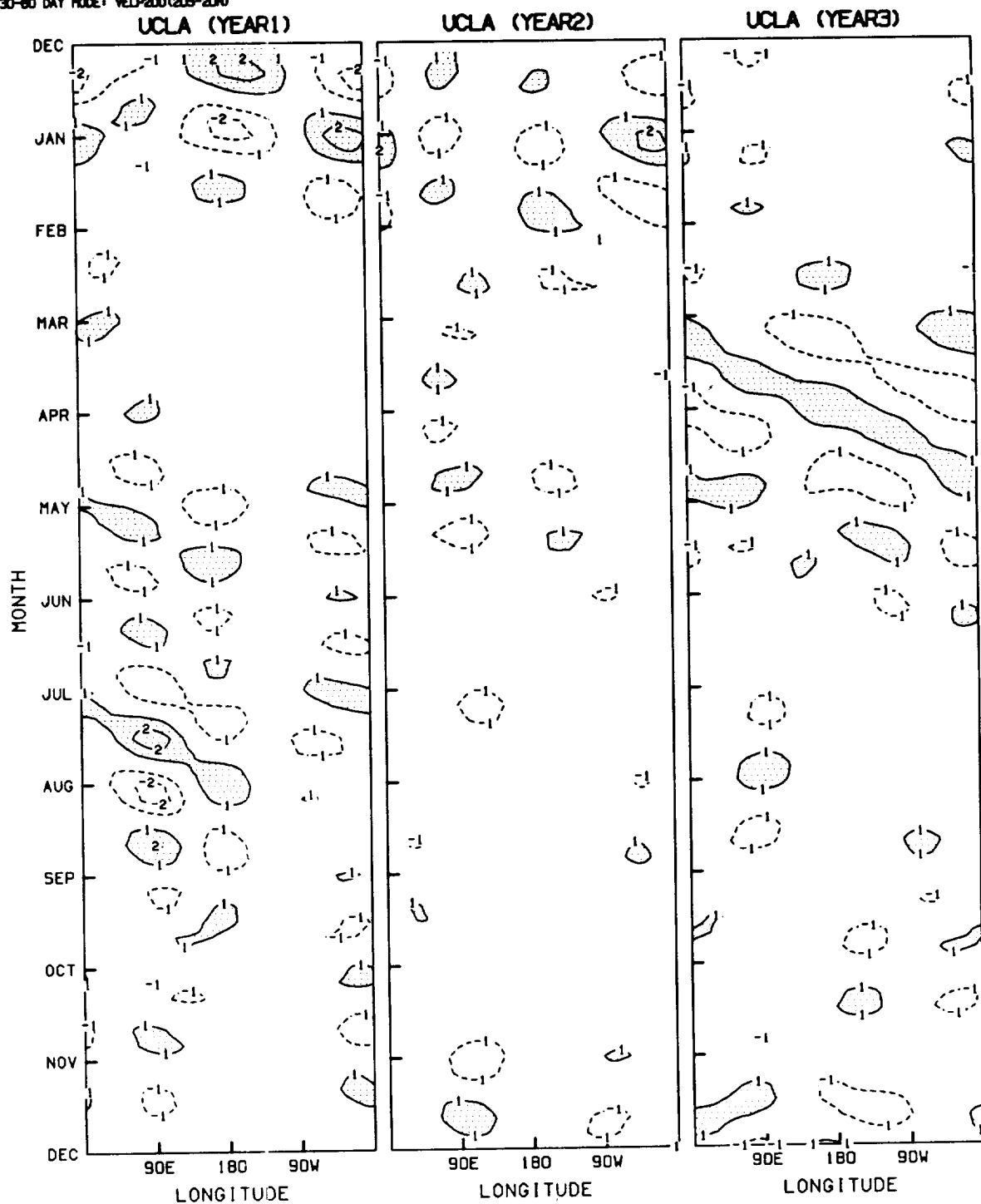
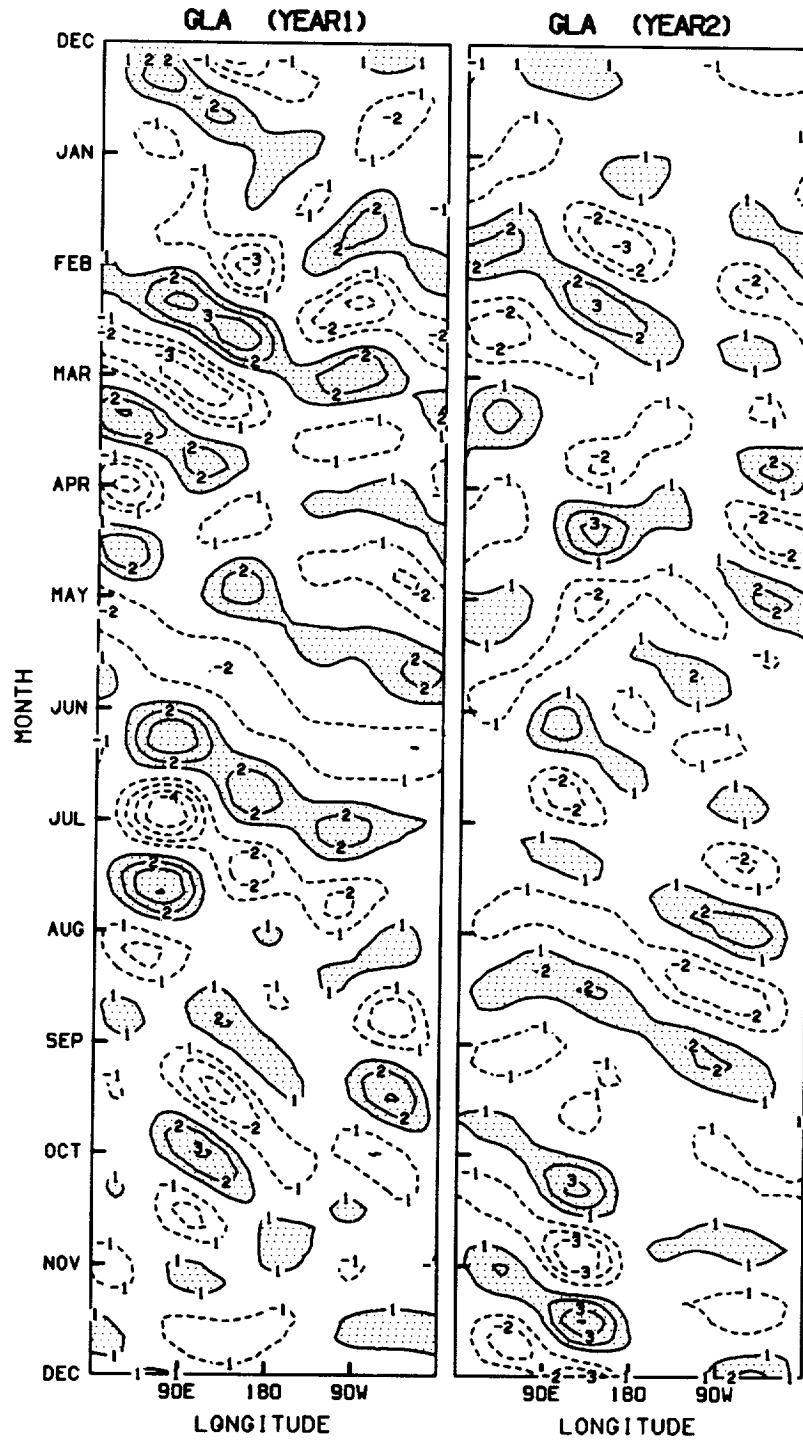


Figure 9

INDEX FOR 30-60 DAY MODE: VCLP200(205-20N)



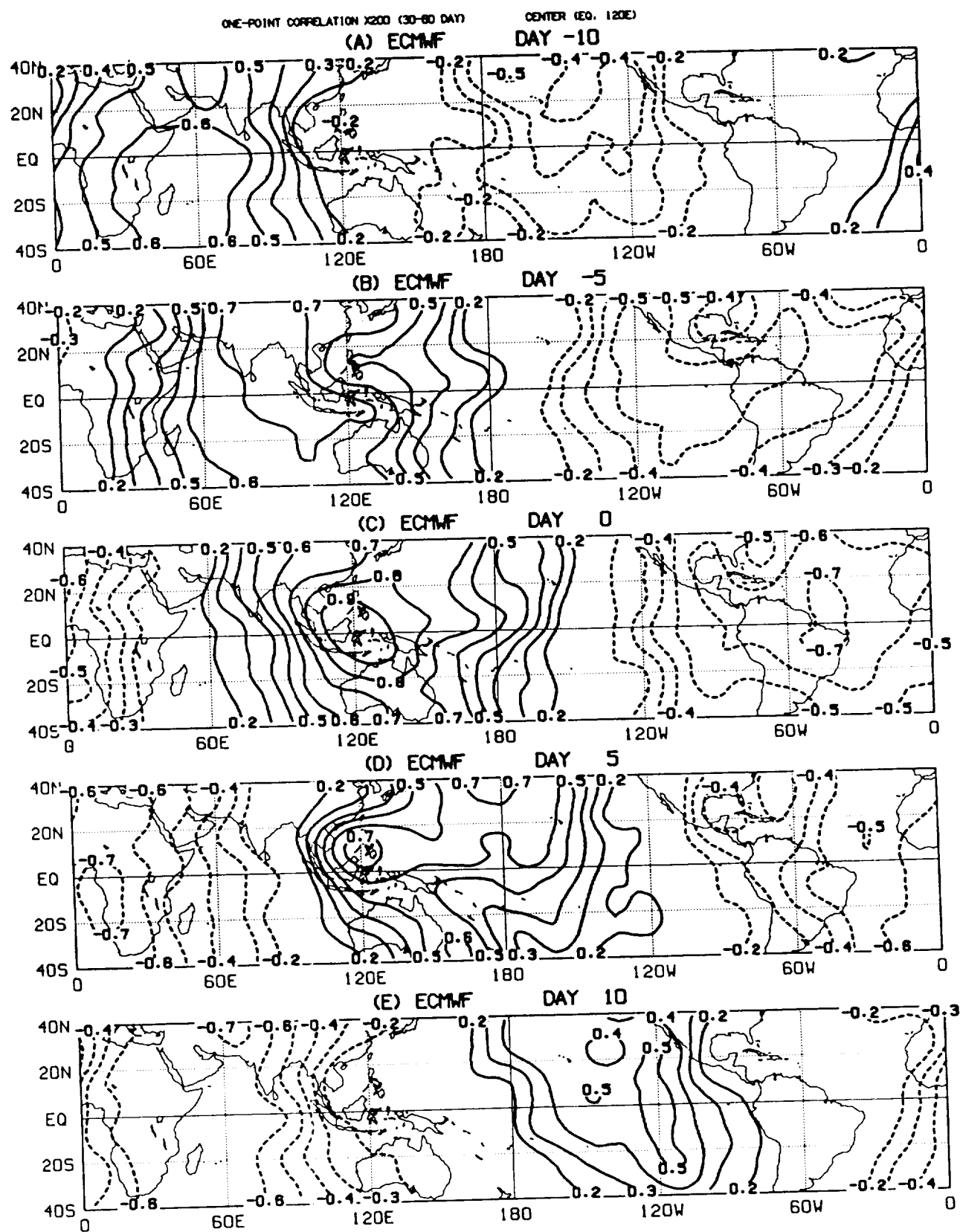
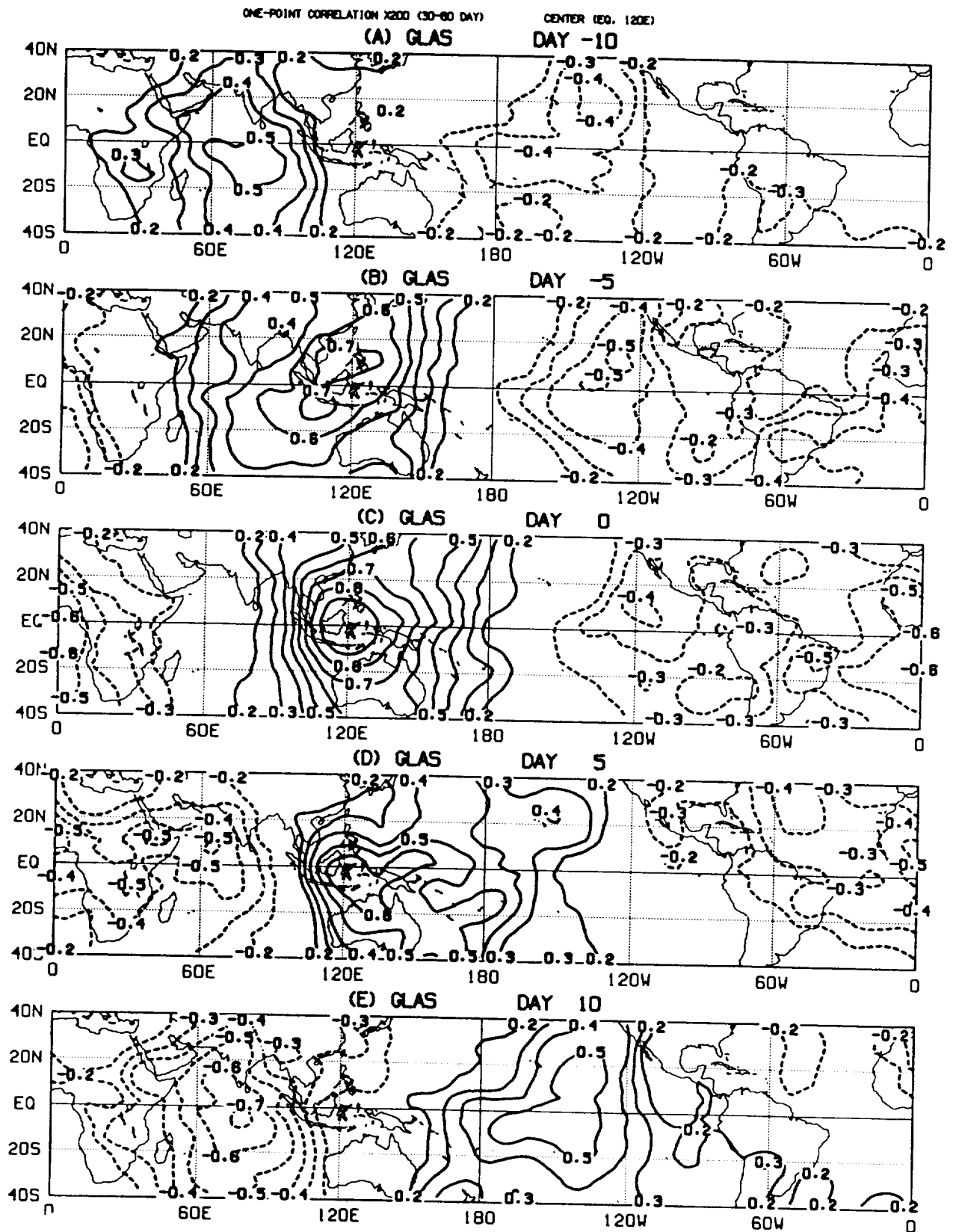


Figure 11



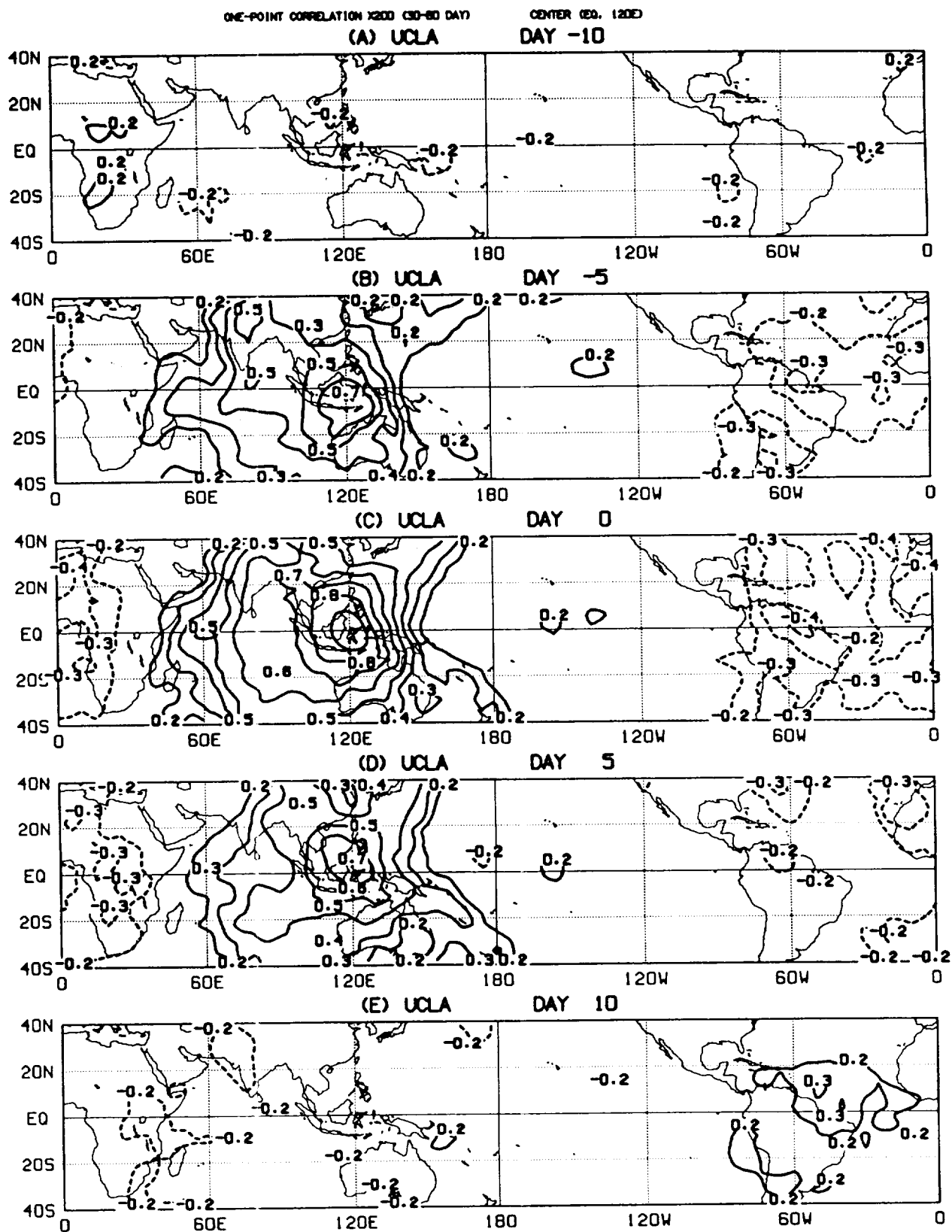
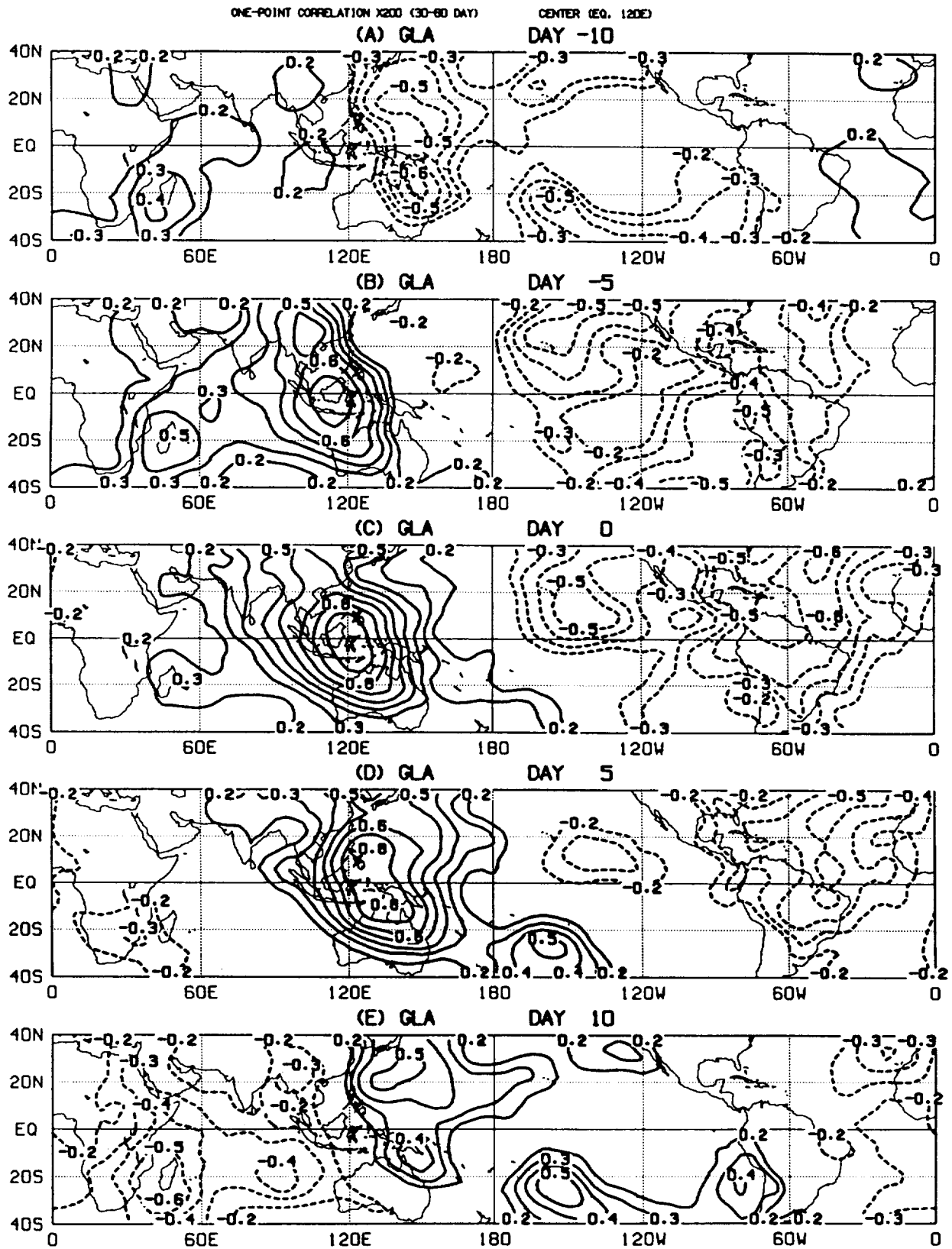


Figure 13



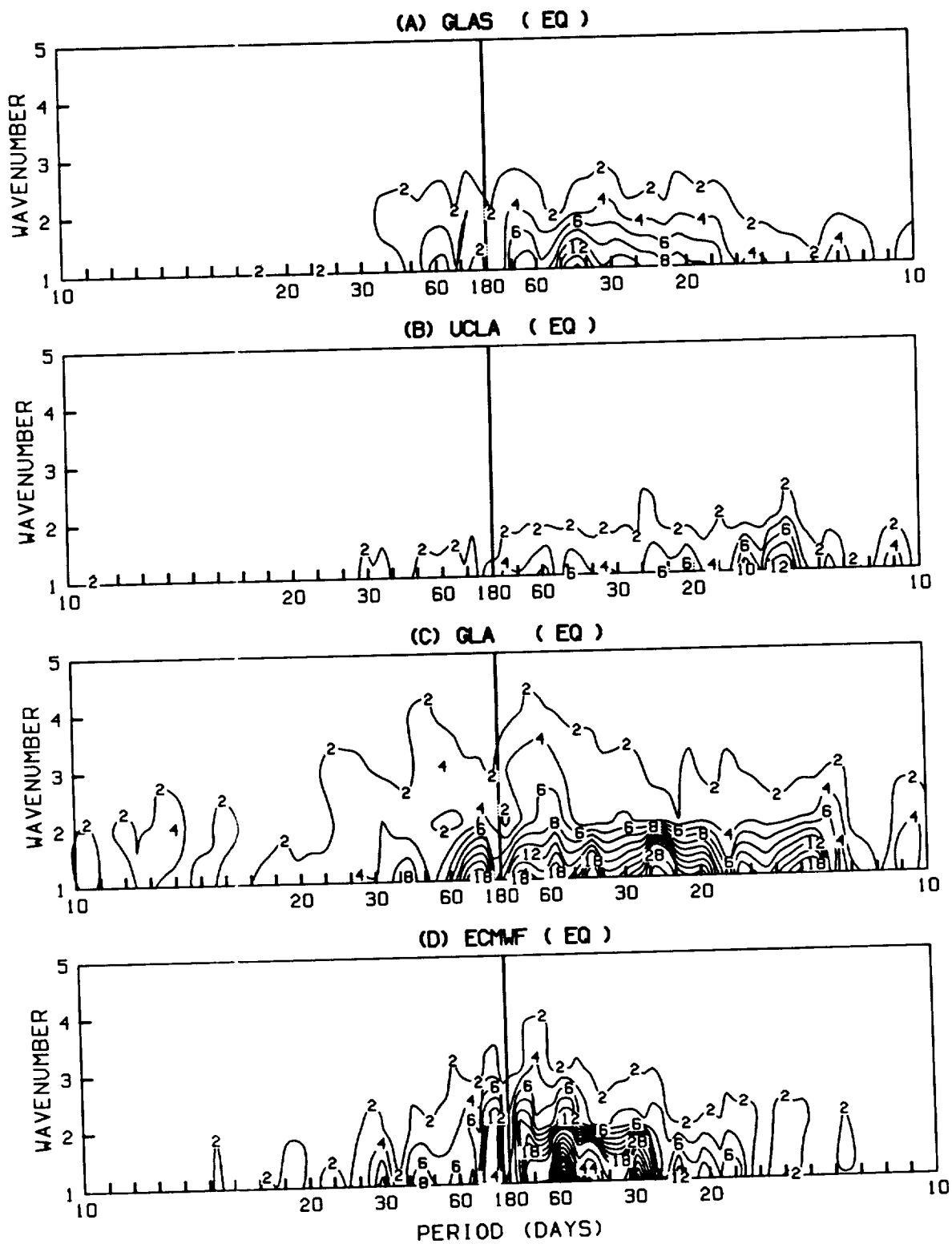


Figure 15

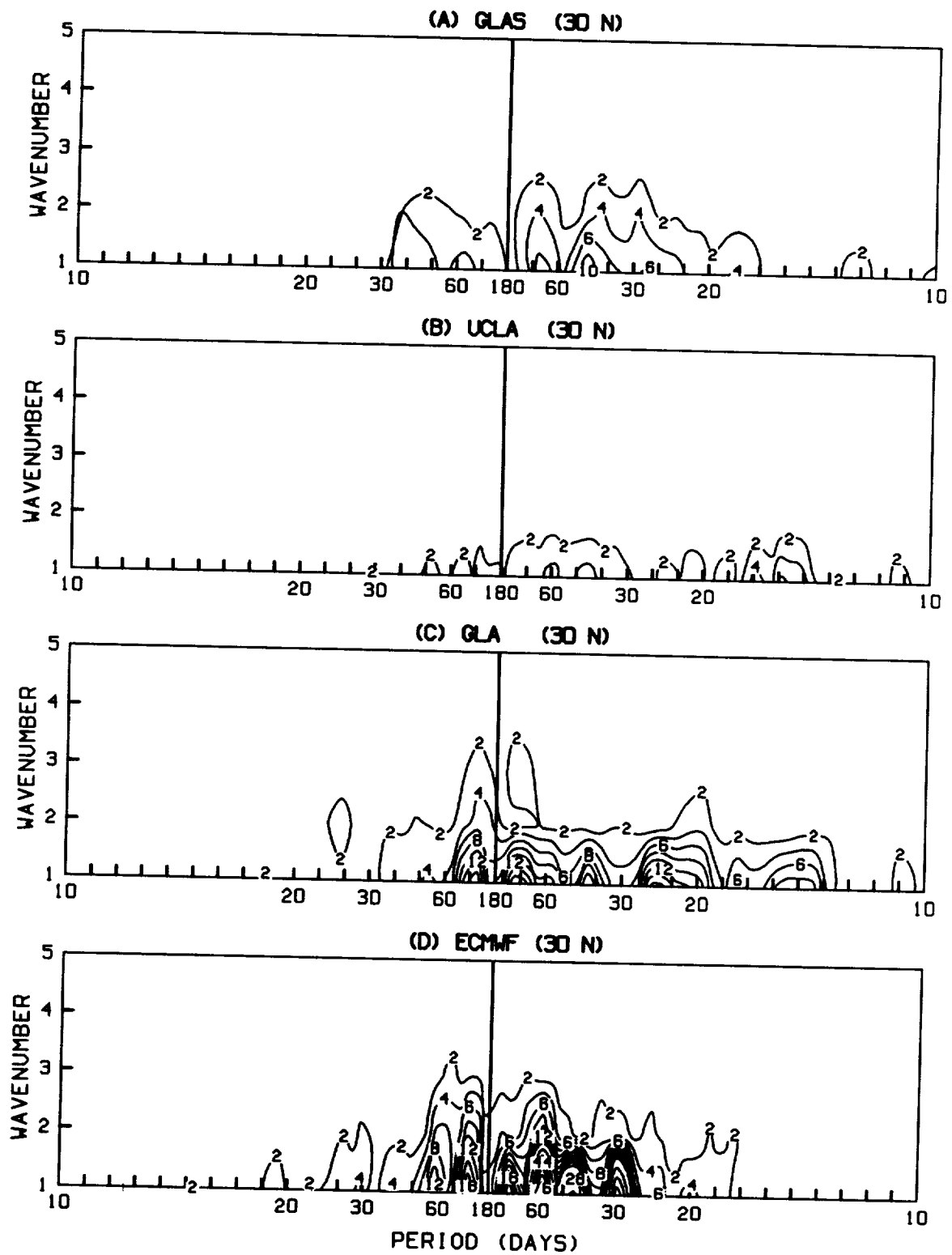


Figure 16

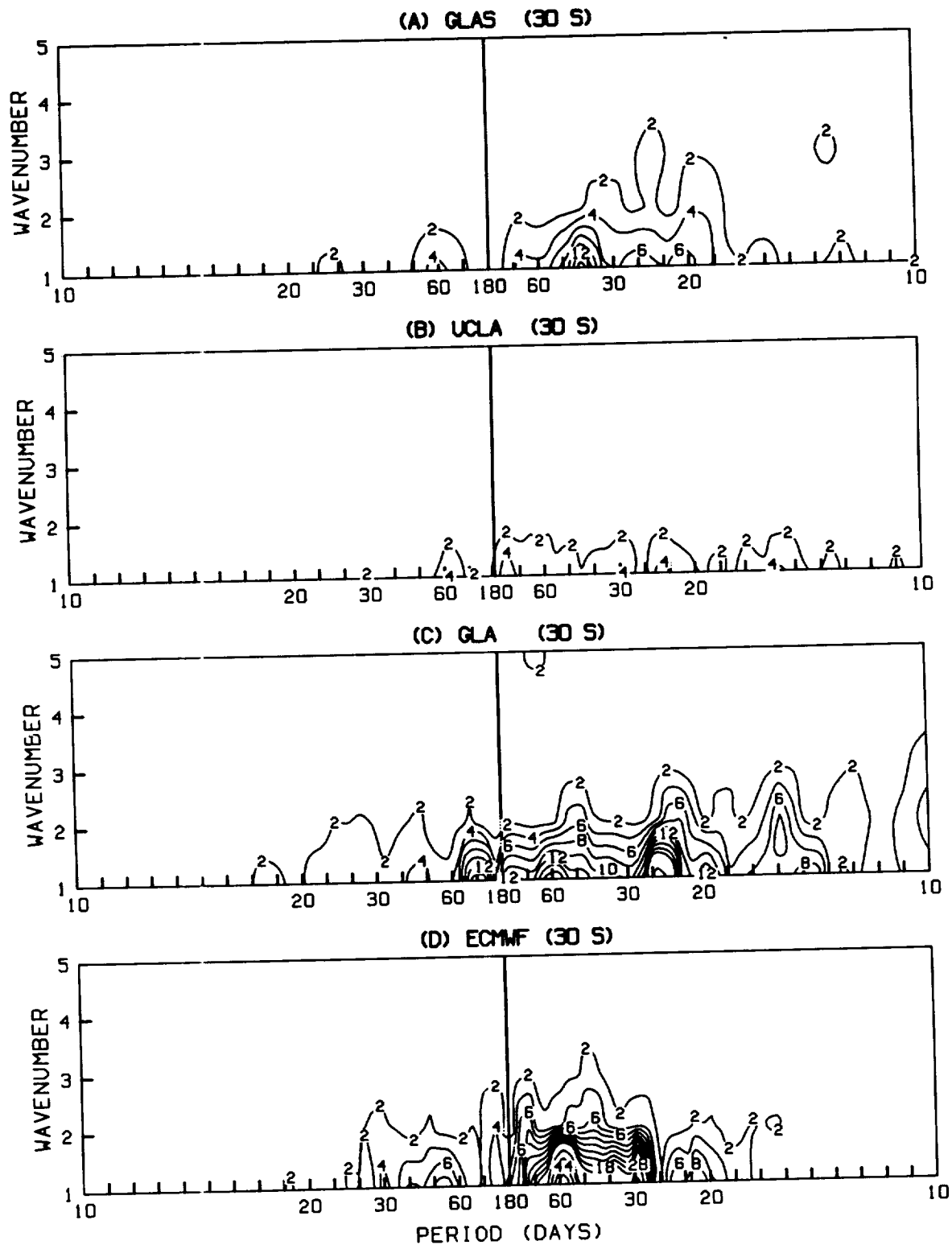
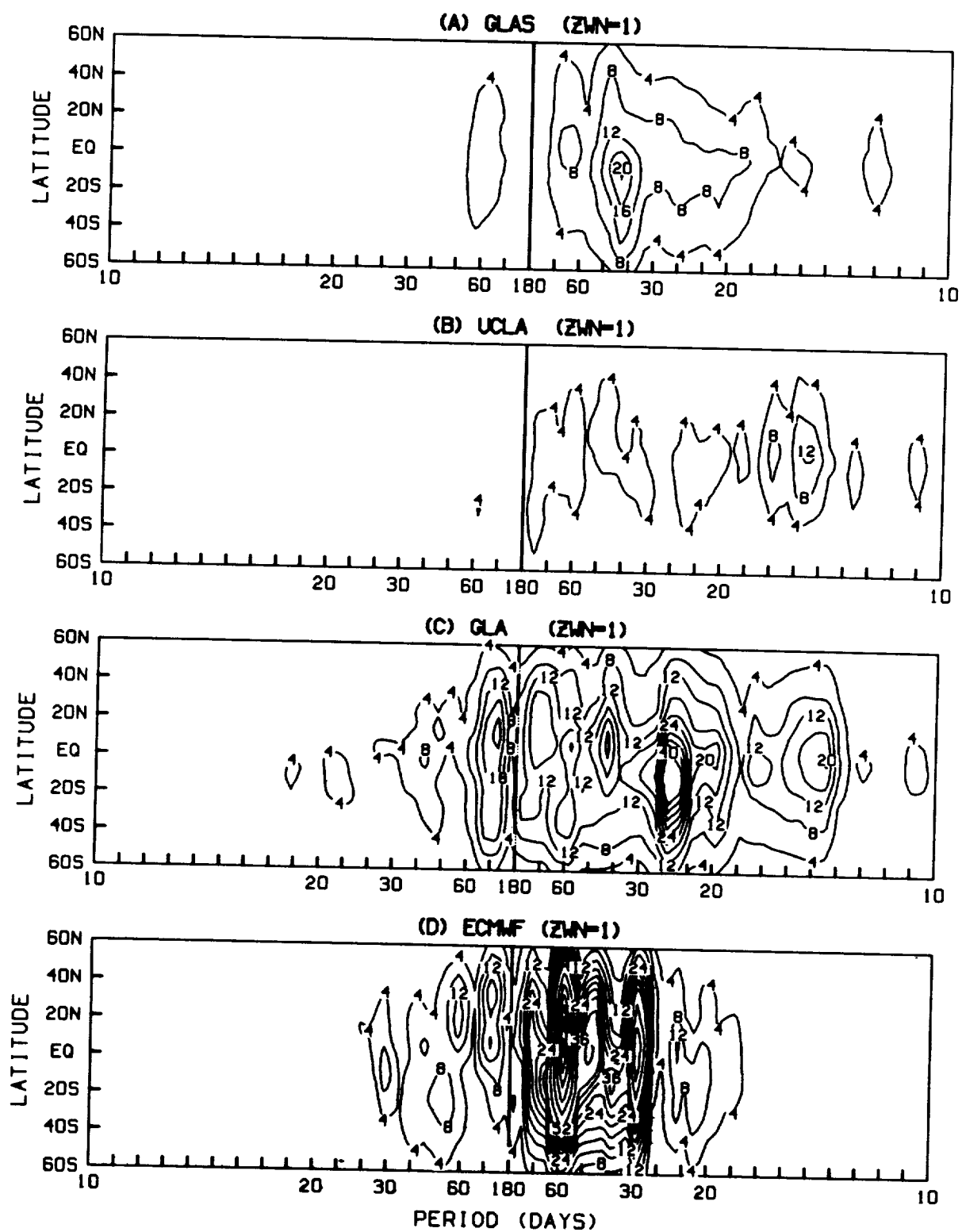


Figure 17



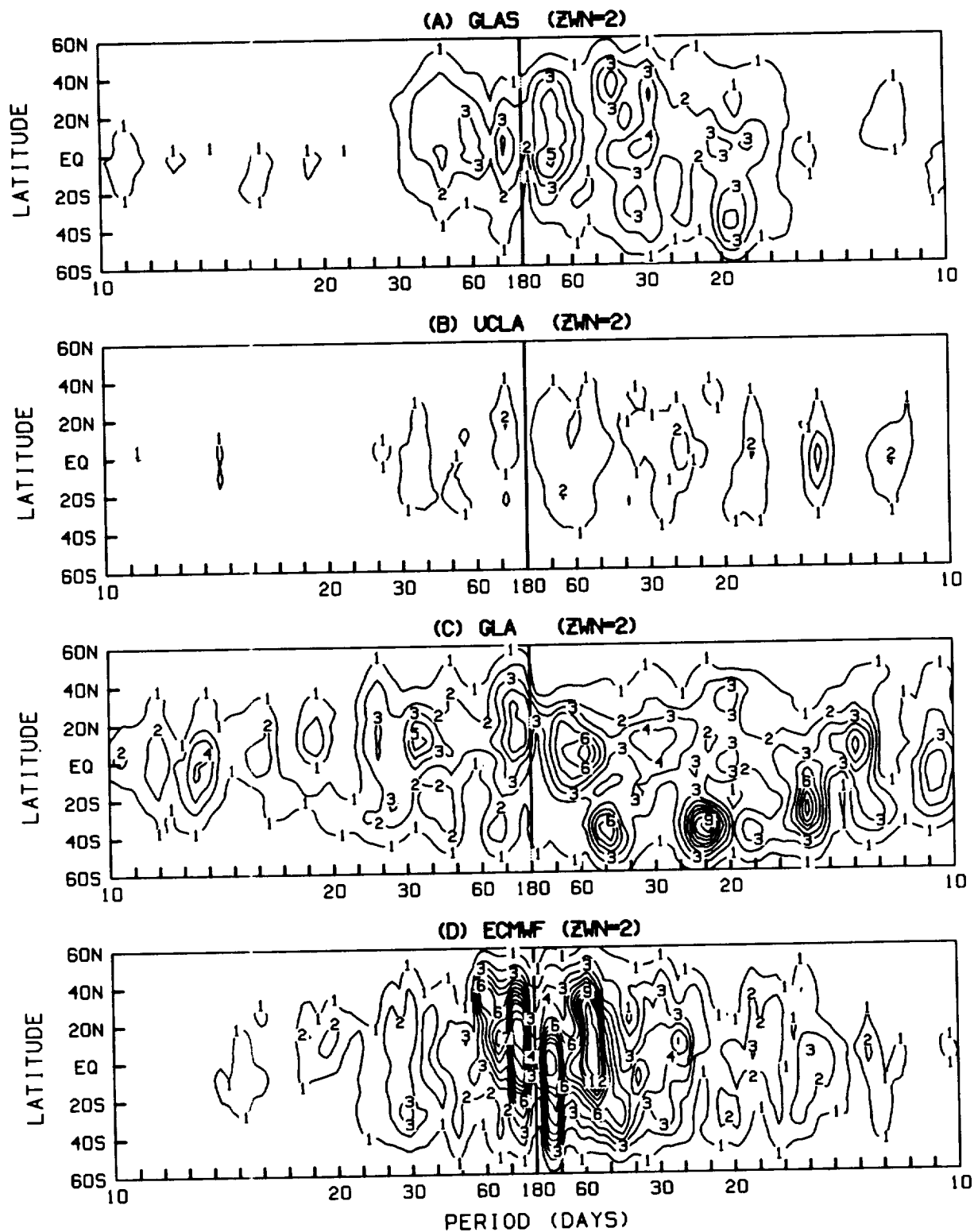


Figure 19

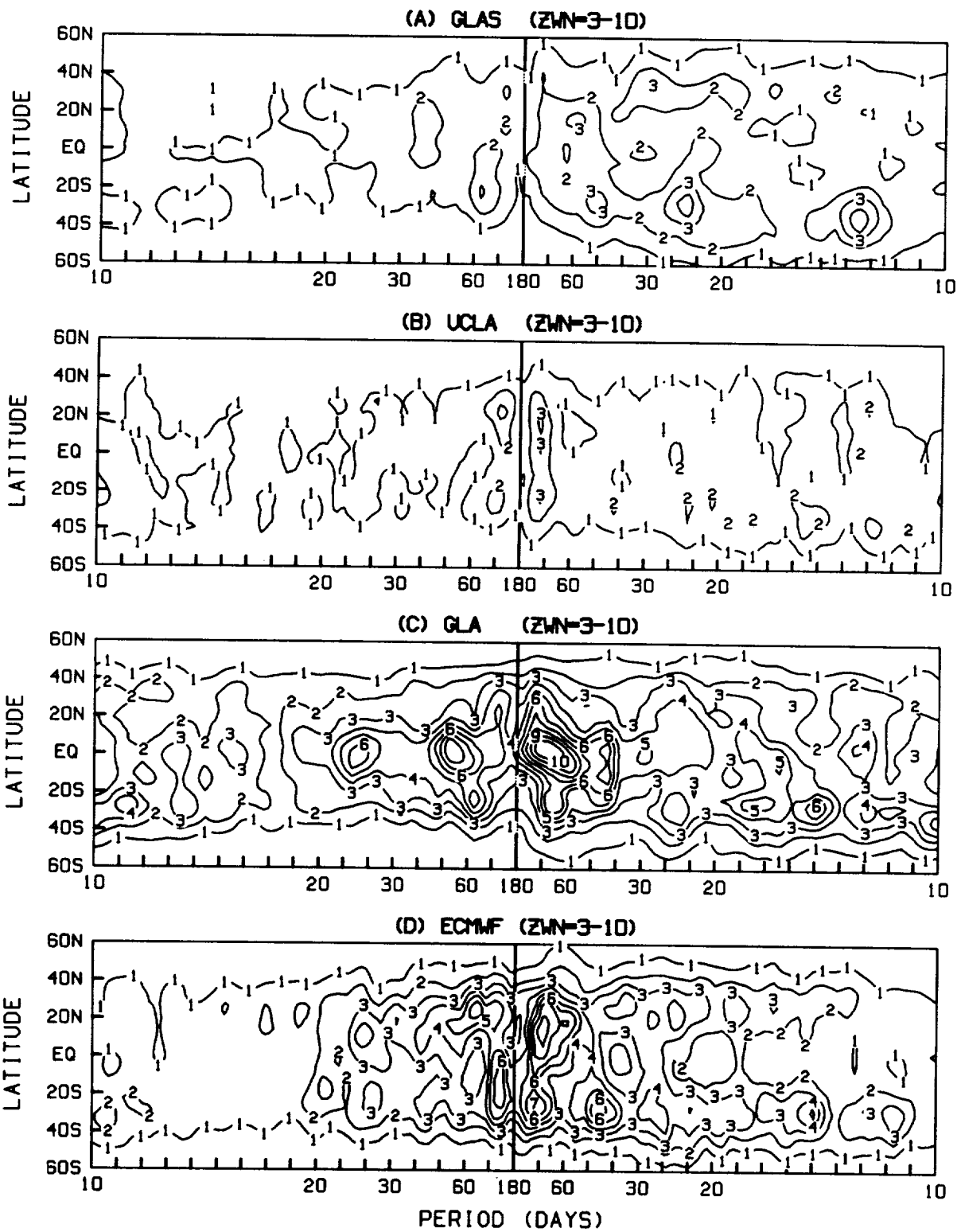


Figure 20

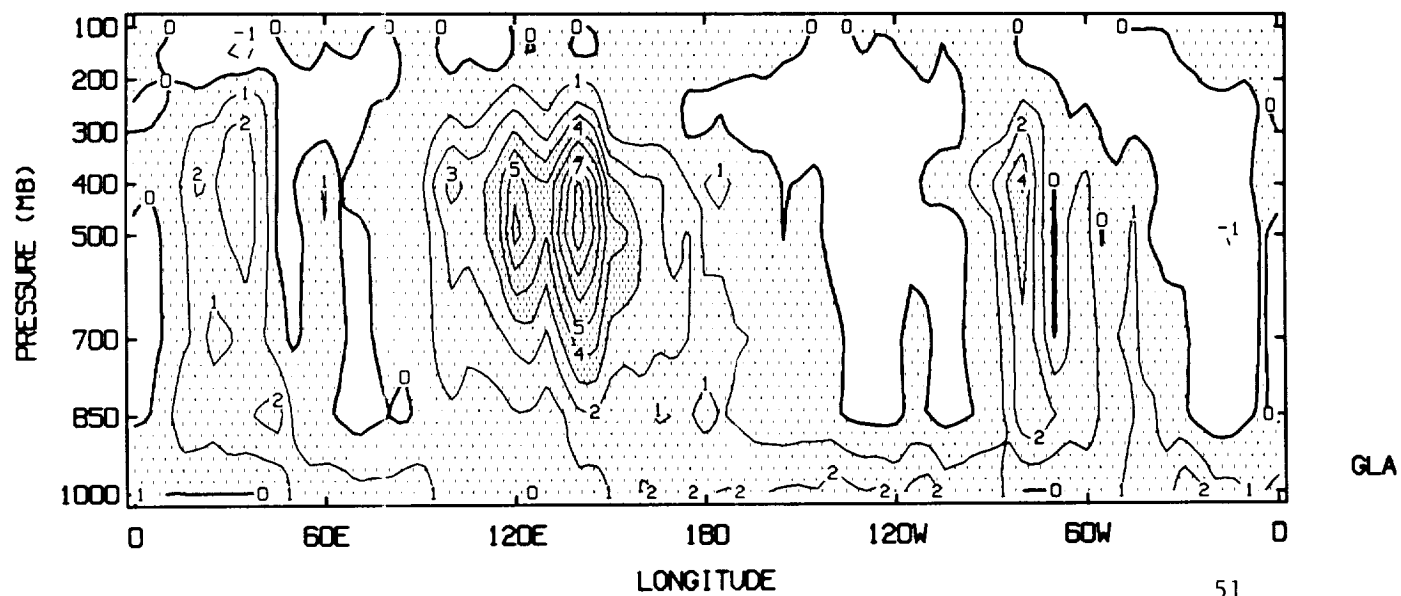
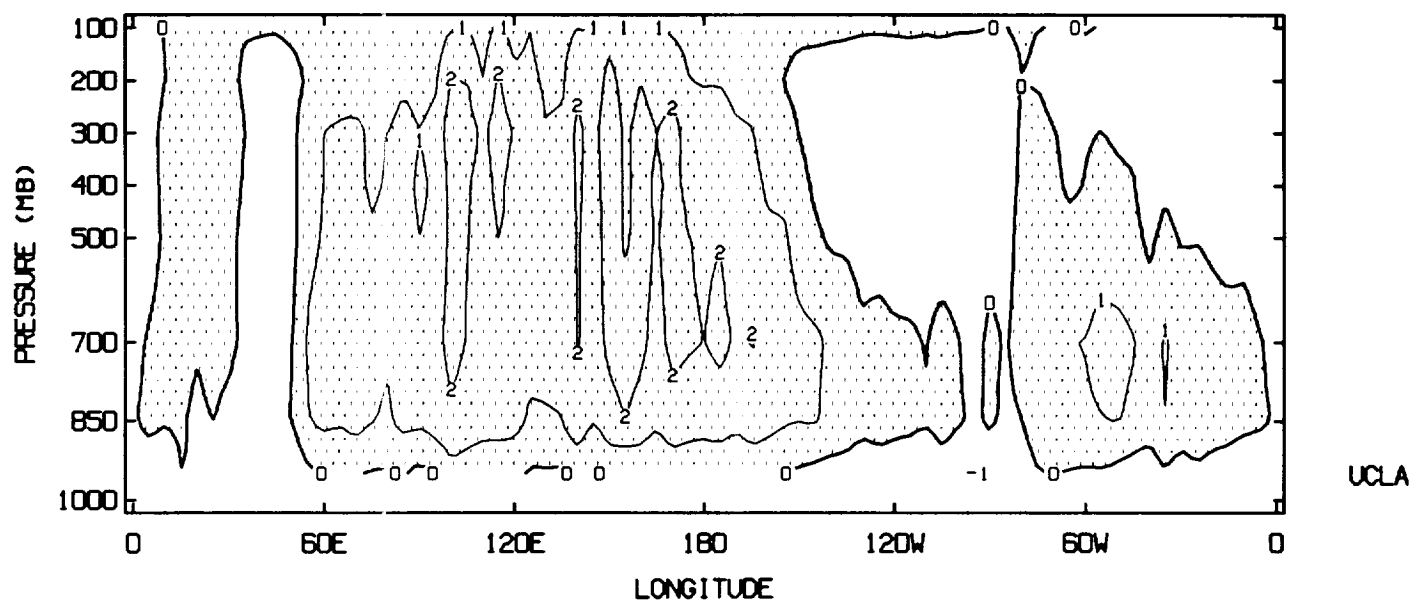
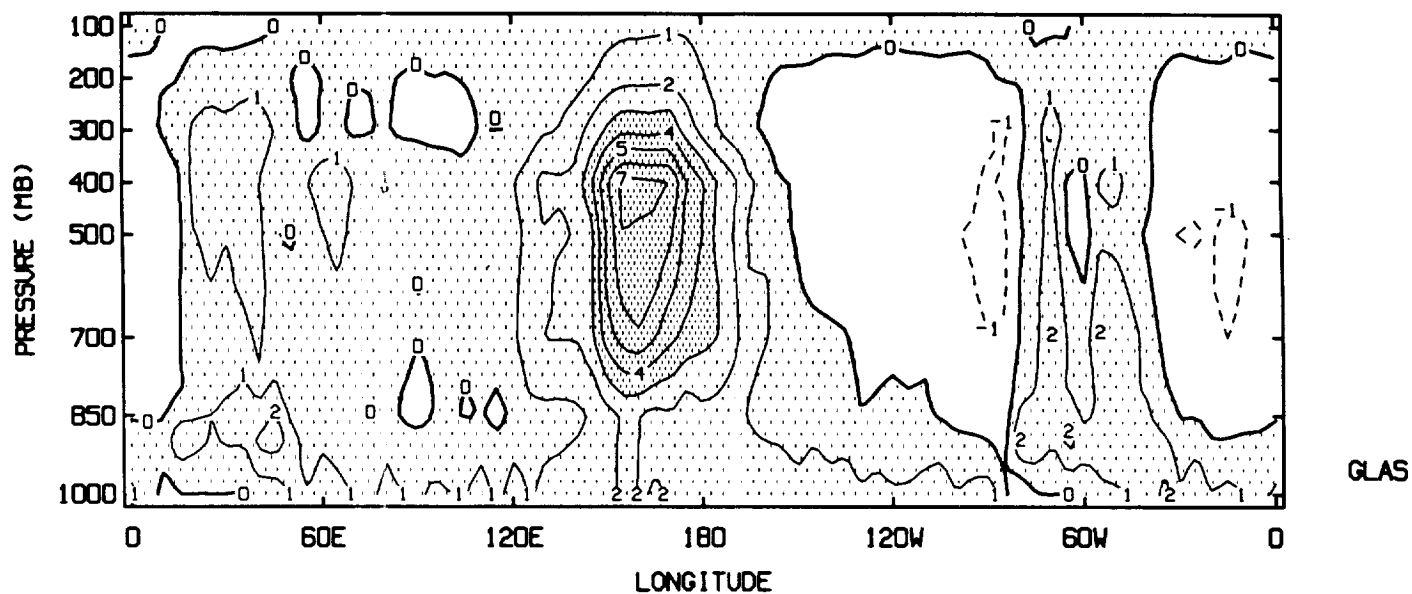


Figure 21

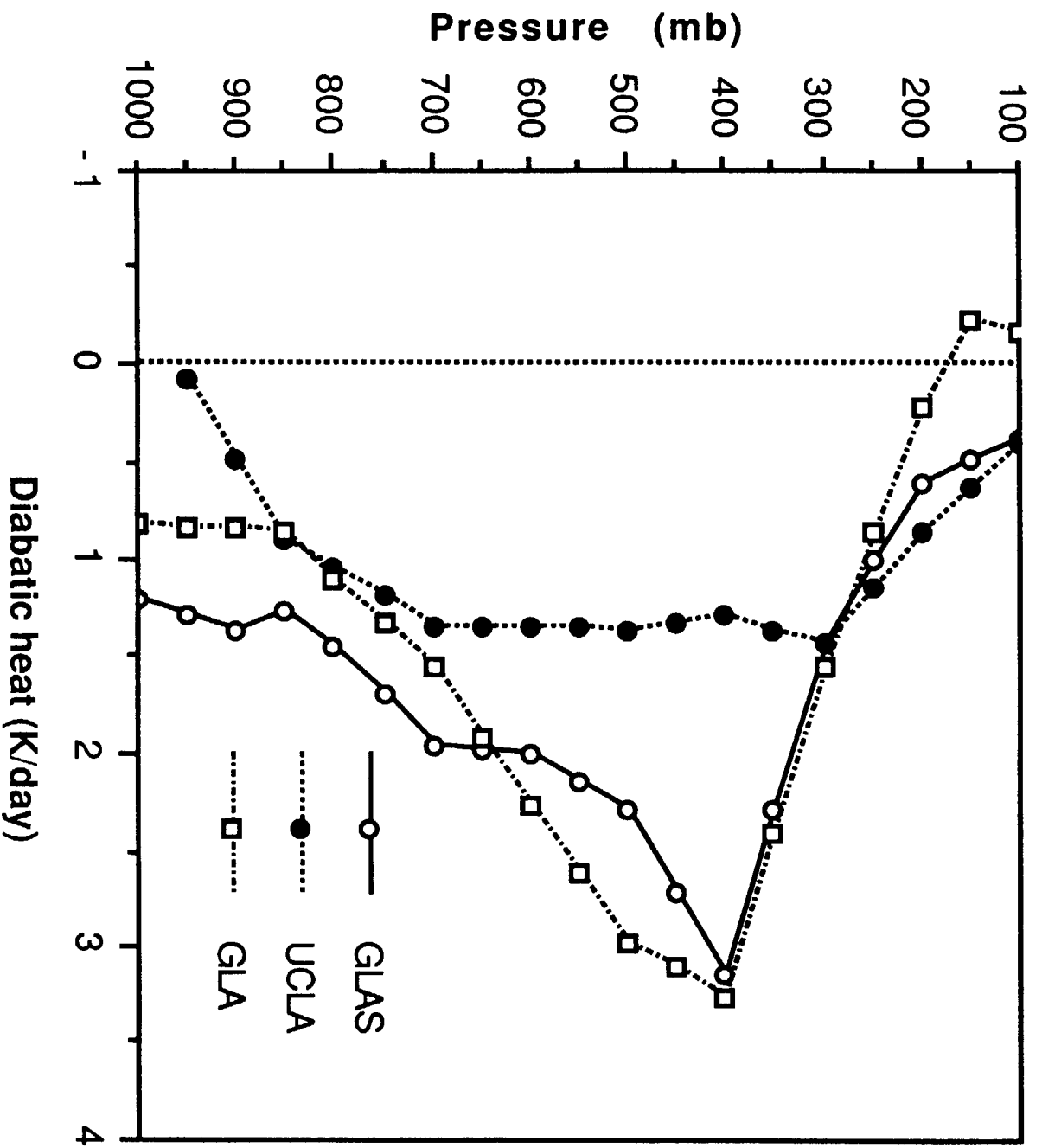


Figure 22

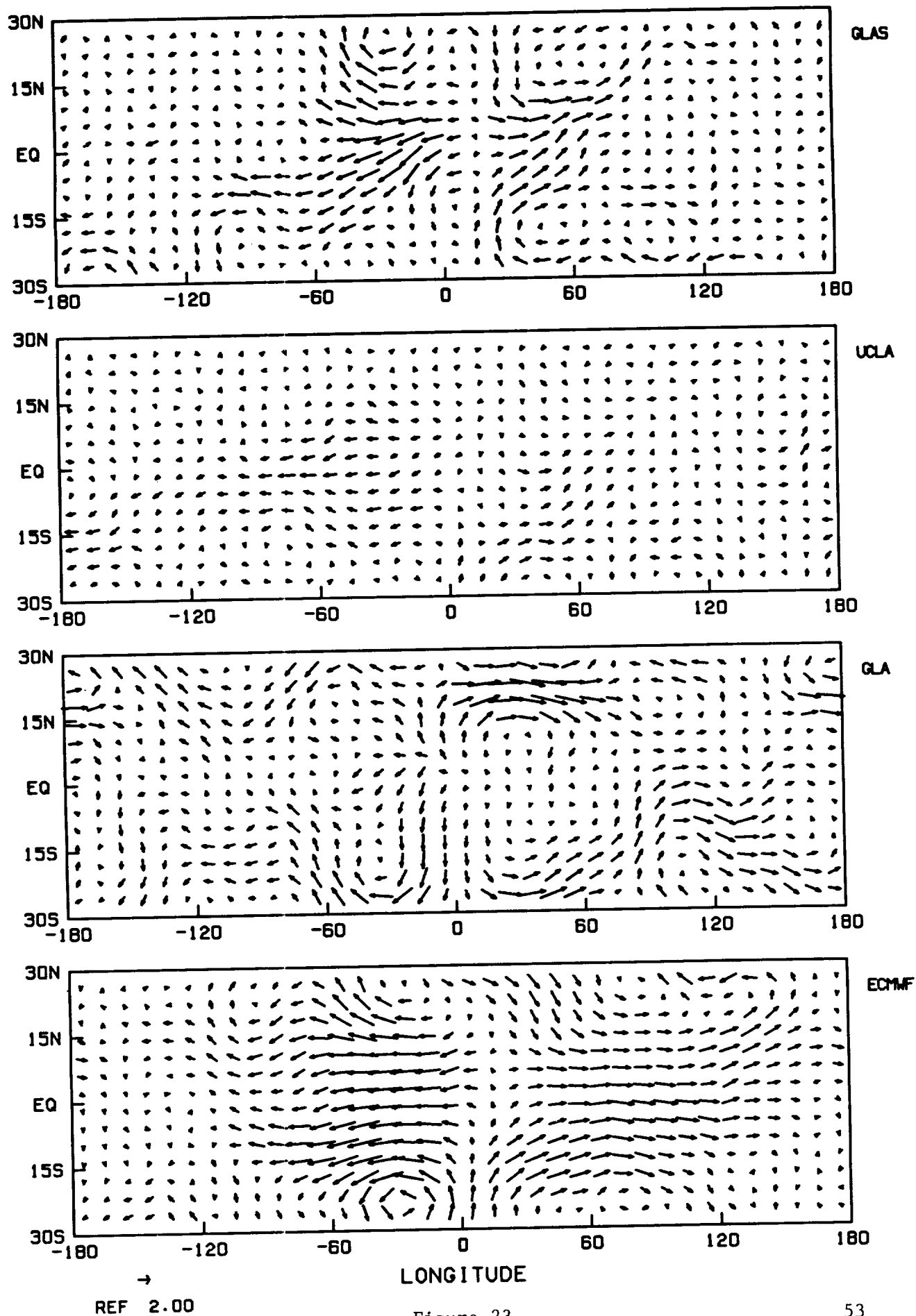


Figure 23

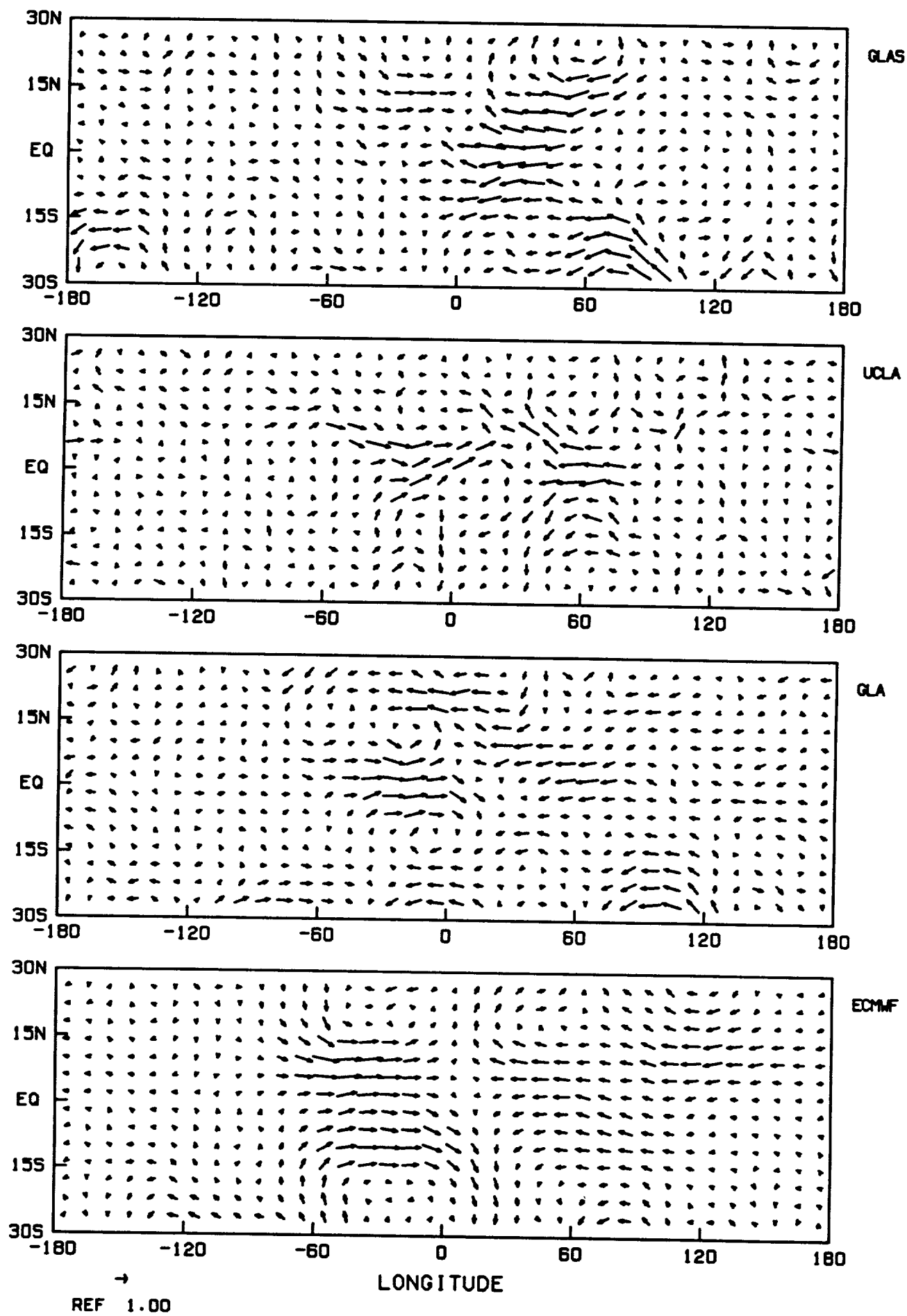


Figure 24

COMPOSITE 200MB QPH (60E-180)

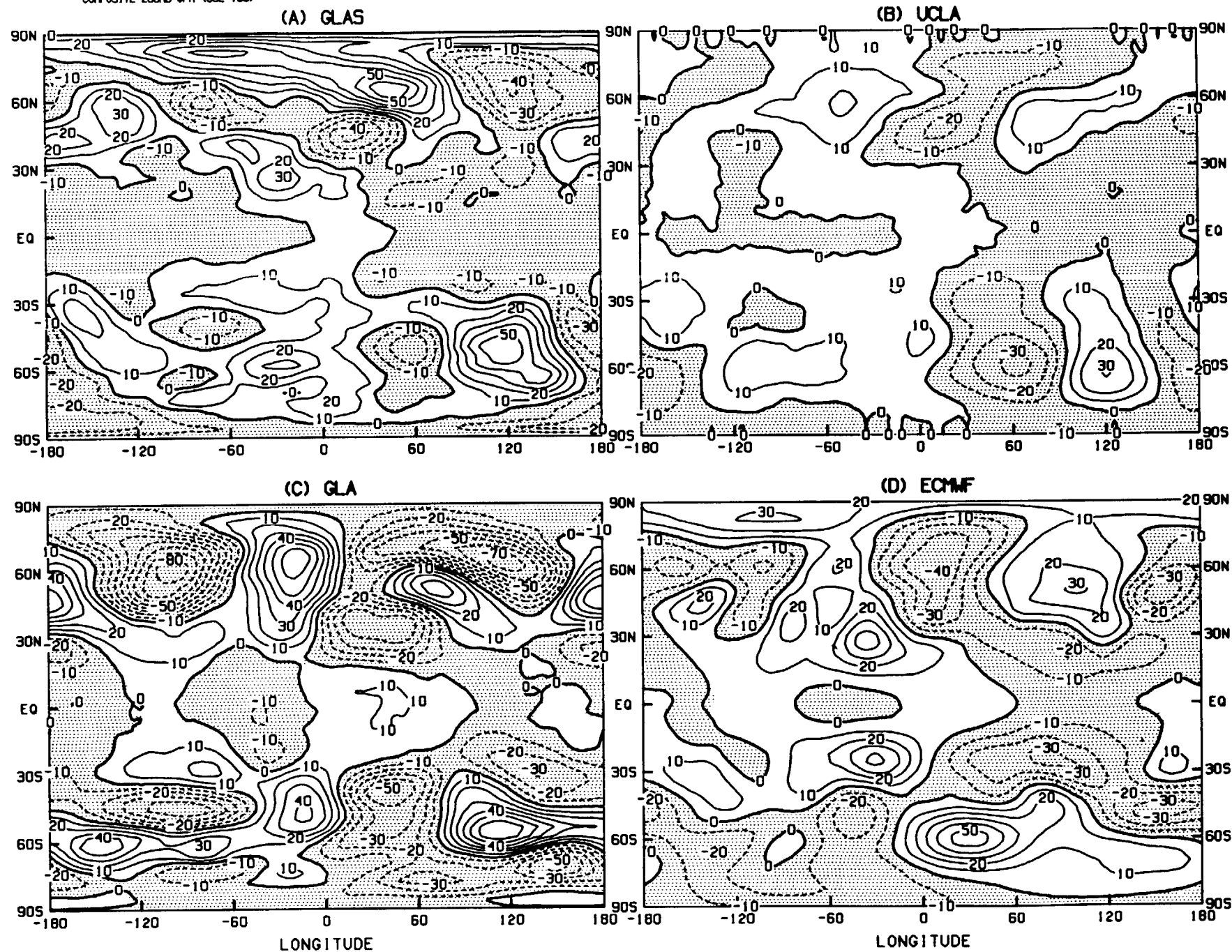


Figure 25

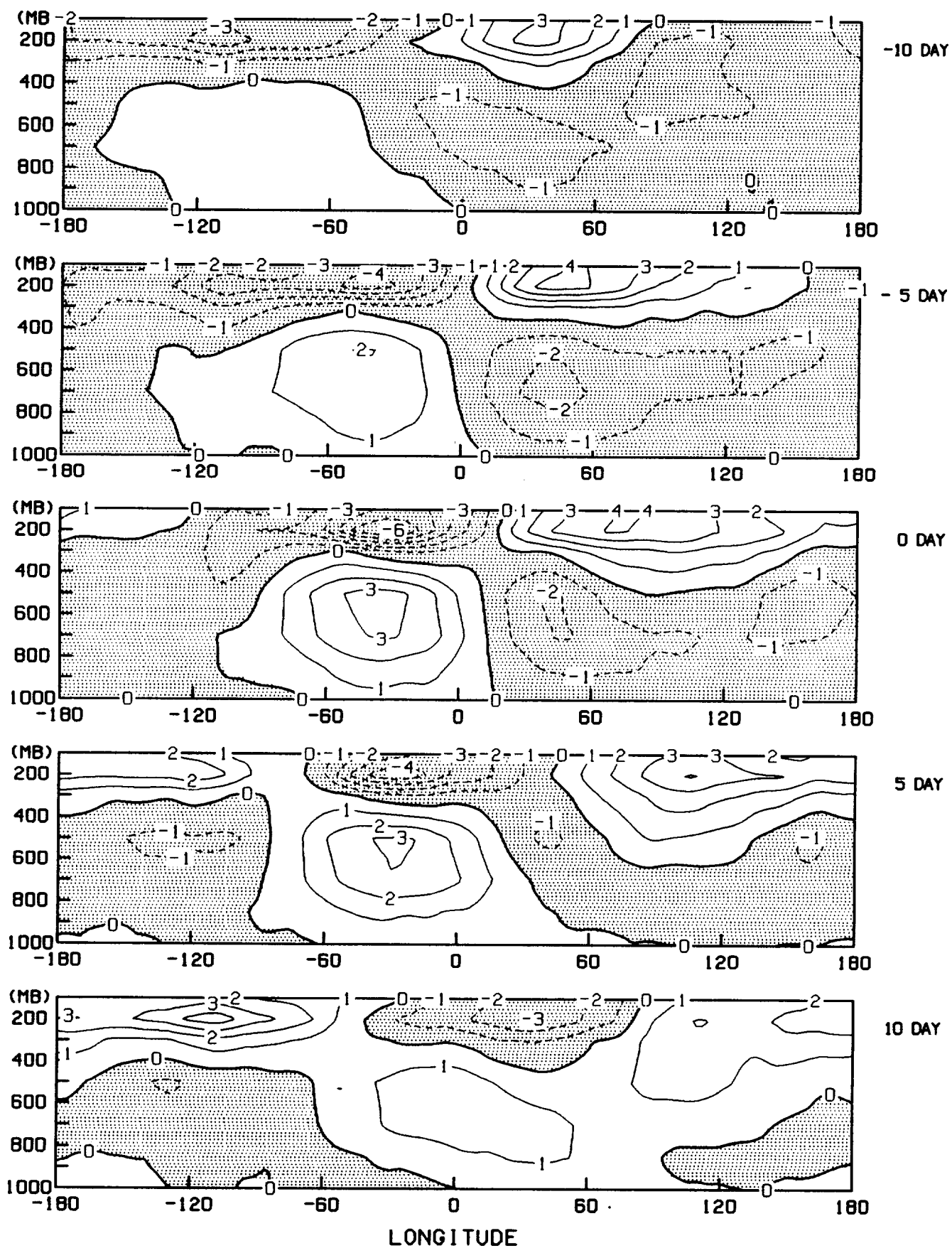


Figure 26

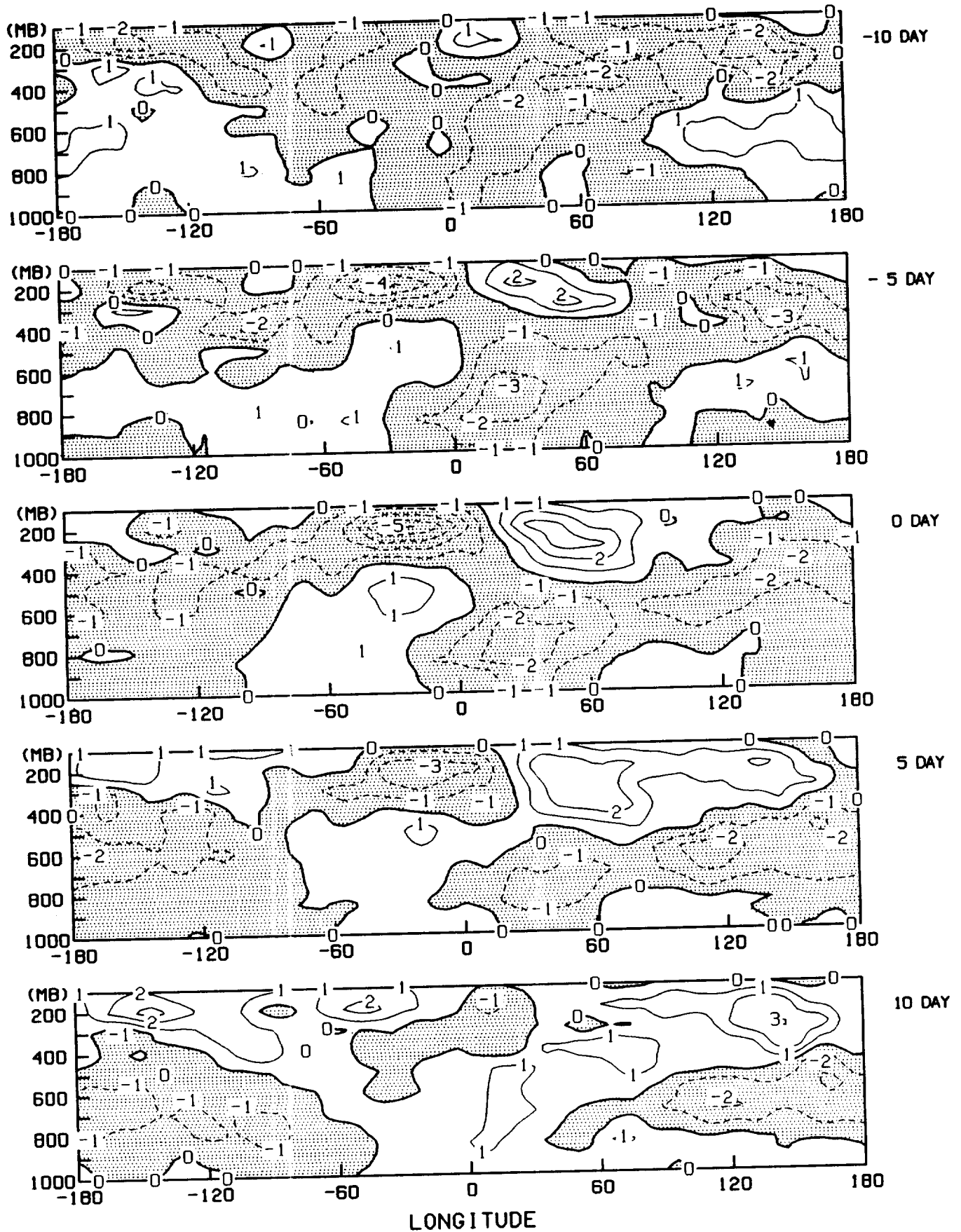


Figure 27

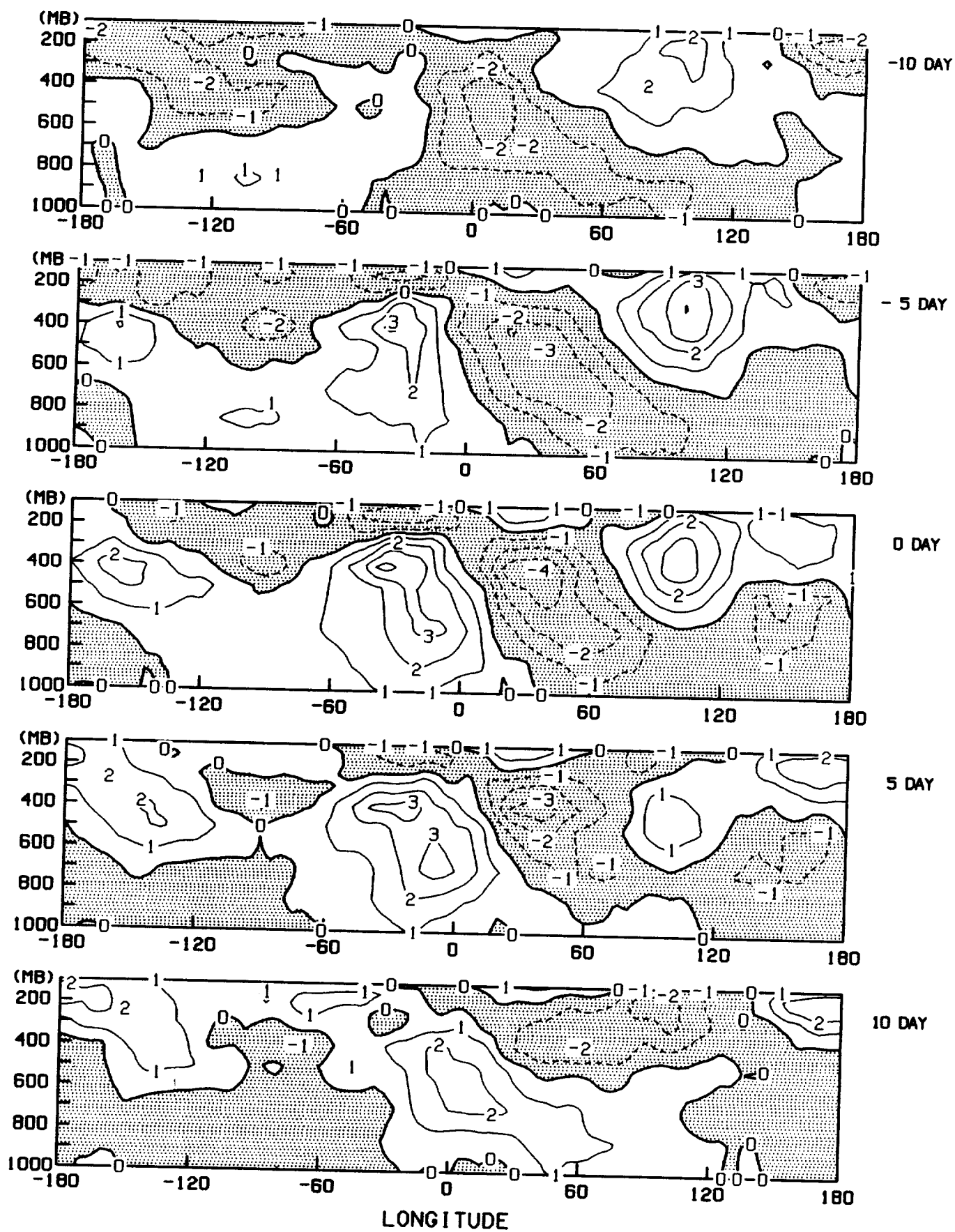


Figure 28

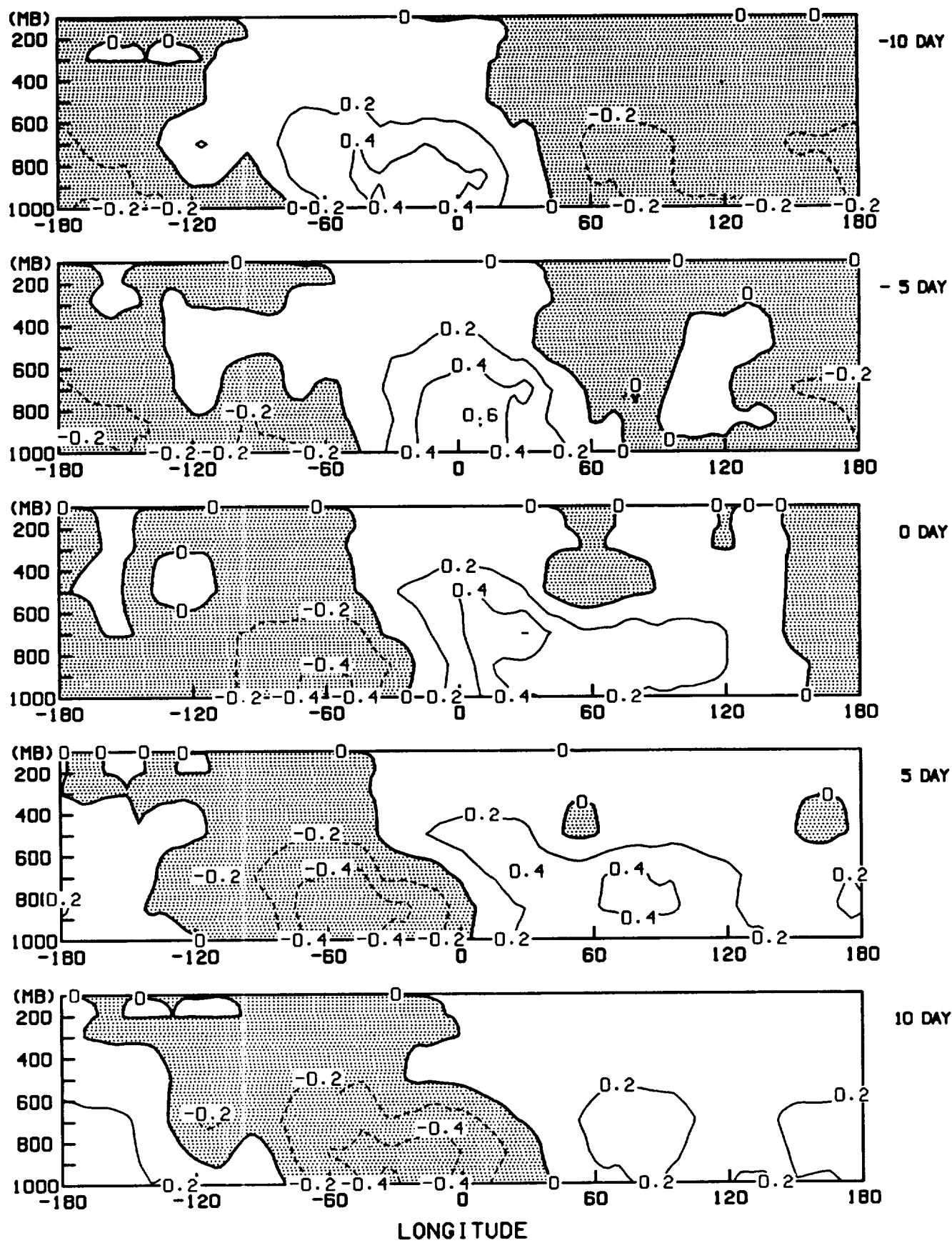


Figure 29

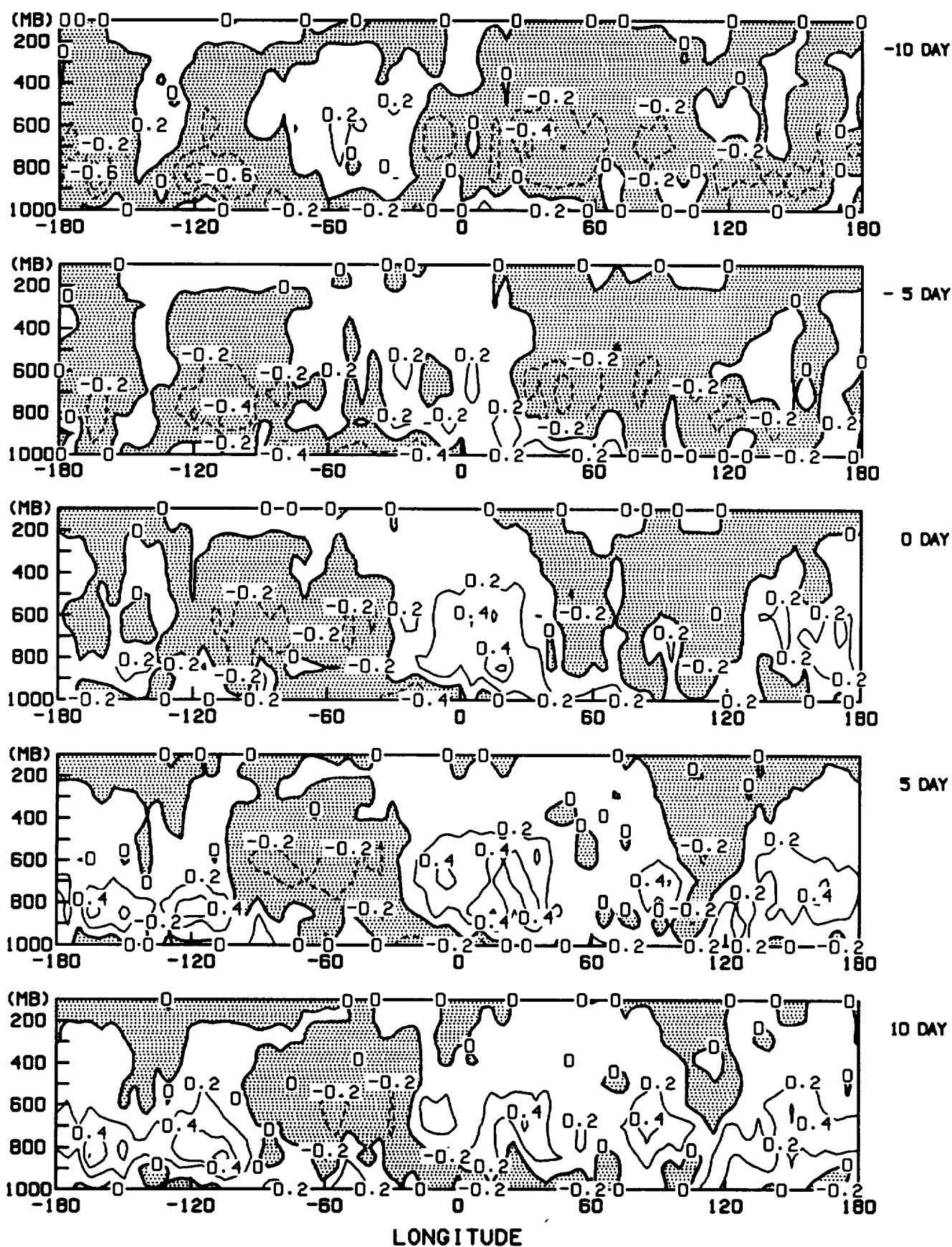
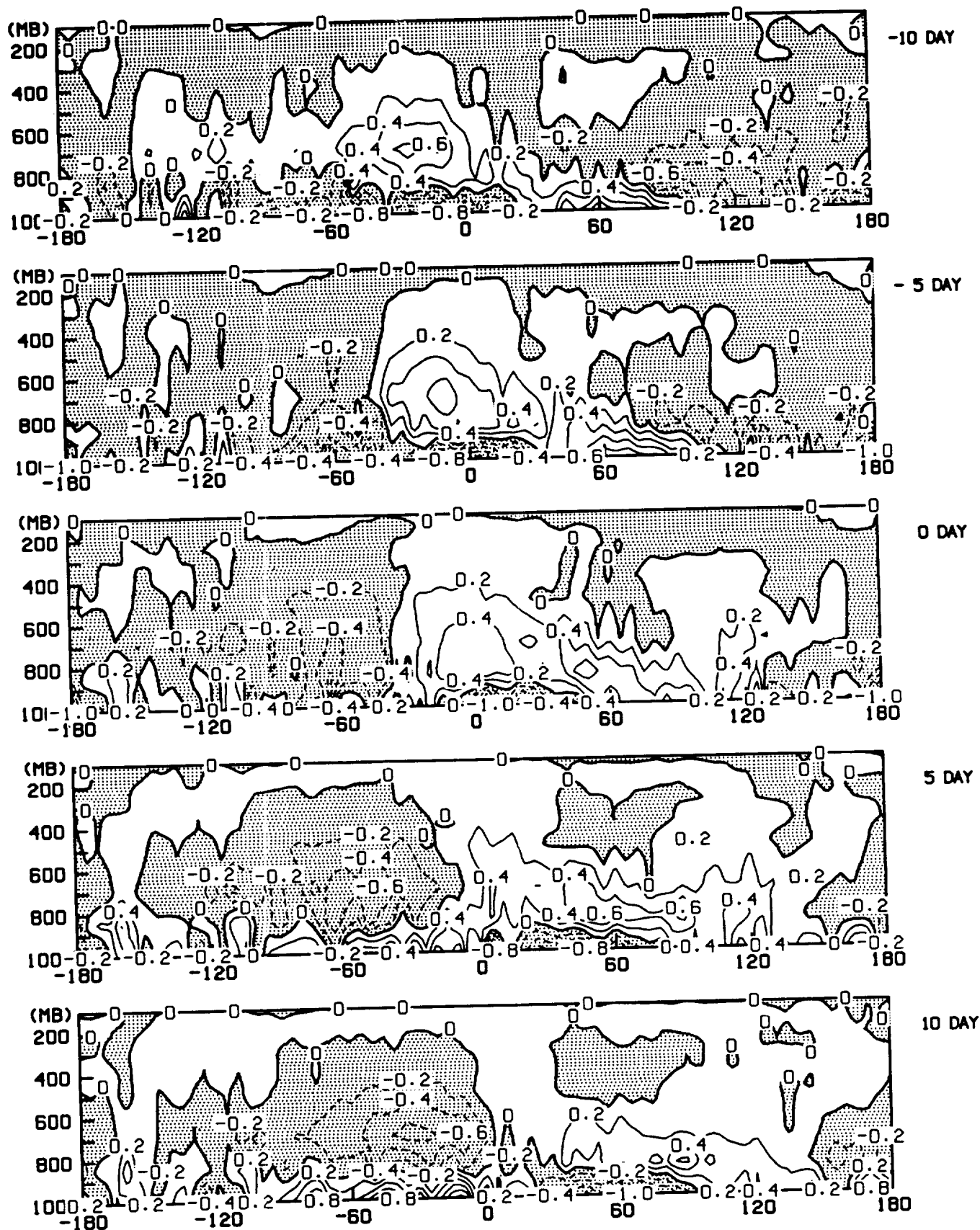


Figure 30



LONGITUDE

Figure 31

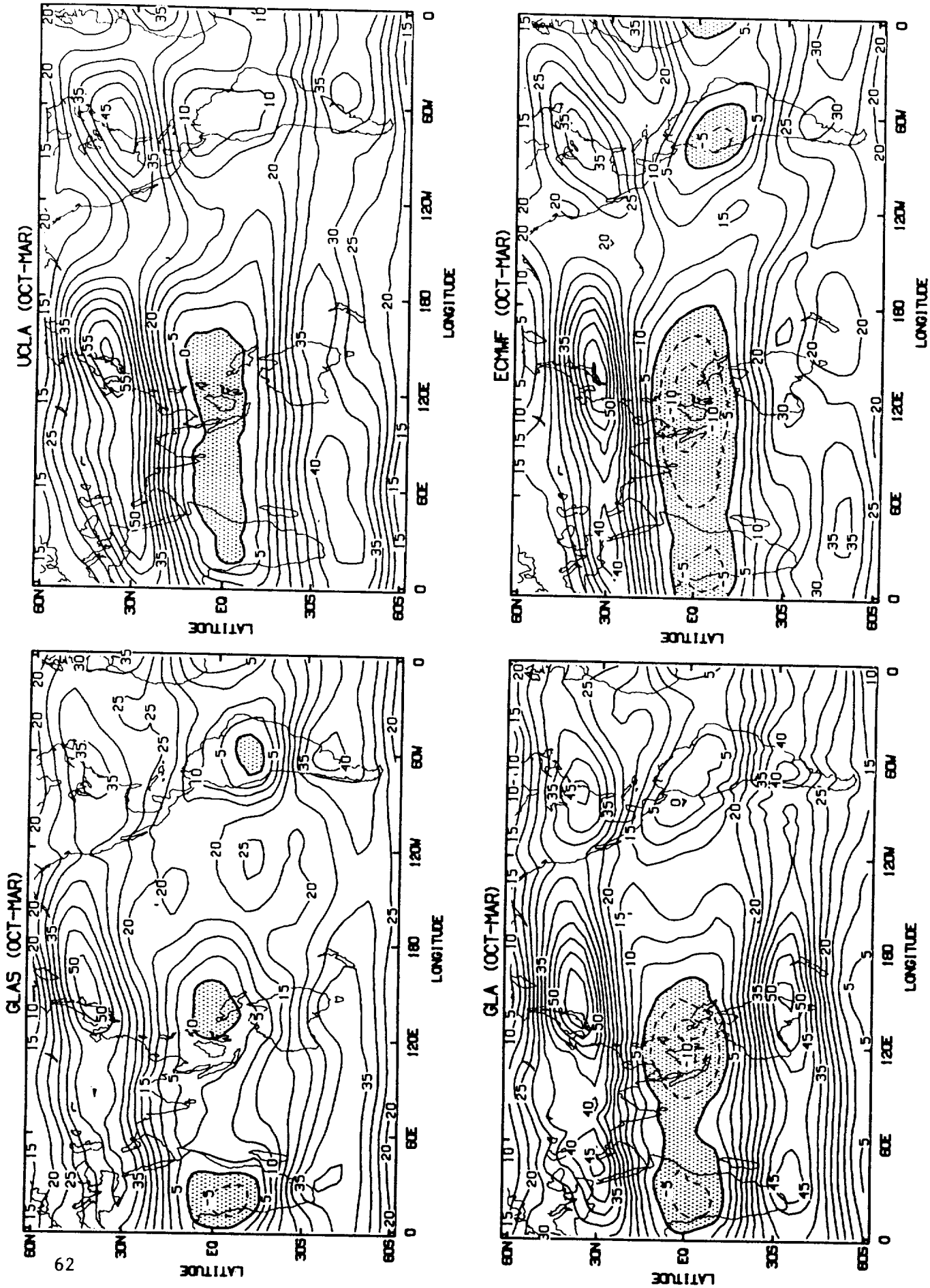


Figure 32

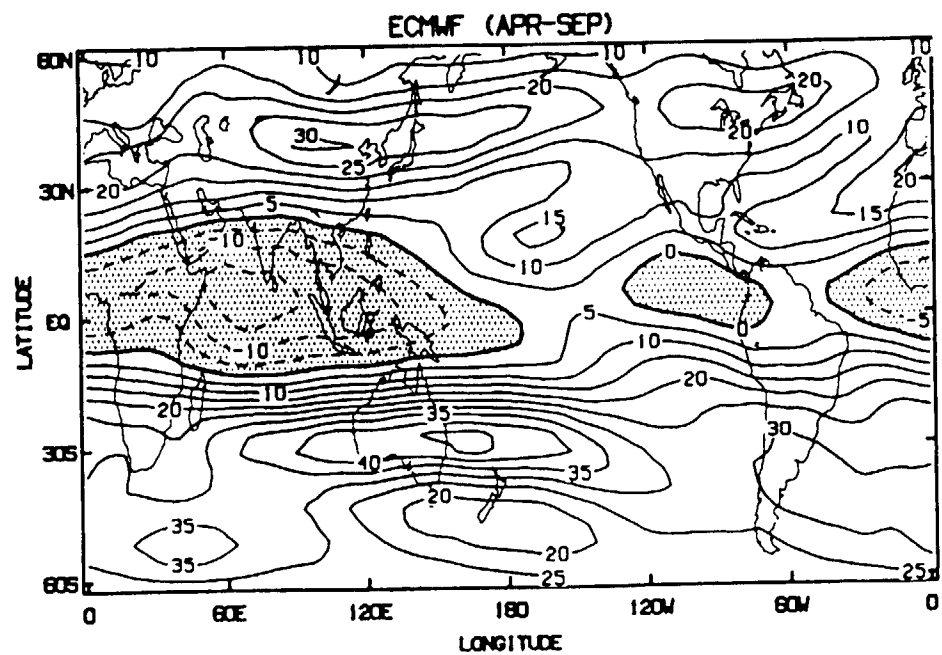
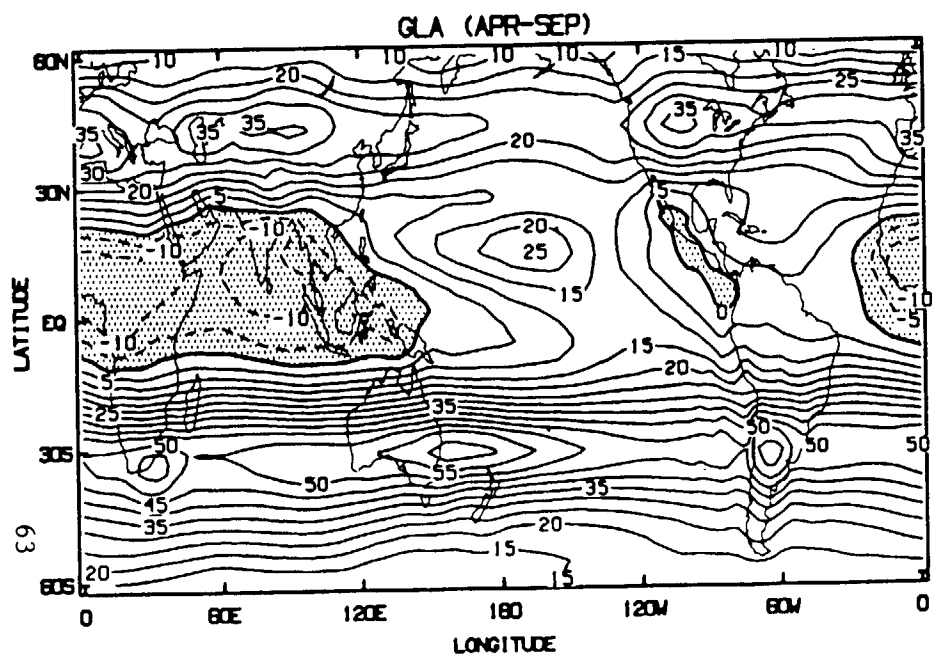
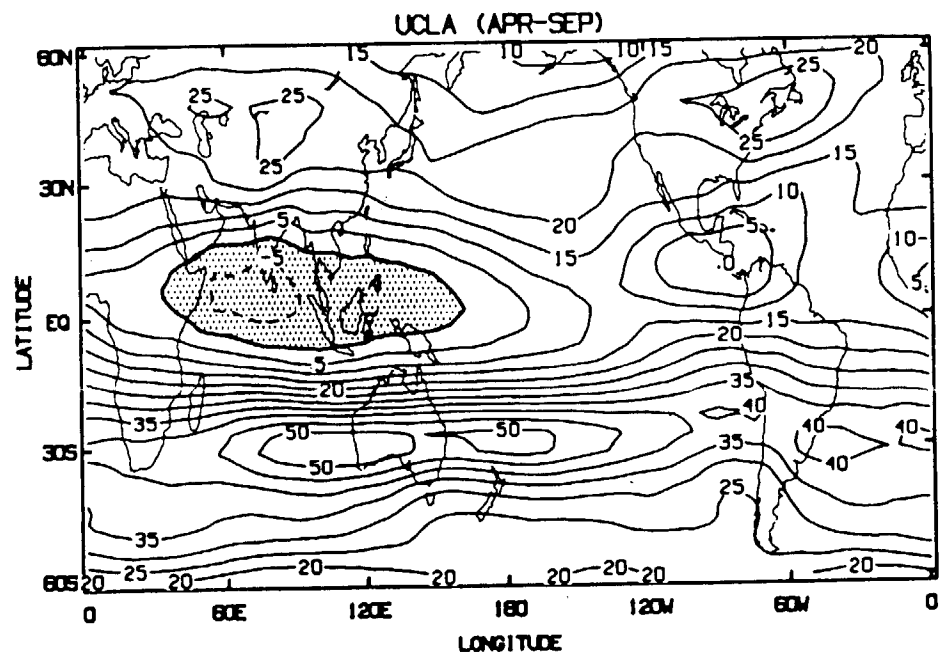
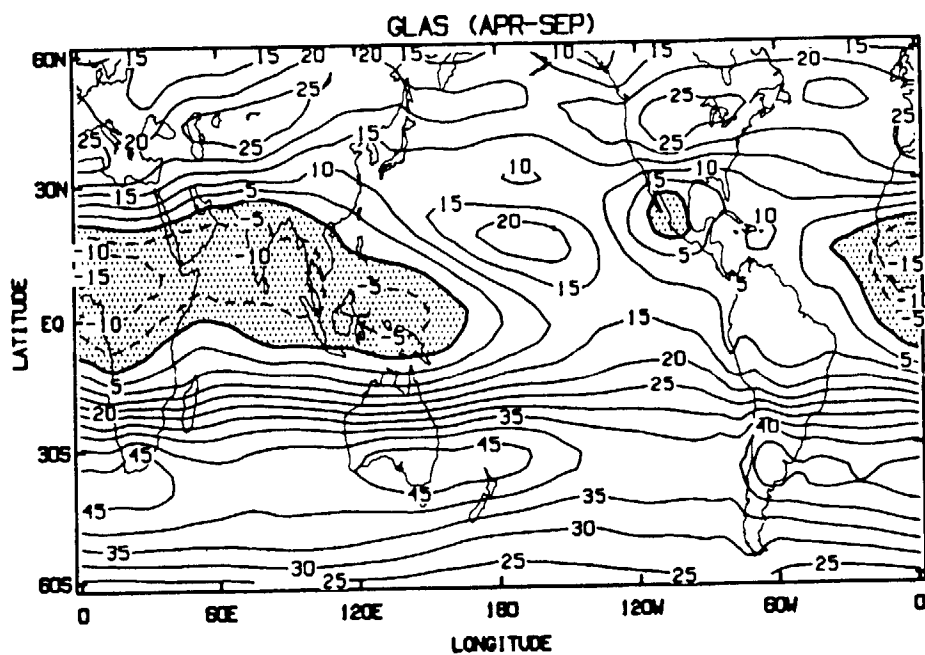
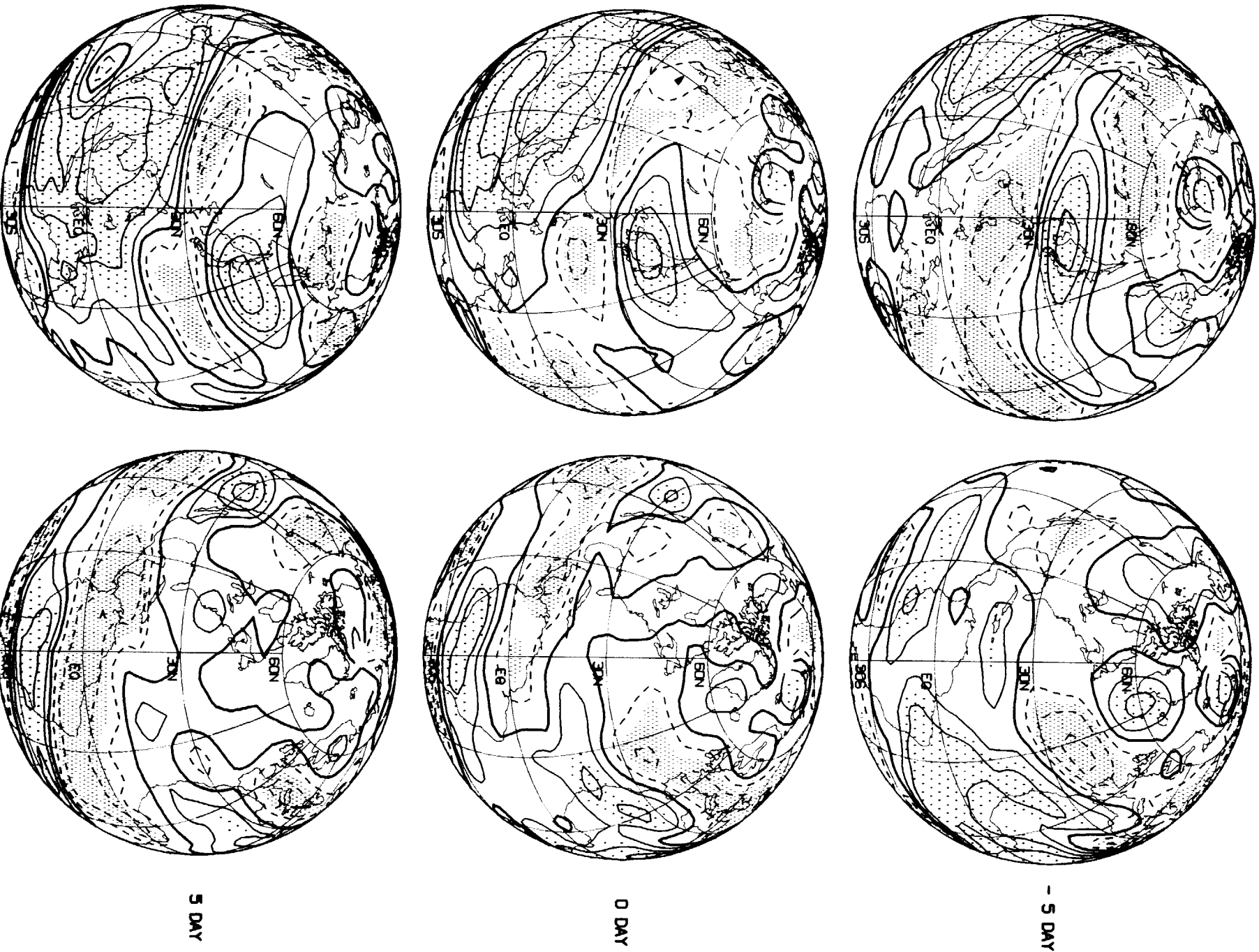


Figure 33



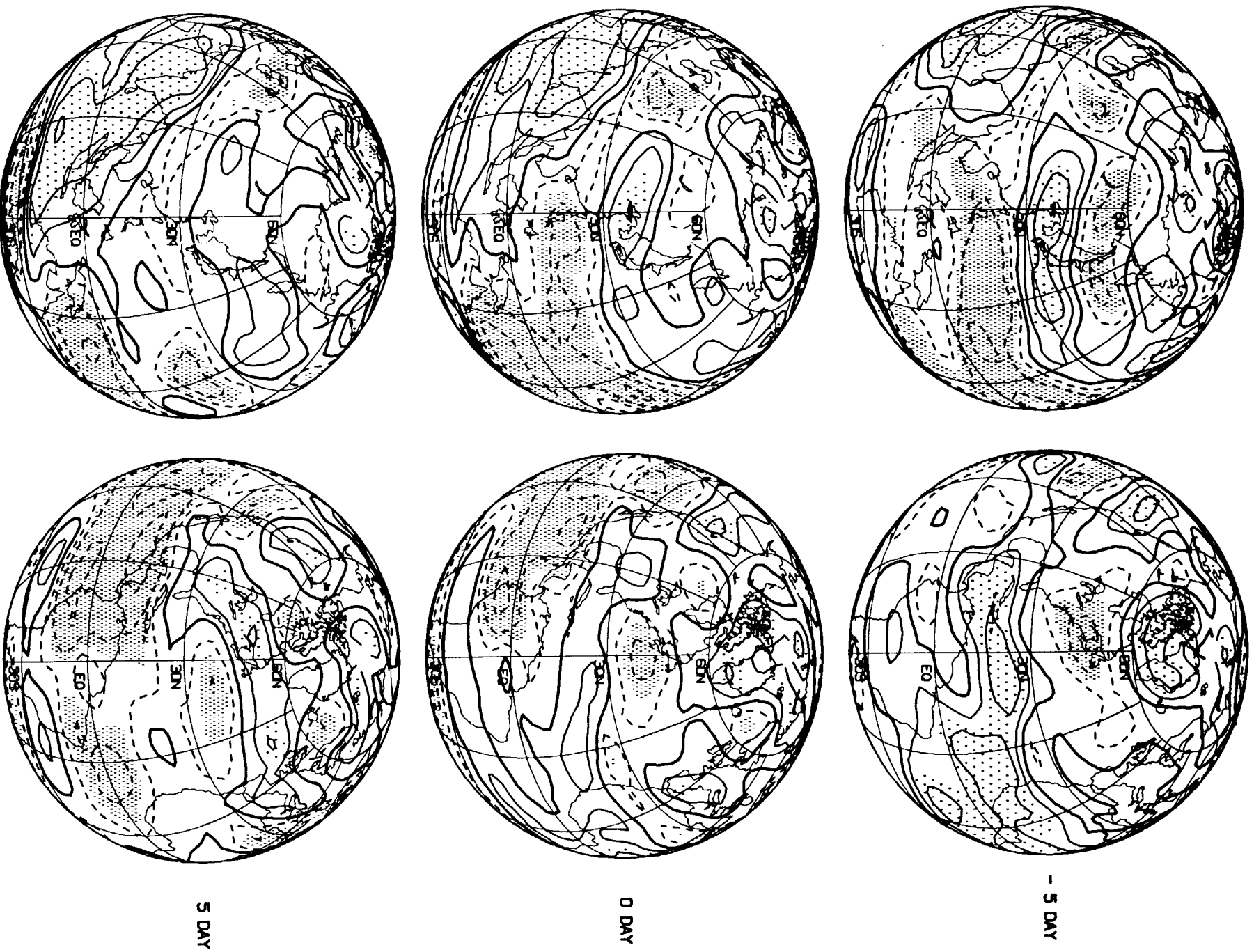
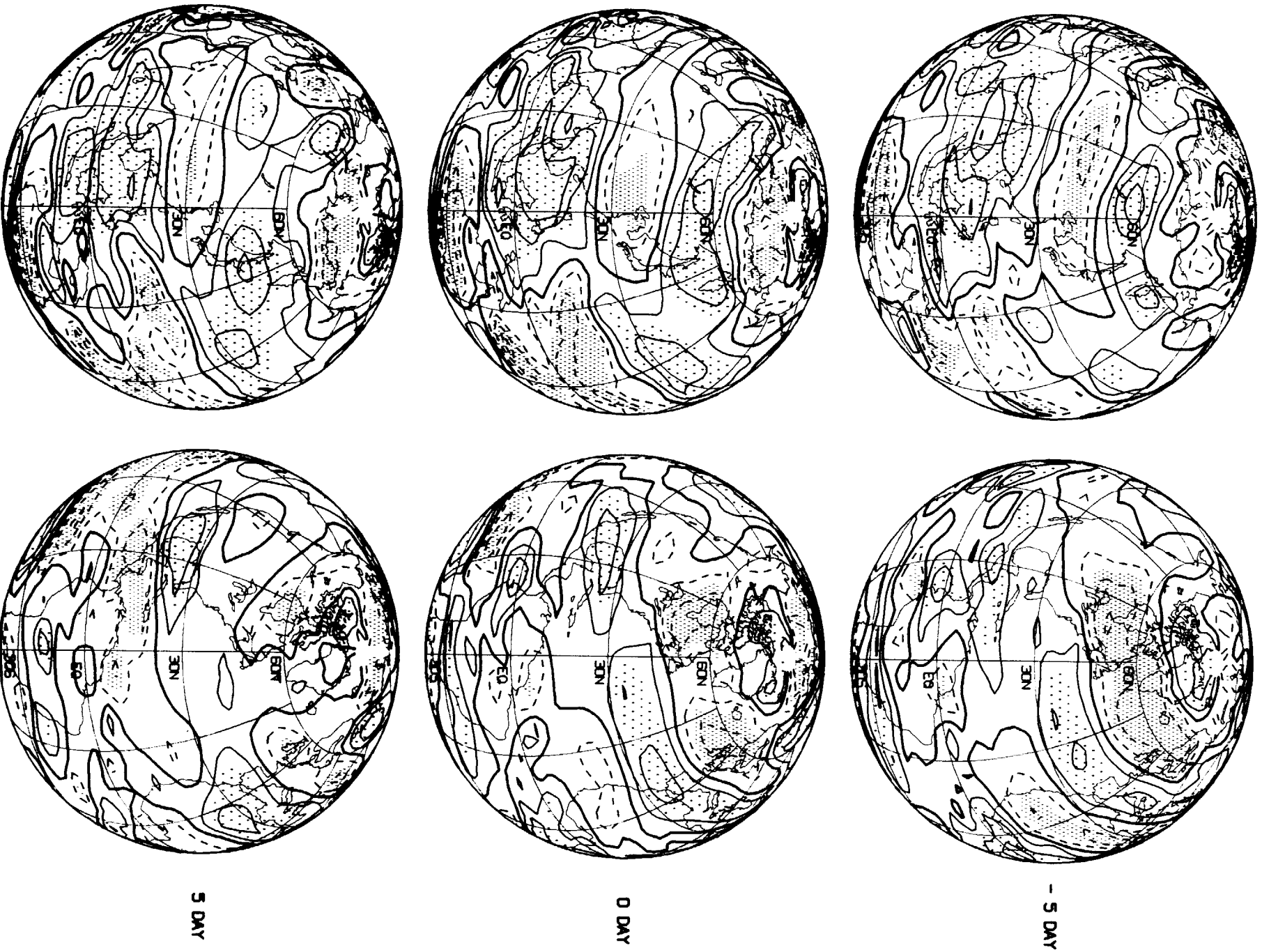
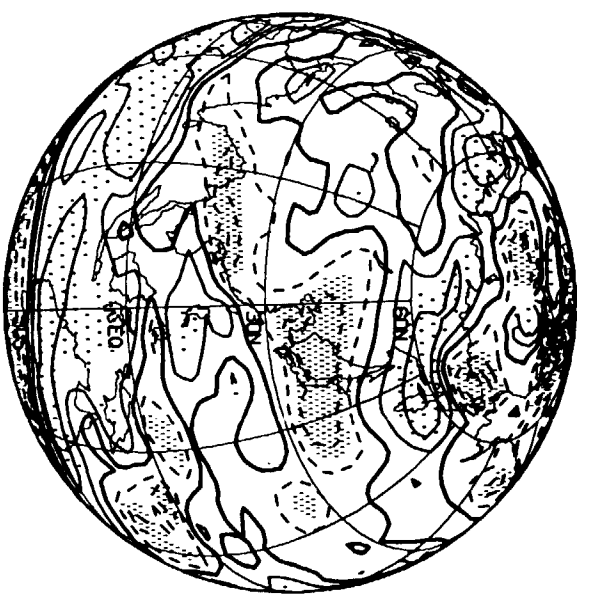


Figure 35



GLAS (APR-SEP)



- 5 DAY



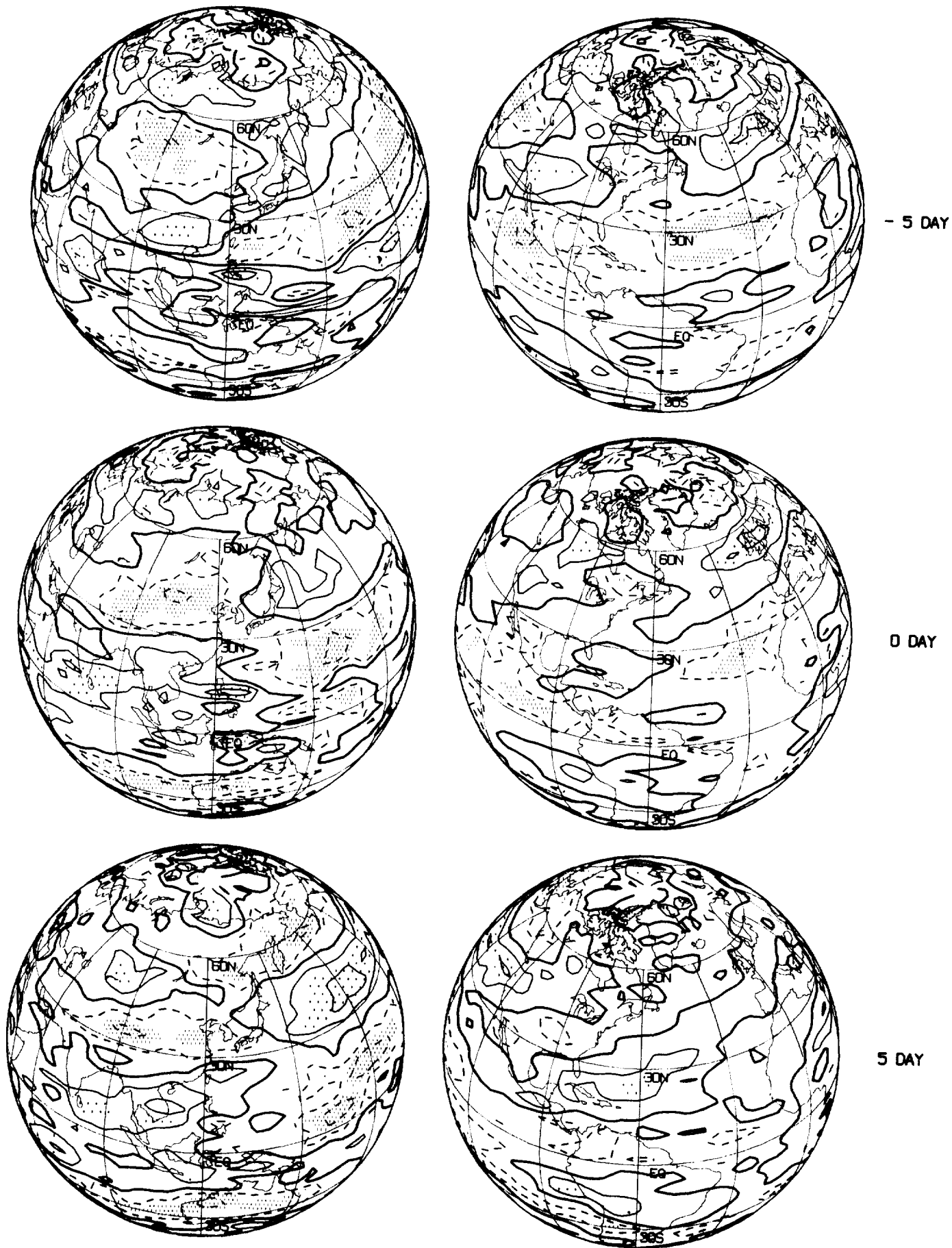
0 DAY



5 DAY



Figure 37



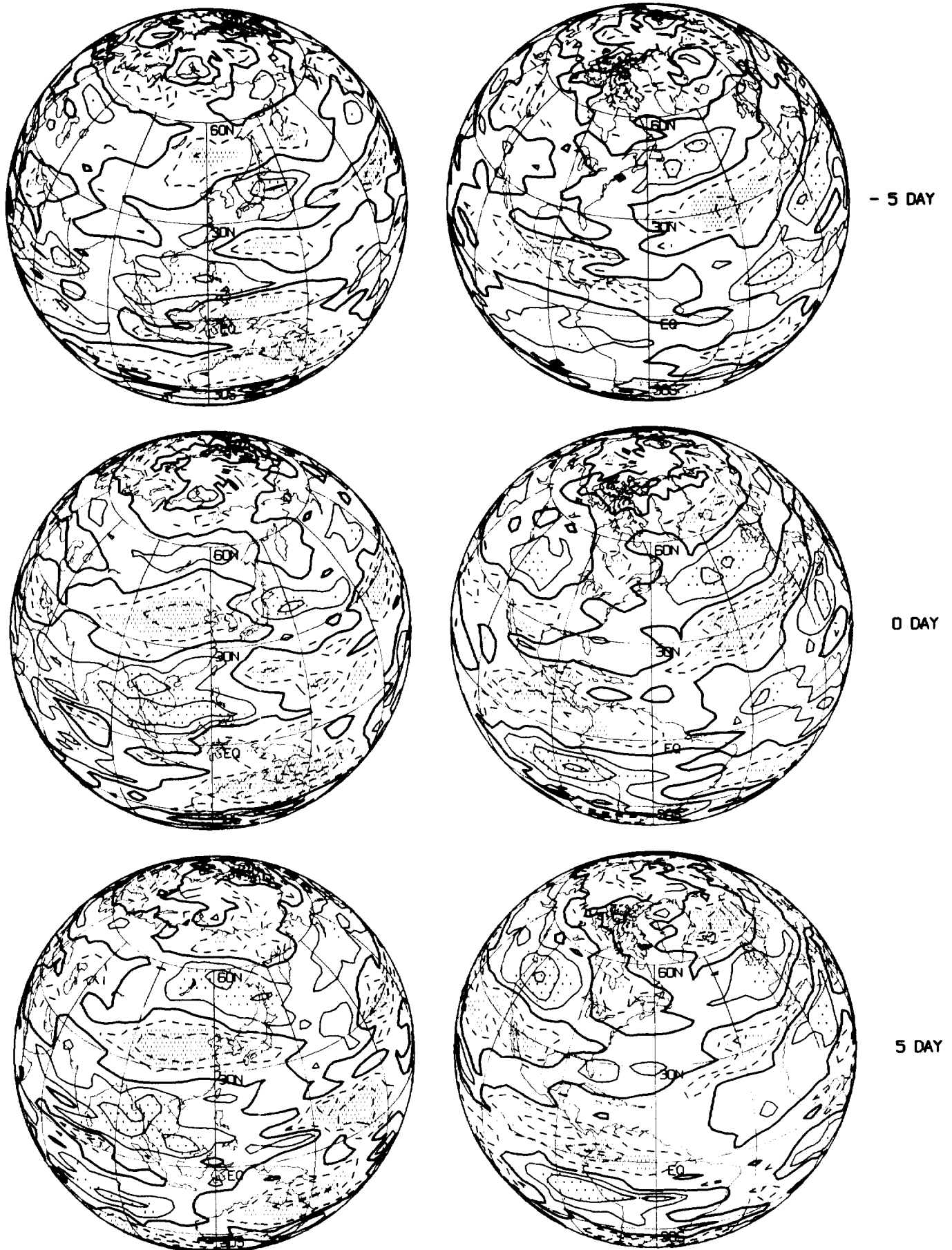
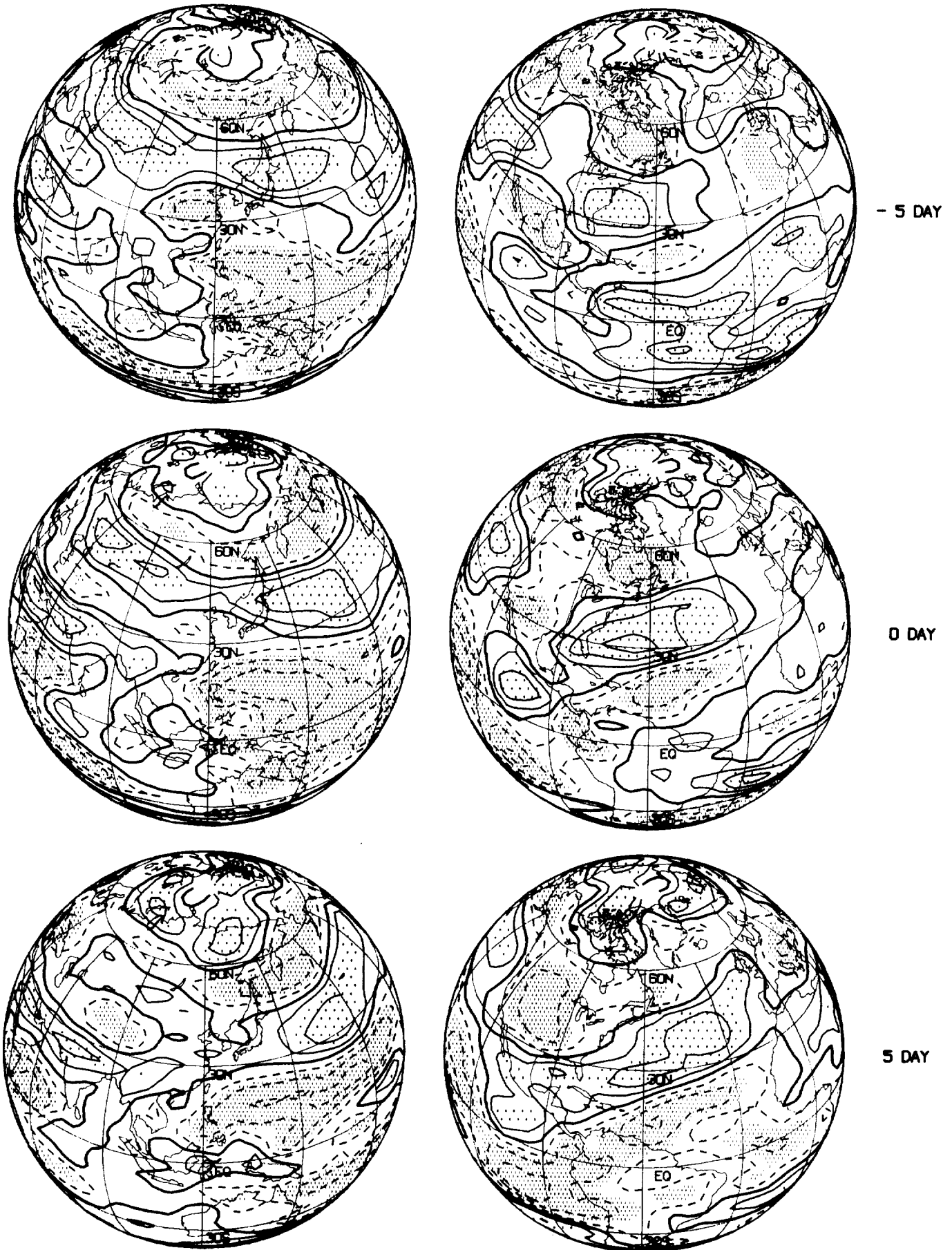


Figure 39



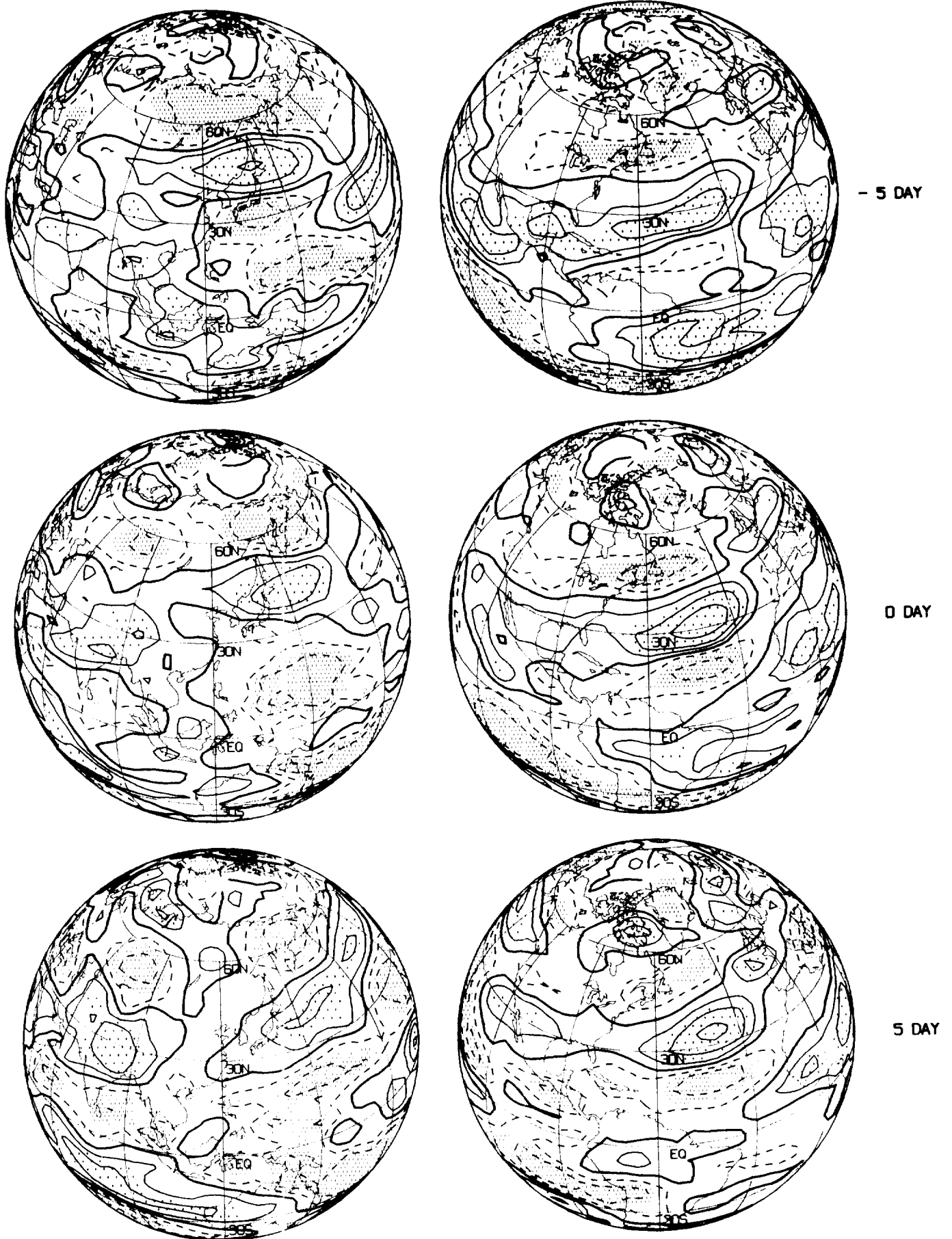


Figure 41

APPENDIX : SEASONAL MEAN PATTERNS

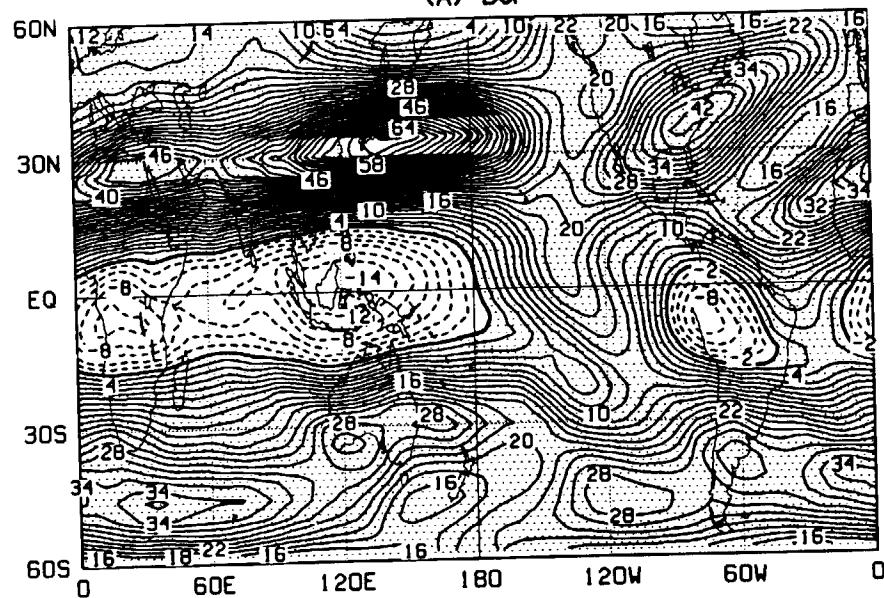
A. Longitude-latitude maps

A1	Seasonal mean u-wind at 200 mb for ECMWF analyses. Contour interval is 2.0 m s ⁻¹ . Positive regions are shaded.
A2	Same as A1, except for GLAS GCM.
A3	Same as A1, except for UCLA GCM.
A4	Same as A1, except for GLA GCM.
A5	Same as A1, except for 200 mb v-wind.
A6	Same as A5, except for GLAS GCM.
A7	Same as A5, except for UCLA GCM.
A8	Same as A5, except for GLA GCM.
A9	Same as A1, except for 850 mb u-wind.
A10	Same as A 9, except for GLAS GCM.
A11	Same as A9, except for UCLA GCM.
A12	Same as A9, except for GLA GCM.
A13	Same as A1, except for 850 mb v-wind.
A14	Same as A13, except for GLAS GCM.
A15	Same as A13, except for UCLA GCM.
A16	Same as A13, except for GLA GCM.
A17	Same as A1, except for 200 mb divergence. Contour interval is 2.0x10 ⁻⁶ s ⁻¹ .
A18	Same as A17, except for GLAS GCM.
A19	Same as A17, except for UCLA GCM.
A20	Same as A17, except for GLA GCM.
A21	Same as A1, except for 200 mb velocity potential. Contour interval is 2.0x10 ⁶ m ² s ⁻¹ .
A22	Same as A21, except for GLAS GCM.
A23	Same as A21, except for UCLA GCM.

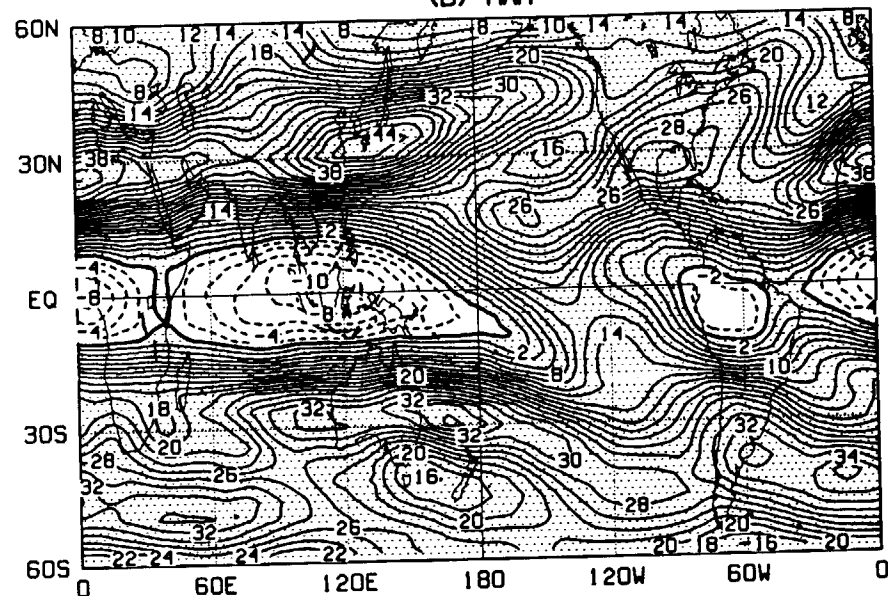
- A24 Same as A21, except for GLA GCM.
- A25 Seasonal mean precipitation for GLAS GCM. Contour interval is 5.0 mm day⁻¹.
Values greater than 5.0 mm day⁻¹ are shaded and values greater than 10.0 mm day⁻¹
with darker shading.
- A26 Same as A25, except for UCLA GCM.
- A27 Same as A25, except for GLA GCM.

SEASONAL MEAN 200MB U (ECMWF)

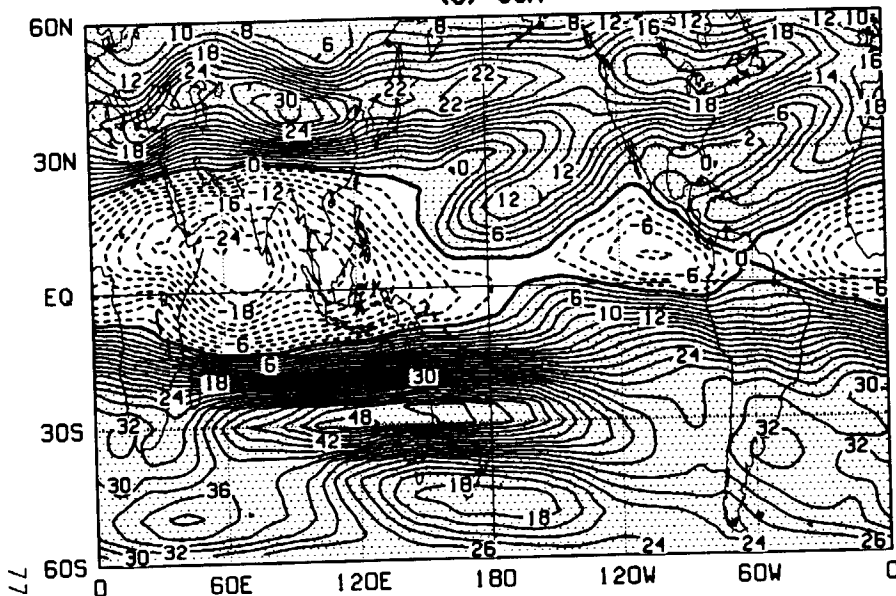
(A) DJF



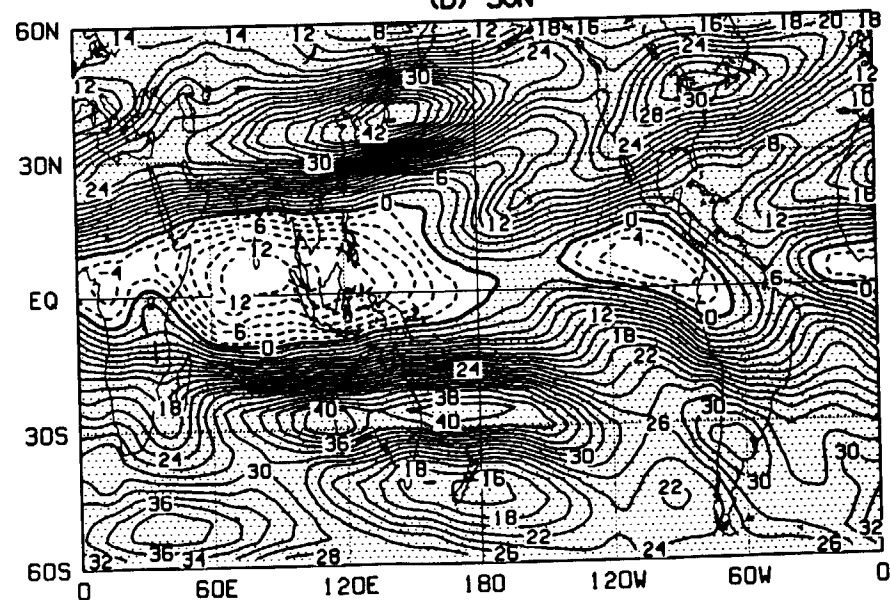
(B) MAM

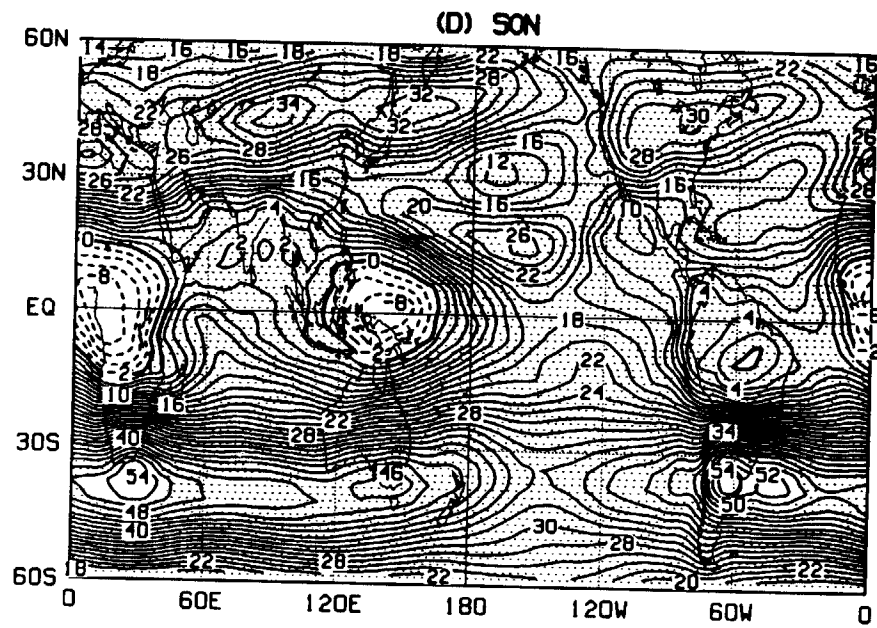
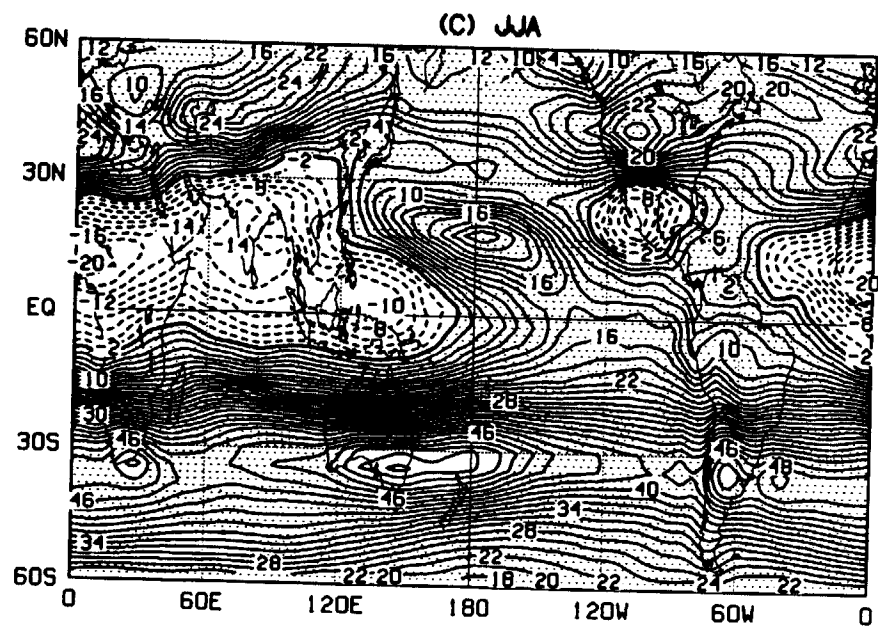
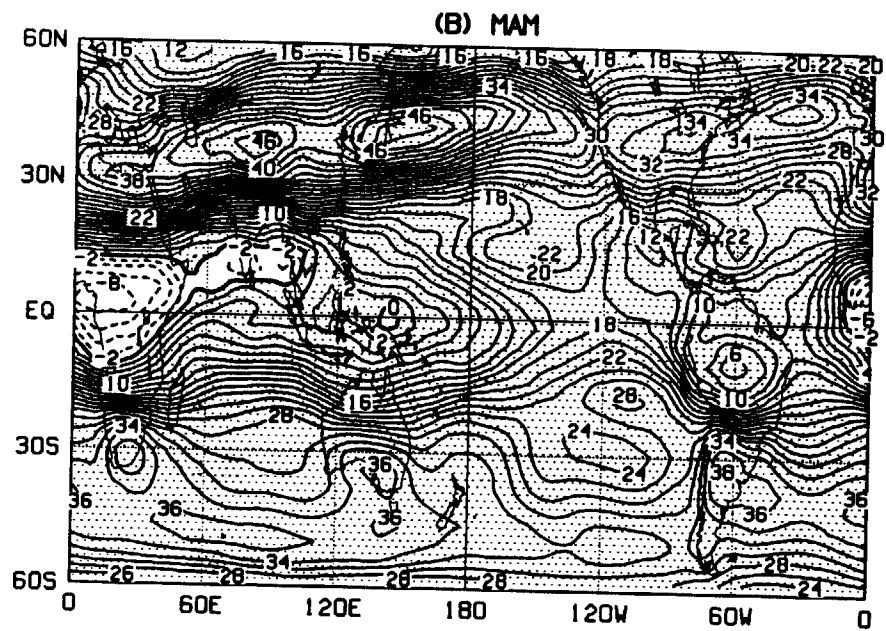
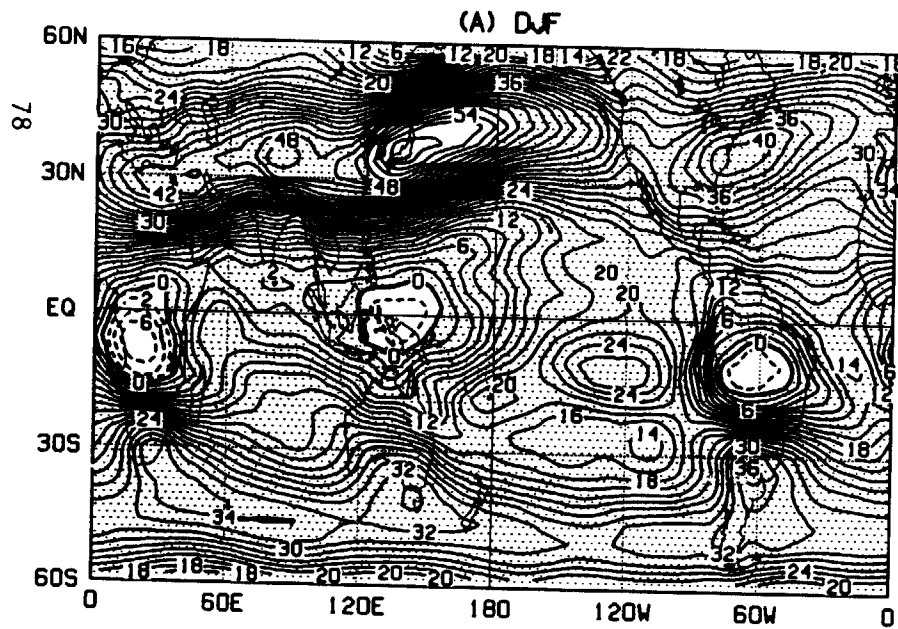


(C) JJA



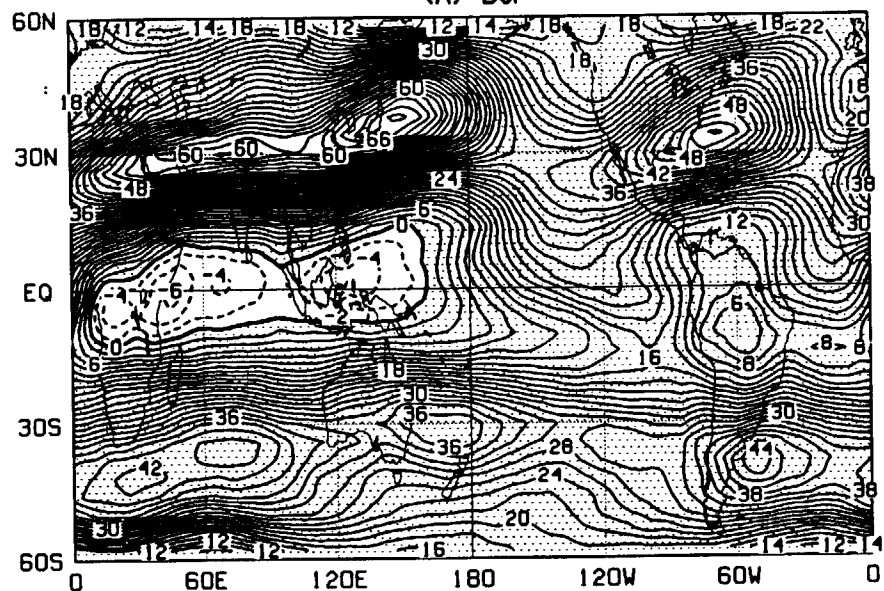
(D) SON



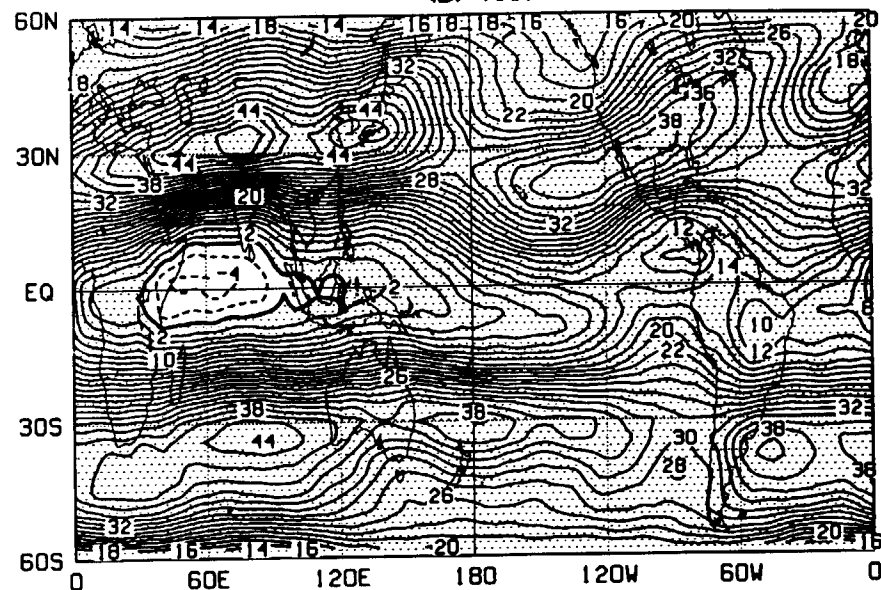


SEASONAL MEAN 200MB U (UCLA)

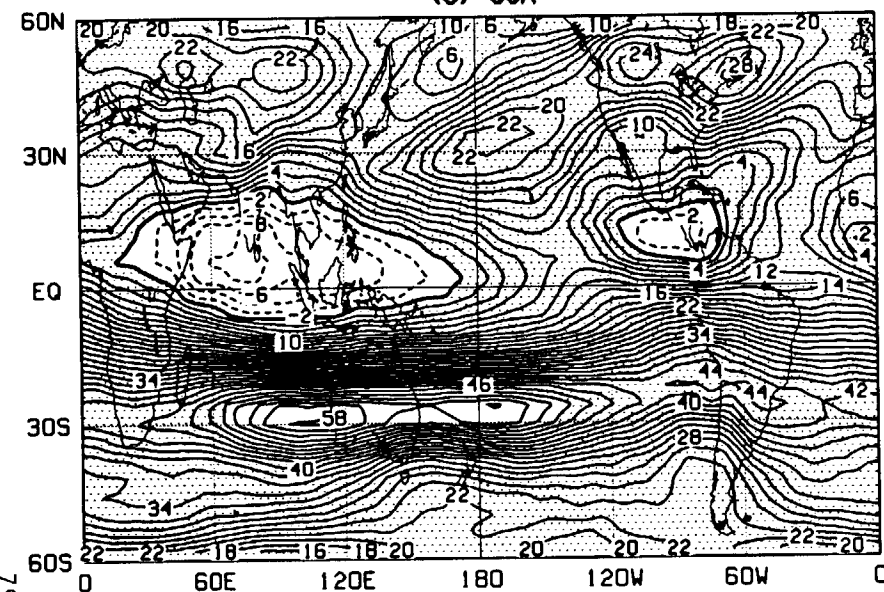
(A) DJF



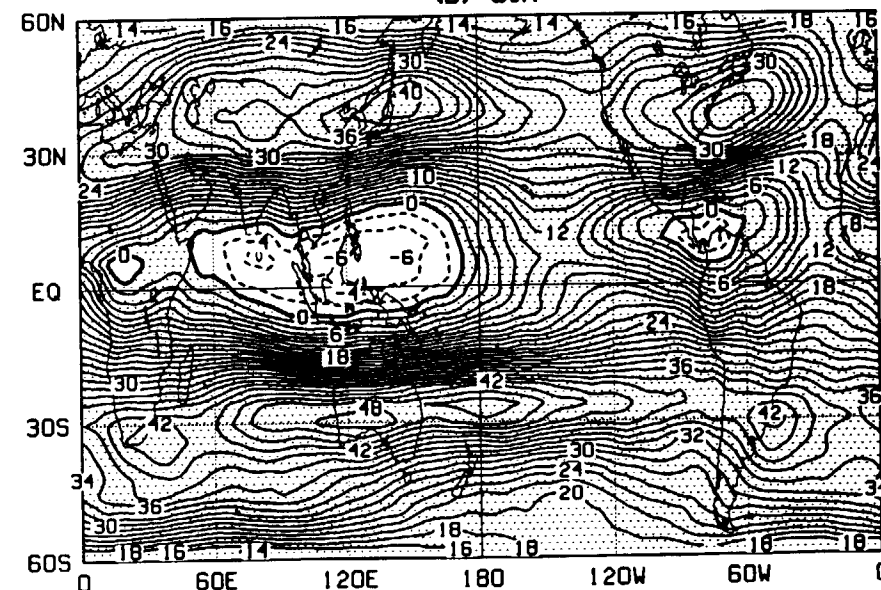
(B) MAM

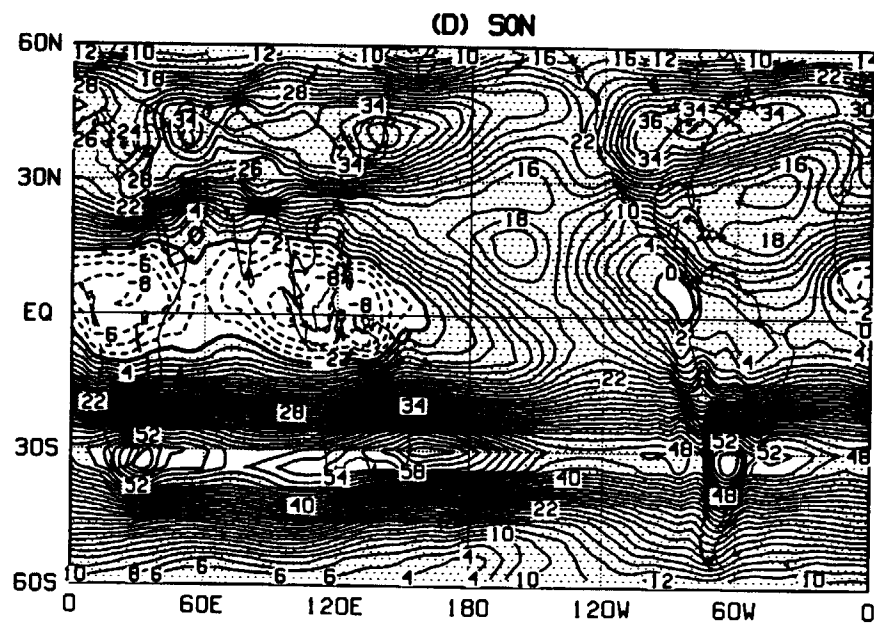
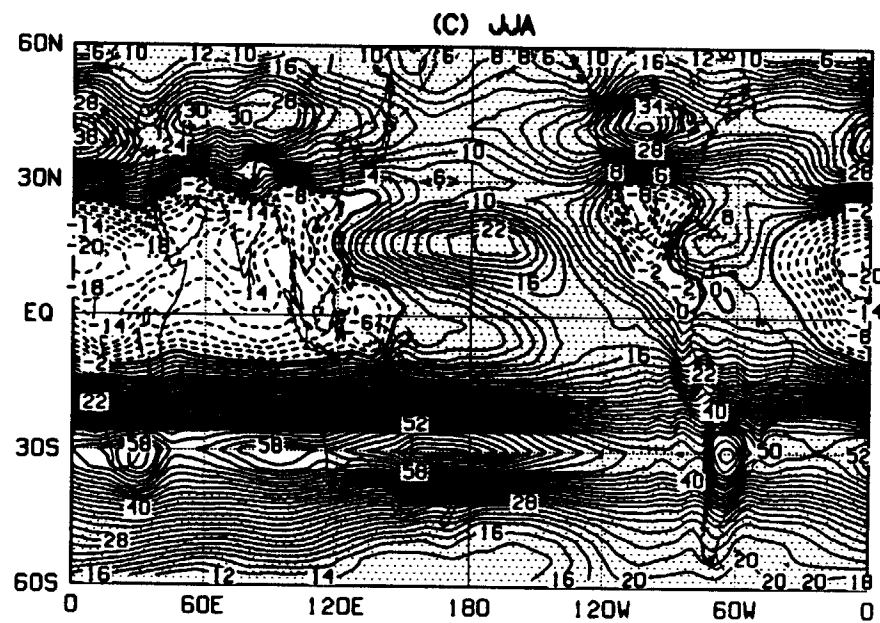
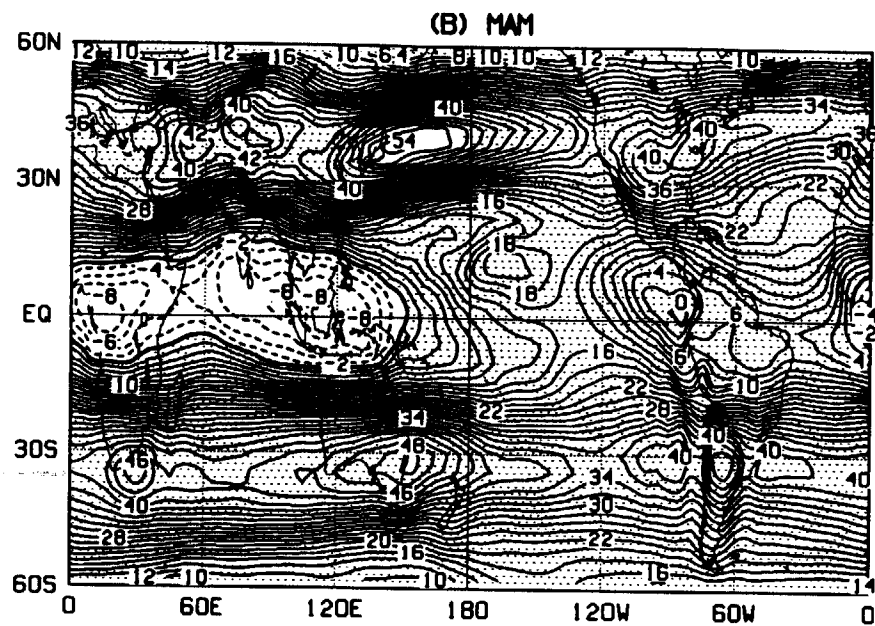
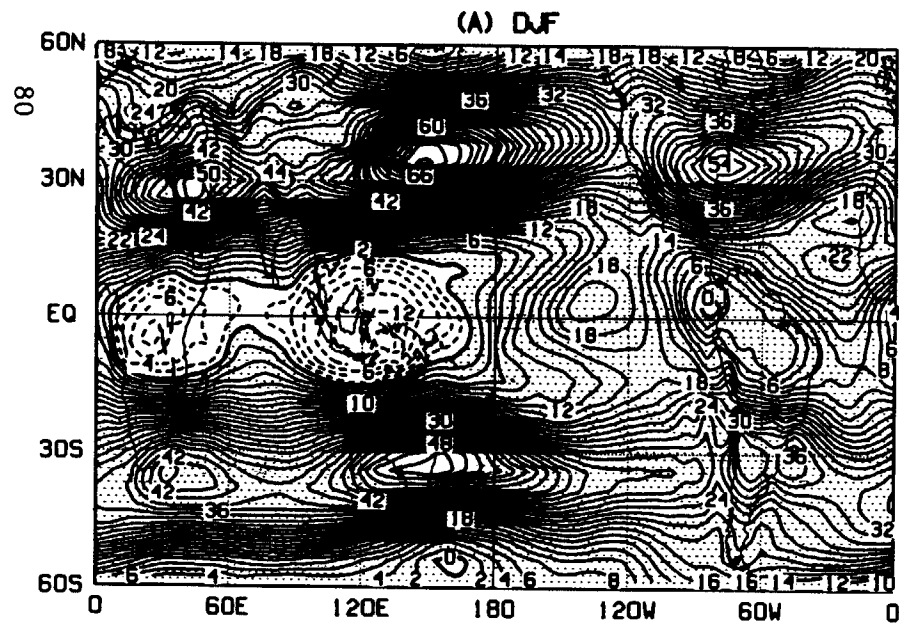


(C) JJA



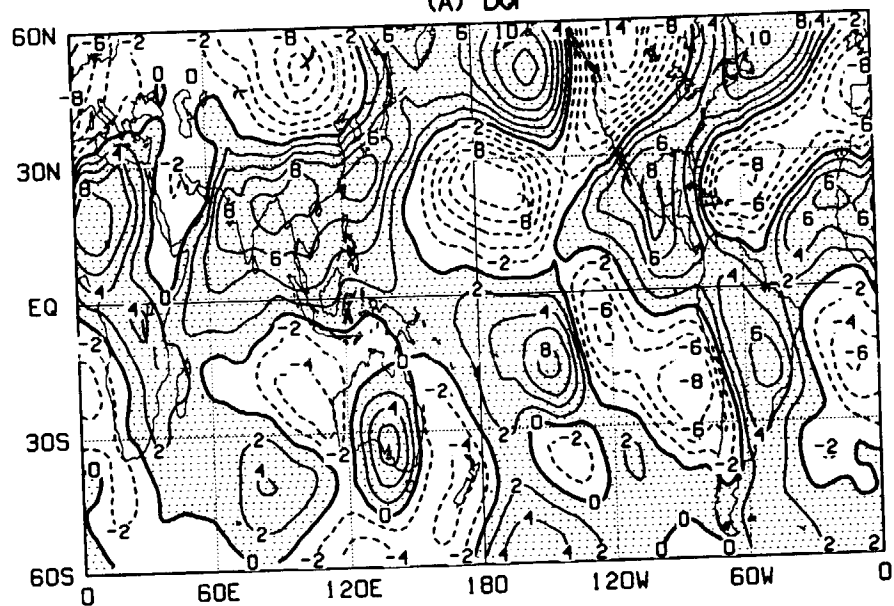
(D) SON



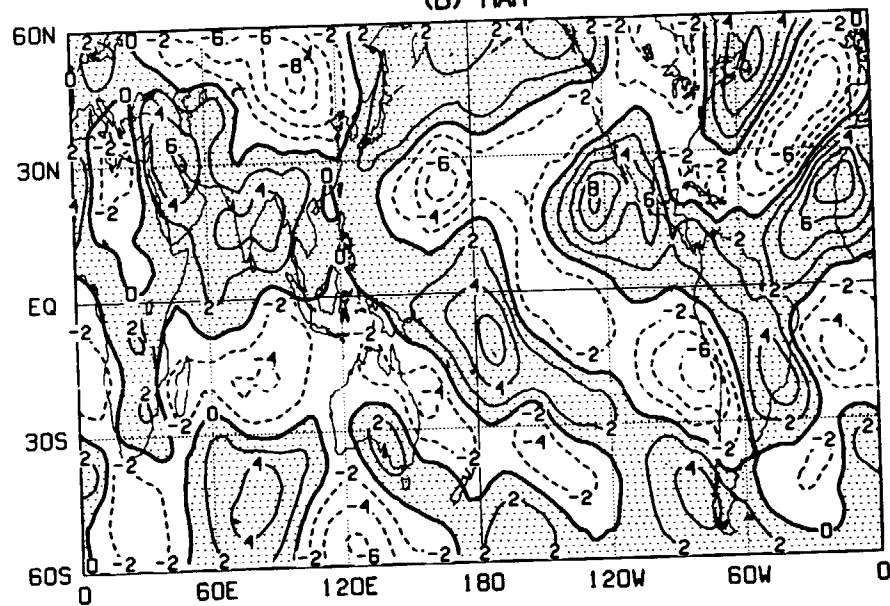


SEASONAL MEAN 200MB V (ECHM5)

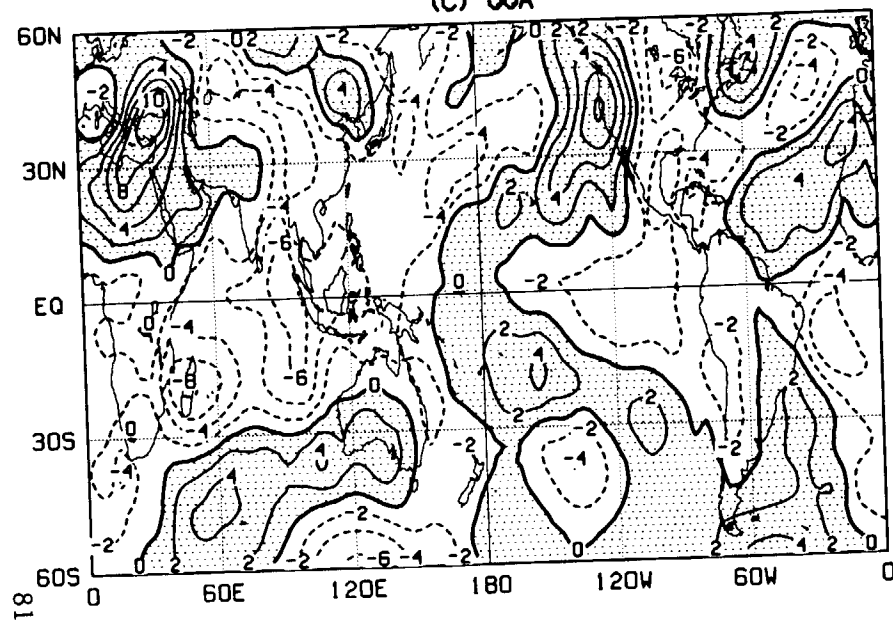
(A) DJF



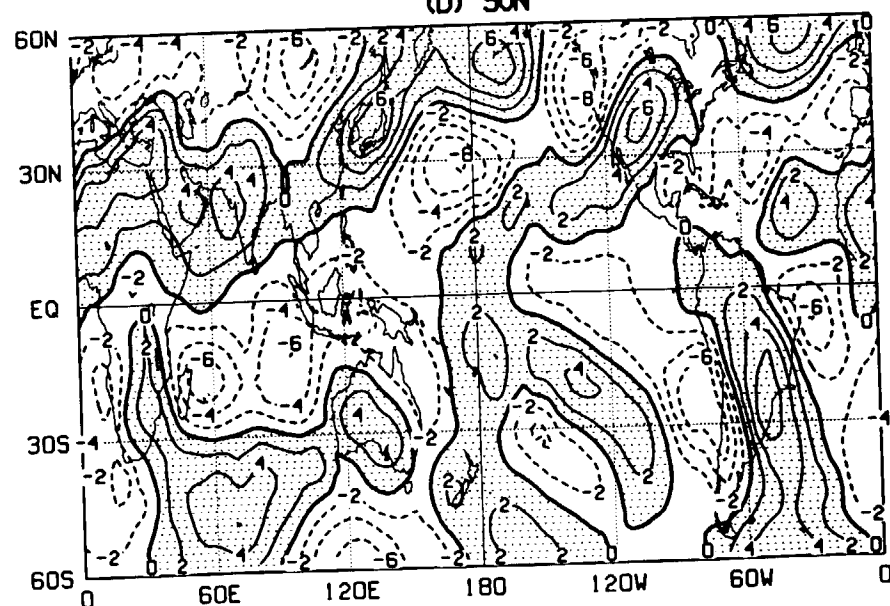
(B) MAM

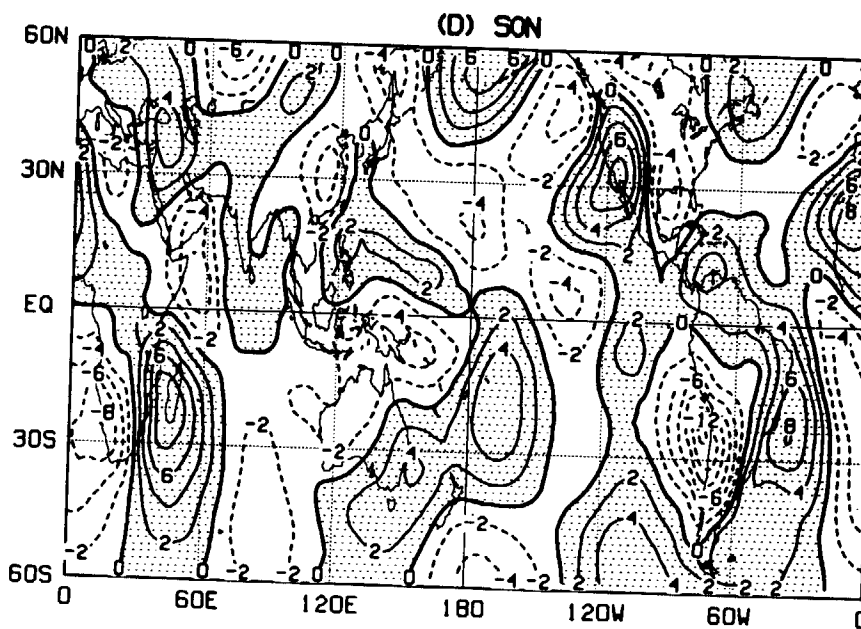
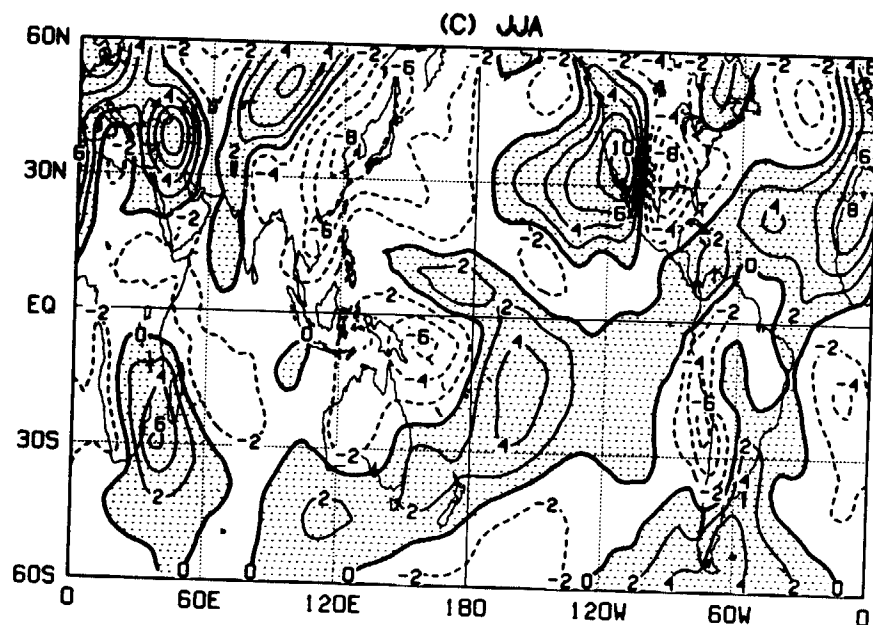
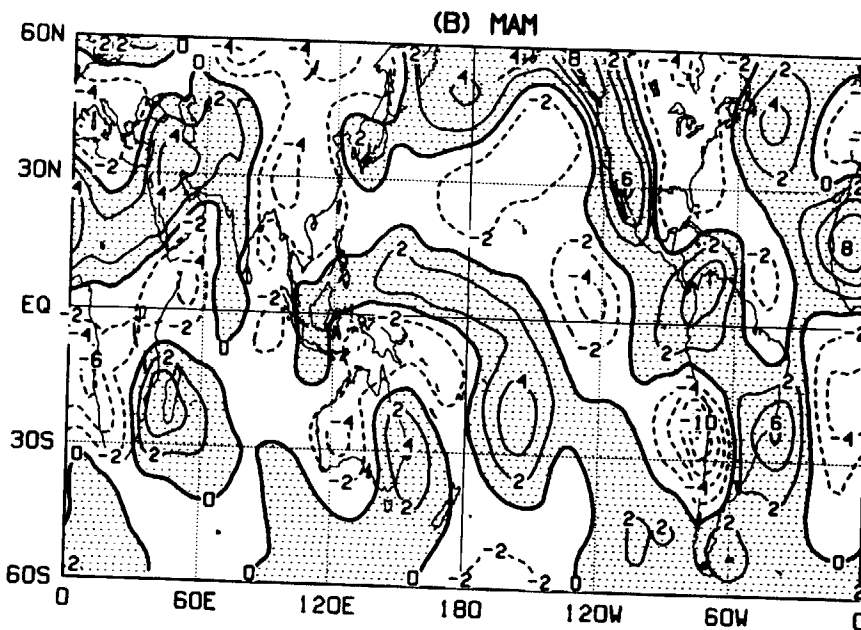
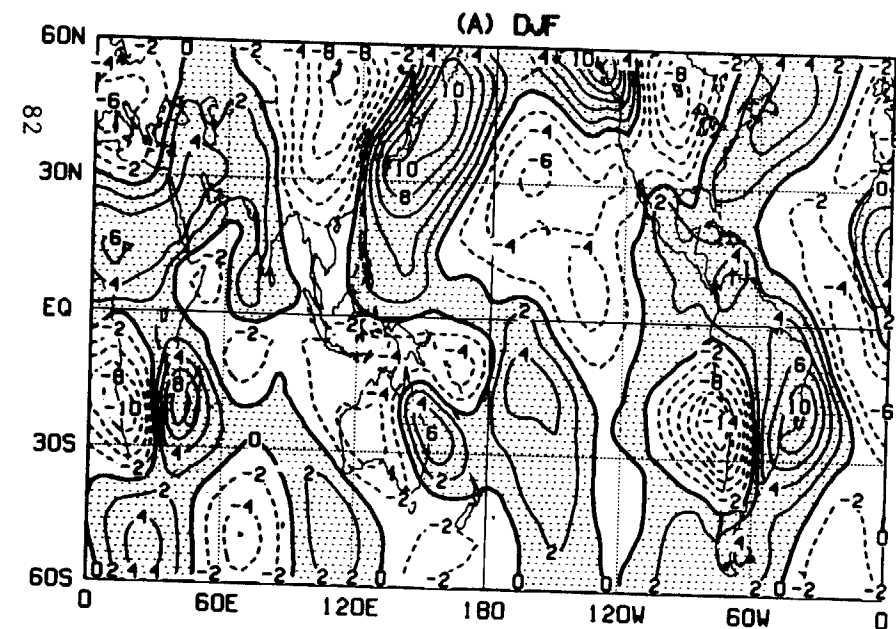


(C) JJA



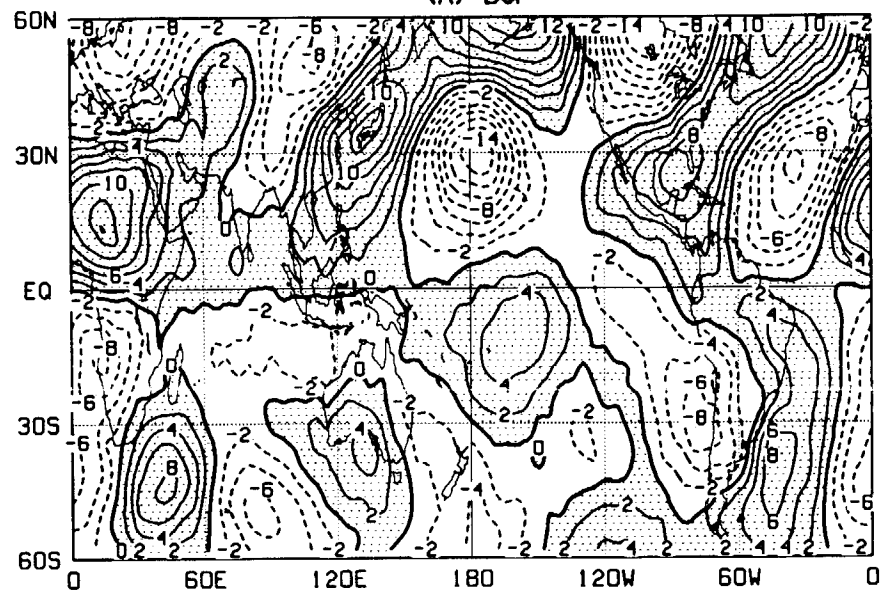
(D) SON



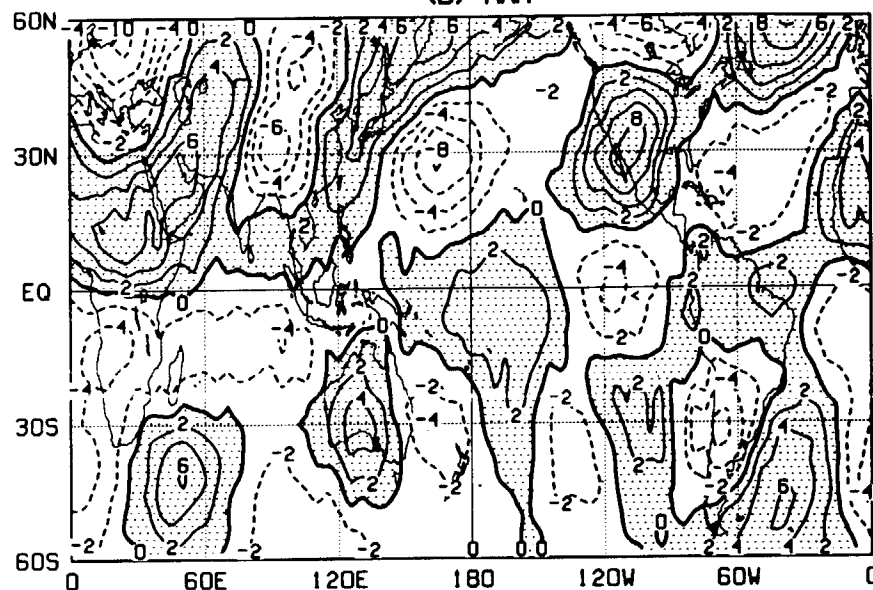


SEASONAL MEAN 200MB V (UCLA)

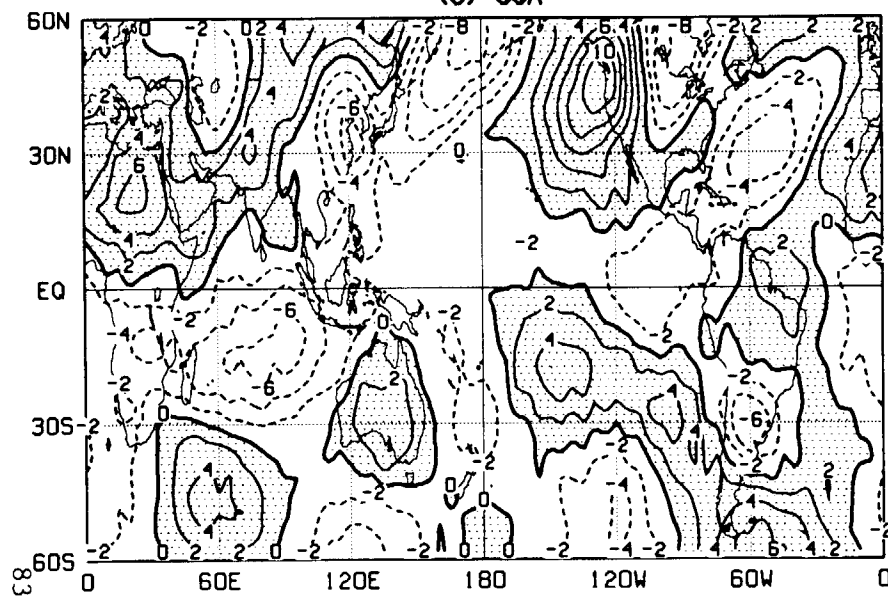
(A) DJF



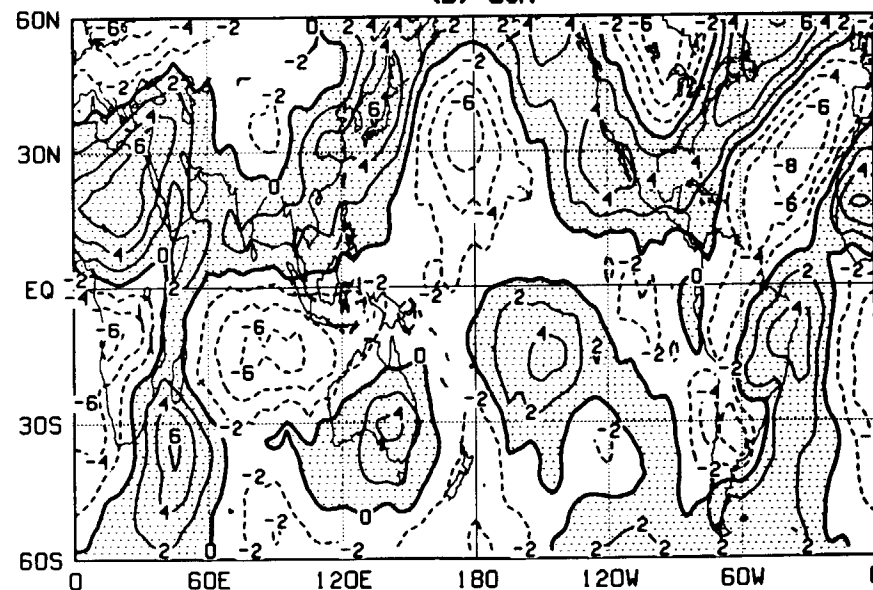
(B) MAM

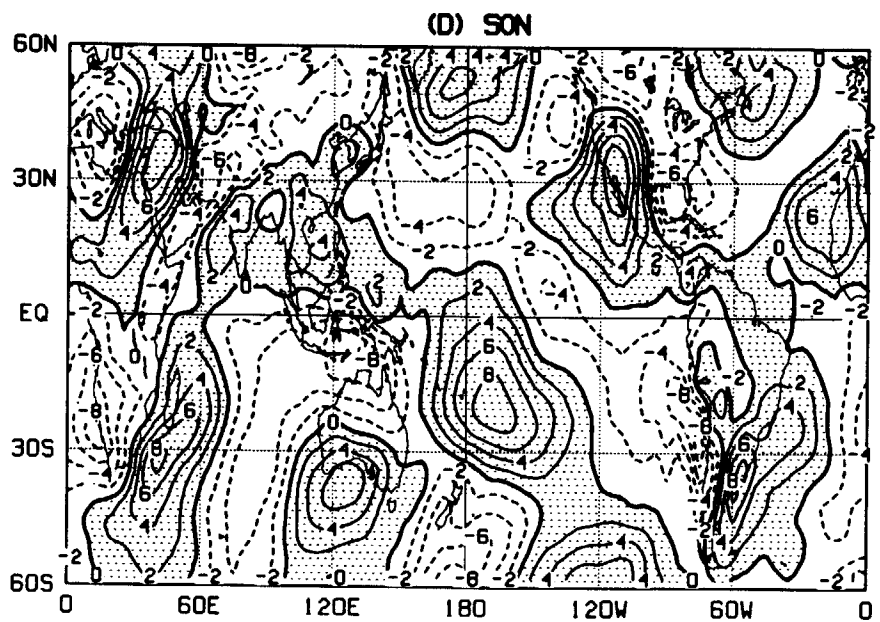
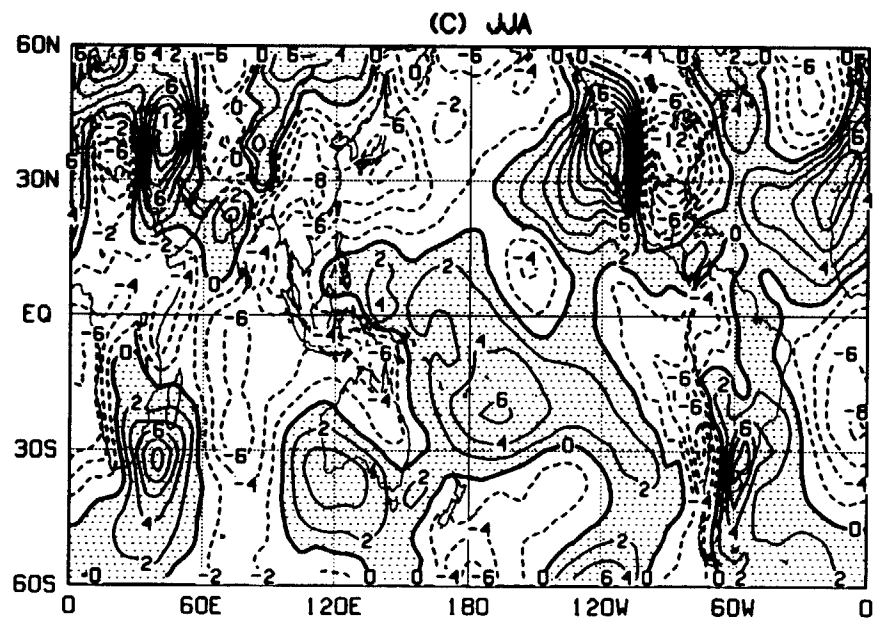
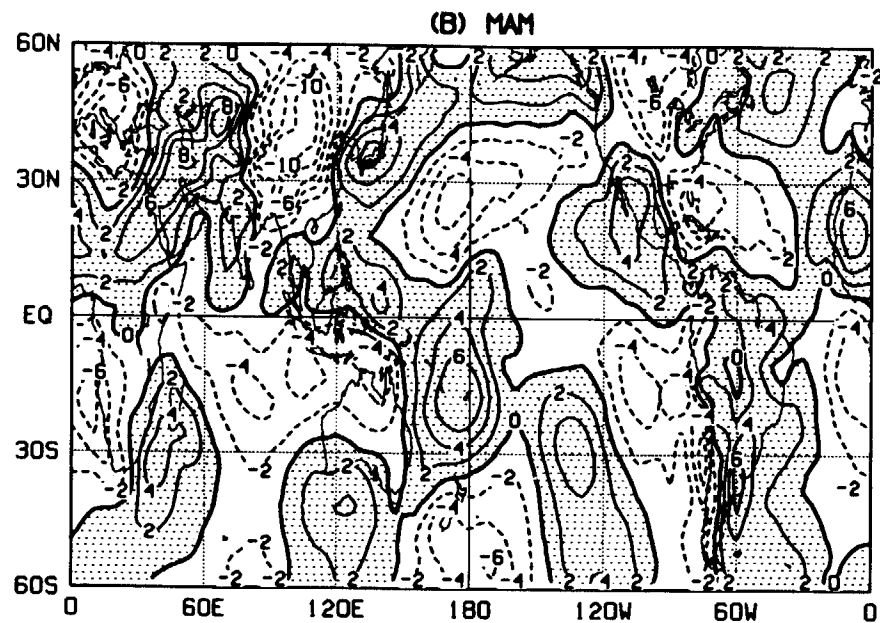
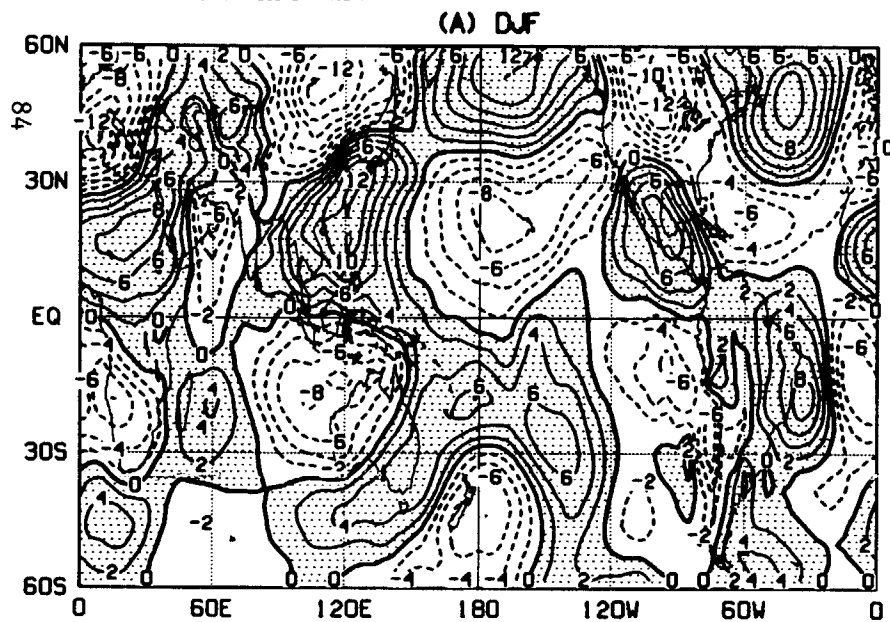


(C) JJA



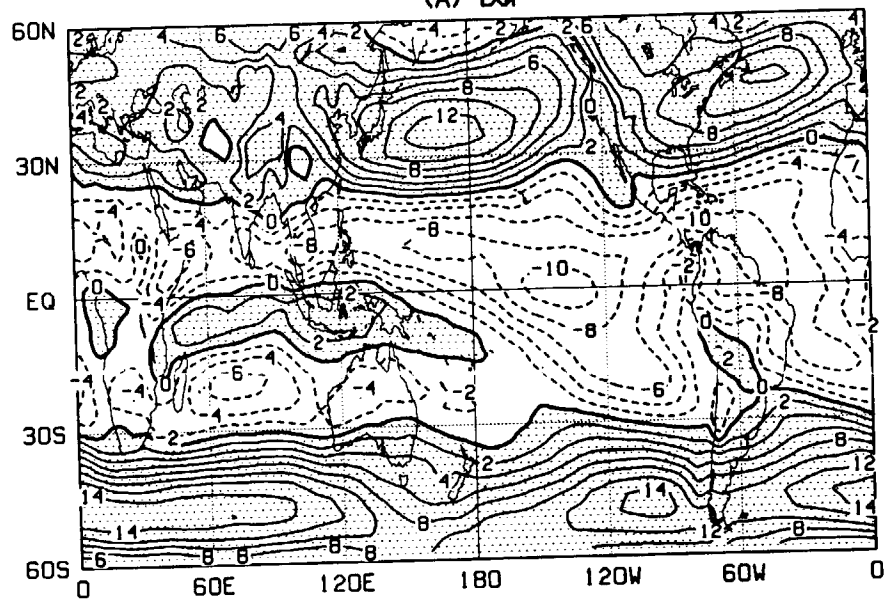
(D) SON



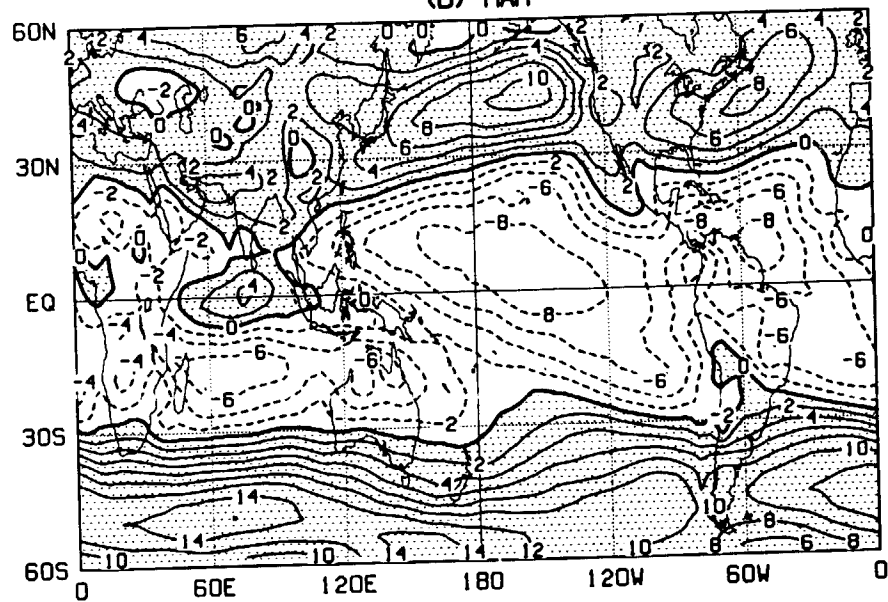


SEASONAL MEAN 850MB ZONAL WIND (CM/SEC)

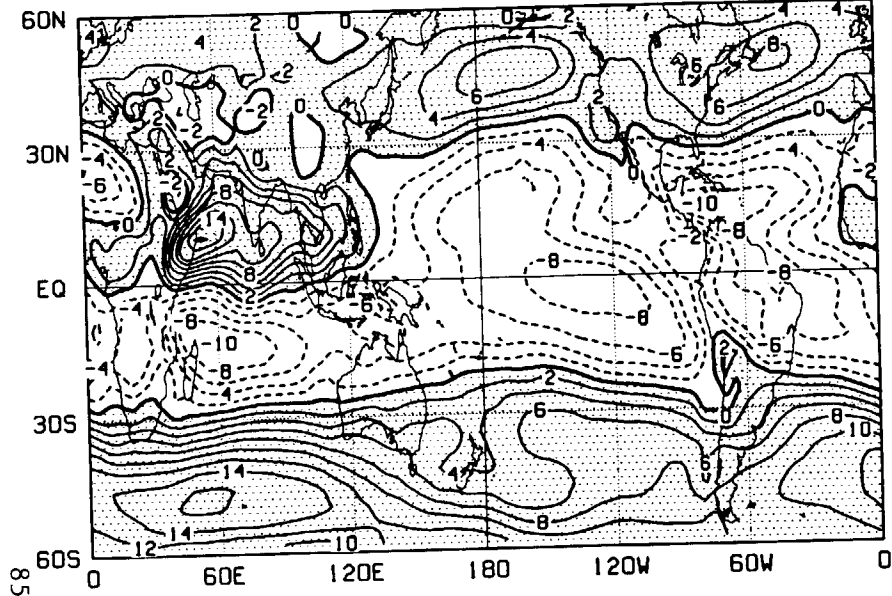
(A) DJF



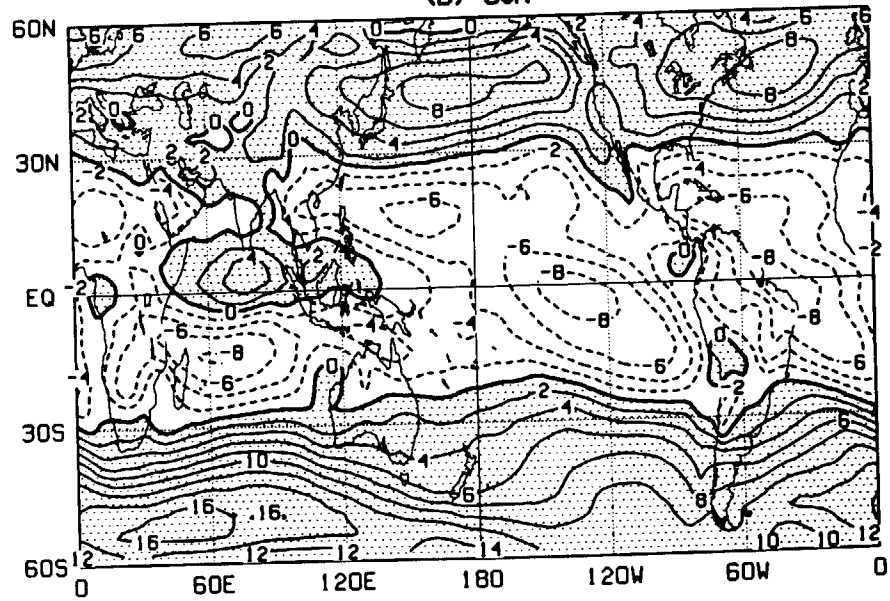
(B) MAM



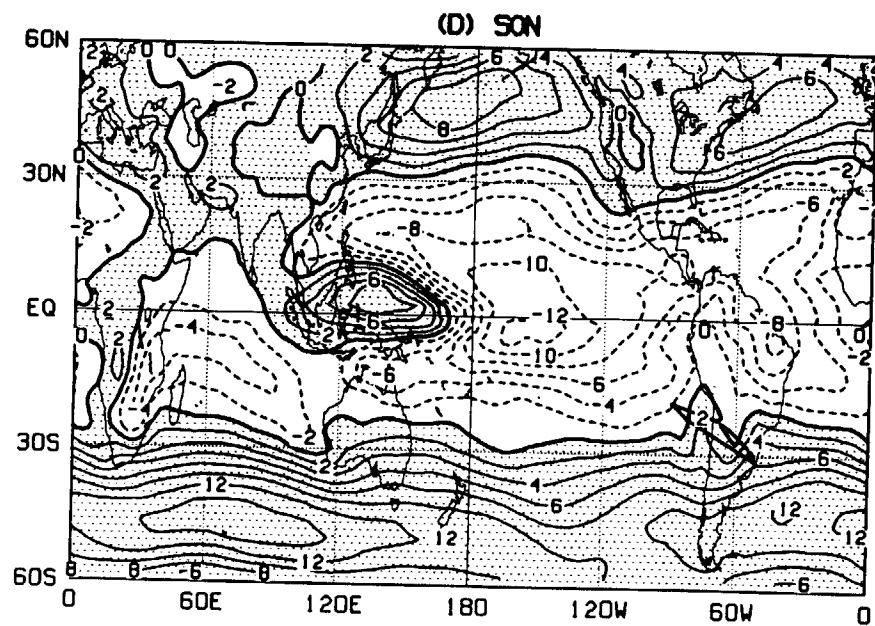
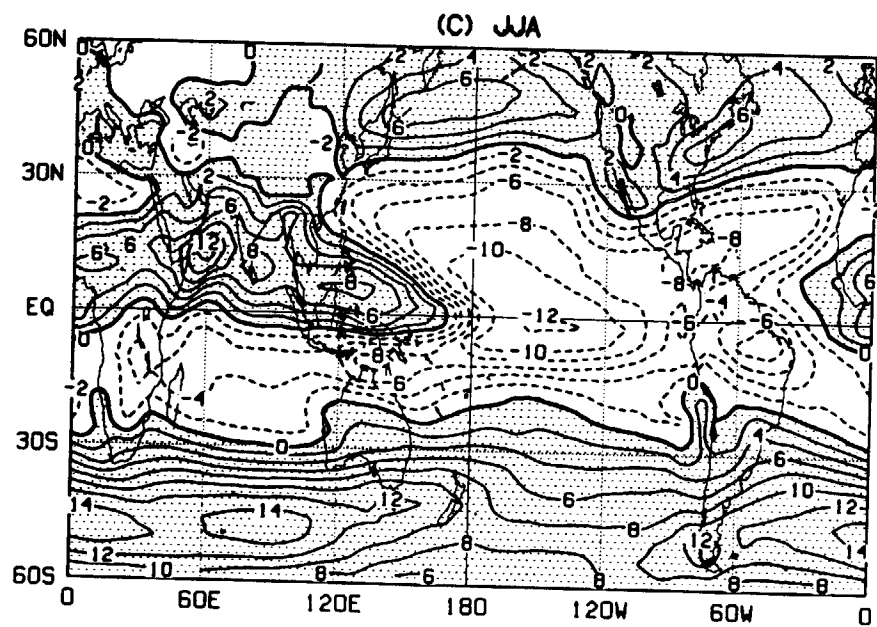
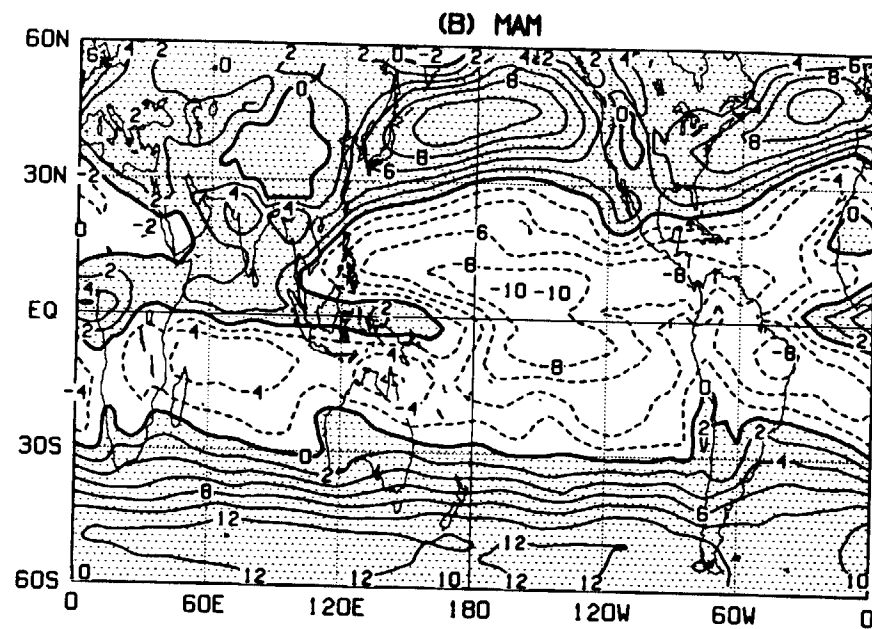
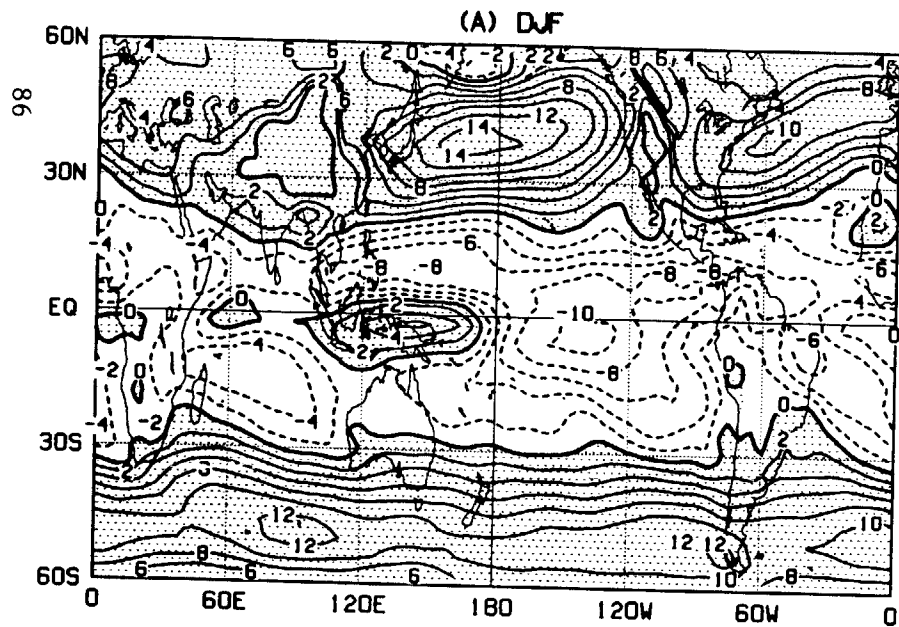
(C) JJA

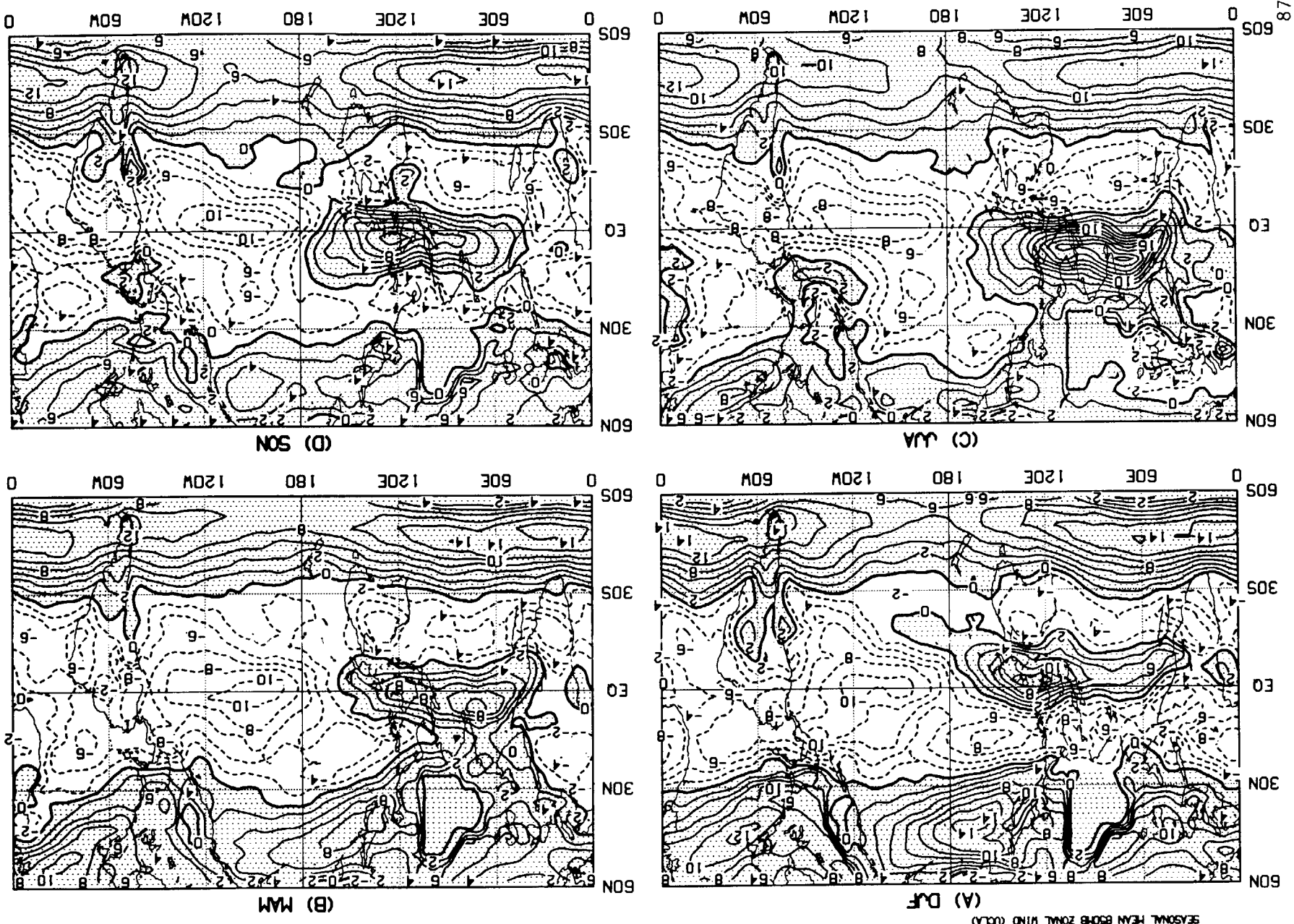


(D) SON

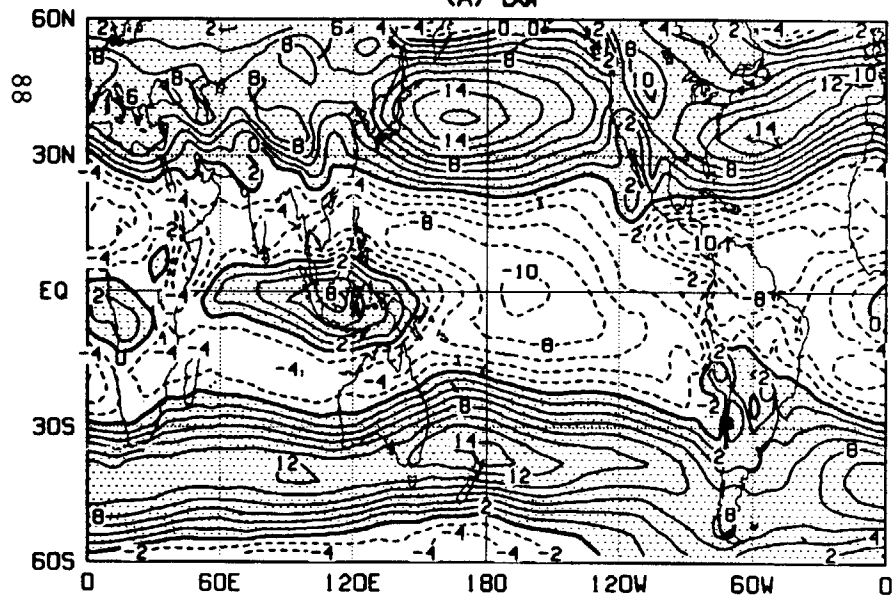


SEASONAL MEAN 650MB ZONAL WIND (GLAS)

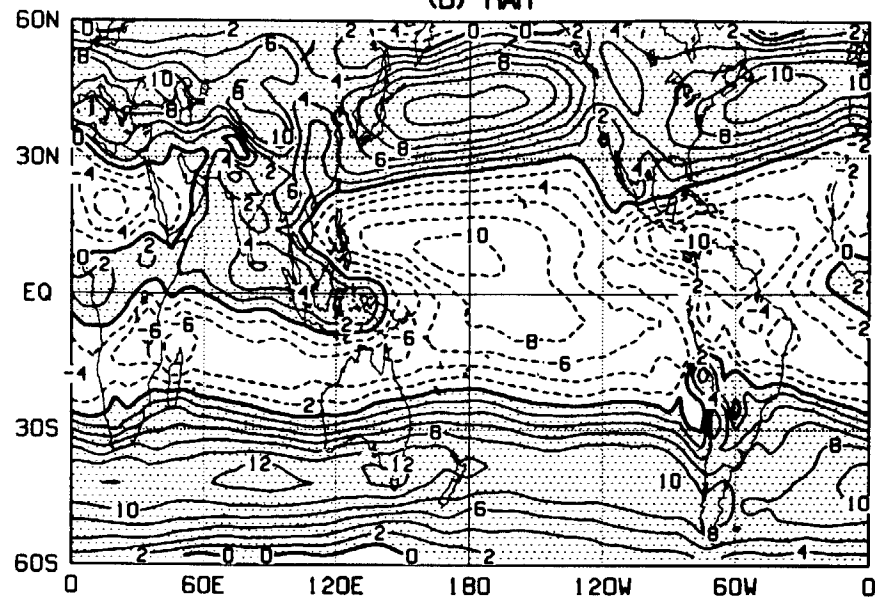




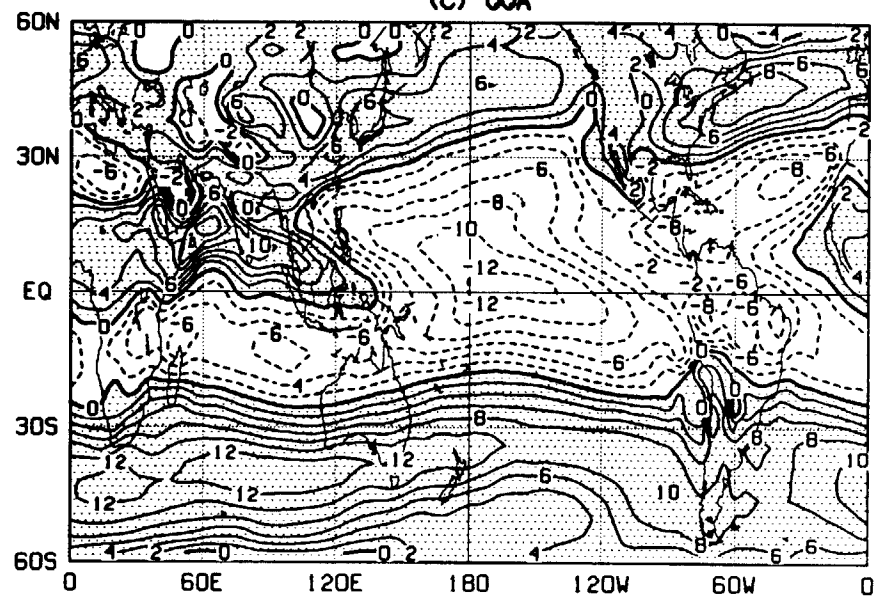
(A) DJF



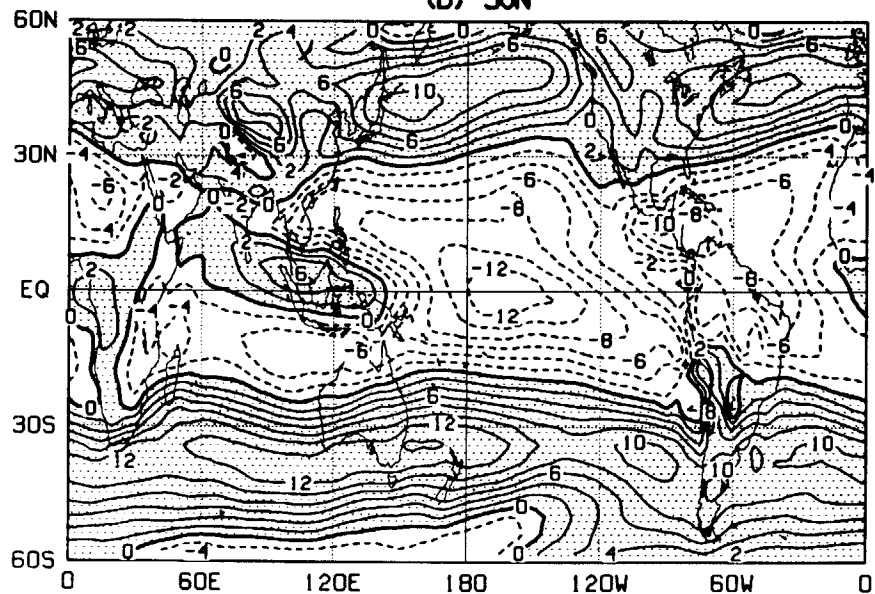
(B) MAM



(C) JJA

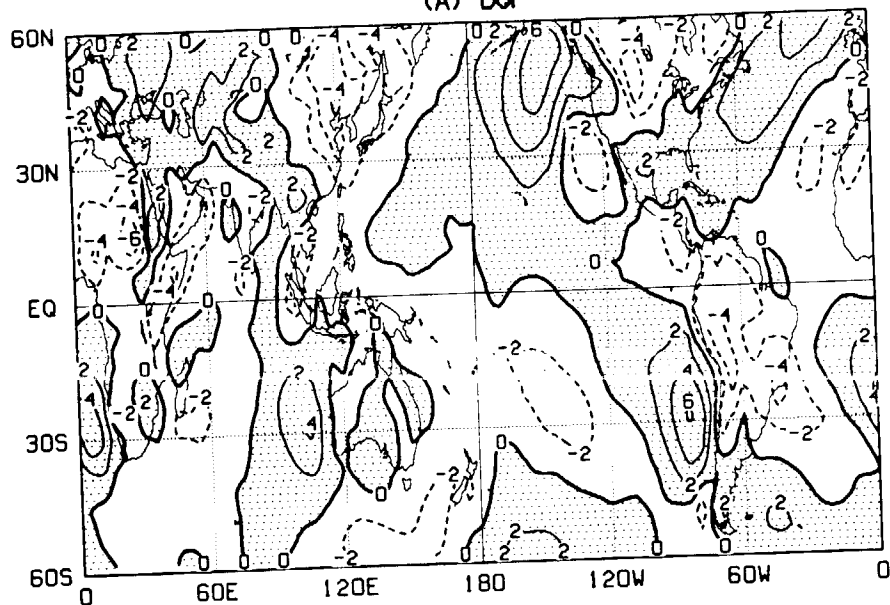


(D) SON

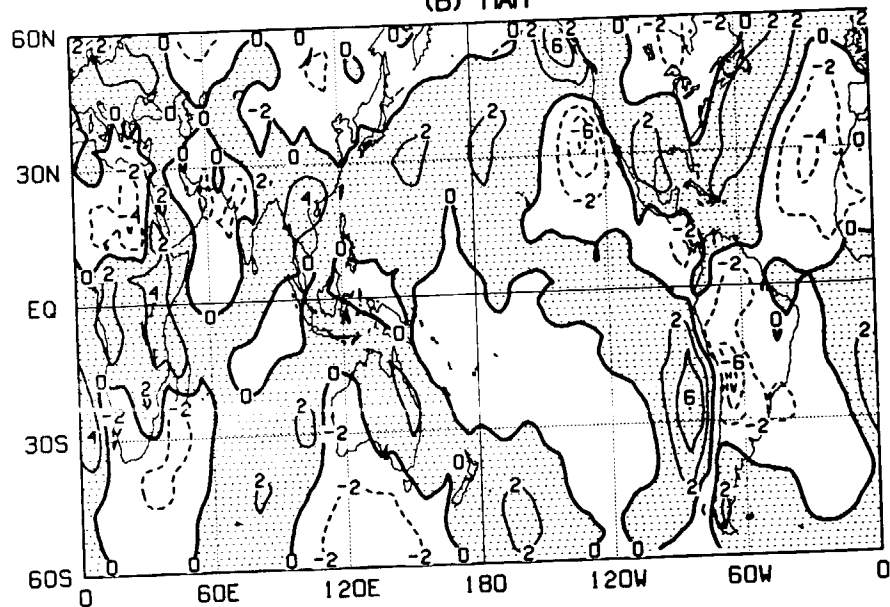


SEASONAL MEAN 850MB V (ECHMWF)

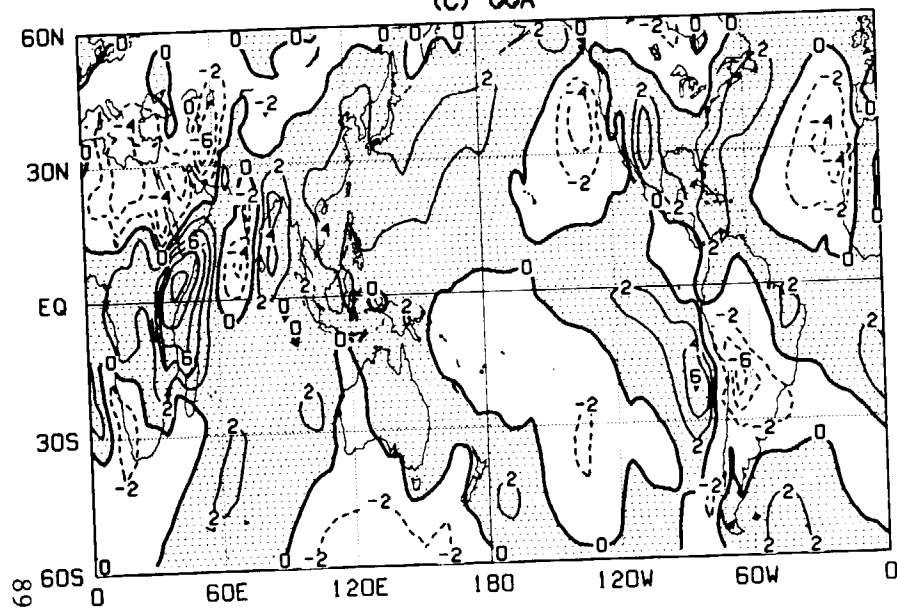
(A) DJF



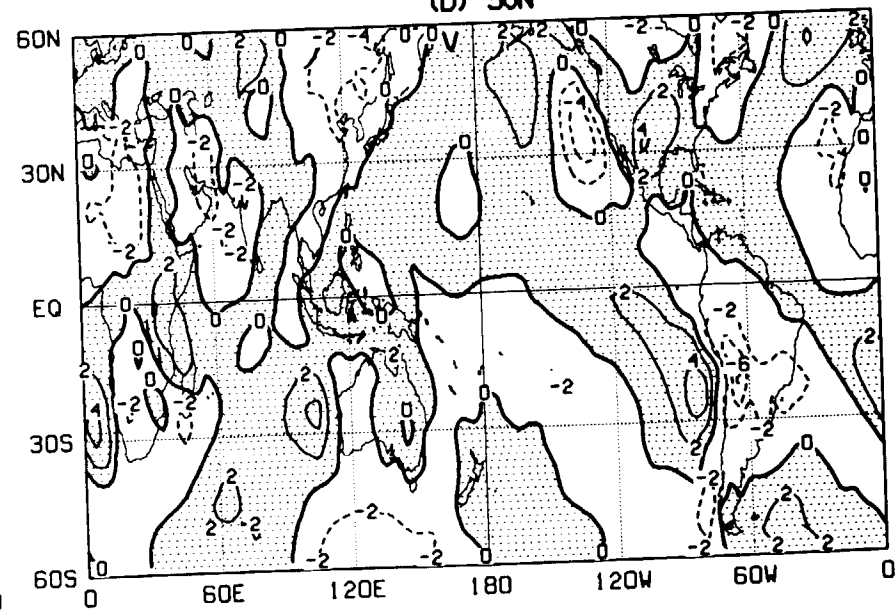
(B) MAM

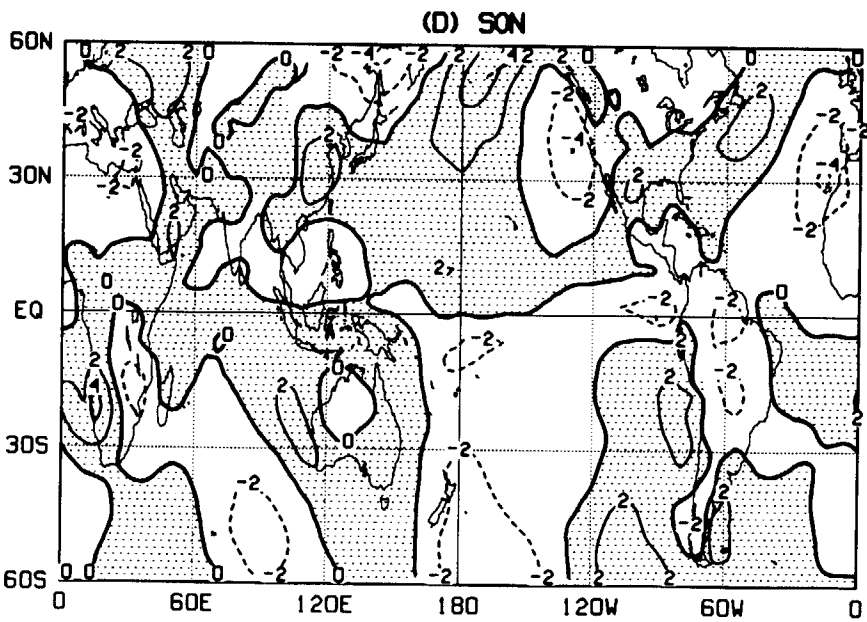
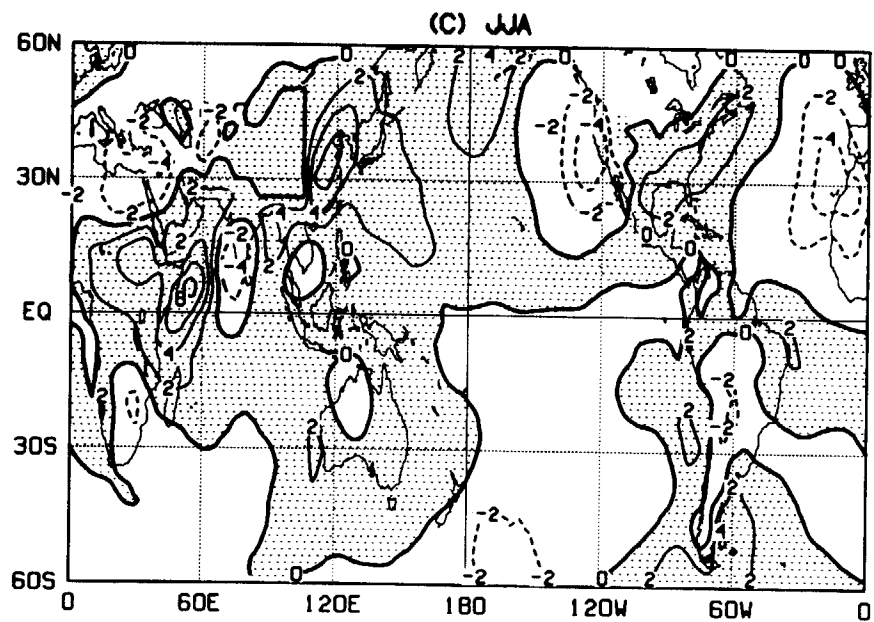
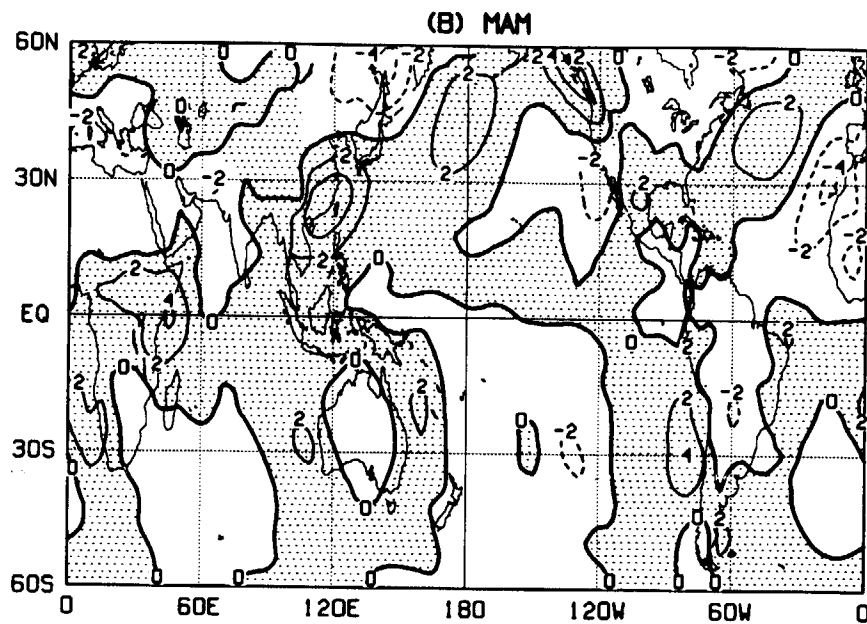
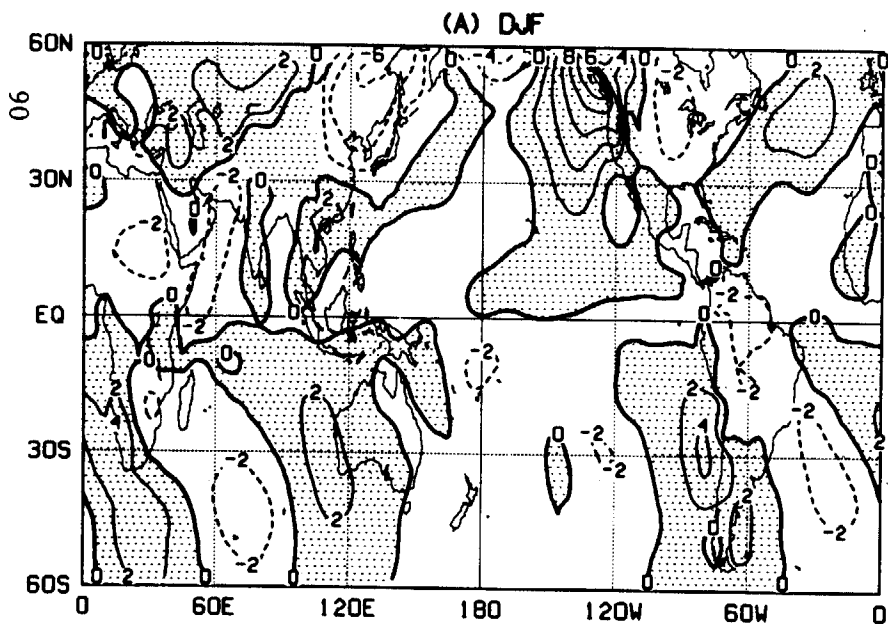


(C) JJA

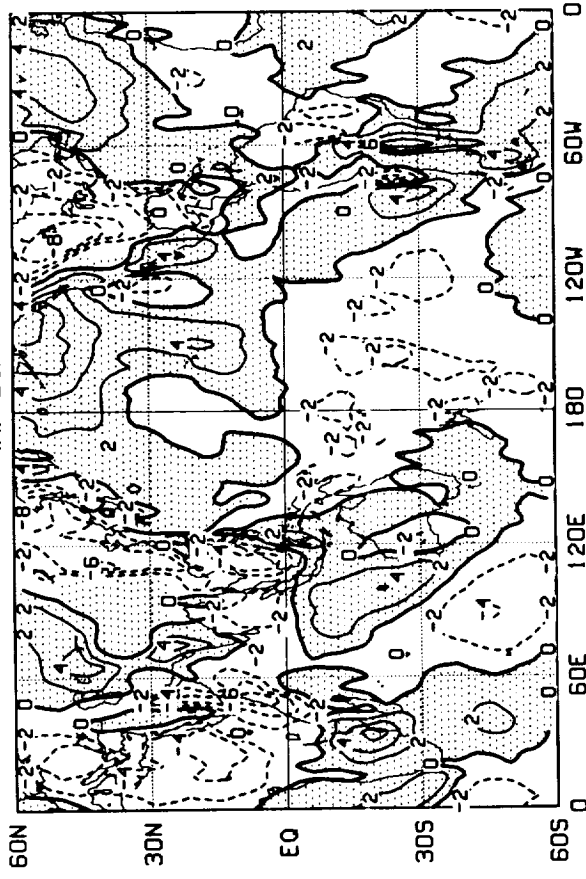


(D) SON

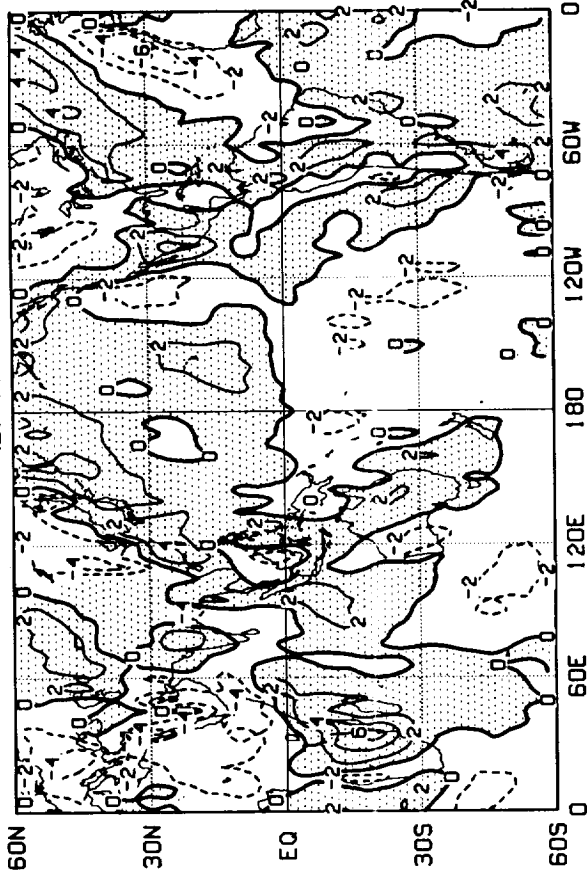




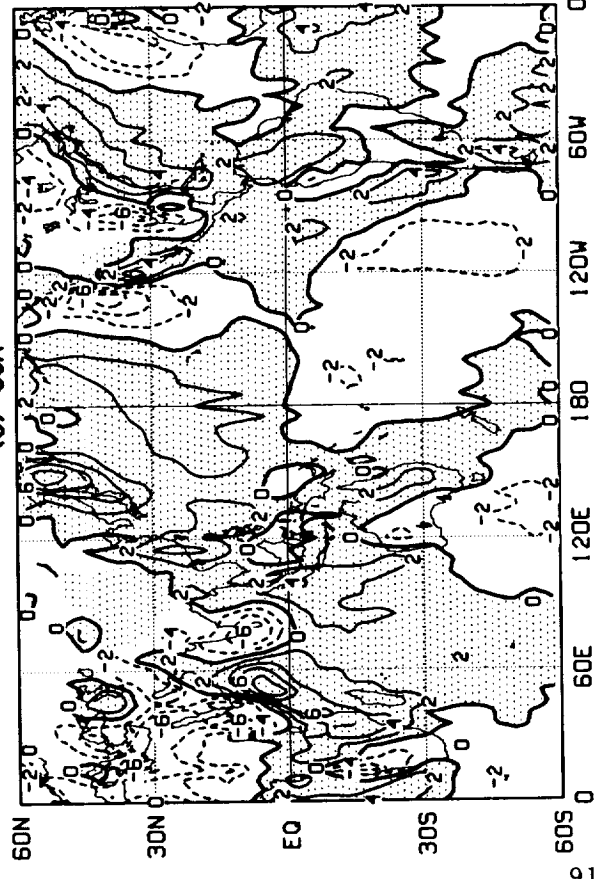
(A) DJF



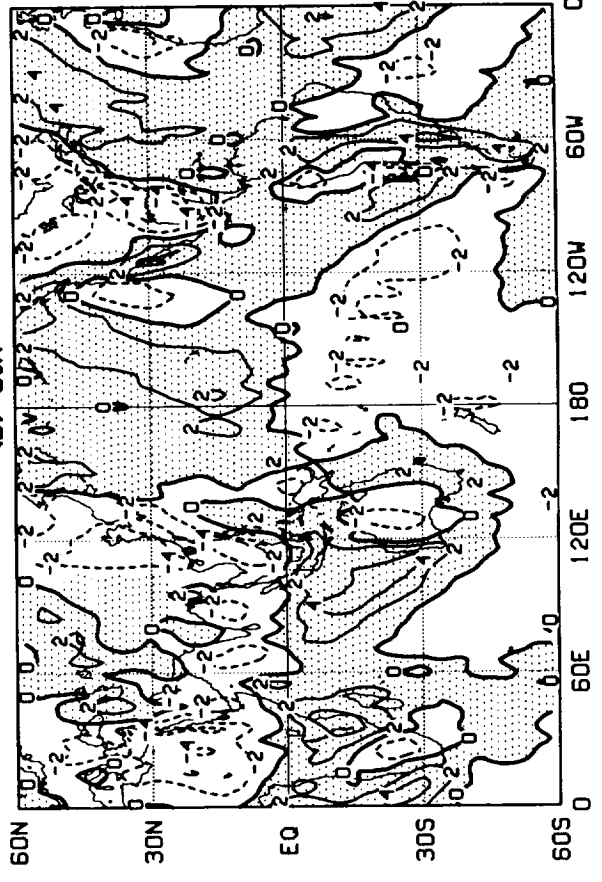
(B) MAM



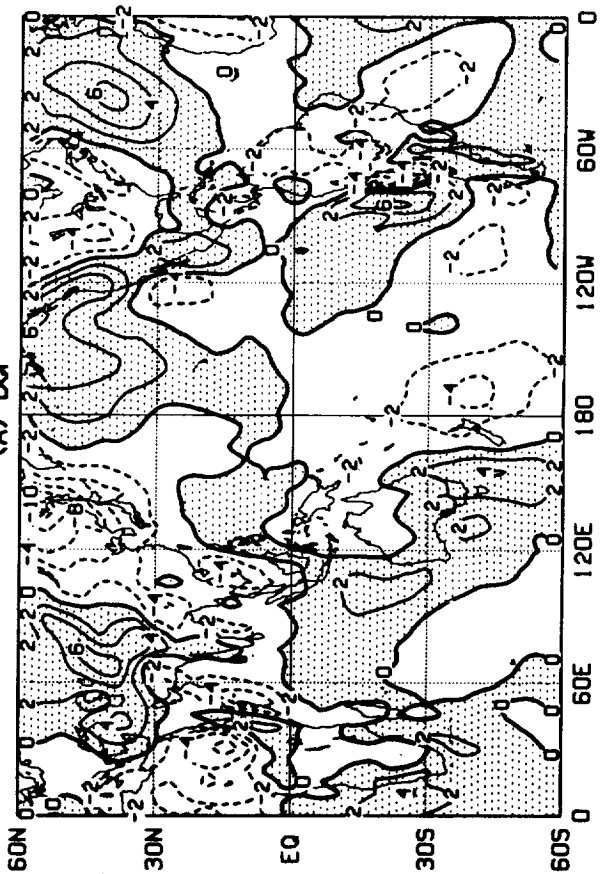
(C) JJA



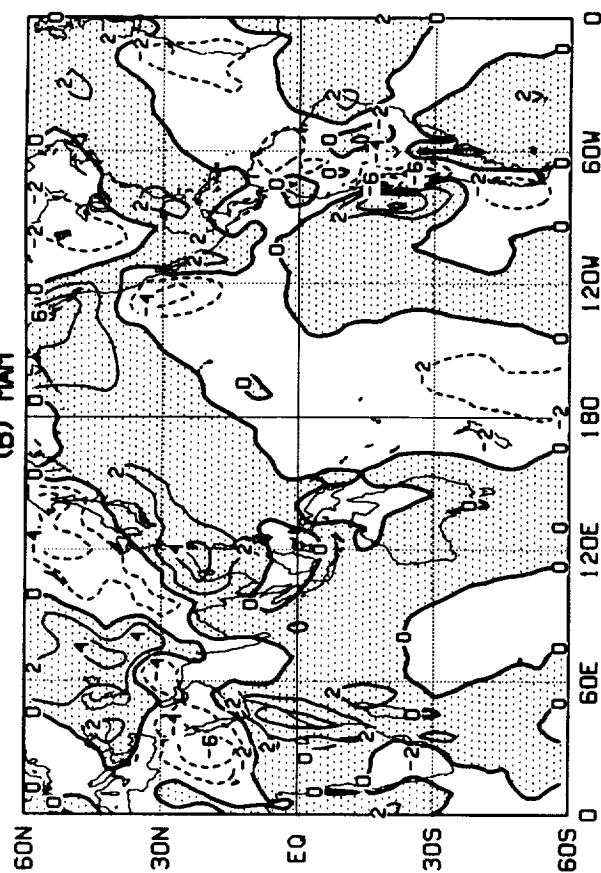
(D) SON



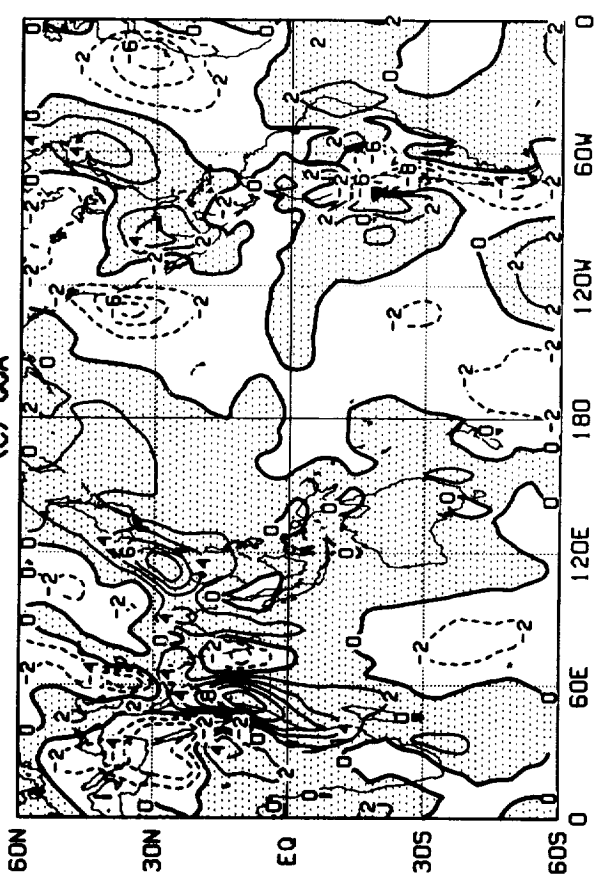
(A) D.J.F



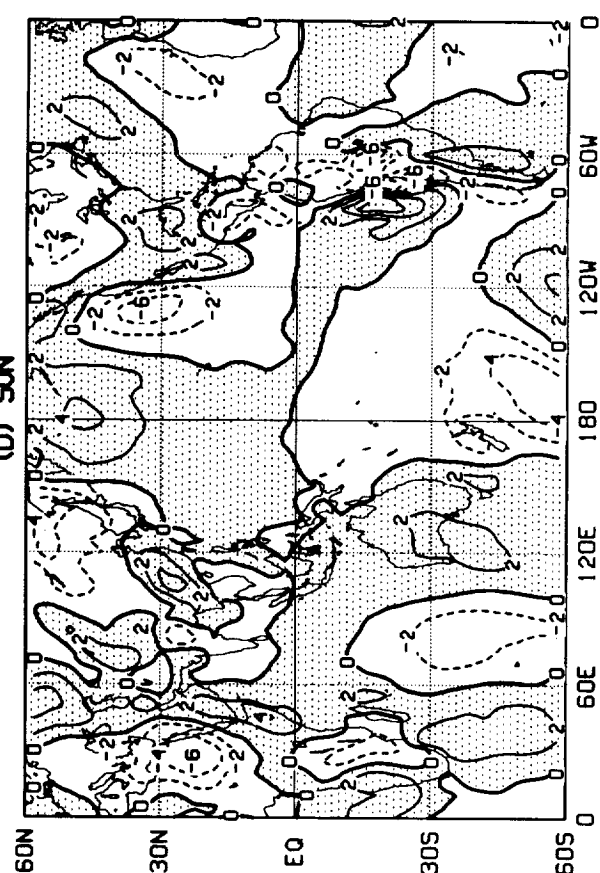
(B) M.A.M

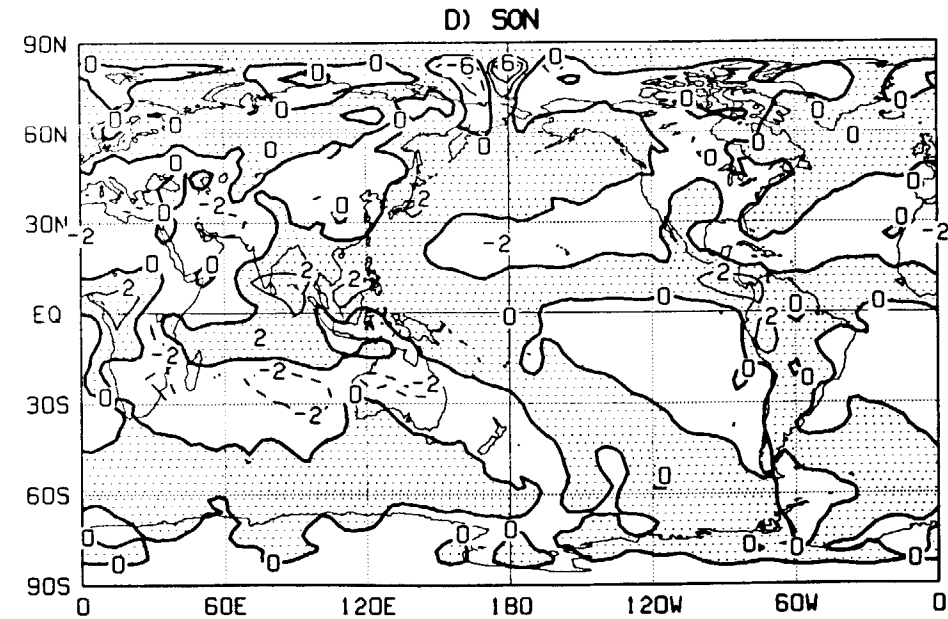
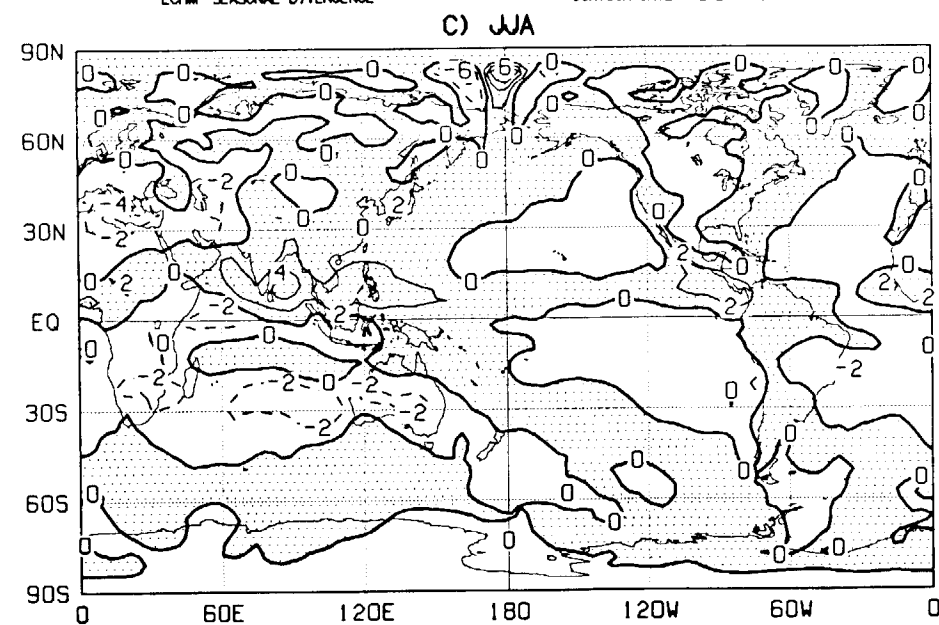
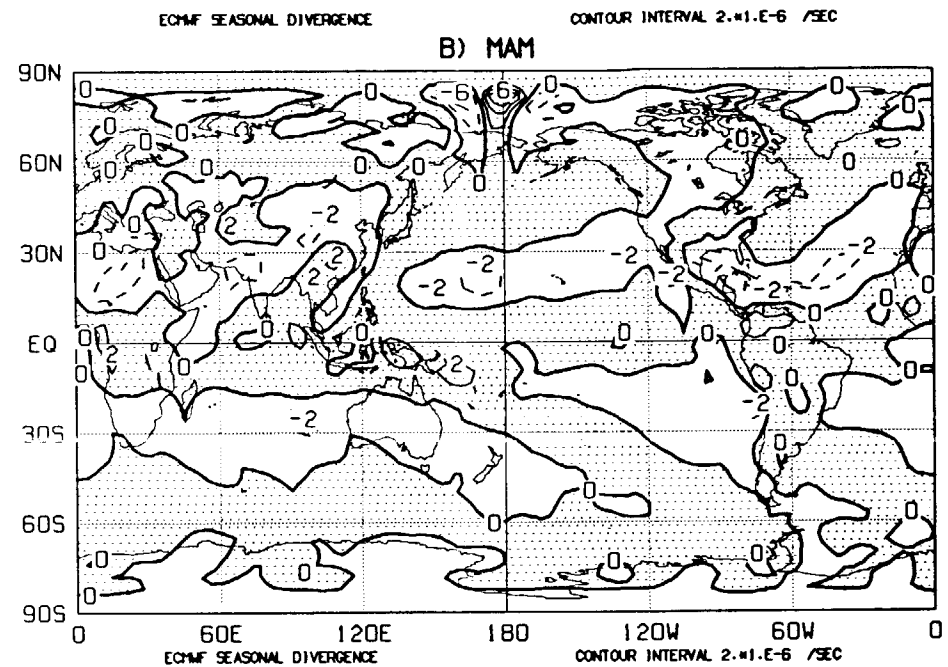
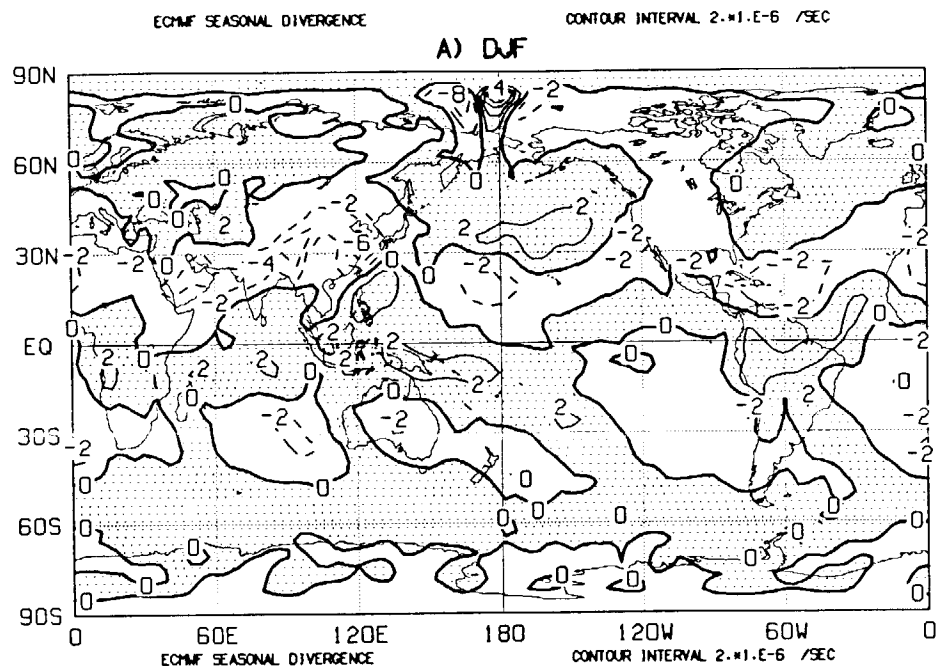


(C) J.J.A



(D) S.O.N

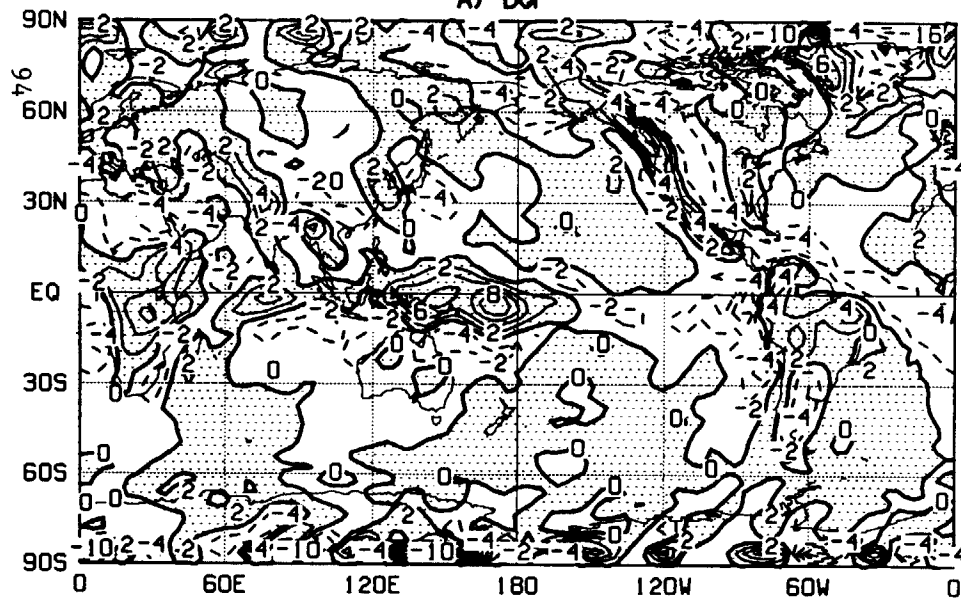




SEASONAL MEAN 200 MB DIVERGENCE (D221)

CONTOUR INTERVAL 2×10^{-6} /SEC

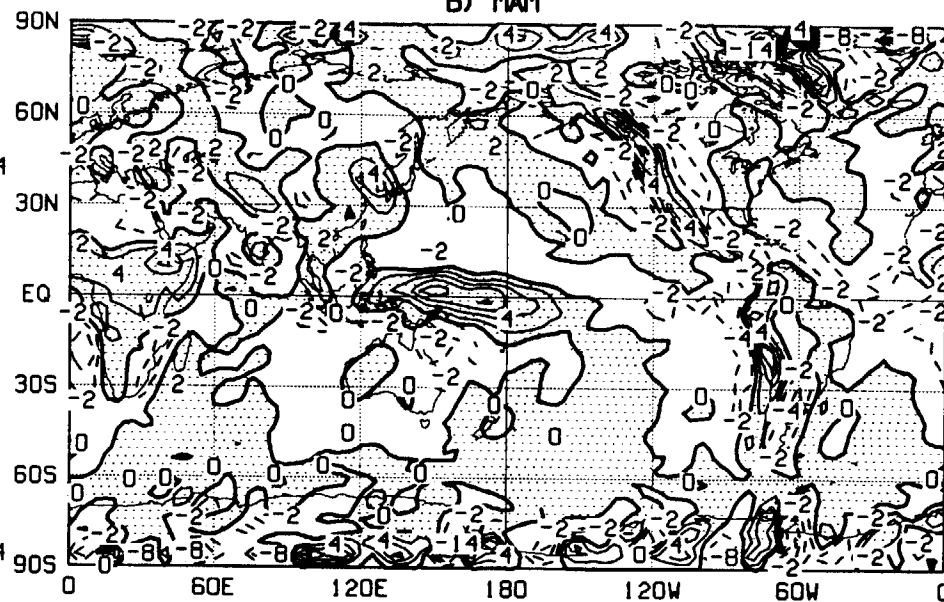
A) DJF



SEASONAL MEAN 200 MB DIVERGENCE (D221)

CONTOUR INTERVAL 2×10^{-6} /SEC

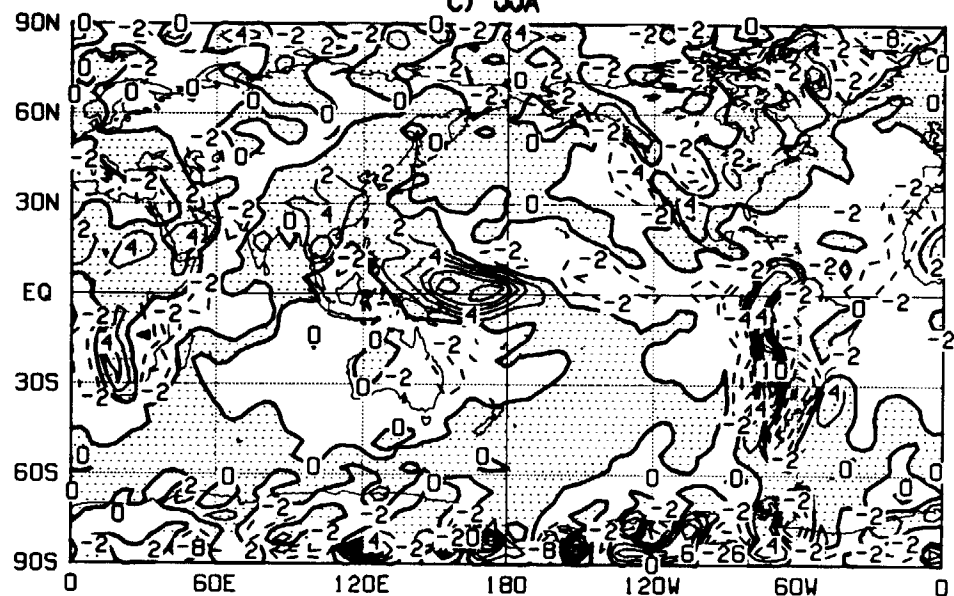
B) MAM



SEASONAL MEAN 200 MB DIVERGENCE (D221)

CONTOUR INTERVAL 2×10^{-6} /SEC

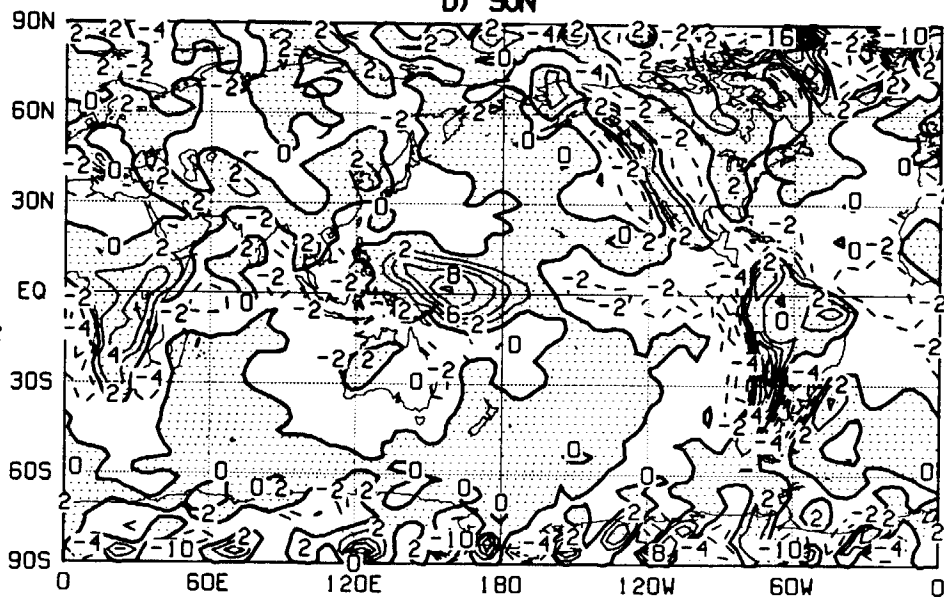
C) JJA



SEASONAL MEAN 200 MB DIVERGENCE (D221)

CONTOUR INTERVAL 2×10^{-6} /SEC

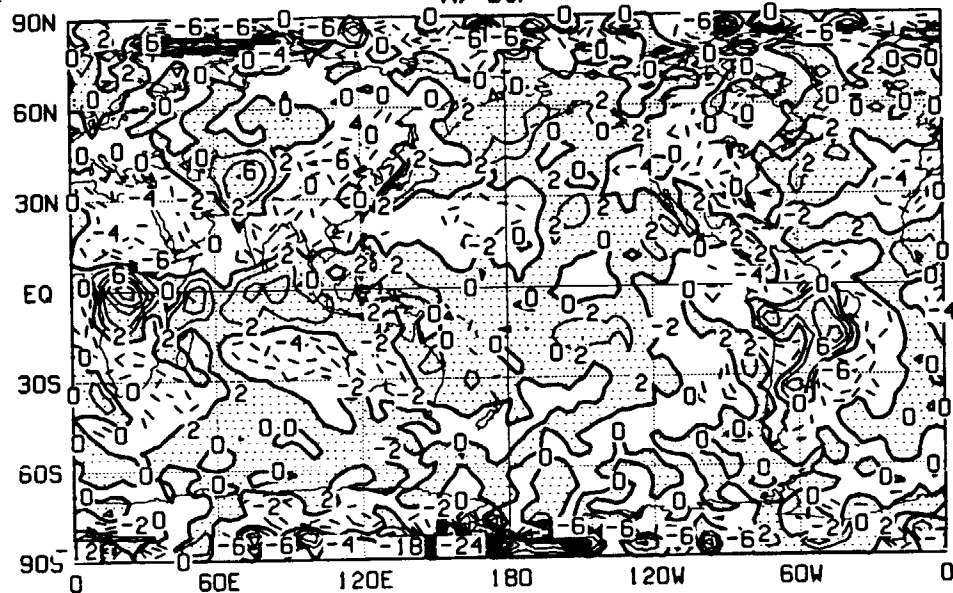
D) SON



SEASONAL MEAN 200 MB DIVERGENCE (UCLA)

CONTOUR INTERVAL 2×10^{-6} /SEC

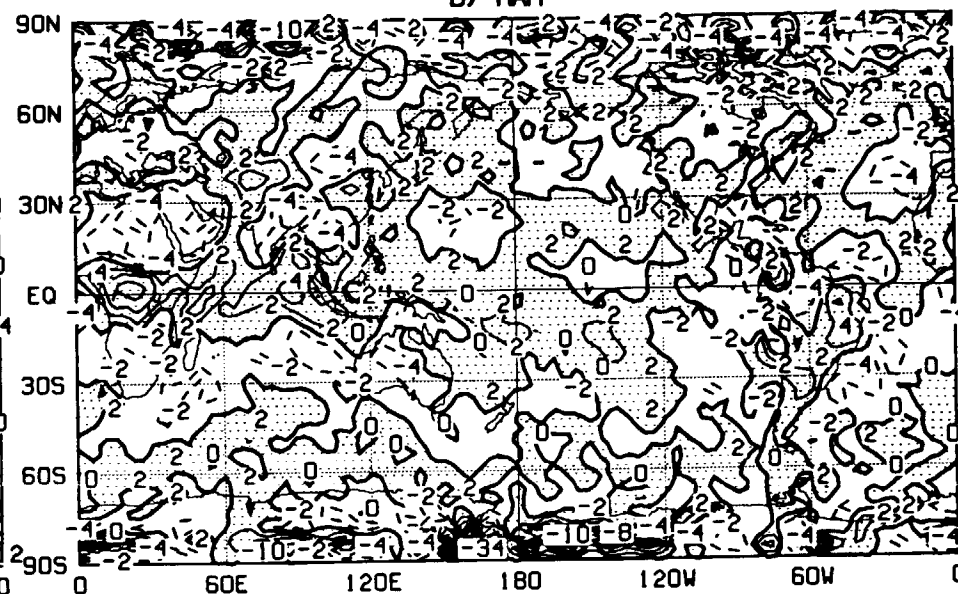
A) DJF



SEASONAL MEAN 200 MB DIVERGENCE (UCLA)

CONTOUR INTERVAL 2×10^{-6} /SEC

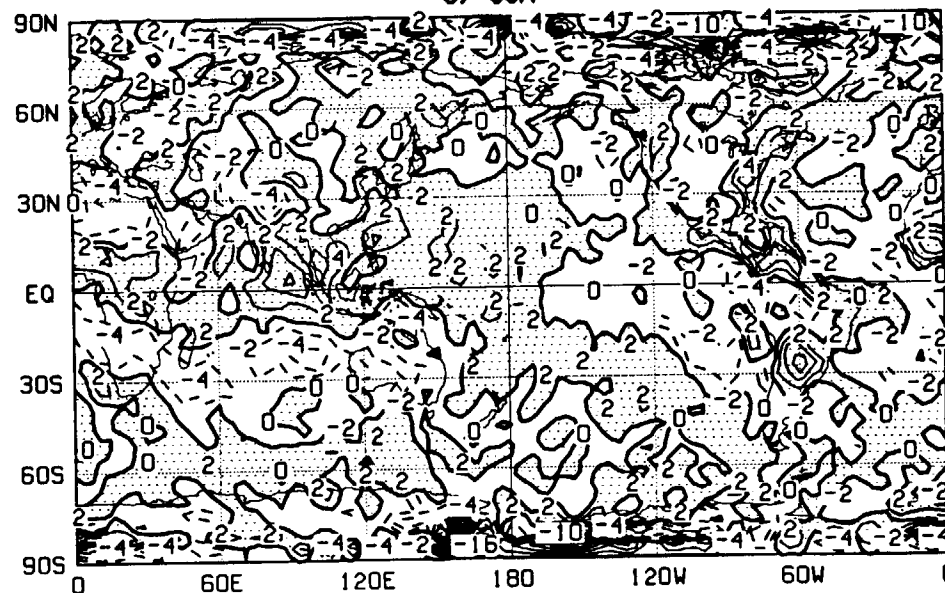
B) MAM



SEASONAL MEAN 200 MB DIVERGENCE (UCLA)

CONTOUR INTERVAL 2×10^{-6} /SEC

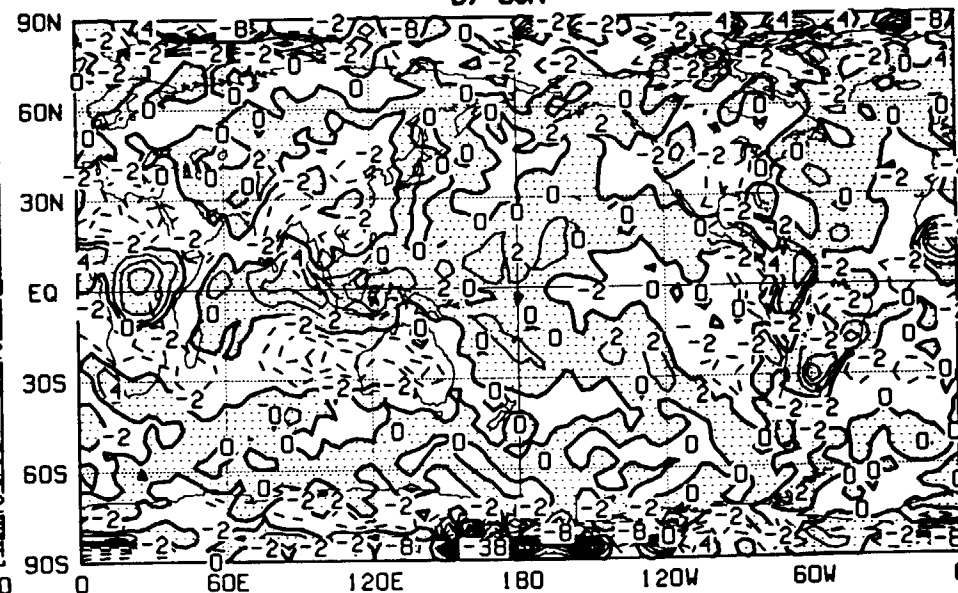
C) JJA

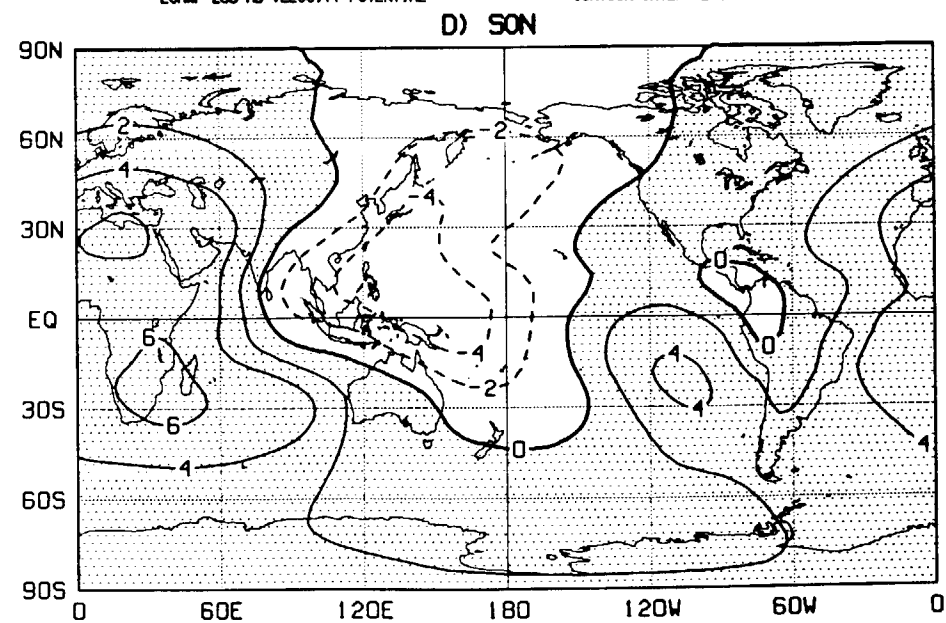
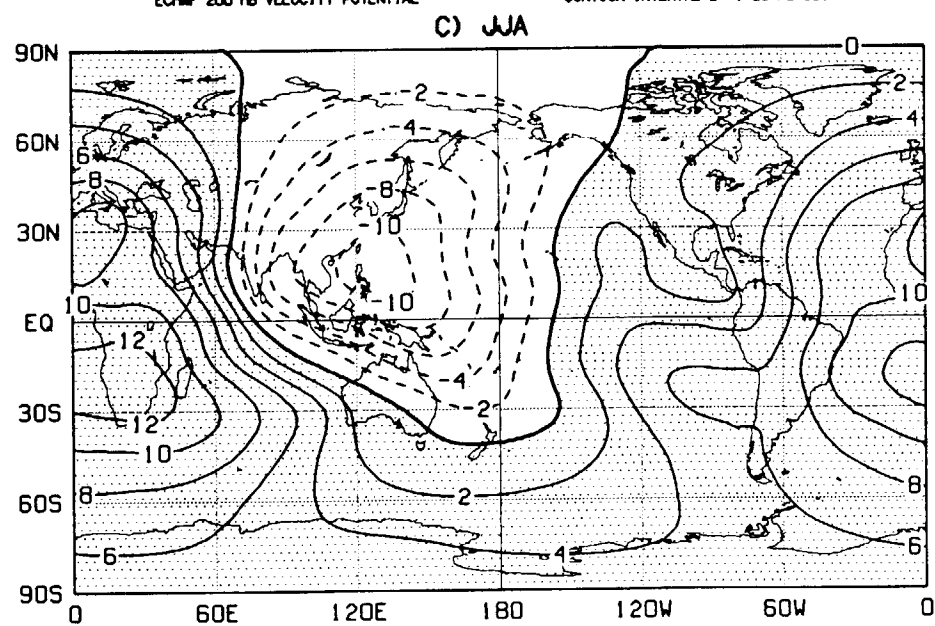
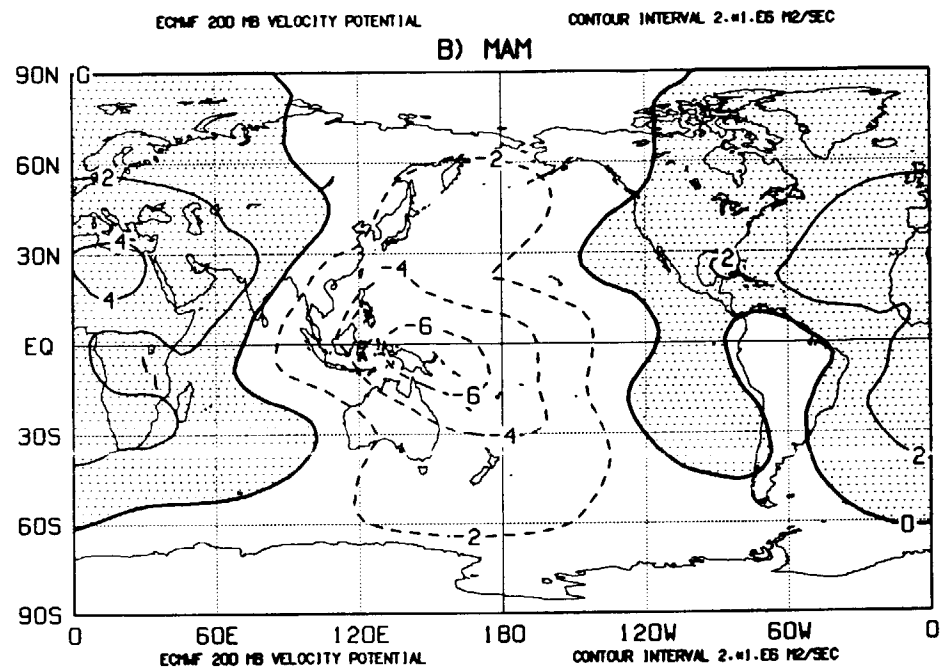
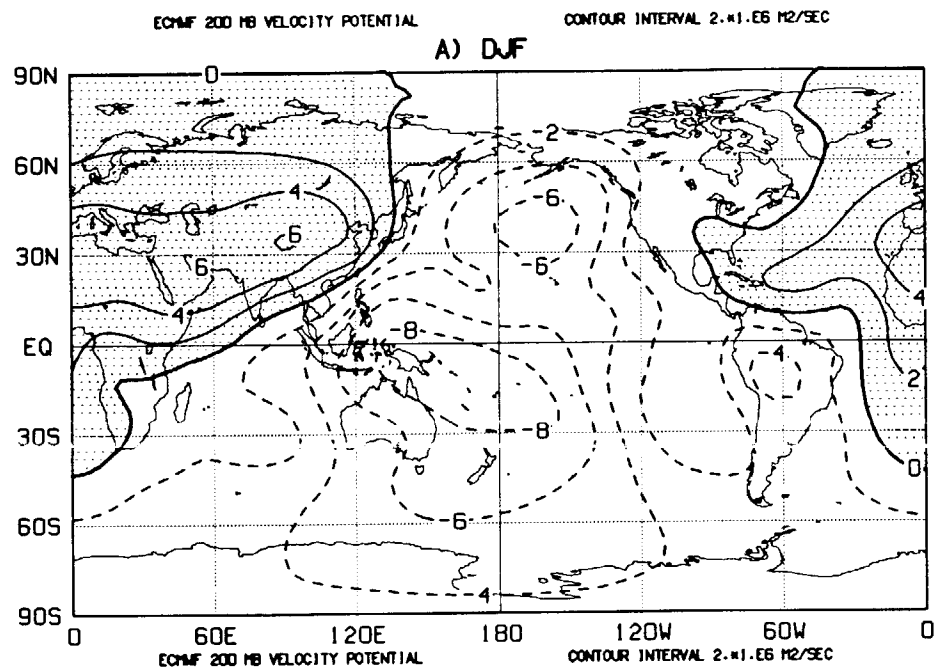


SEASONAL MEAN 200 MB DIVERGENCE (UCLA)

CONTOUR INTERVAL 2×10^{-6} /SEC

D) SON

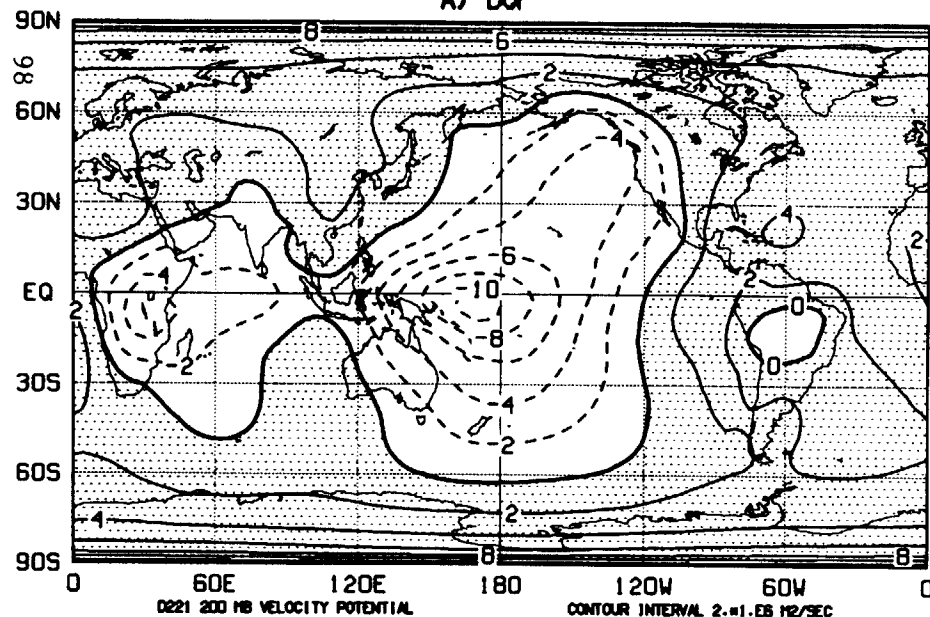




D221 200 MB VELOCITY POTENTIAL

CONTOUR INTERVAL 2. = 1.65 M2/SEC

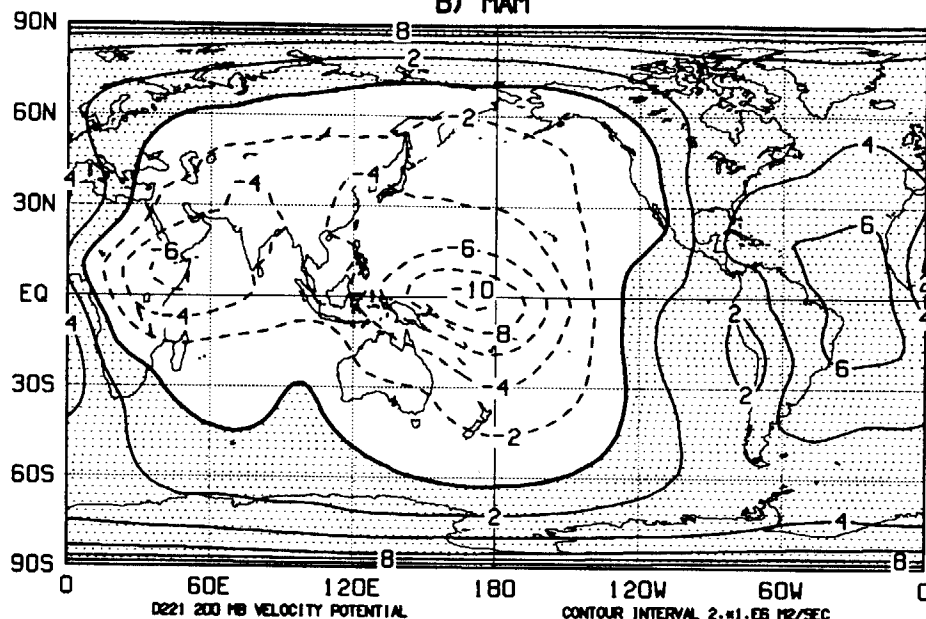
A) DJF



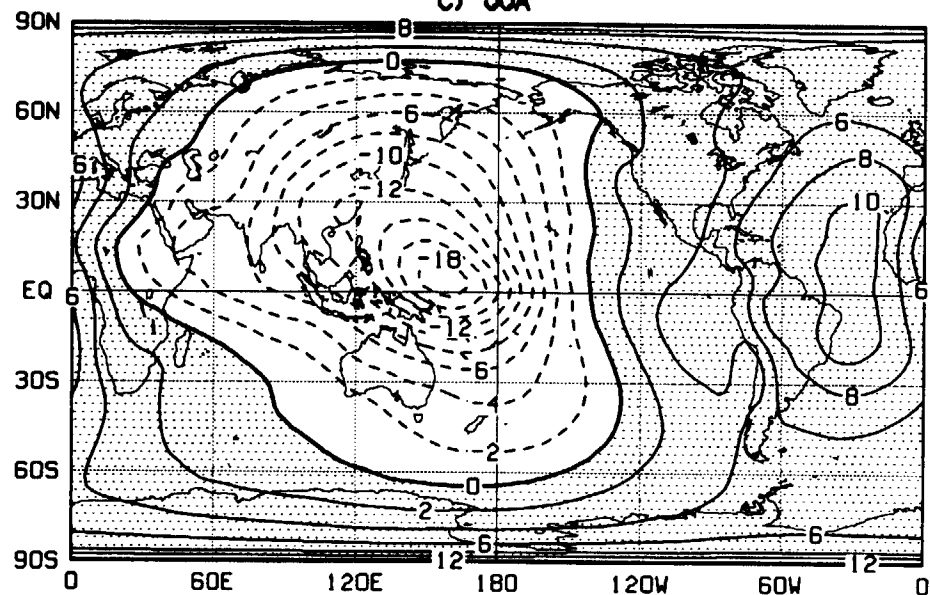
D221 200 MB VELOCITY POTENTIAL

CONTOUR INTERVAL 2. = 1.65 M2/SEC

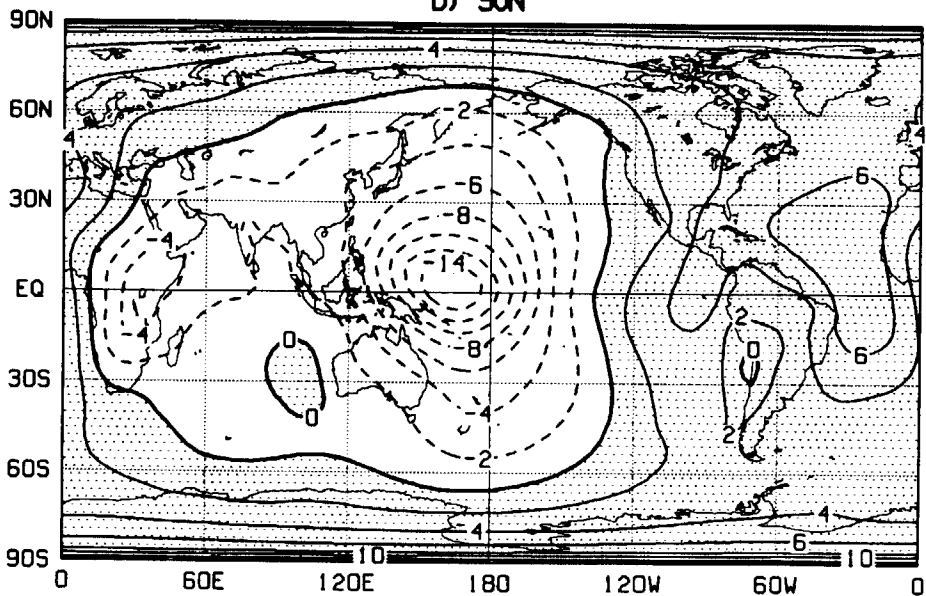
B) MAM

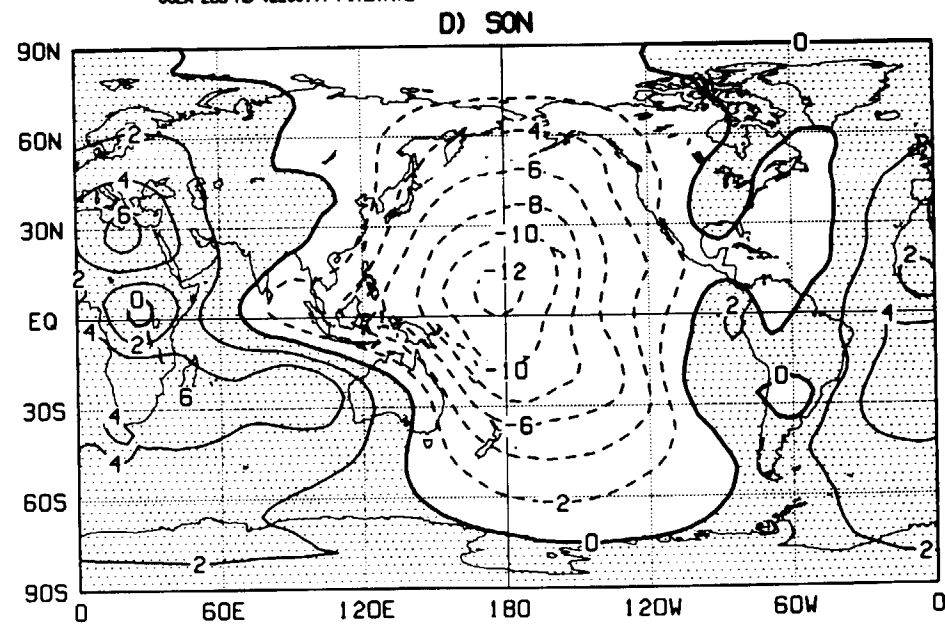
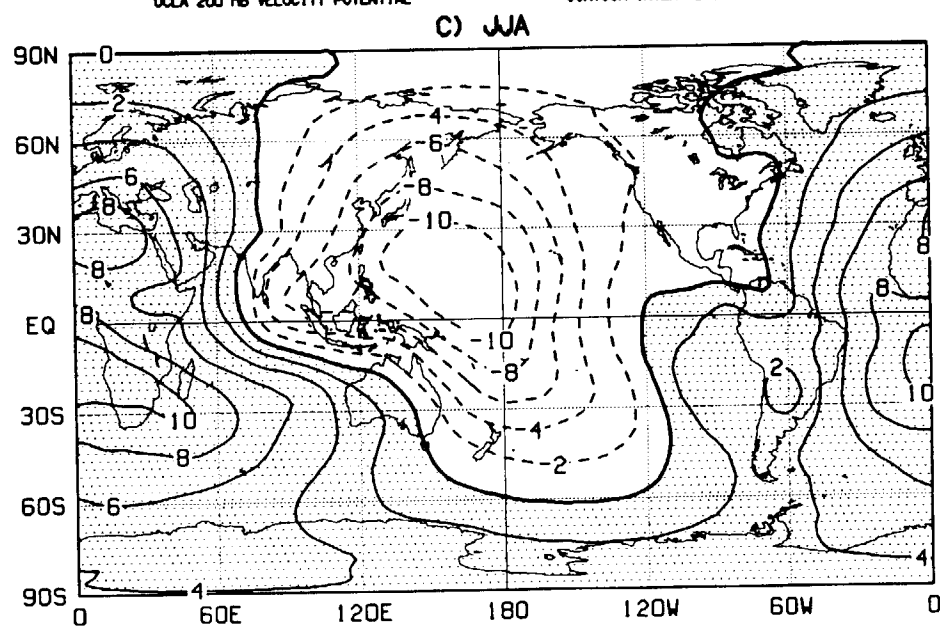
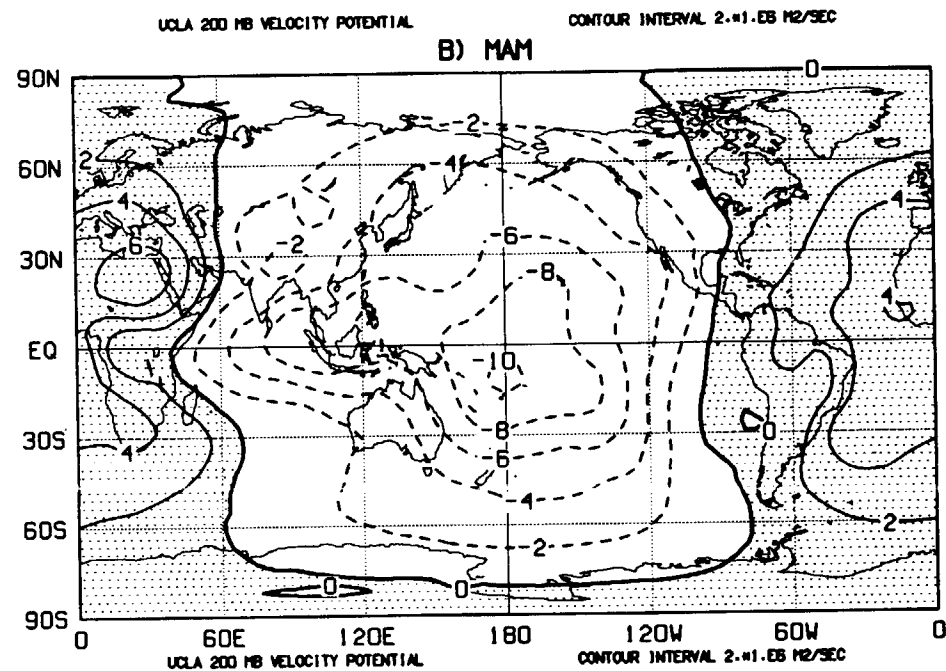
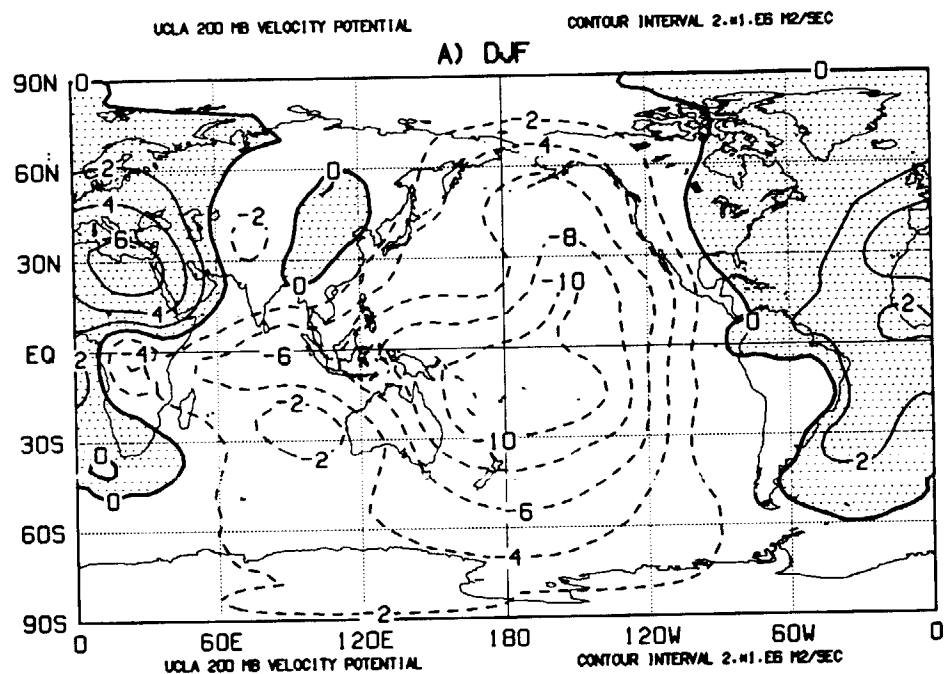


C) JJA



D) SON

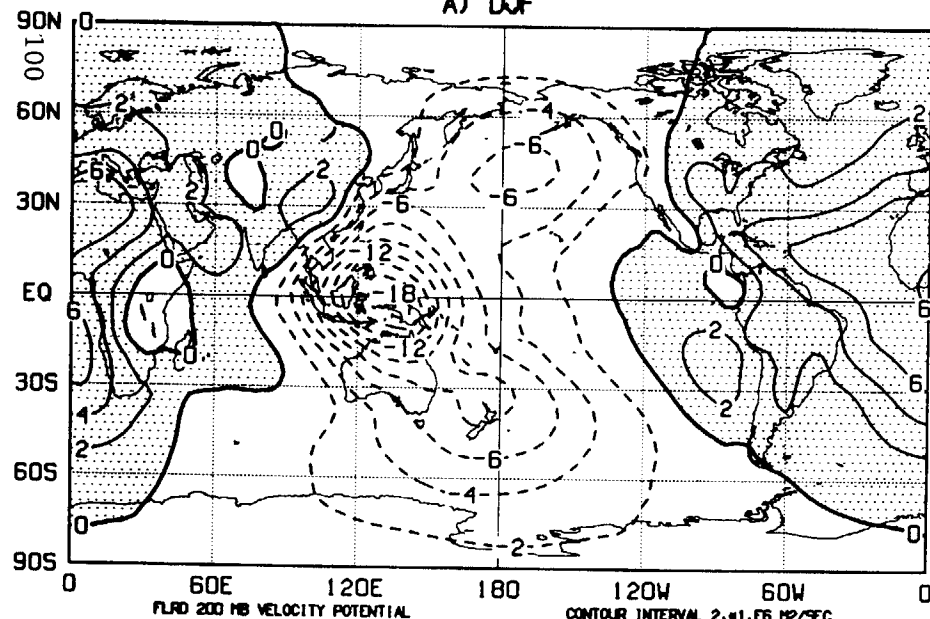




FLUD 200 MB VELOCITY POTENTIAL

CONTOUR INTERVAL 2. *1.E5 M2/SEC

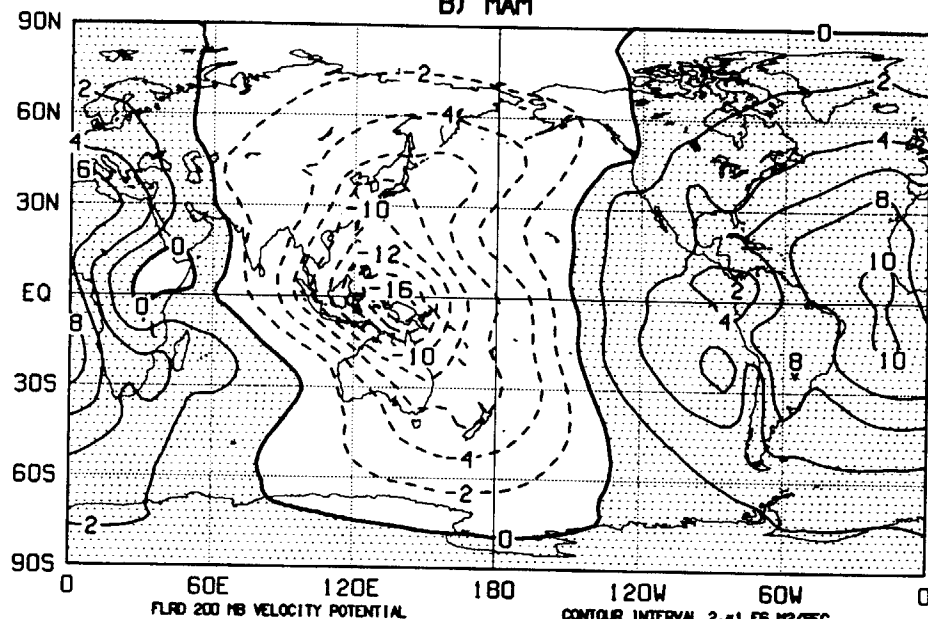
A) DJF



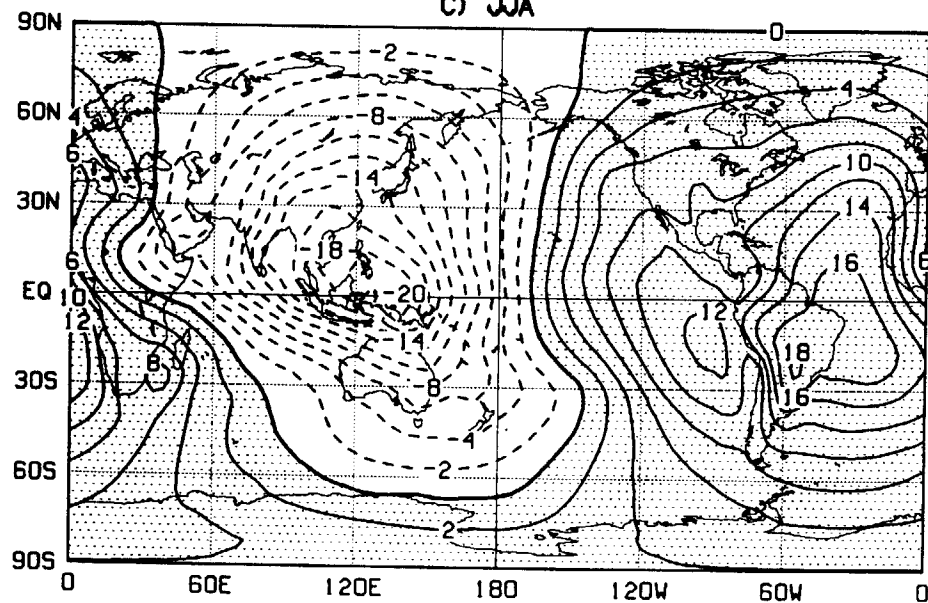
FLUD 200 MB VELOCITY POTENTIAL

CONTOUR INTERVAL 2. *1.E5 M2/SEC

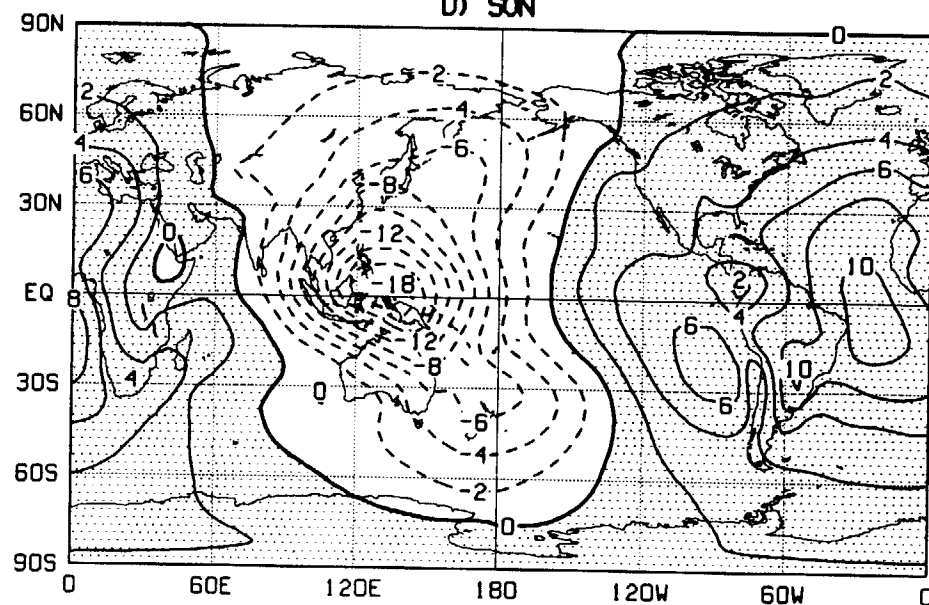
B) MAM



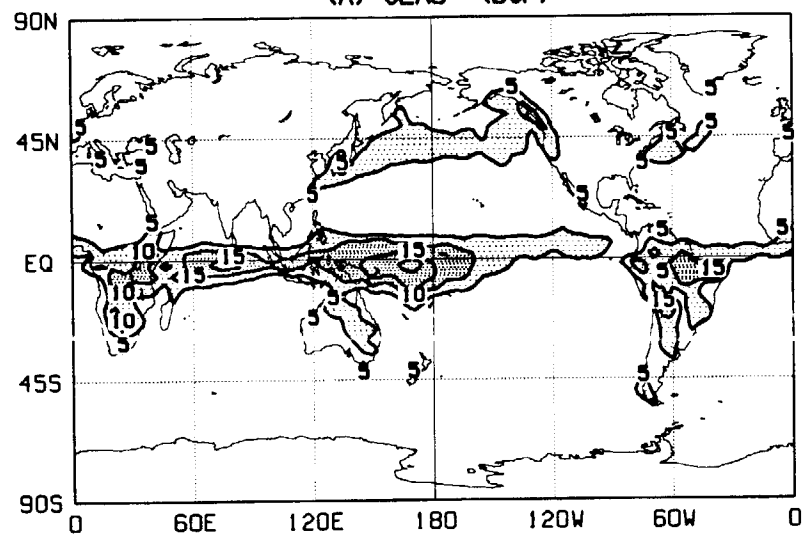
C) JJA



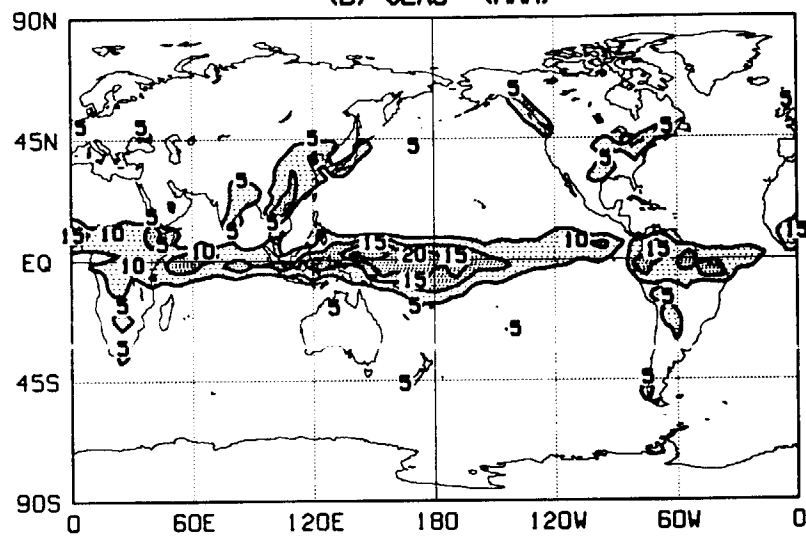
D) SON



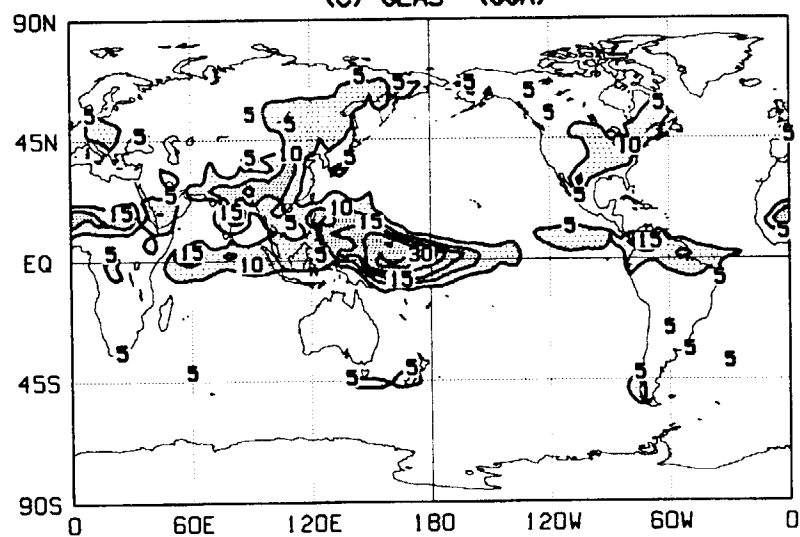
(A) GLAS (DJF)



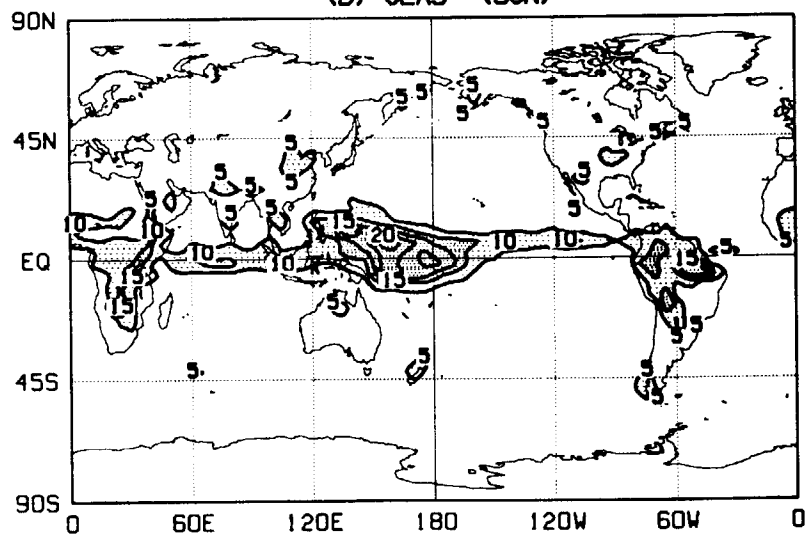
(B) GLAS (MAM)

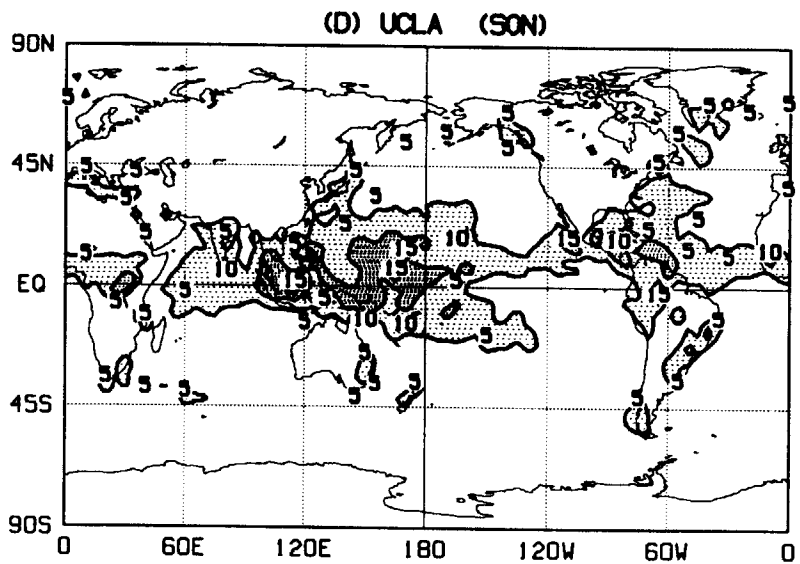
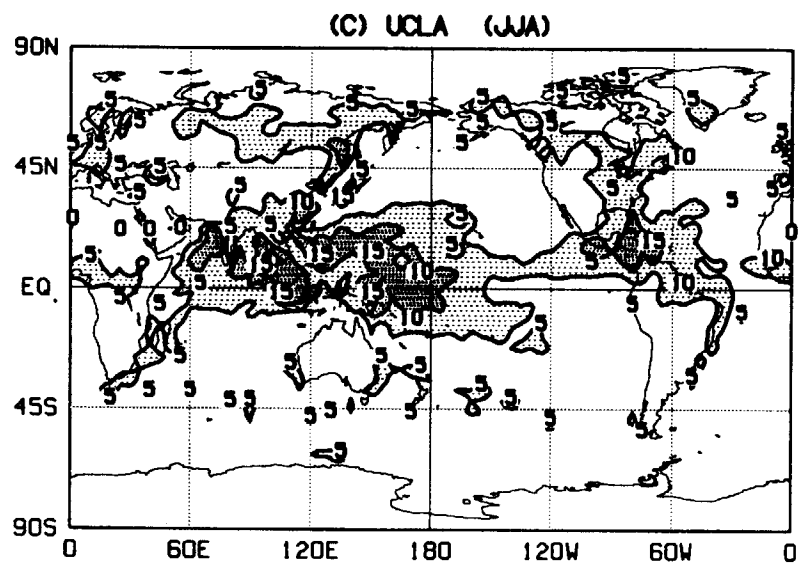
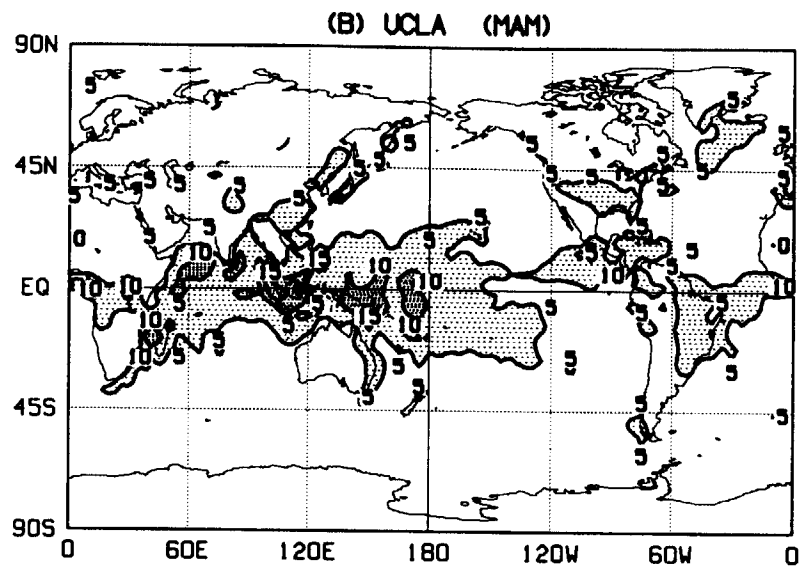
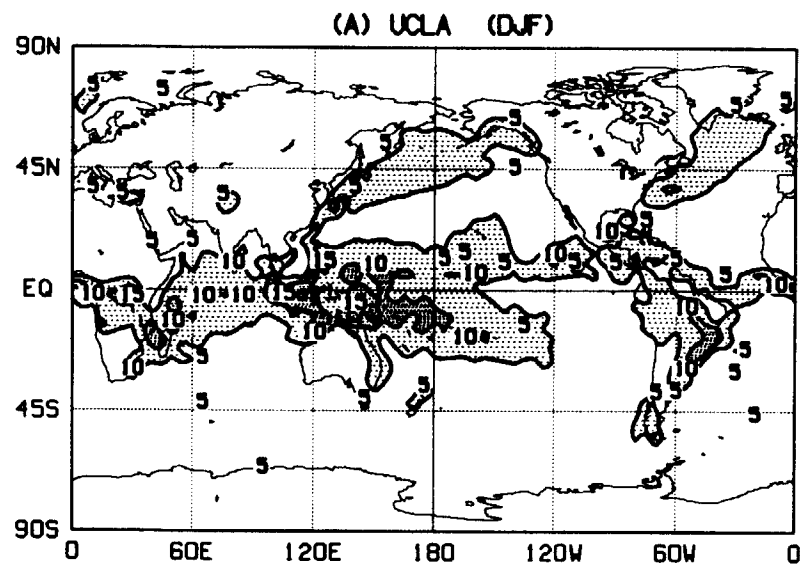


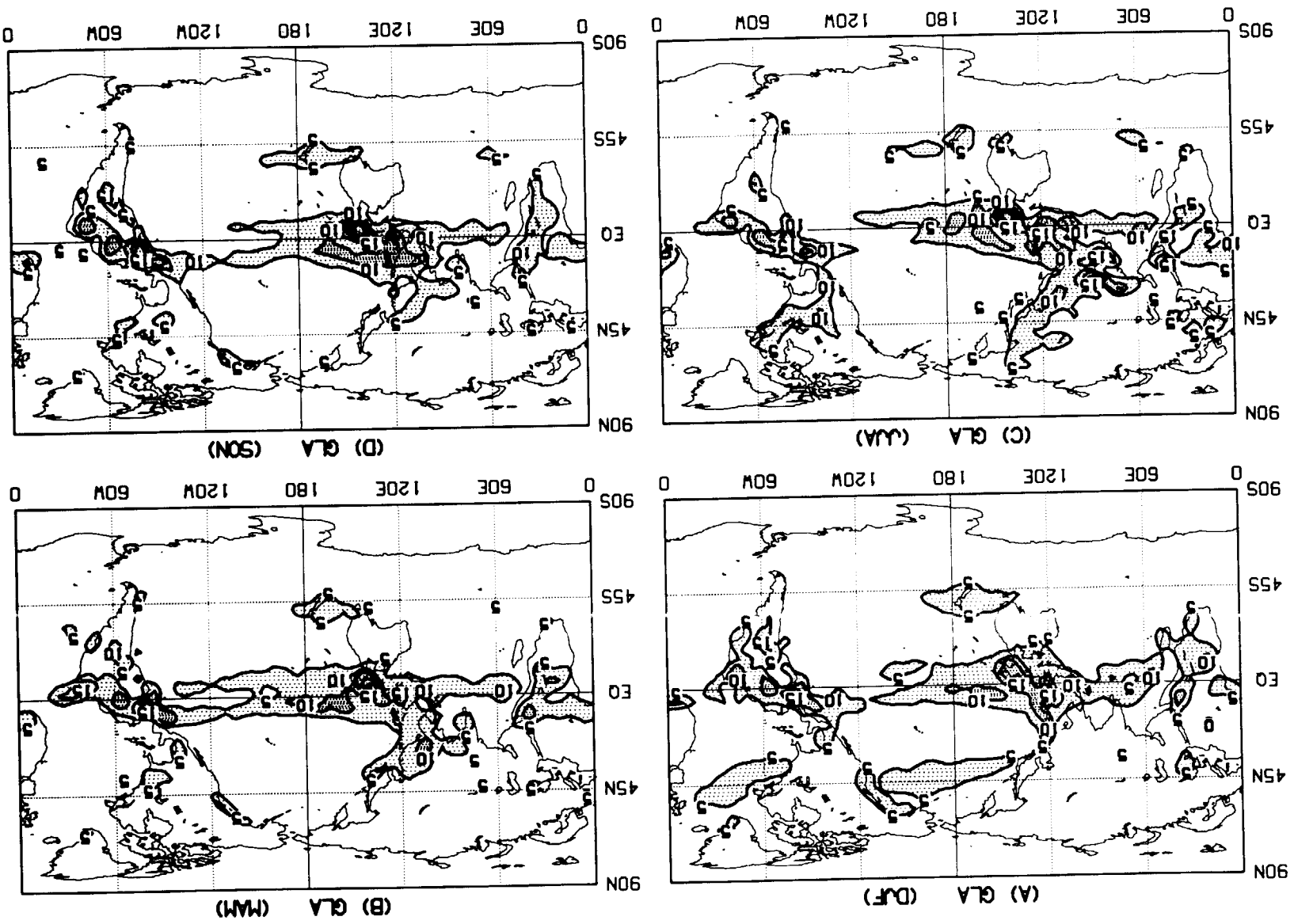
(C) GLAS (JJA)



(D) GLAS (SON)

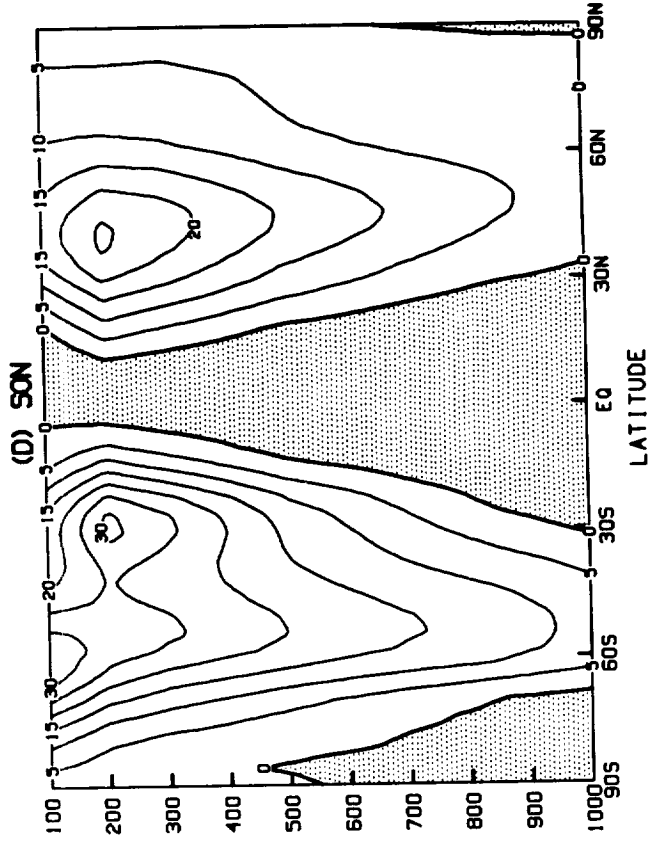
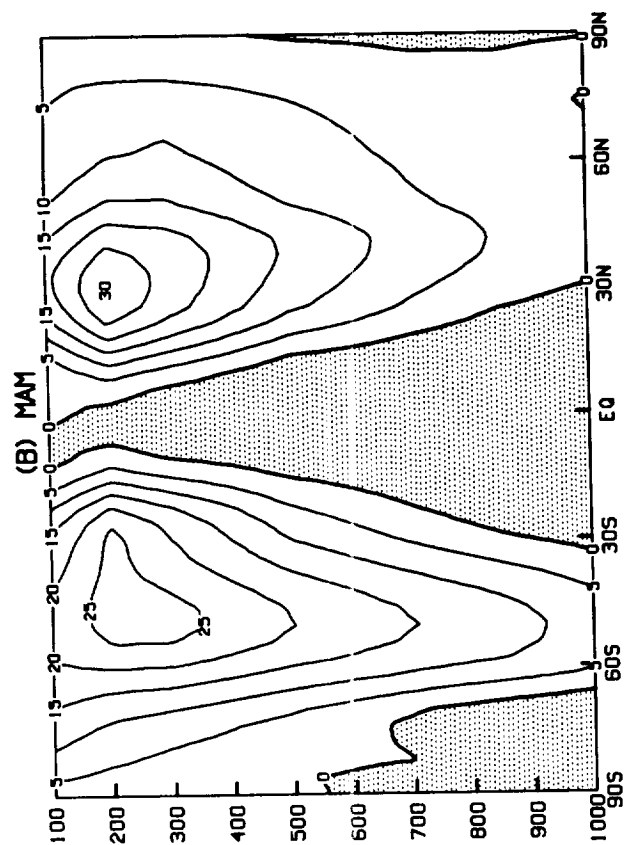
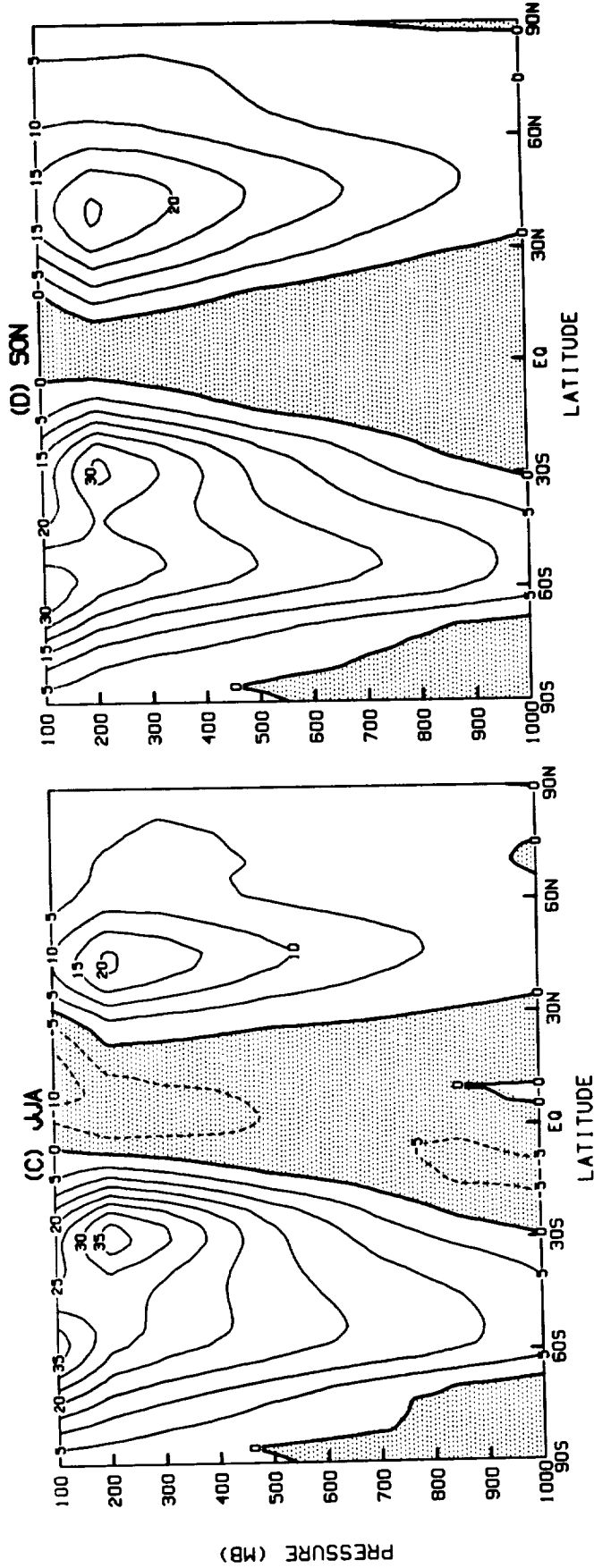
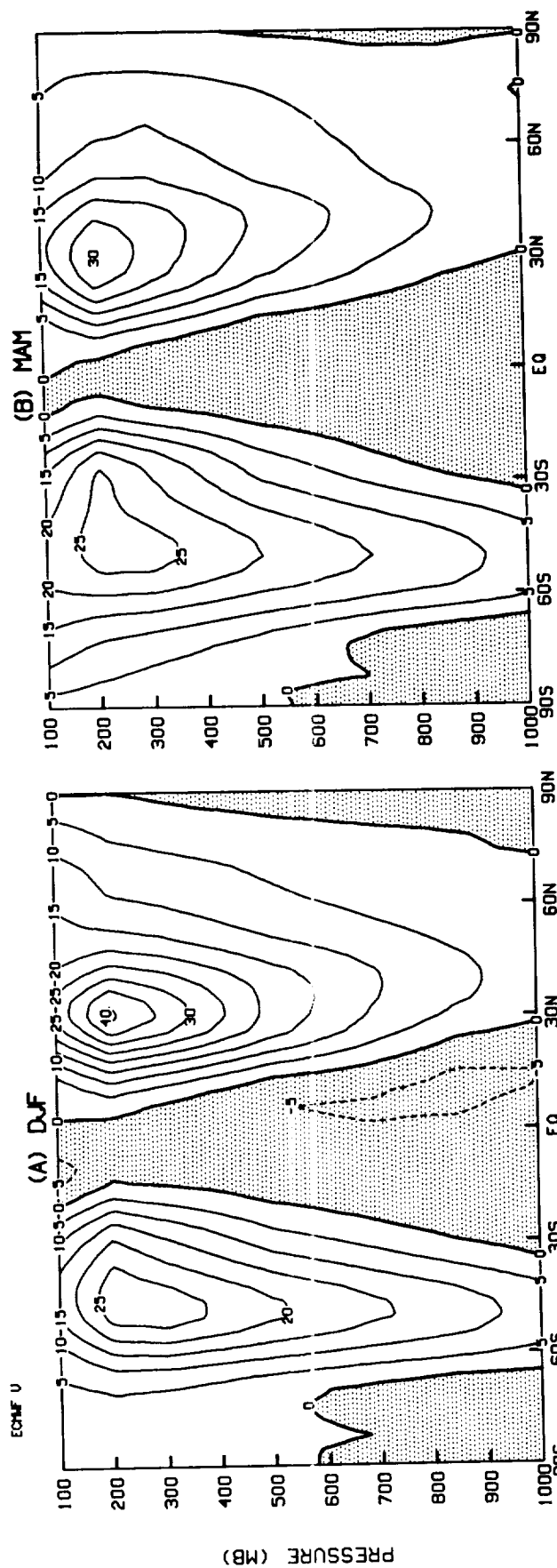




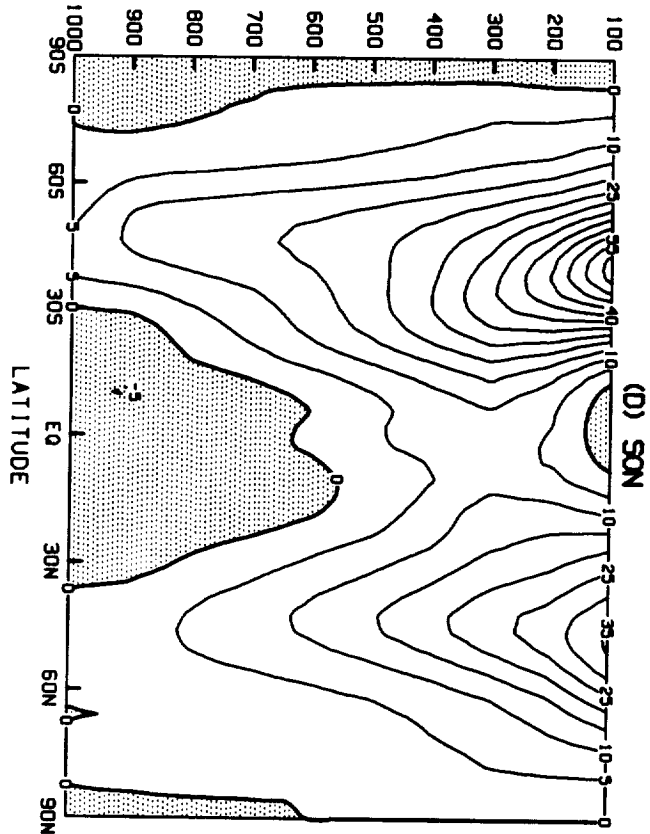
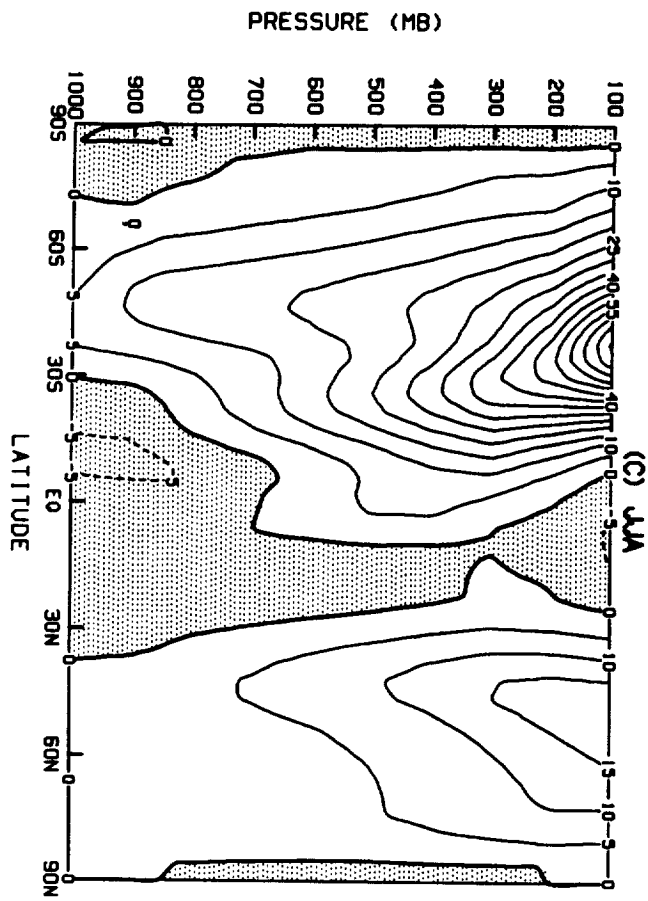
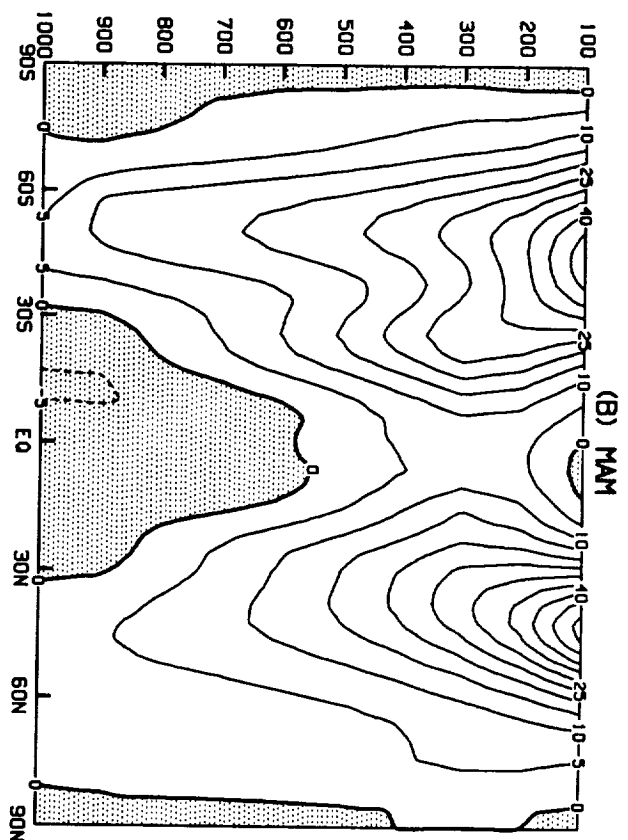
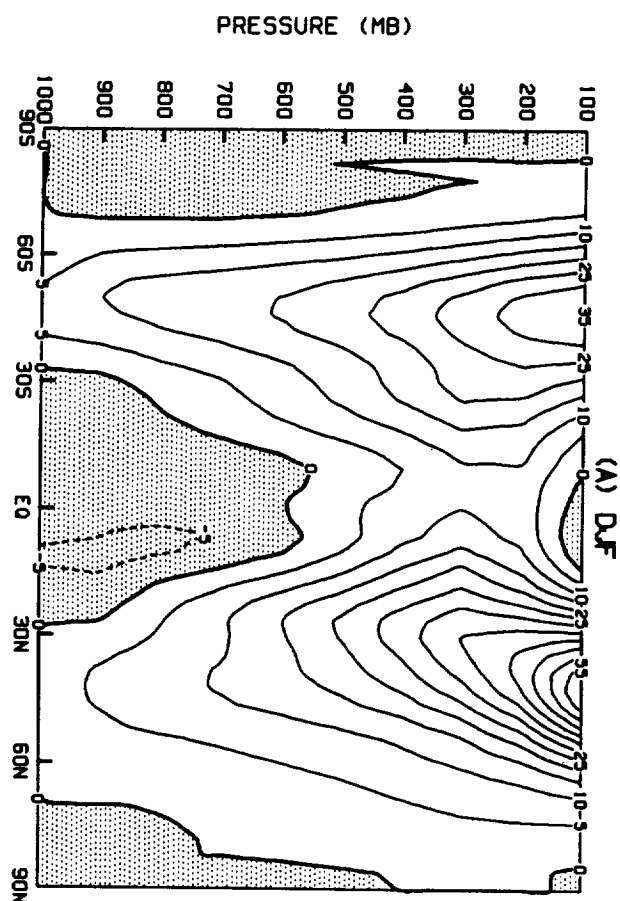


B. Latitude-pressure sections

- B1 Latitude-pressure sections of seasonal mean u-wind for ECMWF analyses.
Contour interval is 5.0 m s^{-1} . Easterlies are shaded.
- B2 Same as B1, except for GLAS GCM.
- B3 Same as B1, except for UCLA GCM.
- B4 Same as B1, except for GLA GCM.

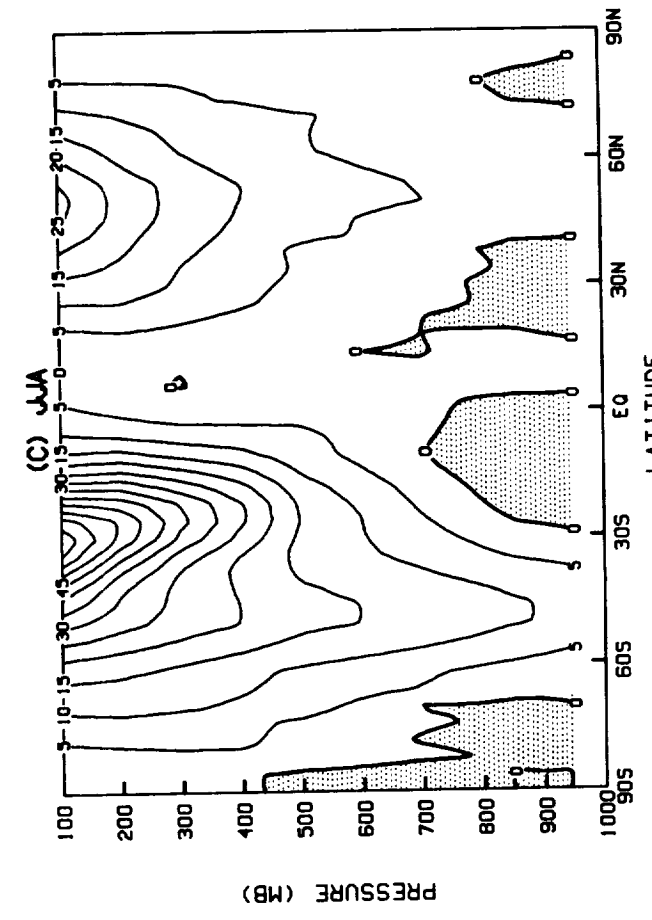
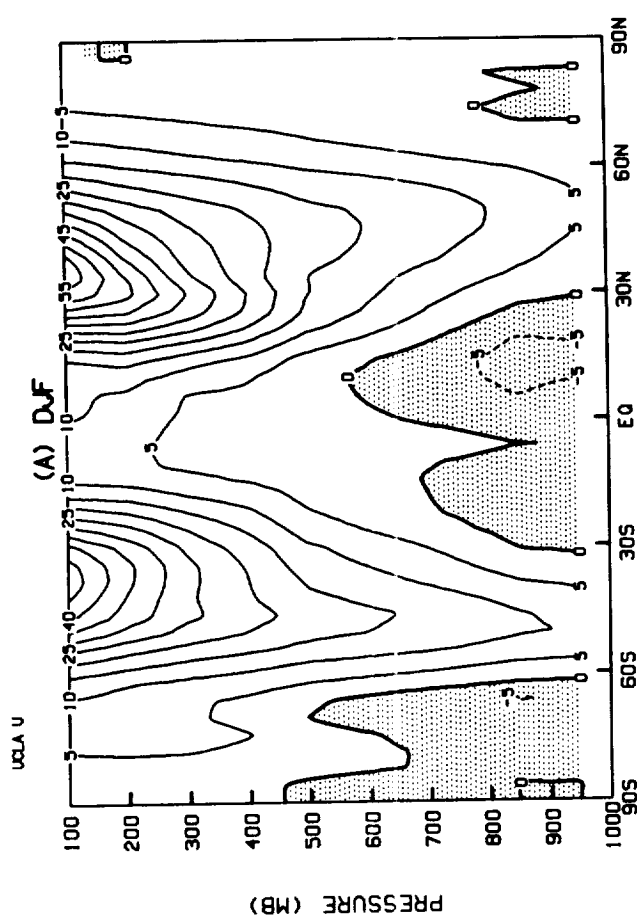
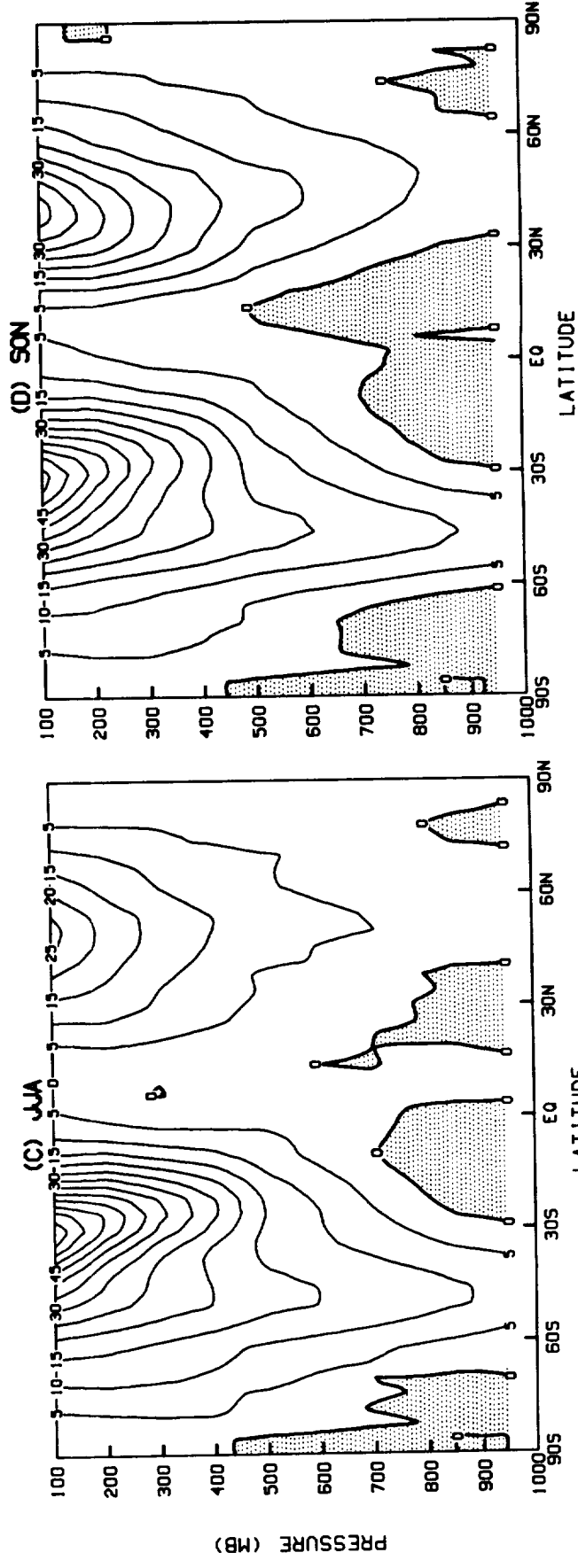
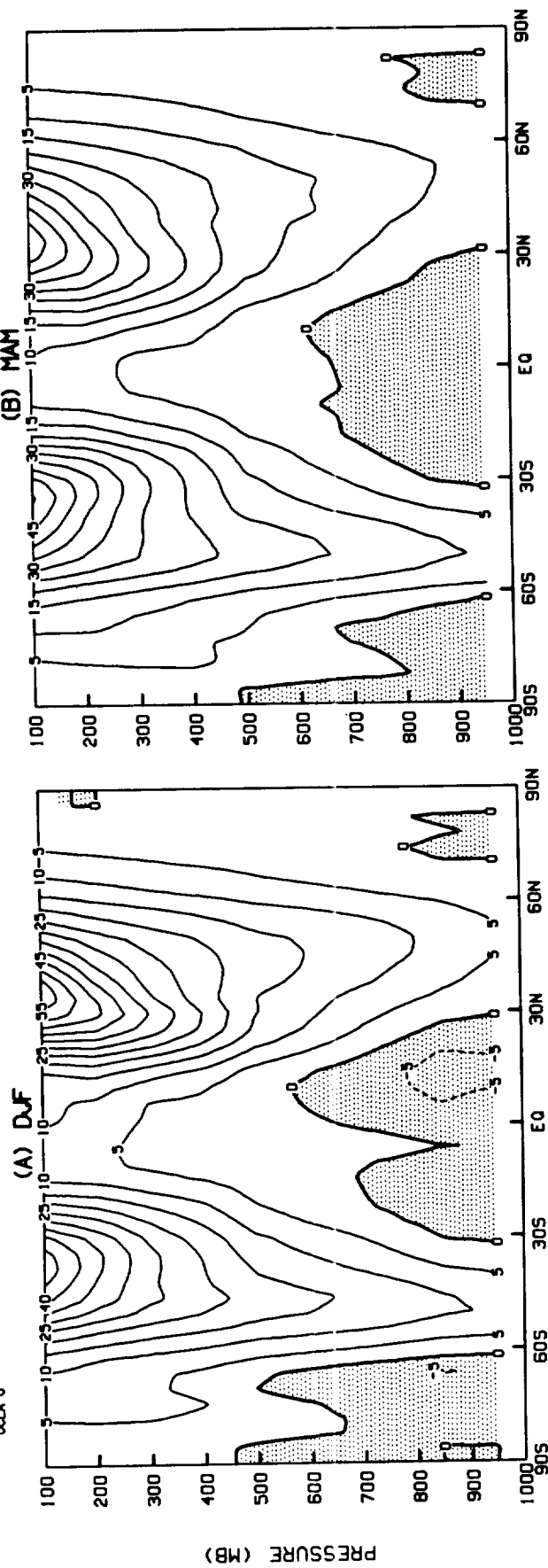


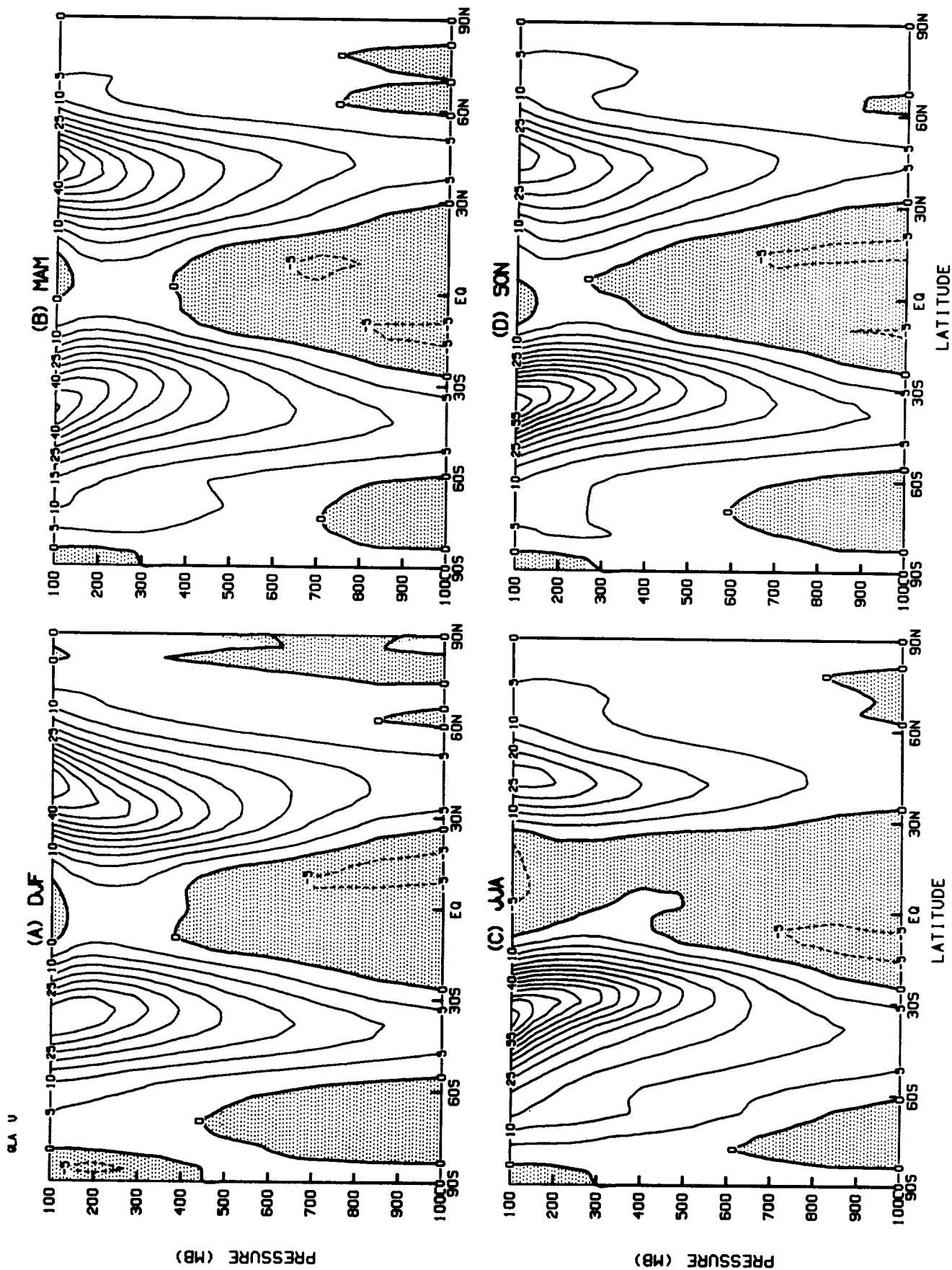
2.5 U



B2

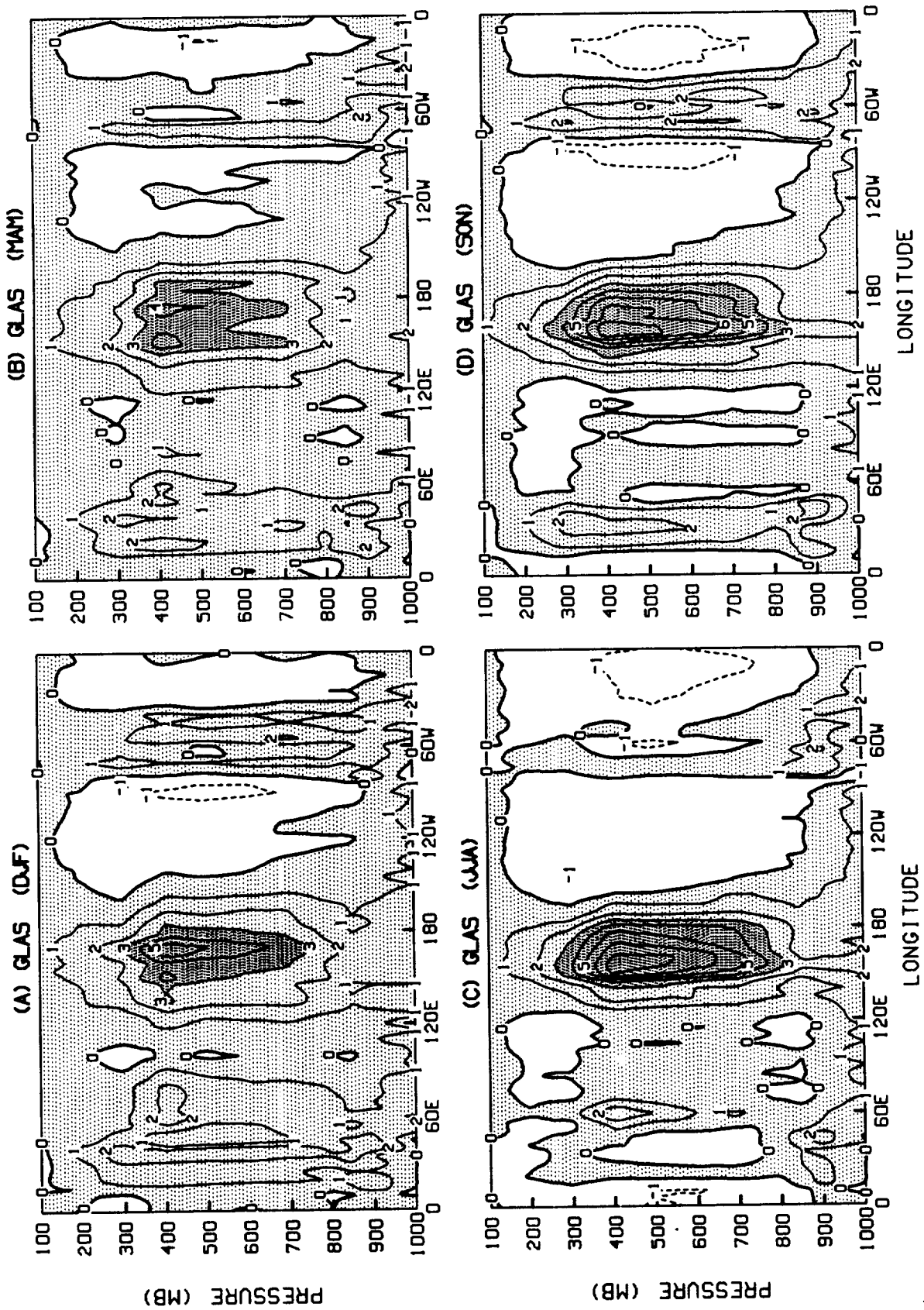
UCLA U

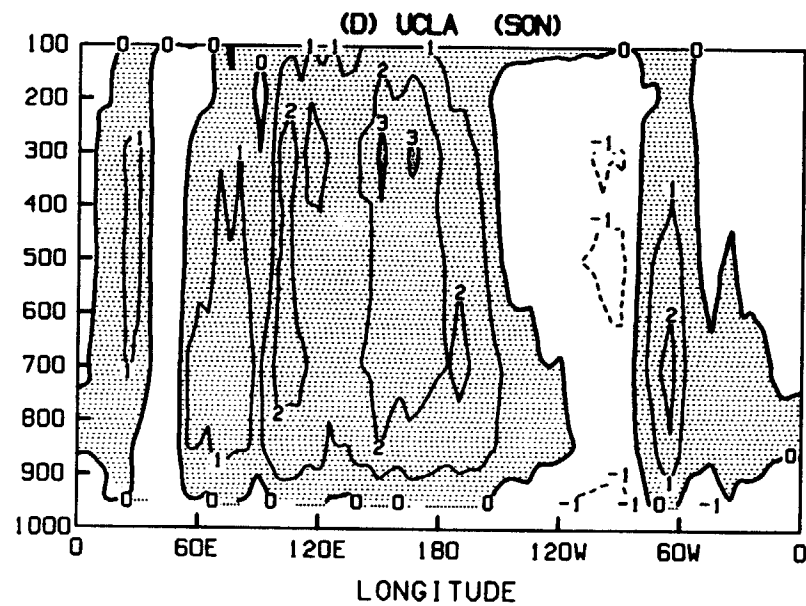
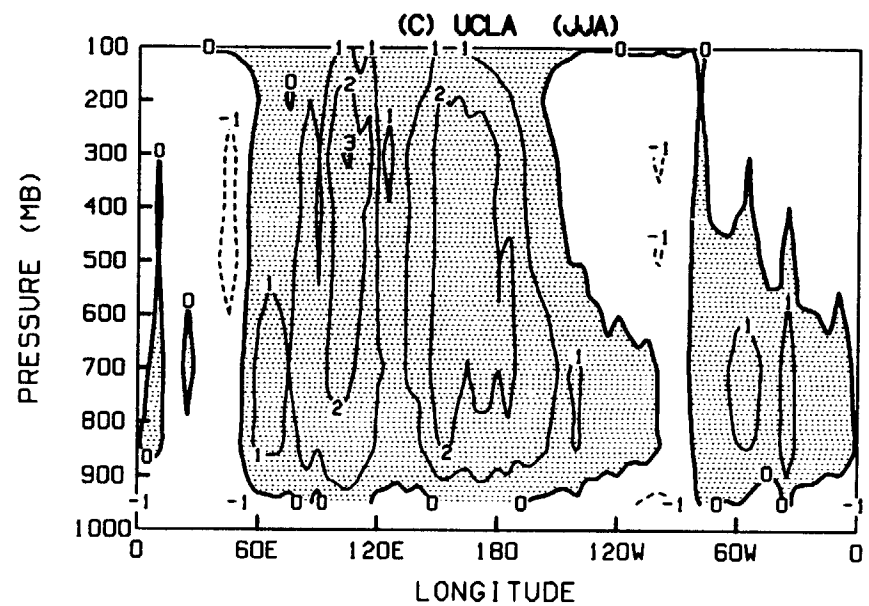
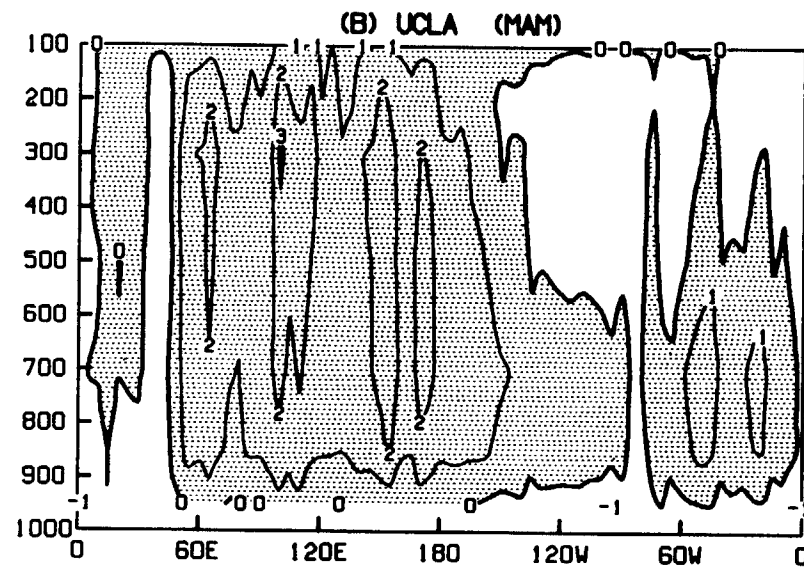
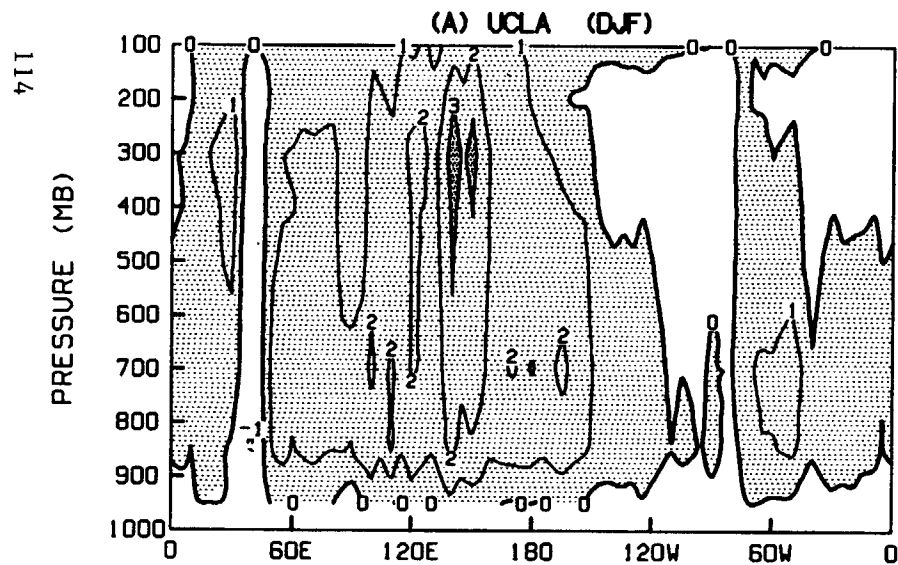


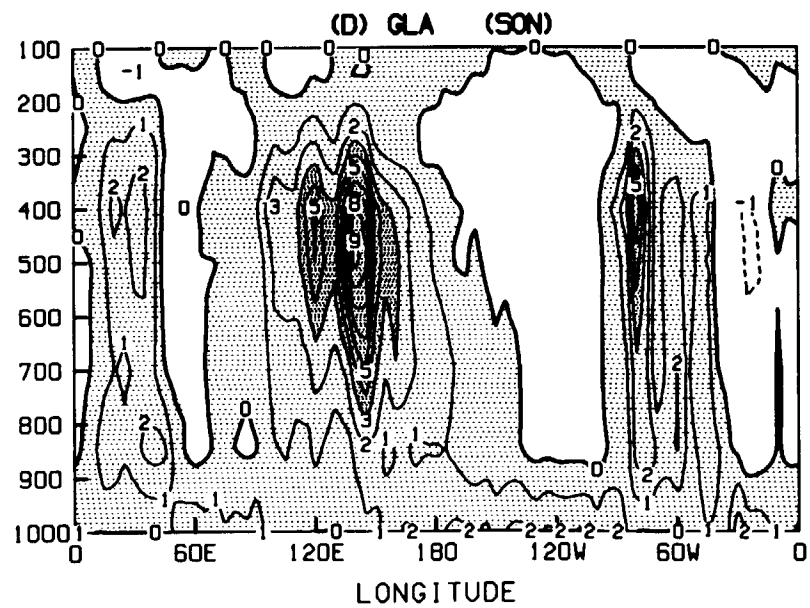
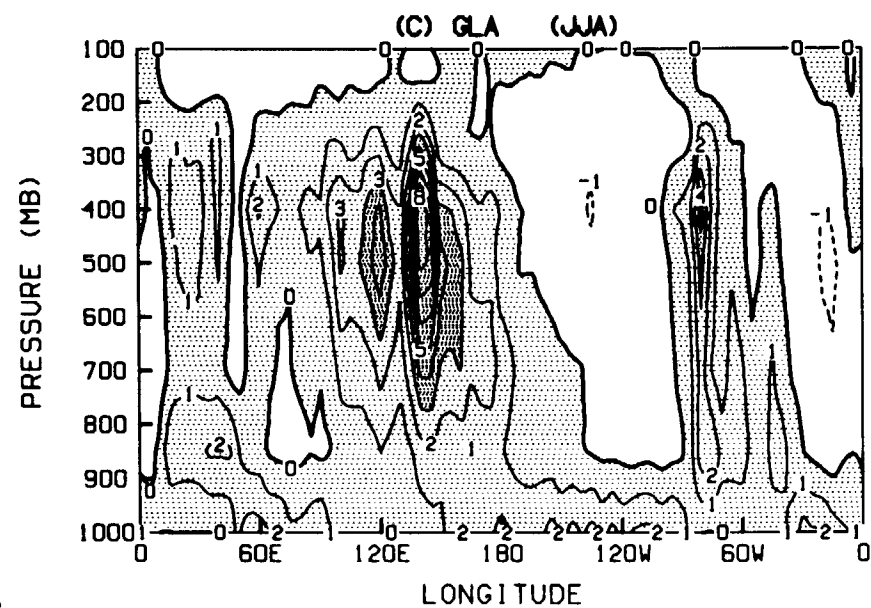
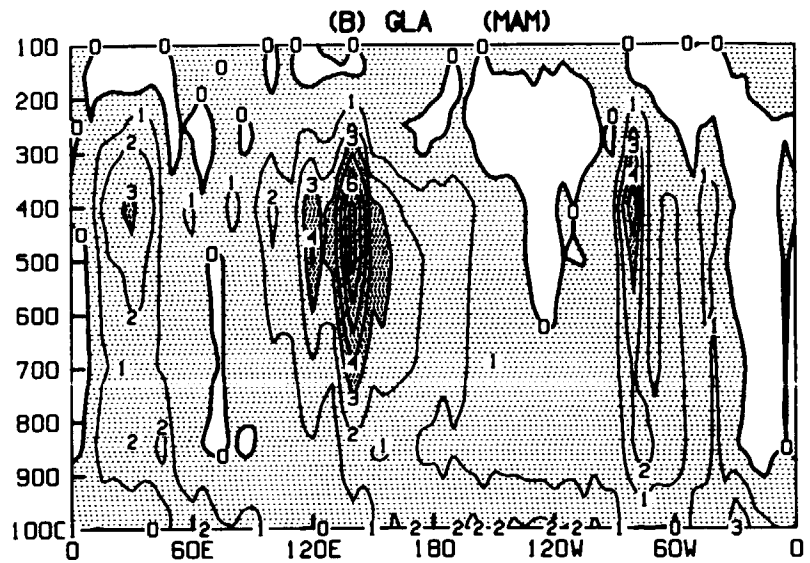
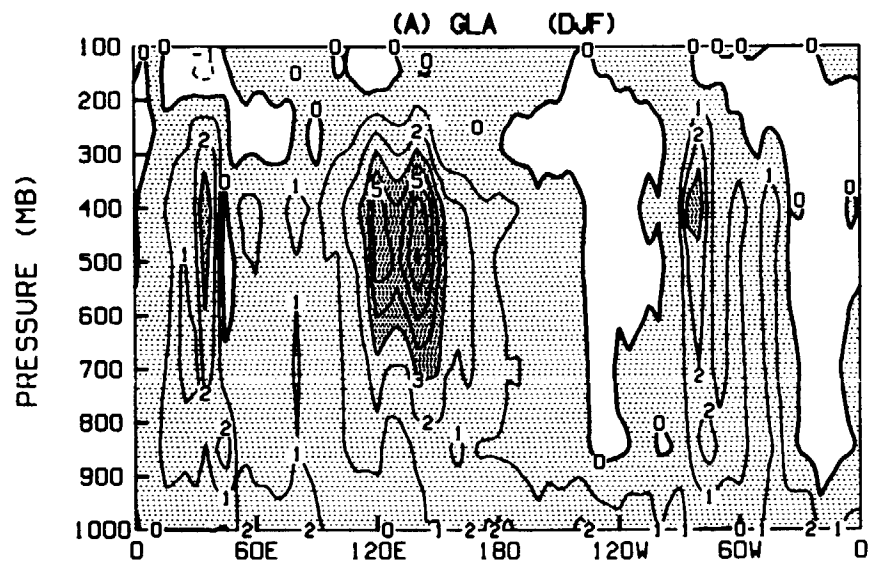


C. Longitude-pressure sections

- C1 Longitude-pressure sections of seasonal mean diabatic heating in the tropics (10°S-10°N) for GLAS GCM. Contour interval is 1.0 °K day⁻¹. Positive heatings are shaded and values greater than 3.0 °K day⁻¹ with darker shading.
- C2 Same as C1, except for UCLA GCM.
- C3 Same as C1, except for GLA GCM.







Report Documentation Page

1. Report No. NASA TM-100764		2. Government Accession No.		3. Recipient's Catalog No.	
4. Title and Subtitle An Intercomparison of Intraseasonal Variability in General Circulation Models and Observations				5. Report Date August 1990	
				6. Performing Organization Code 911	
7. Author(s) Chung-Kyu Park, David M. Straus, Ka-Ming Lau, and Siegfried D. Schubert				8. Performing Organization Report No. 90E02836	
				10. Work Unit No.	
9. Performing Organization Name and Address NASA/Goddard Space Flight Center Greenbelt, Maryland 20771				11. Contract or Grant No.	
				13. Type of Report and Period Covered Technical Memorandum	
12. Sponsoring Agency Name and Address National Aeronautics and Space Administration Washington, D.C. 20546-0001				14. Sponsoring Agency Code	
15. Supplementary Notes Chung-Kyu Park - Centel Federal Services Corporation, Reston, Virginia. David M. Straus - Department of Meteorology, University of Maryland, College Park, Maryland. Ka-Ming Lau and Siegfried D. Schubert - NASA/Goddard Space Flight Center, Greenbelt, Maryland.					
16. Abstract Low-frequency oscillations appearing in three GCM seasonal cycle integrations are compared with the analyses of the ECMWF. All three models have the same resolution: 4 degrees latitude by 5 degrees longitude, with 9 levels. The dominant phase speeds and the different vertical structure of the heating profiles in the GCMs are in general agreement with current theory involving the positive feedback between latent heating and moist static stability. All three GCMs fail to capture the detailed evolution in the different stages of the development and decay of the oscillation. The results suggest that an improvement in the boundary layer moisture processes may be crucial for a better simulation of the oscillation.					
17. Key Words (Suggested by Author(s)) Low-frequency oscillation General Circulation Model (GCM) ECMWF Seasonal Cycle Analyses				18. Distribution Statement Unclassified - Unlimited Subject Category 47	
19. Security Classif. (of this report) Unclassified		20. Security Classif. (of this page) Unclassified		21. No. of pages 121	
22. Price					

